ISSN: 3082-849X (Online)
Volume 1 · Issue 2
June 2025

Engineering Science in ADDITIVE MANUFACTURING

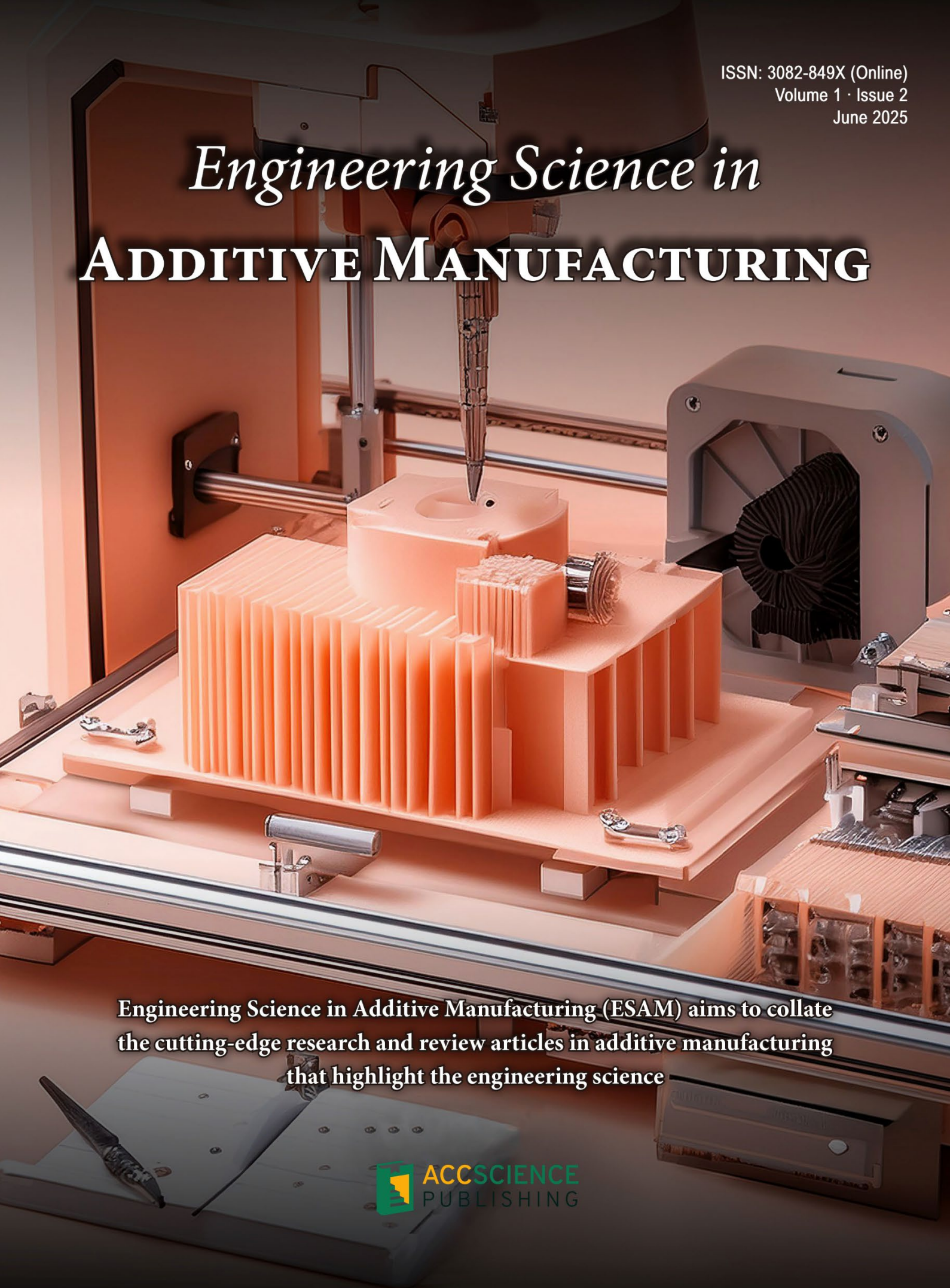

Engineering Science in Additive Manufacturing (ESAM) aims to collate the cutting-edge research and review articles in additive manufacturing that highlight the engineering science

ACCSCIENCE PUBLISHING

Engineering Science in Additive Manufacturing

Online ISSN: 3082-849X

Engineering Science in Additive Manufacturing (ESAM) aims to collate the cutting-edge research and review articles in additive manufacturing that highlight the engineering science. The journal covers all fundamentals of additive manufacturing, including its principles and applications. The journal publishes articles that acknowledge the significant development in the field and its disruptive nature in the industry. ESAM provides a platform for publishing articles that advance the in-depth understanding of additive manufacturing. The journal also welcomes papers that employ theories, numerical methods and/or simulations that demonstrate relevance to the additive manufacturing community.

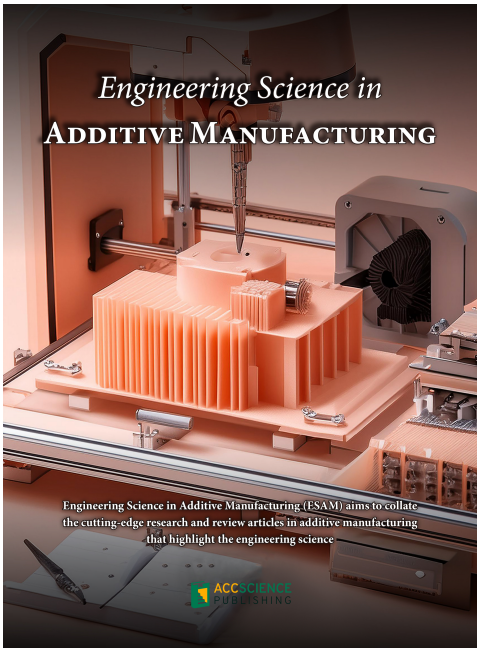

About the Publisher

AccScience Publishing is a publishing company based in Singapore. We publish a range of high-quality, open-access, peer-reviewed journals and books from a broad spectrum of disciplines.

Contact Us

Managing Editor
esam.office@accscience.sg

AccScience Publishing
9 Raffles Place, Republic Plaza 1 #06-00 Singapore 048619.

Volume 1 • Issue 2 • June 2025
ISSN 3082-849X (online)

ENGINEERING SCIENCE IN ADDITIVE MANUFACTURING

Editor-in-Chief
Swee Leong Sing
National University of Singapore, Singapore

ACCSCIENCE PUBLISHING
Access Science Without Barriers

ENGINEERING SCIENCE IN ADDITIVE MANUFACTURING

ISSN: 3082-849X (online)

Editorial and Production Credits

Publisher: AccScience Publishing
Managing Editor: Shirley Lu
Production Editor: Sharmila Velapasamy
Article Layout and Typeset: Sinjore Technologies (India)

For all advertising queries, contact esam.office@accscience.sg.

Supplementary file

Supplementary files of articles can be obtained at https://accscience.com/journal/ESAM/1/2.

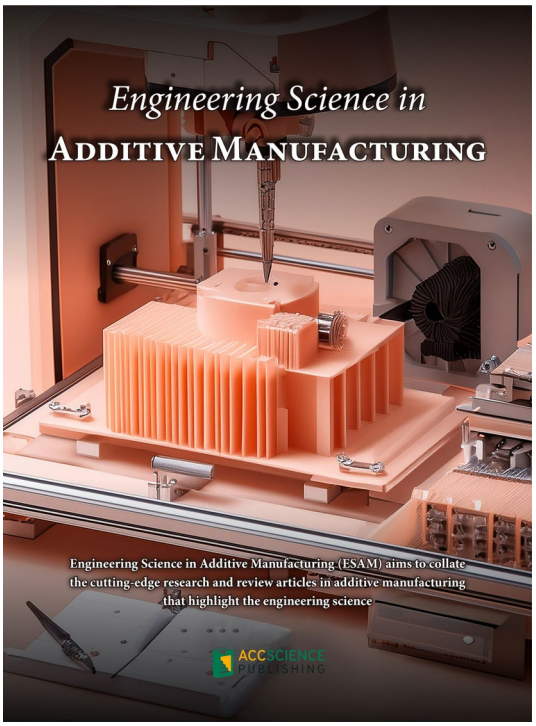

Disclaimer

AccScience Publishing is not liable to the statements, perspectives, and opinions contained in the publications. The appearance of advertisements in the journal shall not be construed as a warranty, endorsement, or approval of the products or services advertised and/or the safety thereof. AccScience Publishing disclaims responsibility for any injury to persons or property resulting from any ideas or products referred to in the publications or advertisements. AccScience Publishing remains neutral with regard to jurisdictional claims in published maps and institutional affiliations.

Engineering Science in Additive Manufacturing

Editorial Board

Editor-in-Chief

*Editorial Board Members**

ACCSCIENCE PUBLISHING

Volume 1 | Issue 2 | June 2025

Engineering Science in Additive Manufacturing

https://accscience.com/journal/ESAM

CONTENTS

ACCSCIENCE PUBLISHING

Engineering Science in Additive Manufacturing

REVIEW ARTICLE

Recent progress in electromagnetic microwave absorption of additively manufactured carbon fiber-reinforced polymer structures

Quanjin Ma[1†], Ke Dong[1†], Feirui Li[1†], Yanjie Wu[2†], Jing Tian[2], Ming Yu[3], and Yi Xiong[1*]

[1]School of Automation and Intelligent Manufacturing, Southern University of Science and Technology, Shenzhen, Guangdong, China

[2]School of Electronic Science and Engineering, University of Electronic Science and Technology of China, Chengdu, Sichuan, China

[3]Department of Electronic and Electrical Engineering, Southern University of Science and Technology, Shenzhen, Guangdong, China

Abstract

Recent advances in additive manufacturing have significantly expanded the design and fabrication capabilities of carbon fiber-reinforced polymer (CFRP) structures, particularly in the context of electromagnetic microwave absorption (EMWA). This review provides a comprehensive overview of the current state of research on EMWA properties of additively manufactured CFRP structures, focusing on EMWA mechanisms, polymer material, and additively manufactured microwave absorbers. Key topics include the EMWA mechanisms inherent to various fiber-reinforced materials and the role of additive manufacturing processes in tailoring EMWA performance. Moreover, the review paper summarizes the electromagnetic characteristics of various fiber-reinforced materials and evaluates the microwave absorption performance of additively manufactured absorbers, highlighting the trade-offs between electromagnetic and load-bearing performance. Furthermore, challenges and future perspectives are discussed to provide new insights into enhancing EMWA and balancing EMWA with load-bearing capabilities. It explores new possibilities for next-generation advanced additively manufactured CFRP microwave absorbers that maintain excellent load-bearing properties.

Keywords: Electromagnetic microwave absorption; Microwave absorption mechanism; Microwave absorber; Additive manufacturing; Microwave absorbing materials; Load-bearing performance

†*These authors contributed equally to this work.*

***Corresponding author:**
Yi Xiong
(xiongy3@sustech.edu.cn)

Citation: Ma Q, Dong K, Li F. Recent progress in electromagnetic microwave absorption of additively manufactured carbon fiber-reinforced polymer structures. *Eng Sci Add Manuf.* 2025;1(2):025160008. doi: 10.36922/ESAM025160008

Received: April 15, 2025

Revised: June 3, 2025

Accepted: June 4, 2025

Published online: June 16, 2025

1. Introduction

With the development of radar technology and increased utilization of electromagnetic waves, the problem of electromagnetic pollution has grown more serious, necessitating immediate redress. To reduce electromagnetic interference (EMI) in military, industrial, and residential applications, it is imperative to develop novel materials for electromagnetic microwave absorption (EMWA).[1] EMWA uses various materials, including carbon- and ferrite-based materials, ceramic materials have recently drawn much interest because of

their exceptional strength, chemical stability, lightweight nature, and high-temperature resilience.[2,3] Concerns around EMI, or interference from electronic components impacting the environment, have been raised owing to the utilization of several electronic products.[4-7] Due to its low voltage and high integration, modern electronic equipment is vulnerable to EMI, which can seriously impair its functionality. For example, Shi *et al.*[8] investigated the 3D-printed carbon-based conformal EMI shielding module for integrated electronics, which exhibited an ultralight architecture (0.076 $g{\cdot}m^{-3}$) and remarkable shielding effectiveness capability (61.4 dB). Furthermore, it is impossible to ignore the possible harm to human health, given the extensive usage of electronic devices. Therefore, effective electromagnetic absorption (EMA) techniques are essential to resolving these problems, and materials that can absorb electromagnetic fields have attracted interest.[1] These absorbed materials can reduce electromagnetic waves by either reflecting them on their surface, absorbing and dissipating them within the material, or using both strategies, depending on their specific characteristics.[9]

A type of functional material that may absorb or drastically reduce microwaves that shine on their surfaces is known as microwave-absorbing material. Functional material has been widely used in sensor design, electromagnetic protection, aircraft electromagnetic stealth, and other areas.[10] Recently, many functional materials that absorb electromagnetic radiation have been studied.[11-13] For example, Zhang *et al.*[14] proposed the facile preparation strategy to construct 3D reduced graphene oxide-supported N-doped carbon nanotube (CNT) on reduced graphene oxide as multi-functional materials, which showed a minimal reflection loss of −33.2 dB at 13.3 GHz. Carbon fibers (CFs) and carbon-based composites are superior microwave-absorbing materials, which are lightweight, corrosion-resistant, electrically conductive, environmentally stable, compatible with mass production, and amenable to design freedom, with examples including CF,[15] graphene,[16] carbon black,[17] and nanotube materials.[18] However, because of its better dielectric qualities, CF materials have various disadvantages, such as poor impedance matching, which may perform better in microwave absorption since it does not lose magnetic energy.[19] Consequently, the modification of CF-reinforced polymer (CFRP) composites is the main research interest in improving microwave absorption with excellent mechanical performance.[20] For example, Tang *et al.*[21] prepared lightweight zirconium-modified carbon-carbon composites to improve oxidation resistance, which reached a minimum reflection loss (RL_{min}) of −61.1 dB. The incorporation of zirconium can make the composites exhibit better microwave absorption performance.

Many researchers are interested in additive manufacturing to create materials that absorb microwave radiation.[22,23] These printable materials can be made by attaching conductive films to the surface of the structure, applying microwave-absorbing coatings, or incorporating electrical or magnetic absorbers into the printing matrix. Although its mechanical characteristics, shape memory effects, and functional structures have been extensively studied, several works have investigated microwave absorption. For example, Gao *et al.*[24] performed the long continuous CF (LCCF) to reach strong electromagnetic performance and excellent mechanical strength. It achieved broadband effective absorption (reflection loss, RL < −10 dB) over the frequency range of 3.4 – 18 GHz with maximum bending strength of 110.5 MPa. Therefore, in microwave-absorbing materials, the CF-reinforced 3D printing technique has great potential for research and application.[25] Multimaterial 3D printing has emerged as a promising research direction for tailoring EMWA properties by precisely controlling material composition and structural design.[2,26,27] For instance, Zhang *et al.*[27] conducted multi-material fused deposition modeling (FDM) to manufacture structural-functional integrated absorbers with multiscale structures possessing tunable broadband microwave absorption. It provides new insights and a novel approach to the design and rapid fabrication of lightweight structural absorbers.

Machine learning (ML) has emerged as a powerful tool for optimizing multifunctional CFRP structures that balance mechanical strength and EMA performance.[28] Traditional trial-and-error approaches are often time-consuming and limited in handling complex design constraints.[29] ML algorithms, particularly deep neural networks (DNNs) and genetic algorithm (GA)-based optimization can efficiently explore vast design spaces by correlating processing parameters, microstructural features, and performance metrics.[30] For example, Wang *et al.*[31] developed the ML-based method for co-design and optimization of microwave-absorbing/load-bearing multifunctional structures. It was indicated that the optimized multi-functional structure achieved more than 90% absorption in the frequency range of 2.5 – 18.0 GHz and superior load-bearing performance. Zhang *et al.*[32] investigated the evolutionary algorithm-based integrated design of material-structural microwave absorption on radiant honeycomb metastructure. It achieved the integration of material functionality and structural design and provided effective absorption across a broad frequency range. The integration of additive manufacturing, advanced materials, and ML-driven optimization holds great promise for realizing multi-functional CFRP structures with superior mechanical and EMA properties.

This review article summarizes the EMWA properties of CFRP composites, focusing on experimental research and material design strategies. The paper also examines key factors influencing mechanical and EMWA performance, including CFRP preparation techniques, fiber orientation, distribution, and volume fraction, as well as methods to enhance microwave absorption capabilities. A comparative analysis of various CFRP modification approaches highlights the trade-offs between strategies, offering insights into optimizing material properties for specific applications. The review article also explores future research directions to develop advanced CFRP-based EMWA composites for industrial use, emphasizing the potential to address current challenges and inspire further innovation in high-performance EMWA materials.

2. Electromagnetic microwave absorption mechanism

Figure 1 illustrates the reflection, refractive index, and scattering of electromagnetic waves that strike an object's surface. The term "EMA material" is a classification material that can both absorb and project electromagnetic wave energy onto their surface and significantly attenuate the energy received on their surface.[33] It reduces electromagnetic wave interference by reflecting, refracting, and scattering little energy. Matching properties and attenuation characteristics are the main requirements for materials to achieve effective EMA. The EMWA mechanism for fiber-reinforced polymer constructions that are additively built is summarized in Table 1.

2.1. Impedance matching

Equation I is typically used to compute the impedance matching, which represents the human-emitted electromagnetic wave's capacity for reflection.

$$\left|\frac{Z_{in}}{Z_o}\right| = \sqrt{\frac{\mu_r}{\varepsilon_r}} tanh\left[j\left(\frac{2\pi}{c}\right)\sqrt{\mu_r \varepsilon_r}\, fd \right] \quad \text{(I)}$$

where Z_{in} is the input impedance, Z_o is the free-space impedance, μ_r is the complex permeability, ε_r is the complex permittivity, j is an imaginary unit, c is the speed of light in vacuum, f is the frequency of the electromagnetic wave, and d is the thickness of the EMA material.

2.2. Attenuation constant

The degree to which the EMA material can absorb the electromagnetic wave is indicated by the attenuation coefficient α, which shows the electromagnetic wave's attenuation ability per unit length. A significant portion of the electromagnetic wave energy within the targeted frequency range must be absorbed by the EMA material and converted into other types of energy. Typically, Equation II is used to calculate the attenuation coefficient:

$$\alpha = \frac{\sqrt{2}\pi f}{c} \times \sqrt{\left(\mu''\varepsilon - \mu'\varepsilon'\right) + \sqrt{\left(\mu''\varepsilon - \mu'\varepsilon'\right)^2 + \left(\mu''\varepsilon + \mu'\varepsilon'\right)^2}} \quad \text{(II)}$$

where f electromagnetic wave frequency, c is the speed of light in a vacuum, ε' is the real part of complex permittivity, ε'' is the imaginary part of complex permittivity, μ' is the real part of complex permeability, and μ'' is the imaginary part of complex permeability.

2.3. Reflection loss

When waves are reflected, reflection loss takes place, necessitating an effective shield to deflect most incident electromagnetic waves. When charged particles in a conductive substance interact with the electromagnetic field, reflection loss results. The amount of loss energy is correlated with the material's magnetic permeability concerning a vacuum (μ_r) and electrical conductivity (σ_r). Generally, the percentage of electromagnetic waves that result in reflection losses increases with an EMA material's electrical conductivity and decreases with its magnetic permeability.

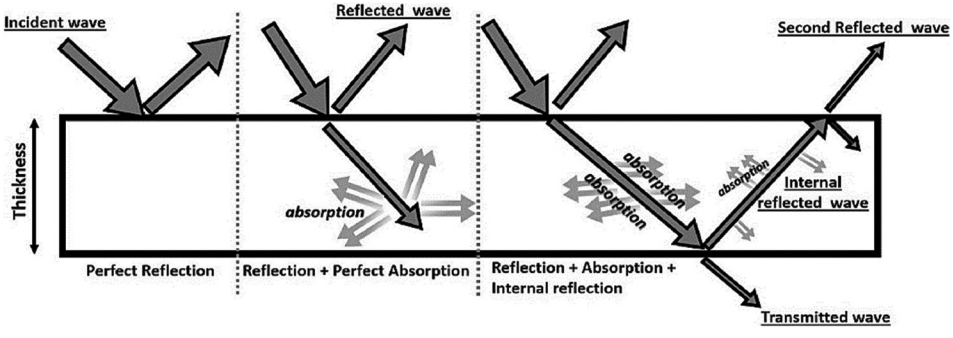

Figure 1. Electromagnetic wave interaction and absorption mechanism.[34] Copyright © 2020 Elsevier. Reproduced with permission of Elsevier.

Table 1. Summary of electromagnetic microwave absorption mechanism in additively manufactured carbon fiber-reinforced polymer structures

Mechanism type	Description	Typical frequency range (GHz)	Main parameters	Advantages	Limitations	Optimization strategies
Impedance matching	Minimizes reflection by aligning material's wave impedance with free space	Broadband (2 – 18 GHz)	Relative permittivity, permeability, thickness	Maximizes microwave entry into the material	Sensitive to frequency and thickness variations	Graded porosity or multilayer designs
Attenuation constant	Measures the microwaves lose energy in the material	Varies	Dielectric/magnetic loss, conductivity	Stronger attenuation means better absorption	Balance with impedance matching	Optimizes carbon fiber alignment and infill density
Reflection loss	Quantifies the microwave energy absorbed rather than reflected	Tunable for specific bands	Surface impedance, thickness	A direct indicator of absorption performance	Requires precise thickness control	Designs metamaterial surfaces (honeycomb, pyramids)
Dielectric loss	Energy absorption through charge polarization and conduction	Effective at higher frequencies	Dielectric loss tangent, conductivity	Naturally high in CFRPs due to carbon fibers	Can cause an impedance mismatch	Adds nano-fillers like graphene; control fiber orientation
Magnetic loss	Energy dissipation through magnetic interactions	Best at 1 – 10 GHz	Magnetic loss tangent, resonance effects	Enhances low-frequency absorption	Requires magnetic additives	Incorporates ferrite particles
Interference loss	Cancels waves through strategic phase differences	Narrowband (tunable)	Layer thickness, reflection phases	Enables thin absorbers	Narrow effective bandwidth	Alternating layers with precise thickness

Abbreviation: CFRP: Carbon fiber-reinforced polymer.

2.4. Dielectric loss

Electromagnetic waves interact with a dielectric medium to create carriers that can conduct electricity through the material. Figure 2 shows internal dielectric current and loss in various scenarios. When applied, an electric field causes a conduction current, which causes electrical energy to dissipate and dielectric losses. Displacement or capacitance current is the phrase used to describe the current that does not release energy when charged geometrically. Polarization relaxation is associated with the conduction current produced in an alternating electric field by EMA materials with a particular conductivity. It appears as a polarized effect inside the electric field and is caused by the loss of polarization. Dielectric relaxation loss (tgδrel) will occur if the polarization rate is slower than the electric field fluctuation rate. The current is connected to the free charge and results in losses as conductivity losses ($tg\delta_c$) are produced by the medium's conductivity.

The net efficiency parameter of the energy transfer process is the dielectric loss tangent angle ($\tan\delta_e$). The greater $\tan\delta_e$ indicates enhanced coupling between electromagnetic waves and the material within the absorbing body, resulting in increased loss and improved absorption performance.[36] The relaxation process with dipole and interfacial polarization is examined in the relationship between ε' and ε'' to properly depict the polarization relaxation impact in the electromagnetic wave attenuation process. According to the classical Debye theory using Cole–Cole images, each semicircle represents one polarization relaxation phenomenon. Typically, the polarization relaxation process is more robust when the Cole–Cole semicircle is larger and the electromagnetic wave is incident on the absorber surface.[37] The dielectric loss tangent is given by the ratio of the imaginary part (ε'') to the real part (ε') of the complex permittivity, as expressed in Equation III.

$$\tan\delta_e = \frac{\varepsilon''}{\varepsilon'} \quad \text{(III)}$$

2.5. Magnetic loss

In addition to dielectric losses, which indicate a material's ability to sustain a magnetic field within a medium, magnetic loss is a crucial part of the electromagnetic loss process. The primary cause of magnetic loss in the microwave range is believed to be eddy current loss, which happens when an external electric field transforms the work done on a magnetic material into heat energy during magnetization or demagnetization. Eddy current loss (Co), which is the energy dissipation brought on by induced currents in a

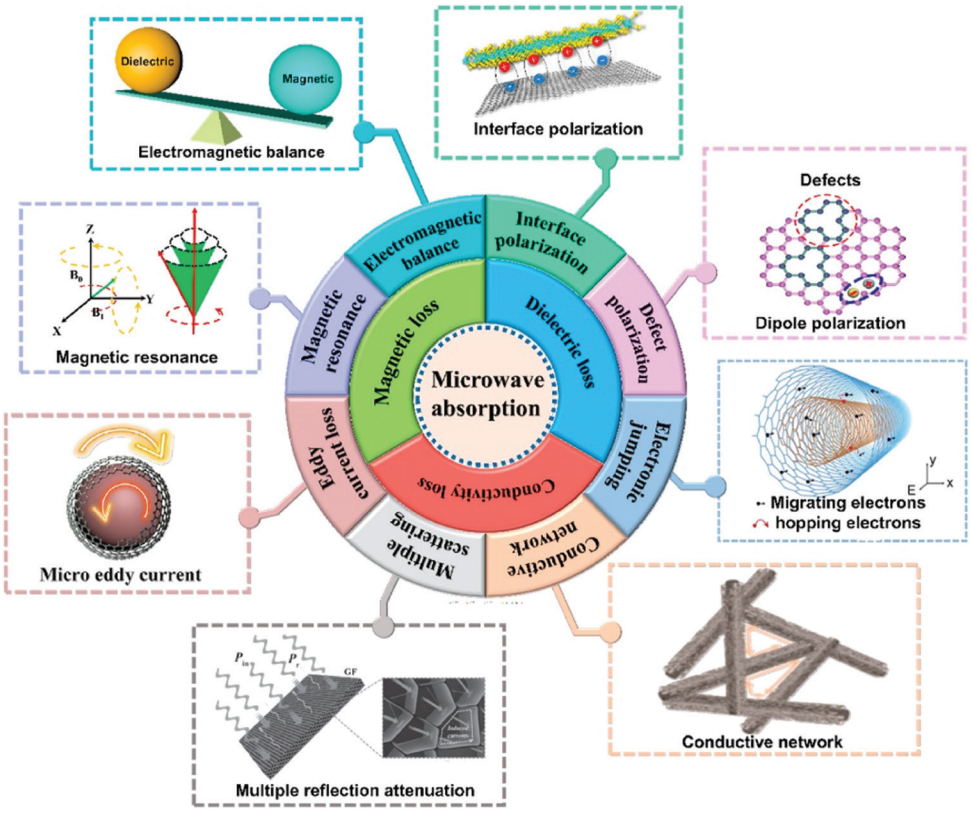

Figure 2. Electromagnetic wave loss with various microwave mechanisms.[35] Copyright © 2021 The Chinese Ceramic Society. Reproduced with permission of Elsevier.

magnetic conductor moving inside a fluctuating magnetic field, may be calculated using Equation IV:

$$C_o = \approx 2\pi\mu_o\mu'^2\sigma D^2 f \quad \text{(IV)}$$

By creating a magnetic field in the opposite direction of the initial alternating current (AC) field, the eddy current protects the magnetizing field inside the magnet and exponentially reduces the strength of the AC field, which ultimately results in the skinning effect. The magnetic loss factor, which is based on the ratio of μ' to μ'', indicates the capacity of a medium to retain a magnetic field. The skinning depth of the material and magnetic loss factor can be expressed as follows:

$$\mathrm{tg}\delta = \frac{\mu''}{\mu'} \quad \text{(V)}$$

$$\delta = \sqrt{\frac{2\rho}{\omega\mu\sigma}} \quad \text{(VI)}$$

where δ is penetration depth, ω is angular frequency, $\omega=2\varpi f$, ρ is resistivity, and σ is conductivity.

2.6. Interference loss

Interferometric loss is dependent on the idea that electromagnetic waves interfere with one another and cancel each other out, giving rise to a zero net return. It places particular demands on the actual material. Refraction and reflection occur when an electromagnetic beam traveling in parallel hits a material's surface. An outgoing wave is produced from the surface of the material by the lower metal plate reflecting the incident component of the electromagnetic wave. The propagation direction of the wave stays constant. Based on the absorbing material's quarter wavelength, the absorption principle states that these waves cancel each other at this point, significantly lowering the total reflected wave. The entering and outgoing waves have a phase difference of precisely 180° since the thickness of the absorbing material is equal to a quarter wavelength. To enable better EMA characteristics and cause the incident and reflected waves in the material to be out of phase, the thickness t is set to be an odd multiple of the quarter wavelength in the material.

$$t = n\frac{\lambda m}{4} \quad \text{(VII)}$$

$$\lambda_m = \frac{\lambda d}{\sqrt{|\mu_r||\varepsilon_r|}} \quad \text{(VIII)}$$

where t is the thickness of the material, λ_m is the wavelength of the material itself, and λ_d is the free space wavelength. $|\pi_r|$ and $|\varepsilon_r|$ are the moduli of relative magnetic permeability μ_r and relative permittivity ε_r, respectively.

3. Electromagnetic microwave characteristics of various fiber-reinforced materials

3.1. CF-reinforced composites

Because of their superior electrical conductivity, low weight, and mechanical durability, CF-reinforced composites have become very effective EMWA materials. Dielectric loss and energy dissipation are improved by the numerous internal reflections, and scattering of incident electromagnetic waves is made possible by the high aspect ratio and interconnected network of CFs. For example, Elhassan *et al.*[38] investigated the efficient synthesis of Fe_3O_4/PPy double-carbonized core-shell-like composite for broadband EMA. It achieved exceptional EMWA properties as a wide effective absorption band of 4.64 GHz and a minimum RL of −26 dB at 1.6 mm. Moreover, randomly distributed CFs tend to produce greater isotropic absorption, whereas aligned fibers can create anisotropic electromagnetic responses,[39] which may be customized for specific polarization-dependent applications.

Recent studies have concentrated on improving the matrix composition and CF concentration for better broadband absorption and impedance matching.[20] For example, Tang *et al.*[40] investigated the prominent fiber orientation effect and enhanced the electromagnetic wave anisotropic properties. Copper fibers with slender dimensions form abundant, flexible, multisize equivalent waveguide attenuator structures that promote vector superposition and interference effects, exhibiting RL peaks at 7 GHz and 12 GHz. Additive manufacturing is frequently used to create these composites' porous or layered architectures, which further enhance performance by adding more interfacial polarization sites and impedance gradients. High-tech manufacturing methods such as *in situ* polymerization and magnetic field-assisted alignment are used to improve CF-reinforced absorbers' reproducibility.

For structural applications where both load-bearing capacity and stealth functioning are necessary, CF-reinforced composites are especially appealing due to their mechanical-electromagnetic performance. The electromagnetic microwave absorption properties of CF depend significantly on its type and structural characteristics.[19] High-modulus CFs, with their highly graphitic and ordered crystalline structure, exhibit strong electrical conductivity, which tends to reflect rather than absorb microwaves. In contrast, low-modulus or polyacrylonitrile (PAN)-based CFs contain more amorphous regions, reducing conductivity and enhancing dielectric loss, making them more effective for absorption. In addition, the physical form of the fiber plays a role—continuous CFs reflect microwaves along their alignment, while short-cut or randomly dispersed fibers improve impedance matching and promote internal scattering, increasing absorption. To optimize performance, CFs are modified through oxidation, surface treatments, or hybridization with magnetic particles like Fe_3O_4, which combine dielectric and magnetic loss mechanisms for broader absorption bandwidths.[41]

The key mechanisms governing microwave absorption in CF include conductive loss, dielectric loss, and magnetic loss, each playing a critical role depending on the fiber's composition and structure.[42] Conductive loss dominates in highly graphitic CFs, where free electrons interact with electromagnetic fields, converting microwave energy into heat—though excessive conductivity can lead to unwanted reflection rather than absorption. Dielectric loss, more prominent in disordered or functionalized CFs, arises from dipole polarization and interfacial effects, enhancing energy dissipation.[43] When combined with magnetic materials like iron oxides or ferrites, magnetic loss further improves absorption by introducing additional energy conversion pathways. Effective microwave absorption ultimately relies on balancing these mechanisms while optimizing impedance matching to minimize surface reflection and maximize penetration into the material.[25] While recycled or bio-based CFs can enhance the sustainability of CF composites without compromising electromagnetic performance, their absorption bandwidth and intensity can be further increased via integration with other lossy materials, such as magnetic nanoparticles or conductive polymers.

3.2. CFs coated with other materials

Researchers have investigated covering CFs with magnetic or conductive materials, such as metals, metal oxides, or conductive polymers, to improve the EMWA performance of CFs. These coatings improve microwave attenuation by introducing extra loss mechanisms such as improved conductivity, magnetic resonance, and interfacial polarization. For instance, compared to uncoated CFs, nickel-coated CFs are effective over a larger frequency range because of the conductive nickel layer and its intrinsic ferromagnetic characteristics, which cause dielectric and magnetic losses.

The homogeneity, adherence, and thickness of the coatings are largely determined by the coating processes, such as chemical vapor deposition, electrochemical deposition, or electroless plating. While hybrid coatings that combine conductive and magnetic materials, like FeO_4-polypyrrole multilayers, have shown synergistic effects for broadband absorption, a thin and uniform nickel coating on CFs has been demonstrated to achieve reflection losses below −40 dB in the Ku-band. These coated CFs can be further incorporated into polymer matrices through additive printing to create intricate, lightweight absorbers with specialized electromagnetic characteristics. Figure 3 illustrates the fabrication procedure of CFs coated with other materials. It highlights four distinct coating strategies for CFs, each optimizing EMA through tailored material and structural modifications. The electroless FeCoNi-plated CFs introduce magnetic loss via a uniform metallic coating, ideal for low-frequency applications, whereas the porous NC-Co3O4/CF composites (Figure 3A). Figure 3B presents nanoporosity and heterostructures to enhance dielectric loss and bandwidth. The hierarchical CoNC@ CF-PLA composites stand out by integrating atomic-scale magnetic sites with 3D-printed polymer matrices, achieving deep absorption (−45 dB) through multi-scale design (Figure 3C). In contrast, the CNT/CF and SiC_f hybrids prioritize high-frequency performance (CNTs) or thermal stability (SiC_f), demonstrating adaptability to operational environments (Figure 3D). Comparatively, methods shown in Figure 3B and C excel in broadband absorption due to their porous and hierarchical architectures, whereas those illustrated in Figure 3A and D provide specialized solutions for magnetic or extreme-condition applications. The progression from simple coatings (Figure 3A) to complex multi-material systems (Figure 3C) underscores a broader trend toward combining multiple loss mechanisms and scalable manufacturing. These innovations collectively expand the design space for CF-based absorbers, balancing performance, durability, and manufacturability.

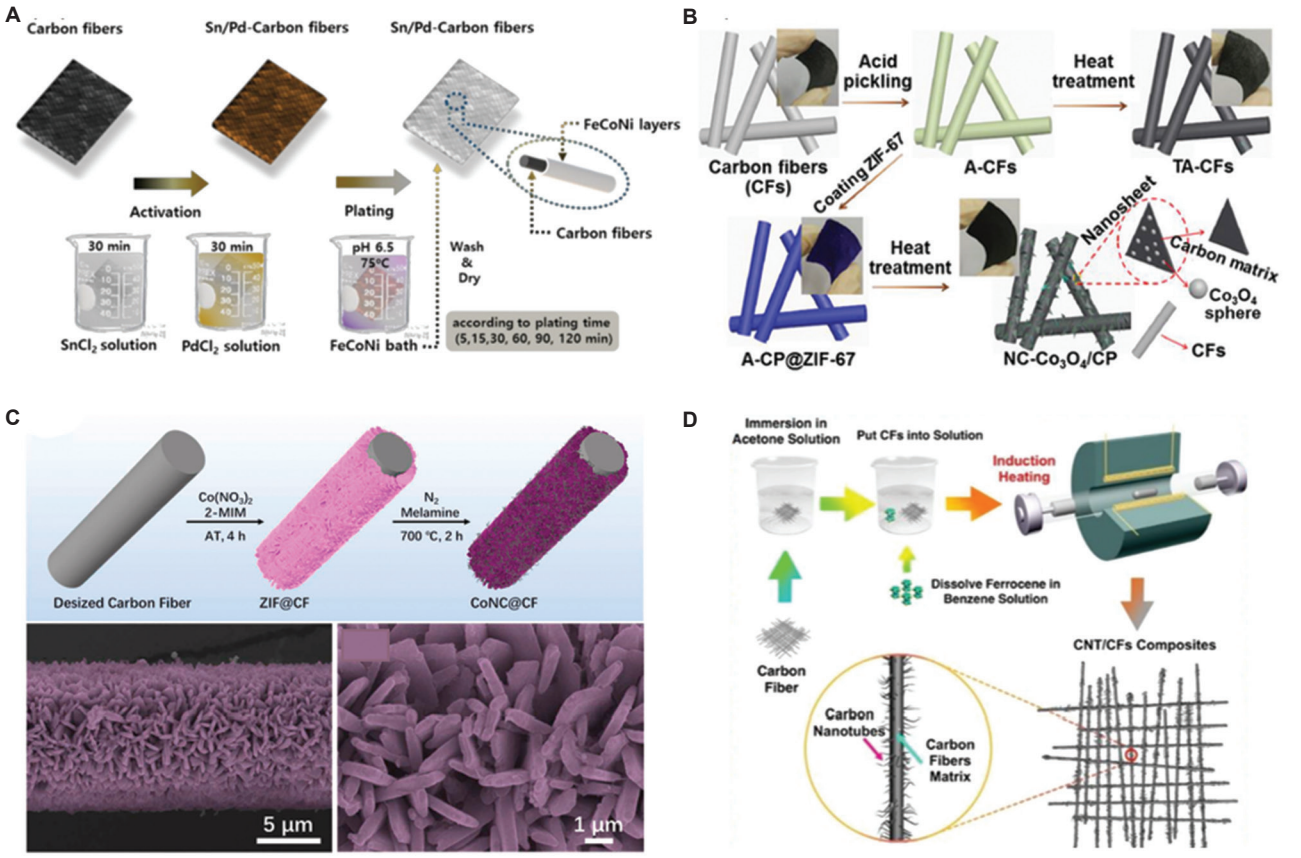

Figure 3. Fabrication procedure of CFs coated with other materials: (A) CFs prepared by electroless FeCoNi-plating.[44] Reproduced under the terms and conditions of the Creative Commons Attribution (CC BY) license. (B) Porous NC-Co_3O_4/CF composites.[45] Copyright © 2017 American Chemical Society. Reproduced with permission of the American Chemical Society. (C) CoNC@CF-PLA composites with the hierarchical nanostructure.[46] Copyright © 2022 Elsevier. Reproduced with permission of Elsevier. (D) CNT/CFs and SiC_f fibrous materials.[33] Copyright © 2023 Elsevier. Reproduced with permission of Elsevier.
Abbreviations: CF: Carbon fiber; CNT: Carbon nanotube.

3.3. CF-based hybrid materials

The capacity of CF-based hybrid materials to combine the structural advantages of CFs with the benefits of numerous functional fillers has drawn much attention owing to their EMWA properties. These hybrids exploit the synergistic effects between several loss processes, such as magnetic resonance, dipole polarization, and conductive networks, to achieve excellent broadband absorption. A multiscale conductive network produced by CFs hybridized with CNTs or graphene sheets improves dielectric loss across a broad frequency range by enhancing interfacial polarization and electron hopping.

Strategic filler distribution and alignment are frequently used in the design of CF-based hybrid materials to maximize impedance matching and reduce reflection. These hybrids' spatial organization can be precisely controlled through additive manufacturing processes, resulting in graded or patterned structures that improve wave attenuation. There is increasing promise for high-performance, customizable CF-based hybrid absorbers as the development of additive manufacturing. The creation of multipurpose hybrids with energy-absorbing or self-sensing properties creates new possibilities for intelligent electromagnetic protection systems. These cutting-edge materials make next-generation EMWA systems with previously unheard-of performance characteristics possible.

3.4. Hollow- and porous CFs-based materials

The structural properties of hollow and porous CFs (PCFs) have made them novel materials for EMWA properties. To improve impedance matching with free space, these fibers hollow cores and porous walls produce a large surface area and several air-material contacts, increasing dielectric loss and decreasing the effective permittivity. Hollow CFs packed with magnetic nanoparticles or lightweight conductive polymers have shown remarkable absorption capabilities. For instance, Tan *et al.*[47] investigated CNTs/CNFs@CF construction of 3D network hierarchical structures toward multiple synergistic losses. The minimum RL was achieved at −66.00 dB at 1.00 mm, and the maximum effective absorption bandwidth was 4.48 GHz at 1.29 mm. It implies a good prospect for the continuous large-scale preparation of ultrathin and efficient electromagnetic wave absorbers.

Template-assisted techniques, chemical activation, or controlled pyrolysis of polymer precursors are commonly used to manufacture hollow and PCFs. Porous CF designs, including lattice or foam-like structures, may now be precisely designed thanks to recent developments in additive printing, further optimizing electromagnetic wave attenuation. Through the creation of incremental permittivity transitions, 3D-printed PCF-reinforced composites with graded porosity minimize surface reflections and demonstrate broadband absorption. The addition of supplementary fillers to the porous framework, like graphene oxide or MXenes, improves interfacial polarization and conductivity loss. Figure 4 presents the fabrication procedure of hollow- and PCFs-based composite materials, each tailored for enhanced EMA through distinct structural and compositional strategies.

In Figure 4A, Co_3O_4/carbon composite nanofibers is produced via electrospinning and carbonization, where cobalt oxide nanoparticles embedded in carbon nanofibers (CNFs) introduce magnetic loss and interfacial polarization. In contrast, Figure 4B shows the creation of $Fe/Fe_3O_4/C$ hollow fibers, leveraging a sacrificial template to form a hollow core, which improves impedance matching and reduces density while the iron-based components enhance magnetic loss. In Figure 4C, hierarchical porous carbon nanofibers are fabricated using $CaCO_3$ as a porogen, resulting in multiscale porosity that optimizes wave penetration and multiple scattering for broadband absorption. In Figure 4D, silica nanoparticle templates and selective etching are employed to produce N-doped porous CFs, combining high surface area for dielectric loss with nitrogen doping for improved conductivity. Comparatively, Figures 4B and C demonstrate the excellent lightweight designs and broadband performance due to their hollow and hierarchical porous structures, whereas Figures 4A and D depict the integration of magnetic or heteroatom-doped functionalities. The choice of method depends on the target application: the methods illustrated in Figures 4A and B are ideal for magnetic-dielectric synergy, whereas those in Figure 4C and D prioritize tunable porosity and surface chemistry for tailored absorption properties.

Table 2 summarizes several electromagnetic microwave characteristics of various CF-based materials, revealings several essential trends in CF-based microwave absorbers. Firstly, absorber thickness shows a clear correlation with performance-thinner absorbers (1 – 2 mm) like the SCF+TiO_2/paraffin system achieve remarkable RL_{min} of −46.3 dB, whereas thicker designs (4 – 4.5 mm) generally show reduced effectiveness. Second, hybrid systems incorporating magnetic materials with CF demonstrate superior bandwidth performance, with CF/$CoFe_2O_4$ achieving an exceptional 6.48 GHz bandwidth at −10 dB threshold. Third, paraffin wax emerges as a particularly effective matrix material, which enables the best-performing absorbers in the dataset, likely due to its favorable dielectric properties and ability to disperse fillers uniformly. It is shown that nanoscale modifications (*e.g.*, TiO_2 coating, MnO_2 nanowires) consistently enhance absorption compared to plain CF, with all nanowire-modified systems achieving RL_{min} below −28 dB. Notably,

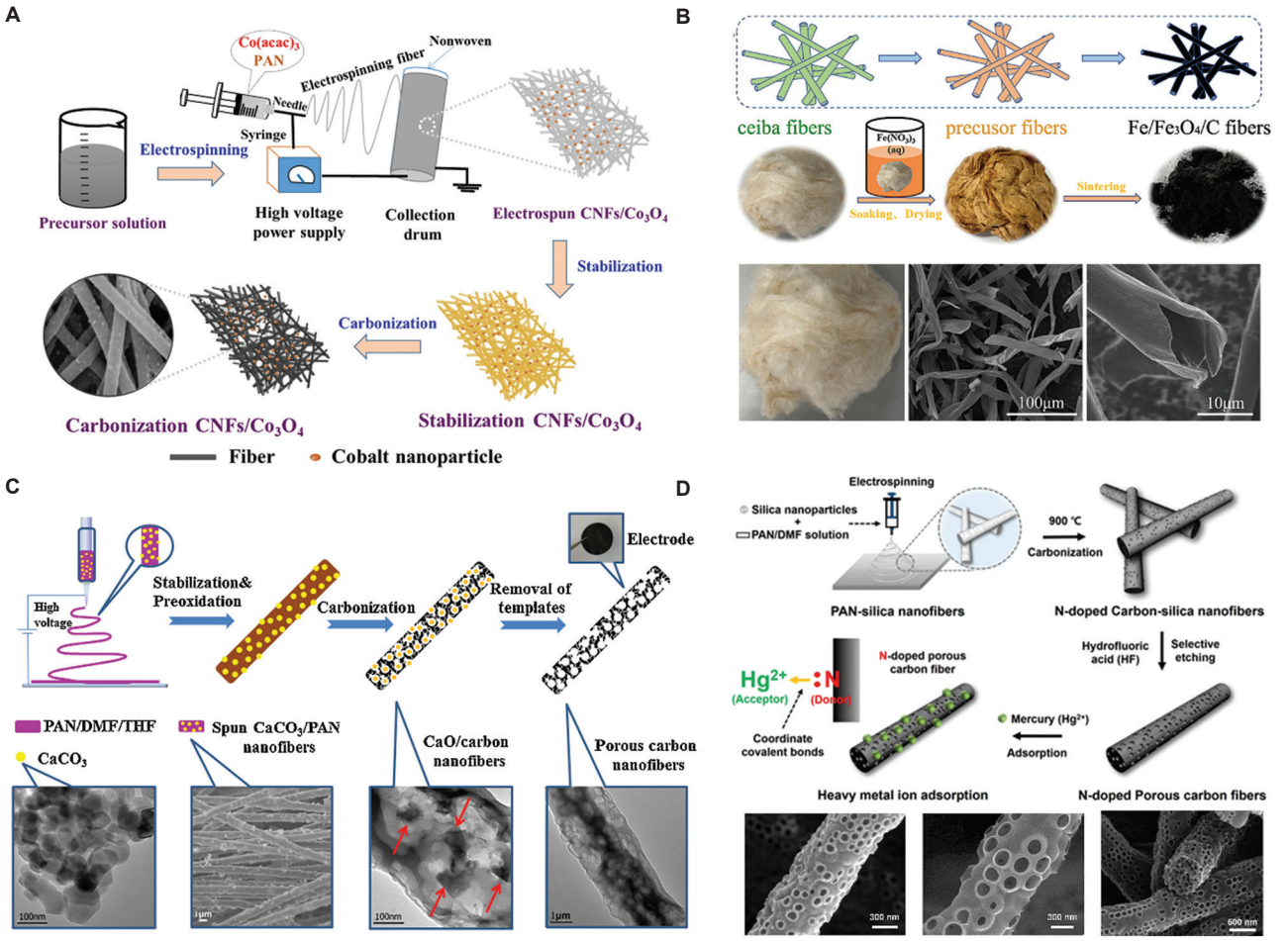

Figure 4. Fabrication procedure of hollow- and PCF-based composite materials: (A) Co_3O_4/carbon composite nanofibrous membrane.[48] Reproduced under the terms and conditions of the Creative Commons Attribution (CC BY) license. (B) Fe/Fe_3O_4/C hollow fibers.[49] Copyright © 2024 Elsevier. Reproduced with permission of Elsevier. (C) Hierarchical PCFs.[50] Copyright © 2016 Elsevier. Reproduced with permission of Elsevier. (D) PCFs.[51] Copyright © 2018 Elsevier. Reproduced with permission of Elsevier.
Abbreviations: CNF: Carbon nanofiber; DMF: Dimethylfirmamide; PAN: Polyacrylonitrile; PCF: Porous carbon fiber; THF: Tetrahydrofuran.

the CF/$CoFe_2O_4$ hollow fiber composite stands out and combines broad bandwidth (6.48 GHz) with deep absorption (−55.33 dB). It is suggested that combined magnetic-hollow fiber architectures may represent an optimal design approach. It is highlighted that the most effective CF absorbers combine: (i) nanoscale surface modifications, (ii) magnetic component integration, and (iii) optimized structural designs (hollow/porous architectures), while maintaining relatively thin profiles (<3 mm) for practical applications.

4. Electromagnetic microwave performance of various additively manufactured microwave absorbers

The field of fiber-reinforced polymer (FRP) absorbers has undergone a transformative shift with the advent of the additive manufacturing process, enabling the fabrication of metastructures with unprecedented geometric complexity and functional precision. Figure 5 presents the recent progress on various designs on additively manufactured fiber-reinforced polymer absorbers, from bio-inspired configurations like bamboo-inspired metastructures to mathematically optimized forms such as triply periodic minimal surfaces (TPMS).[64] These architectures are not merely aesthetic but engineered to enhance energy absorption, vibration damping, and acoustic performance by leveraging tailored stress distribution and resonant frequencies. The laminate metastructure (LM)[65] and conical absorbers, for instance, demonstrate how layered and tapered geometries can progressively dissipate energy under dynamic loads, whereas TPMS designs exploit their high surface-area-to-volume ratios for multi-functional applications.

Table 2. Summary of electromagnetic microwave characteristics of various carbon fiber-based materials

Type	Reinforcement/ Absorber configuration	Matrix	Frequency range (GHz)	Bandwidth of RL < −10 dB (GHz)	Minimum RL (dB)	Thickness (mm)	References
CF-reinforced	SCF+TiO_2	Paraffin	2 – 18	2.4	−46.3	1.0	52
	CNF	Epoxy	8.2 – 12.4	2.2	−34	2.1	53
	CF	Al_2O_3	8.2 – 12.4	2.2	−42.5	1.6	54
CF-coated	Chopped CF	GGBFS/fly ash	8.2 – 12.4	4.2	−41.63	2.0	55
	CF	ABS	2 – 18	6.6	−40.9	2.2	56
	CF+MnO_2/PANI	Paraffin	8.2 – 12.4	3.0	−23	2.5	57
	CF+Ag/PANI	Paraffin	8.2 – 12.4	2.2	−13.2	2.0	58
	CF+MnO_2 nanowires	Paraffin	2 – 18	3.84	−42.9	1.2	59
	CF+CuO nanowires	Paraffin	2 – 18	2.5	−28.8	1.7	60
CF-based hybrid	CF/FeCo	CF	2 – 18	2.87	−24.05	4.0	61
	CF/Fe	Paraffin	2 – 18	2.9	−36.98	1.8	62
Hollow or PCFs-based	CF/$CoFe_2O_4$	Paraffin	2 – 18	6.48	−55.33	2.42	63
	CNFs/Co_3O_4	Paraffin	2 – 18	6.3	−36.27	2.0	48
	Ceiba fibers/Fe/Fe_3O_4	Paraffin	2 – 18	3.26	−40.1	4.5	49

Abbreviations: CF: Carbon fiber; CNF: Carbon nanofiber; PANI: Polyaniline; PCF: Porous carbon fiber; RL: Reflection loss; SCF: Silica composite nanofibers.

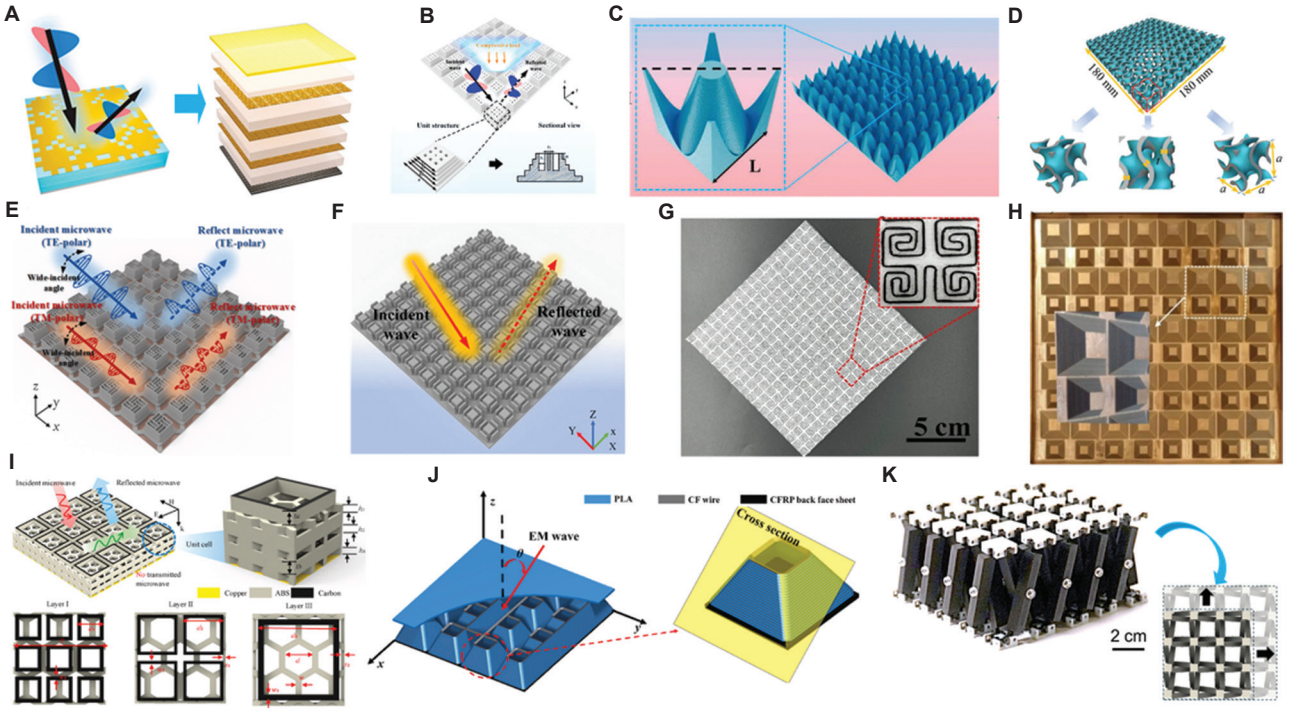

Figure 5. Recent progress on various designs on additively manufactured fiber-reinforced polymer absorbers: (A) Laminate metastructure (LM).[65] Copyright © 2021 Elsevier. Reproduced with permission of Elsevier. (B) Bamboo-inspired metastructure.[69] Copyright © 2023 Elsevier. Reproduced with permission of Elsevier. (C) Conical structure absorber.[70] Copyright © 2024 Elsevier. Reproduced with permission of Elsevier. (D) Triply periodic minimal surface meta-structure.[64] Copyright © 2024 Elsevier. Reproduced with permission of Elsevier. (e) Multiresonant metastructure.[71] Copyright © 2023 Elsevier. Reproduced with permission of Elsevier. (F) Gradient metastructure.[66] Copyright © 2021 Elsevier. Reproduced with permission of Elsevier. (G) Helical pattern metastructure.[72] Reproduced under the terms and conditions of the Creative Commons Attribution (CC BY) license. (H) Different-sized tapered hyperbolic metastructure.[73] Copyright © 2025 Nature Portfolio. Reproduced with open access of Nature Portfolio. (i) Modular metastructure.[67] Copyright © 2023 Elsevier. Reproduced with permission of Elsevier. (G) Pyramidal array sandwich structure (PASS).[68] Copyright © 2023 Elsevier. Reproduced with permission of Elsevier. (K) Crisscross structure.[74] Copyright © 2025 American Association for the Advancement of Science. Reproduced with open access of the American Association for the Advancement of Science.

A striking feature of these additive manufacturing-produced metastructures is their ability to incorporate functional gradients and multiresonant behaviors, as seen in gradient metastructures and helical patterns.[66] Such designs allow spatially varying mechanical properties, enabling targeted energy dissipation across different frequency ranges or load conditions. For example, the modular metastructure[67] and crisscross design highlight the potential for scalable, reconfigurable systems that can be adapted for specific industrial requirements. The pyramidal array sandwich structure (PASS)[68] integrates lightweight, high-stiffness cores with energy-absorbing skins, a critical advancement for applications demanding strength and weight efficiency.

Recent advances in multimaterial additive manufacturing have opened new possibilities for precisely controlling the electromagnetic wave absorption characteristics of 3D-printed structures. By strategically combining materials with different dielectric and magnetic properties within a single structure, researchers can create spatially graded impedance profiles that significantly enhance broadband absorption performance. Several promising techniques have emerged, including: (i) Alternating deposition of conductive (carbon-filled) and insulating polymer layers to create impedance-matching transitions and multiple internal reflection interfaces; (ii) localized incorporation of magnetic nanoparticles (*e.g.*, ferrites) in specific regions to introduce magnetic loss mechanisms; and (iii) functionally graded material distributions that provide smooth transitions in complex permittivity. These approaches leverage the unique capabilities of multimaterial extrusion systems or polyjet printing technologies that can precisely deposit different materials at voxel-level resolution. Experimental studies have demonstrated that such multimaterial designs can achieve reflection losses exceeding −40 dB while maintaining structural integrity, representing a significant improvement over single-material absorbers.

The field of multimaterial printed absorbers presents several promising research directions that remain underexplored. A key opportunity lies in developing dynamic absorption systems where the material composition or microstructure can be actively reconfigured in response to external stimuli (*e.g.*, temperature, electric field, or mechanical stress). Another frontier involves combining conductive polymers with ceramic or elastomeric materials to create absorbers with tunable properties under operational conditions. ML-assisted design could play a crucial role in optimizing these complex multimaterial architectures by predicting the optimal spatial distribution of materials for target frequency bands. In addition, the integration of embedded functional elements (*e.g.*, frequency selective surfaces or resistive patterns) within multimaterial structures could enable novel absorption mechanisms. As multimaterial 3D printing technologies continue to mature, they will enable the creation of next-generation "smart" absorbers with adaptive performance, opening new possibilities for applications in reconfigurable stealth systems, tunable EMI shielding, and intelligent anechoic coatings. The combination of computational design tools, advanced material systems, and high-resolution multi-material printing capabilities represents a powerful approach to overcoming traditional limitations in microwave absorber design.

Figure 6 illustrates the results on electromagnetic microwave performance and electric and magnetic field distributions of additively manufactured microwave absorbers. Recent advancements in additive manufacturing have enabled the development of highly specialized microwave absorbers with tailored electromagnetic properties. These metastructures, including the bamboo-inspired design, multiresonant configurations, and gradient architectures, leverage geometric complexity to achieve superior absorption performance across specific frequency ranges. For instance, the bamboo-inspired metastructure[69] mimics natural fibrous systems to optimize impedance matching, whereas the multiresonant design[71] incorporates multiple resonant frequencies to broaden the absorption bandwidth. The gradient metastructure[66] further refines this approach by spatially varying its properties to create a smooth transition in impedance, minimizing reflections and enhancing energy dissipation. These innovations highlight how bio-inspired and computationally optimized designs can push the boundaries of microwave absorption, offering solutions for applications ranging from stealth technology to EMI shielding in sensitive electronic devices. It has been shown that the field distribution analyses reveal the structural features that control energy dissipation. Cellular structures promote multiple scattering, gradient designs enable progressive wave decay, and resonant elements create localized field enhancement. The most effective absorbers (Figure 6C, 6D and 6G) balance these mechanisms, achieving both broadband performance (>80% bandwidth coverage) and deep absorption (>20 dB), with the gradient and honeycomb designs being particularly noteworthy for maintaining performance. These results collectively demonstrate that the additive manufacturing process enables precise control over electromagnetic field manipulation through hierarchical and multimaterial architectures.

The electric-loss honeycomb metastructure (ELHM)[22] and the double high-impedance surface-loaded honeycomb (DHHC) structure[75] demonstrate the effectiveness of

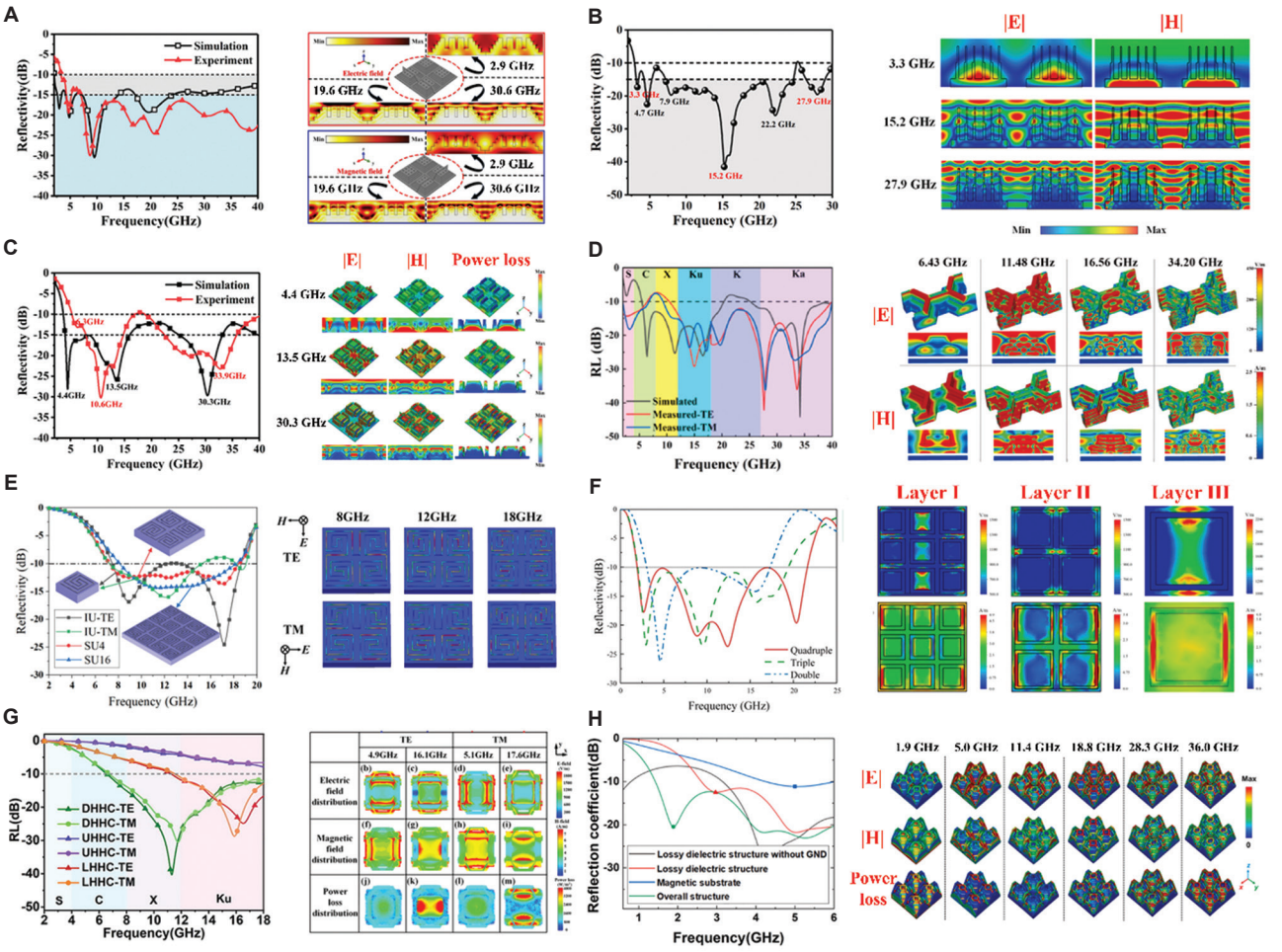

Figure 6. Results on electromagnetic microwave performance and electric and magnetic field distributions of recent additively manufactured microwave absorbers. (A) Bamboo-inspired metastructure.[69] Copyright © 2023 Elsevier. Reproduced with permission of Elsevier. (B) Multiresonant metastructure.[71] Copyright © 2023 Elsevier. Reproduced with permission of Elsevier. (C) Gradient metastructure.[66] Copyright © 2021 Elsevier. Reproduced with permission of Elsevier. (D) Electric-loss honeycomb metastructure (ELHM).[22] Copyright © 2023 Elsevier. Reproduced with permission of Elsevier. (E) Helical pattern metastructure.[72] Reproduced under the terms and conditions of the Creative Commons Attribution (CC BY) license. (F) Modular metastructure.[67] Copyright © 2023 Elsevier. Reproduced with permission of Elsevier. (G) Double high-impedance surface-loaded honeycomb (DHHC) structure.[75] Copyright © 2023 Elsevier. Reproduced with permission of Elsevier. (H) Three-dimensional lossy dielectric metastructure.[76] Copyright © 2025 Elsevier. Reproduced with permission of Elsevier.

combining conductive and dielectric materials to achieve high electromagnetic loss. The ELHM, for example, utilizes a honeycomb lattice infused with lossy materials to dissipate microwave energy through electric and magnetic pathways. Similarly, the DHHC structure employs high-impedance surfaces to trap and attenuate incident waves, showcasing how hybrid designs can enhance performance. The helical pattern metastructure[72] and the 3D lossy dielectric metastructure[76] further illustrate the role of geometric anisotropy in manipulating electric and magnetic field distributions. These designs improve absorption efficiency and tunability, allowing engineers to tailor the response for specific operational frequencies or polarization conditions. Table 3 summarizes the electromagnetic microwave performance of the recent additively manufactured polymer composite absorbers, which shows an excellent advantage of complex metastructure designs. The TPMS metastructure achieves exceptional performance RL_{min} of −47.60 dB with 3.3 mm thickness, whereas simpler conical and pyramidal structures require much greater thicknesses (20 – 21 mm) for comparable bandwidth. It is pointed out that additive manufacturing process enables geometrically optimized structures that maximize absorption efficiency per unit thickness. Several designs achieve remarkably wide bandwidths, particularly the circular metastructure (polylactic acid [PLA]/conductive plastic) covering 16.3 – 54.3 GHz and the gradient metastructure reaching 5.1 – 40 GHz. This broadband capability stems from

Table 3. Summary of electromagnetic microwave performance of recent additively manufactured polymer composite absorbers

Structural design	Material	Frequency range (GHz)	Bandwidth of RL < −10 dB (GHz)	Minimum RL (dB)	Thickness (mm)	References
Bamboo-inspired metastructure	PEEK/FCIPs magnetic composite	2 – 40	3.2 – 40	−15	3	69
Conical structure	NFG/Si/Fe_3O_4/PF composite	2 – 18	3.55 – 18	−21.52	21	70
Propeller-like structure	Carbon black-polypropylene composite	2 – 18	3.4 – 10	−10	10	77
Triply periodic minimal surface metastructure	PDCs-SiC/Si_3N_4 composite	2 – 18	6.88 – 18	−47.60	3.3	64
Multiresonant metastructure	PEEK/FCIPs composite	2 – 30	2.8 – 30	−17.50	3 – 5	71
Gradient metastructure	FCIPs-PEEK composite	2 – 18	5.1 – 40	< −15	10	66
Helical pattern metastructure	Conductive-coated continuous fibre	2 – 20	8 – 18.4	< −10	3.2	72
Modular metastructure	Conductive ink/ABS	1 – 27	3.5 – 25.7	< −10	1.5	67
Circular metastructure	PLA/conductive plastic	2 – 60	16.3 – 54.3	< −10	2.7	78
Pyramidal array sandwich structure	PLA/CF-reinforced plastics	4 – 18	4 – 18	≈ −10	13.5	68
Pyramid metastructure	CNT@APP	2 – 18	2 – 18	−30	20	79
Flexible honeycomb absorber	CF/PA/CIP composite	2 – 18	2.8 – 3.1, 5.1 – 18	−47	2.8	80

Abbreviations: CF: Carbon fiber; CIP: Carbonyl iron particles; CNT: Carbon nanotube; FCIP: Flaky carbonyl iron particles; NFG: Natural flake graphite; PA: Polyamide; PDC: Polycrystalline diamond composite; PEEK: Polyether-ether-ketone; PF: Phenol formaldehyde resin; PLA: Polylactic acid; RL: Reflection loss.

either multiscale structural features or carefully designed impedance gradients that address different frequency ranges within a single component. It is demonstrated that additive manufacturing enables unprecedented control over both material composition and geometric design, allowing engineers to overcome traditional performance trade-offs in microwave absorber development.

5. Recent designs on integrated electromagnetic microwave and load-bearing performance of microwave absorbers

Figure 7 presents recent designs on integrated electromagnetic microwaves and the load-bearing performance of recent additively manufactured microwave absorbers. These innovative designs, including the ELHM,[22] double high-impedance surface-loaded honeycomb structure,[75] and gradient metastructure,[66] represent a paradigm shift in multi-functional material engineering. The geometric diversity showcased spans from the octagon loop with four diagonals[81] to the 3D honeycomb[82] and tree-shaped[83] configurations, demonstrating the computational design and additive manufacturing enable the creation of complex architectures optimized for dual functionality. Particularly, these structures integrate electromagnetic loss mechanisms (through conductive patterns or dielectric compositions) with mechanical reinforcement strategies (via honeycomb cores or biomimetic lattice arrangements), which offers solutions for applications where space and weight constraints demand multi-functional performance.

The electric-loss honeycomb (Figure 7A) and double high-impedance honeycomb structures (Figure 7B) exemplify the cellular architectures can combine substantial compressive strength (1.41 kN load capacity and 6.09 MPa, respectively) with broadband absorption, leveraging their periodic geometries for both mechanical stability and wave scattering. Gradient designs (Figure 7C) achieve progressive impedance matching while maintaining structural integrity (8.46 MPa compressive yield), illustrating the effectiveness of gradual property transitions. More complex geometries such as the octagon loop (Figure 7C) and TPMS-based structures (Figure 7I) have shown exceptional performance, with the octagon loop achieving exceptional 22.46 MPa compressive strength alongside effective absorption, and the TPMS design offering naturally optimized stress distribution. Figure 7H demonstrates that the natural

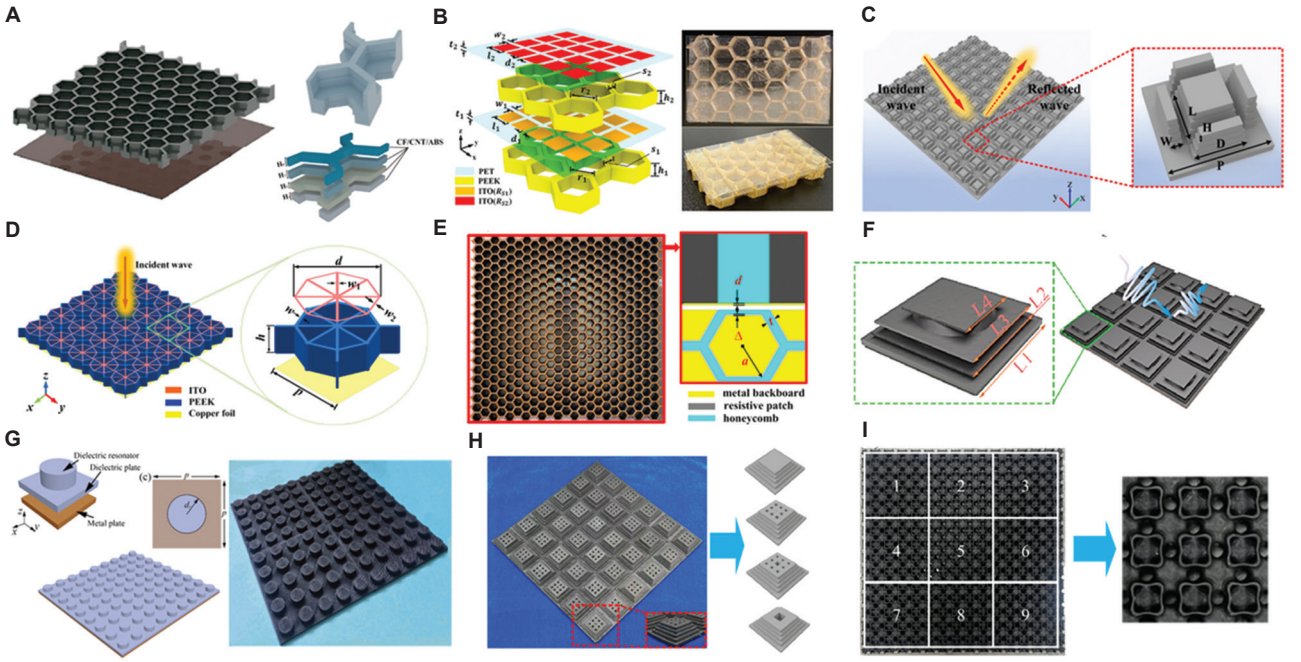

Figure 7. Recent designs on integrated electromagnetic microwave and load-bearing performance of recent additively manufactured microwave absorbers. (A) Electric-loss honeycomb metastructure (ELHM).[22] Copyright © 2023 Elsevier. Reproduced with permission of Elsevier. (B) Double high-impedance surface-loaded honeycomb structure.[75] Copyright © 2025 Elsevier. Reproduced with permission of Elsevier. (C) Gradient metastructure.[66] Copyright © 2021 Elsevier. Reproduced with permission of Elsevier. (D) Octagon loop with four diagonals metastructure.[81] Copyright © 2021 Elsevier. Reproduced with permission of Elsevier. (E) Three-dimensional honeycomb metastructure.[82] Copyright © 2018 Nature Portfolio. Reproduced under the terms and conditions of the Creative Commons Attribution (CC BY) license. (F) Tree-shaped metastructure.[83] Copyright © 2025 Elsevier. Reproduced with permission of Elsevier. (G) Cylindrical-shaped structure.[84] Reproduced under the terms and conditions of the Creative Commons Attribution (CC BY) license. (H) Bamboo-inspired metastructure.[69] Copyright © 2023 Elsevier. Reproduced with permission of Elsevier. (I) Triply periodic minimal surfaces (TPMS)-based metastructure.[85] Copyright © 2025 Wiley. Reproduced with permission of Wiley.

motifs enhance both impact resistance (13.27 MPa) and wideband absorption (3.2 – 40 GHz), whereas the tree-shaped design (Figure 7F) achieves remarkable 38.8 MPa bending strength through its branched architecture. These designs reveal three key principles: (i) Cellular and lattice geometries optimally balance mass efficiency with multifunctionality; (ii) biomimetic approaches successfully translate natural load-bearing strategies to electromagnetic applications; and (iii) gradient designs and TPMS architectures represent particularly promising directions for future development, as they inherently satisfy both mechanical and electromagnetic requirements through their optimized topologies. The progression from traditional honeycombs to advanced biomimetic and mathematical surfaces reflects an evolution toward more sophisticated, performance-driven designs enabled by the geometric design capability of the additive manufacturing process.

Several designs draw inspiration from nature, exemplifying that biomimicry can solve complex engineering challenges. The bamboo-inspired metastructure[69] replicates the natural fiber alignment of bamboo to achieve both mechanical resilience and effective microwave dissipation, whereas the tree-shaped metastructure[83] employs fractal-like branching to optimize stress distribution and electromagnetic wave scattering. The inclusion of TPMS-based designs[85] and cylindrical-shaped structures[84] further highlights the importance of mathematically derived geometries in achieving balanced electromagnetic and mechanical properties. These structures leverage the inherent advantages of periodic minimal surface high strength-to-weight ratios and continuous curvature to create self-supporting frameworks that simultaneously manipulate electromagnetic fields through their intricate surface topologies. The visual progression from simple honeycomb patterns to complex biomorphic forms in the image underscores the evolution of design thinking in this field.

Figure 8 presents recent results on electromagnetic microwave and load-bearing performance of recent additively manufactured microwave absorbers. The bamboo-inspired metastructure[69] exemplifies nature-informed engineering, replicating bamboo's natural fiber alignment to achieve structural resilience and

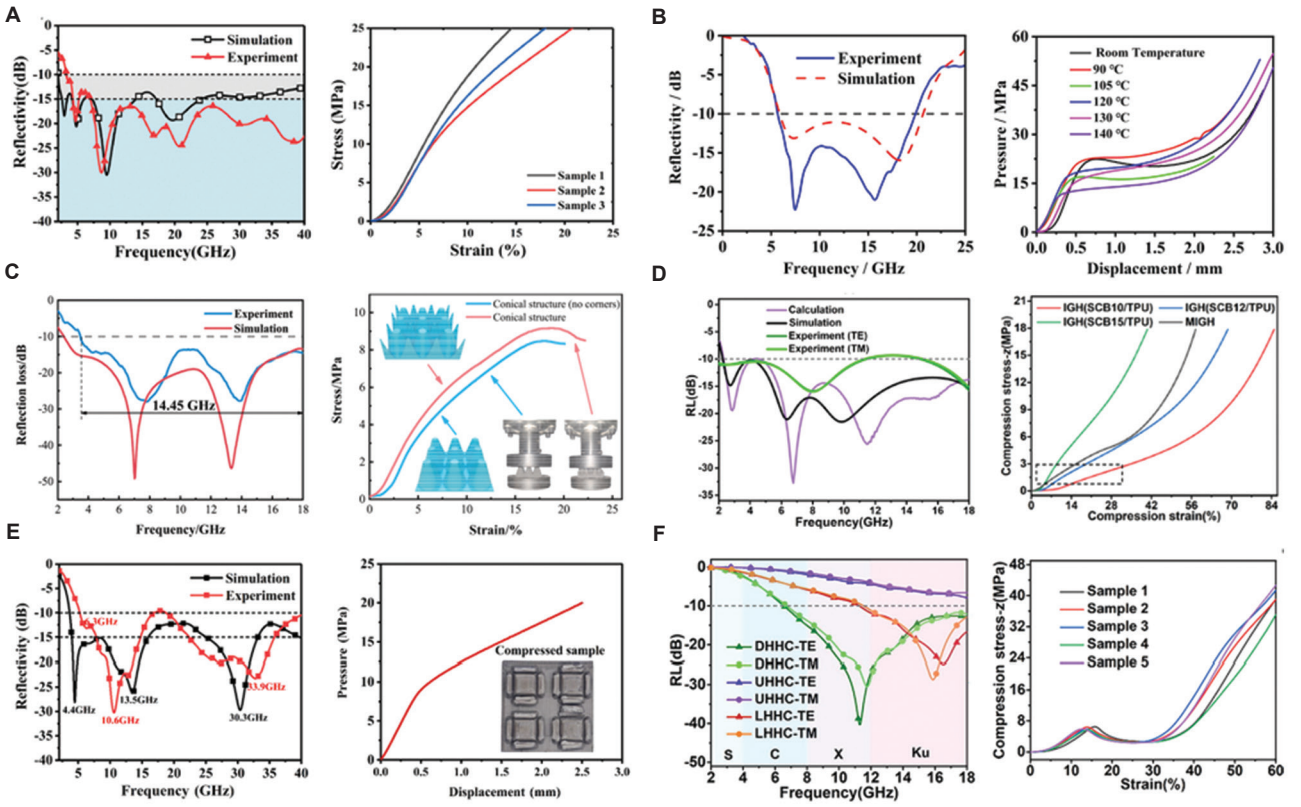

Figure 8. Results on electromagnetic microwave and load-bearing performance of recent additively manufactured microwave absorbers. (A) Bamboo-inspired metastructure.[69] Copyright © 2023 Elsevier. Reproduced with permission of Elsevier. (B) Octagon loop with four diagonals metastructure.[81] Copyright © 2021 Elsevier. Reproduced with permission of Elsevier. (C) Conical structure absorber.[70] Copyright © 2024 Elsevier. Reproduced with permission of Elsevier. (D) Gradient honeycomb metastructure.[86] Reproduced under the terms and conditions of the Creative Commons Attribution (CC BY) license. (E) Gradient metastructure.[66] Copyright © 2021 Elsevier. Reproduced with permission of Elsevier. (F) Double high-impedance surface-loaded honeycomb structure.[75] Copyright © 2023 Elsevier. Reproduced with permission of Elsevier.

effective microwave dissipation. The octagon loop with four diagonal designs[81] and conical structure absorber[70] showcases how geometric optimization can simultaneously address wave impedance matching and mechanical stress distribution. Particularly noteworthy is the gradient honeycomb metastructure,[86] which combines the mechanical advantages of honeycomb cores with spatially varying electromagnetic properties to create a smoothly transitioning impedance profile. These designs collectively represent a significant advancement over traditional absorbers that typically sacrifice structural performance for electromagnetic functionality.

The gradient metastructure[66] and double high-impedance surface-loaded honeycomb structure[75] highlight two distinct yet complementary approaches to multifunctional design. The gradient architecture employs a gradual variation in material composition or geometric parameters to achieve broadband absorption while maintaining structural integrity. In contrast, the double high-impedance honeycomb structure demonstrates how surface modifications to conventional cellular materials can enhance electromagnetic loss and load-bearing capacity. The conical structure absorber[70] represents another innovative approach, using its tapered geometry to provide progressive collapse characteristics under mechanical loads while its carefully designed surface patterning optimizes microwave absorption. Table 4 summarizes the electromagnetic microwave and load-bearing performances of recent additively manufactured polymer composite absorbers, including frequency range, bandwidth of RL, minimum, thickness, and mechanical properties. Recent studies on additively manufactured polymer composite absorbers highlight critical trends in balancing EMA and mechanical performance. Polyether-ether-ketone (PEEK)-based composites, such as the bamboo-inspired metastructure (13.27 MPa compressive strength, 3.2 – 40 GHz bandwidth), demonstrate superior multifunctionality compared to PLA or acrylonitrile butadiene styrene systems, emphasizing the importance of high-performance matrices. Bio-inspired, particularly

Table 4. Summary of the electromagnetic microwave and load-bearing performances of recent additively manufactured polymer composite absorbers

Structural design	Material	Frequency range (GHz)	Bandwidth of RL < −10 dB (GHz)	Minimum RL (dB)	Thickness (mm)	Mechanical properties	References
Bamboo-inspired metastructure	PEEK/FCIPs magnetic composite	2 – 40	3.2 – 40	−15	3	Compressive yield stress: 13.27 MPa	69
Conical structure	NFG/Si/Fe_3O_4/PF composite	2 – 18	3.55 – 18	−21.52	21	Compressive yield stress: 5.21 MPa	70
Electric-loss honeycomb metastructure	CF/CNT/ABS	2 – 18, 2 – 40	2 – 6.8, 10.4 – 40	< −10	8.67, 13.56, 14	Maximum load: 1.41 kN	22
Double high-impedance surface-loaded honeycomb (DHHC) structure	PEEK/ITO/PET	2 – 18	6.73 – 18	−15	4.25	Compressive strength: 6.09 MPa; flexural strength: 3.08 MPa	75
Gradient metastructure	FCIPs-PEEK composite	2 – 18	5.1 – 40	< −15	10	Compressive yield stress: 8.46 MPa	66
Octagon loop with four diagonals metastructure	PEEK/ITO	2 – 30	5.7 – 19.85	< −20	3.97	Compressive yield stress: 22.46 MPa	81
Three-dimensional honeycomb metastructure	PLA	1 – 24	3.53 – 24.00	−31.3	15.51	Compressive yield stress: 10.7 MPa	82
Tree-shaped metastructure	ABS/CF/MWCNT composite	2 – 18, 20 – 40	11.5 – 16	−28.66	10.8	Bending strength: 38.8 MPa	83
Pyramidal array sandwich structure	PLA/CF-reinforced plastics	4 – 18	4 – 18	≈ −10	13.5	Compressive strength: 9.60 MPa	68
Three-dimensional lossy dielectric metastructure	PLA/CB composite	1 – 40	1.36 – 40	< −20	21.4	Compressive strength: 3.75 MPa	76
Curved-wall honeycomb metastructure	Chopped CF/glass fiber	2 – 40	2 – 40	−16.5	20	Compressive strength: 31.3 MPa	87
Gradient honeycomb metastructure	TPU/CB composite	2 – 18	2.23 – 18	−15	15	Compressive strength: 22.89 MPa	86

Abbreviations: ABS: Acrylonitrile butadiene styrene; CB: Carbon black; CF: Carbon fiber; CNT: Carbon nanotube; FCIP: Flaky carbonyl iron particles; ITO: Indium tin oxide; NFG: Natural flake graphite; PEEK: Polyether-ether-ketone; PF: Phenol formaldehyde resin; PLA: Polylactic acid; RL: Reflection loss; TPU: Thermoplastic polyurethane.

honeycomb, lattice, and gradient structures, provide excellent mechanical properties and broadband absorption performance. It revealed an inverse relationship between thickness and mechanical efficiency, with optimal designs (typically 3 – 15 mm) leveraging cellular geometries and gradual property transitions to minimize trade-offs. These insights underscore the potential of advanced polymer materials, architectured metamaterials, and additive manufacturing processes to create lightweight, high-strength absorbers with tunable electromagnetic properties for next-generation applications.

6. Challenges and future perspectives

6.1. Challenges

In developing high-performance additively manufactured CFRP (AM-CFRP) absorbers, one of the main obstacles is ensuring the even distribution of CFs and nanofillers throughout the polymer matrix. Conductive fillers such as graphene or CNTs tend to aggregate during the extrusion-based 3D printing process, resulting in irregular electrical characteristics and variable microwave absorption.[88] Overall efficiency may be decreased by isolated conductive routes caused by this inhomogeneity that reflect electromagnetic waves instead of absorbing them. Furthermore, anisotropy is introduced by differences in fiber alignment and distribution among printed layers, which makes it challenging to forecast and regulate electromagnetic activity.[89-91] Post-processing techniques such as sonication or chemical functionalization may improve dispersion but add complexity to manufacturing.[92] Future solutions might call for sophisticated material formulations or *in situ* mixing technologies to guarantee uniformity during printing.

The main attenuation mechanism AM-CFRP absorbers use is dielectric losses, which could be inadequate, especially at higher frequencies (such as the millimeter-wave and

terahertz bands). Most polymer-based 3D printing filaments do not have magnetic loss mechanisms, limiting their broadband performance in contrast to conventional absorbers that use magnetic materials.[93] The incorporation of magnetic nanoparticles into CFRPs is difficult due to mechanical property degradation, weak interfacial bonding, and nozzle blockage. Furthermore, printability and layer adhesion may be compromised since high filler loadings are frequently needed to achieve high electrical conductivity.[94] The development of hybrid composites, which combine CFs with conductive or magnetic coatings (such as nickel-plated CFs[95]), may close this gap, although processing techniques need to be improved to preserve structural integrity and print fidelity.[96]

Increasing the amount of CF improves EMA but also causes printed structures to become more brittle and less ductile.[97] Layer delamination and poor interlayer adhesion can result from CFRPs' high stiffness, especially in complex geometries, for optimal electromagnetic performance.[98] The final component may also be further weakened by residual strains caused by the thermal expansion mismatch between CFs and polymer matrices during printing.[99] Particularly for automotive and aerospace applications where absorbers must sustain structural loads, striking a balance between mechanical durability and electromagnetic efficacy is essential.[100] Future research could investigate graded material designs, improved fiber orientations, or toughened polymer matrices to lessen these trade-offs without compromising absorption efficiency.

The scalability of AM-CFRP absorbers for industrial applications is restricted by the high cost of CF-reinforced filaments and the difficulty of multimaterial printing.[101] The resolution and throughput needed for the large-scale fabrication of high-performance EMWA structures are difficult for current additive manufacturing techniques.[26] Furthermore, post-processing procedures such as thermal annealing or chemical treatments to improve conductivity increase manufacturing time and cost.[102] Defects brought on by the process, such as voids or uneven layer bonding, might worsen electromagnetic performance. Developments in *in situ* curing methods,[103] high-speed additive manufacturing, and recyclable materials will be crucial to overcoming these obstacles.[104] One major obstacle to broader deployment is the development of scalable, affordable production techniques that preserve exact control over electromagnetic characteristics.

6.2. Future perspectives

Future developments in multimaterial additive manufacturing will witness the seamless integration of multifunctional components into CFRP constructions. Electrical traces, magnetic nanoparticles, and dielectric layers might be accurately deposited in a single production process using hybrid printing techniques that combine FDM with direct ink writing or aerosol jet printing.[105] By using this method, it would be possible to optimize impedance matching across a wide range of frequency bands by producing graded-index absorbers with spatially varied electromagnetic characteristics. Furthermore, the creation of innovative core-shell filament materials in which CFs are covered in lossy nanomaterials such as ferrites or MXenes may improve dielectric and magnetic loss mechanisms while preserving printability.[106] These developments would surmount the present restrictions in obtaining broadband absorption while maintaining structural soundness.

AM-CFRP absorber design will undergo a revolution with the combination of computational electromagnetics and ML.[107] Physics-informed neural networks can make rapid predictions of ideal fiber alignment patterns, infill densities, and metamaterial geometries suited to specific absorption bandwidths. To minimize material consumption and optimize wave attenuation, generative adversarial networks may suggest new, bio-inspired structures.[108] Real-time performance evaluation throughout the printing process may be made possible using digital twin technology, enabling adaptive manufacturing modifications. By drastically cutting down on the typical trial-and-error development cycle, these AI-powered techniques will speed up the process of finding high-performance absorber designs that would be impossible to build using traditional methods.[109] Cloud-based design tools may also facilitate collaboration among workers and experts in the manufacturing, electromagnetics, and material fields in optimization. The emergence of technologies powered by electromagnetic fields offers revolutionary possibilities for overseeing the production and manufacturing process of CFRP and CF. The synthesis, processing, and recycling stages of CFRP can be completed quickly, effectively, and sustainably with this technology. Figure 9 illustrates the functions of several novel approaches, which use electromagnetic radiation forms such as electric currents and microwaves, in drastically cutting energy use, lessening environmental impact, and improving CFRP performance. The rise of electromagnetic field-driven technologies presents disruptive opportunities for managing CF and CFRP manufacturing and production. It offers a rapid, efficient, and environmentally friendly solution for the synthesis, processing, and recycling phases. By utilizing electromagnetic radiation forms such as electric currents and microwaves, these innovative approaches hold promise for significantly reducing energy consumption and lowering environmental impact.

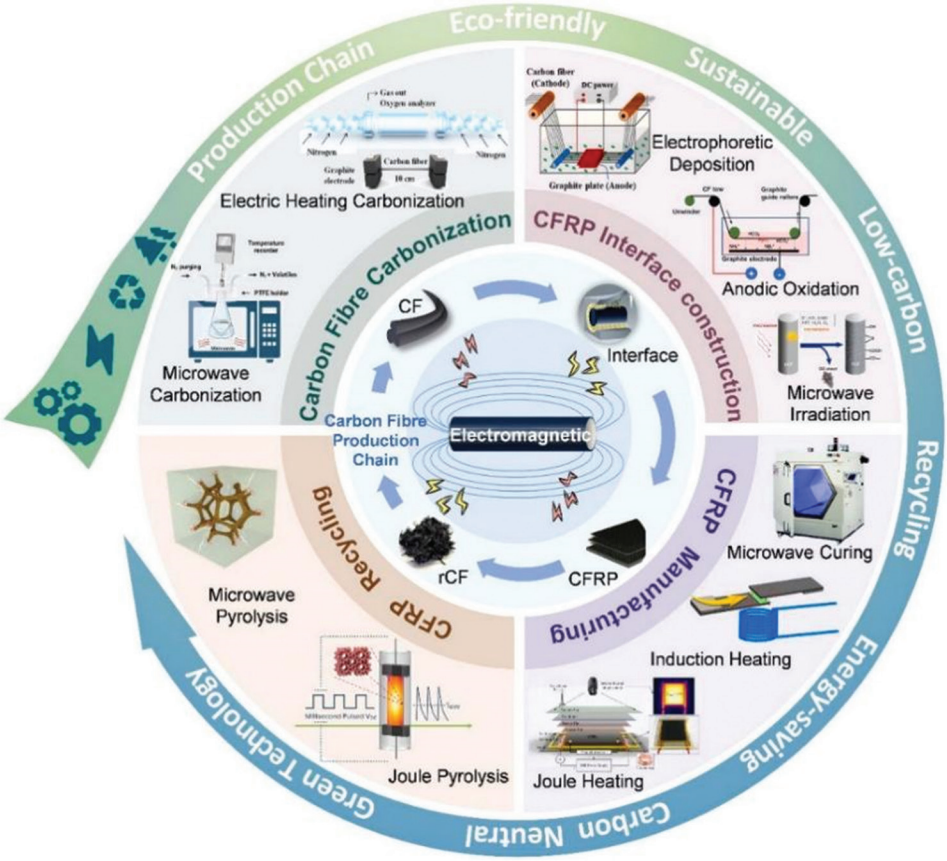

Figure 9. A summary of future perspectives on electromagnetic-driven production chain approaches and applications for CFRP structure.[110] Copyright © 2025. Reproduced with permission of Elsevier.
Abbreviations: CF: Carbon fiber; CFRP: Carbon fiber-reinforced polymer; rCF: Residual carbon fiber.

These methods offer significant advantages over conventional thermal approaches, including reduced energy consumption, faster processing times, and enhanced control over material properties. Microwave-based techniques, in particular, enable selective and uniform heating of CFs, improving the efficiency of carbonization and curing stages while minimizing environmental impact. Joule heating and pyrolysis further contribute to sustainable production by leveraging electrical currents for precise thermal management. These electromagnetic approaches align with the growing demand for greener manufacturing practices in the CFRP industry. The integration of electromagnetic-driven processes into the CFRP production chain holds immense potential for advancing sustainable material manufacturing. Future research should focus on scaling these technologies for industrial adoption, optimizing energy efficiency, and exploring hybrid methods that combine microwave, induction, and Joule heating for tailored material properties. In addition, the development of smart manufacturing systems incorporating real-time monitoring and artificial intelligence (AI)-driven process control could further enhance precision and reduce waste. As industries prioritize decarbonization, electromagnetic-assisted CFRP production may emerge as a key enabler of lightweight, high-performance composites for automotive, aerospace, and renewable energy applications, bridging the gap between sustainability and advanced material performance.

Responsive materials that can dynamically adjust their electromagnetic properties can be incorporated into AM-CFRP absorbers of the next generation.[111] Absorbers that change their microstructure in response to external stimuli such as temperature, electric fields, or mechanical stress may be made possible by 4D printing processes that use shape-memory polymers[109] or liquid crystal elastomers.[112] The absorbers would be efficient over various operating bands owing to their versatility, enabling real-time frequency adjustment. By combining conductive polymers with adjustable dielectric characteristics, active absorption devices that adapt to different danger frequencies may be developed.[113] Critical

absorption components in severe environments could extend their service life by self-healing nanocomposites that incorporate microencapsulated conductive agents. These nanocomposites could autonomously repair slight damage. These innovative material solutions pave the way to the intelligent, multifunctional electromagnetic protection by eliminating the limitations of classic passive absorbers.

With similar electromagnetic performance, bio-based polymer matrices made from renewable resources may eventually replace traditional petroleum-based resins.[114] CFs from end-of-life absorber components will be recovered and reprocessed using closed-loop recycling technologies, which will drastically lower material costs and their negative environmental effects. Developments in low-energy curing techniques, including microwave-assisted curing or photonic sintering, will reduce manufacturing's carbon footprint.In addition, as sustainable substitutes for synthetic CFs, researchers could investigate the usage of carbon compounds obtained from agricultural waste.[115] AM-CFRP absorbers will be positioned as essential elements in the green technology revolution thanks to these environmentally friendly methods and design-for-remanufacturing principles, which also help them comply with the ever-tougher environmental standards in the telecom and aerospace sectors.

Recent breakthroughs in additive manufacturing of CFRP structures have demonstrated remarkable potential for EM wave absorption, particularly when enhanced by ML optimization.[116] ML algorithms, including DNNs and GAs, are now being employed to navigate the complex design space of CFRP composites,[117] optimizing parameters such as fiber orientation,[118] layer thickness, and nanofiller distribution to achieve superior microwave absorption while maintaining structural integrity. These data-driven approaches have enabled the development of graded-index materials and metamaterial-inspired designs[119] that exhibit broadband absorption with reflection losses exceeding −30 dB. Furthermore, ML has significantly reduced the traditional trial-and-error development cycle, allowing for rapid iteration and performance prediction of novel composite architectures.[120] The integration of physics-informed neural networks has further improved accuracy by incorporating fundamental electromagnetic theory into the learning process, resulting in more reliable predictions of absorption characteristics.

Looking ahead, three key trends are poised to transform this field: (i) The development of autonomous self-optimizing systems combining real-time manufacturing monitoring with adaptive ML algorithms that continuously refine material designs during the additive manufacturing process.[121] (ii) The emergence of multi-physics ML models that simultaneously optimize EMA, mechanical strength, thermal management, and other functional requirements for truly multi-functional structures.[122] (iii) The integration of quantum ML to handle the exponentially increasing complexity of multiscale, multimaterial composite designs.[123] Future systems will likely incorporate digital twin technology that evolves with operational experience, enabling CFRP structures to adapt their electromagnetic properties in response to changing environmental conditions or mission requirements.In addition, the application of explainable AI techniques will provide crucial insights into the fundamental structure-property relationships, potentially revealing new design principles for microwave-absorbing materials. As these technologies mature, they will enable the creation of intelligent, responsive CFRP structures for next-generation aerospace, defense, and telecommunications applications, where dynamic control of electromagnetic signatures becomes as essential as static absorption performance.

7. Conclusion

This review comprehensively examines the EMWA properties of additively manufactured CFRP structures, emphasizing their design, performance, and underlying absorption mechanisms. Electromagnetic-absorbing materials based on nanocomposites have been extensively studied due to their exceptional properties, including high absorption efficiency, lightweight nature, thin matching thickness, and broadband attenuation capabilities. These characteristics make them highly promising for next-generation EMI shielding and stealth applications. The fundamental principles of EMI shielding are discussed, highlighting how nanostructured materials enhance absorption through dielectric and magnetic loss mechanisms. A critical aspect of effective EM wave absorption lies in achieving optimal impedance matching, which requires a careful balance between dielectric and magnetic losses. Recent advancements in nanocomposites have demonstrated their potential as high-performance microwave absorbers, offering strong attenuation, low density, and broad frequency coverage. By strategically combining different nanoscale components, researchers have developed hybrid materials that synergize the advantages of individual constituents, resulting in superior absorption performance. These materials exhibit diverse interactions with incoming electromagnetic radiation, enabling tailored responses across various frequency bands.

In the context of AM-CFRP structures, this review underscores that additive manufacturing techniques provide unprecedented control over microstructure

and geometry, facilitating the fabrication of complex, graded, and multifunctional absorbers. The ability to precisely engineer fiber orientation, filler distribution, and metamaterial-inspired designs has significantly improved EMWA efficiency while maintaining structural integrity. Furthermore, integrating conductive and magnetic nanofillers within CFRP matrices has expanded the possibilities for developing lightweight, high-strength absorbers suitable for aerospace, defense, and telecommunications applications. This review consolidates current knowledge on the EMWA mechanisms of AM-CFRP structures, offering insights into material selection, manufacturing optimization, and performance evaluation. The findings presented here establish a foundation for future research, encouraging further exploration of advanced nanocomposites and innovative additive manufacturing strategies to meet the growing demand for high-performance electromagnetic protection systems. By continuing to refine material formulations and fabrication techniques, next-generation AM-CFRP absorbers can achieve even greater efficiency, durability, and versatility in real-world applications.

Acknowledgments

None.

Funding

This work was supported by the Guangdong Innovative and Entrepreneurial Research Team Program (No. 2021ZT09X256), High Level of Special Funds (No. G03034K003), and Shenzhen Science and Technology Program (No. JCYJ20240813100904006).

Conflict of interest

Yi Xiong is an Editorial Board Member of this journal but was not in any way involved in the editorial and peer-review process conducted for this paper, directly or indirectly. Separately, other authors declared that they have no known competing financial interests or personal relationships that could have influenced the work reported in this paper.

Author contributions

Conceptualization: All authors
Data curation: Quanjin Ma, Ke Dong, Feirui Li
Funding Acquisition: Quanjin Ma, Ming Yu, Yi Xiong
Methodology: Quanjin Ma, Ke Dong, Yanjie Wu
Project Administration: Ming Yu, Yi Xiong
Resources: Jing Tian, Ming Yu, Yi Xiong
Writing – original draft: Quanjin Ma, Ke Dong, Feirui Li, Yanjie Wu
Writing – review & editing: Jing Tian, Ming Yu, Yi Xiong

Ethics approval and consent to participate

Not applicable.

Consent for publication

Not applicable.

Availability of data

Not applicable.

References

1. Lv H, Cui J, Li B, Yuan M, Liu J, Che R. Insights into civilian electromagnetic absorption materials: Challenges and innovative solutions. *Adv Funct Mater*. 2024;35:2315722.

   doi: 10.1002/adfm.202315722

2. Wang W, Li Z, Su R, Huang Y, Li Y, He R. Advanced 3D printing accelerates electromagnetic wave absorption from ceramic materials to structures. *NPJ Adv. Manuf.* 2025;2(1):2.

   doi: 10.1038/s44334-024-00013-w

3. Wang YF, Zhu L, Han L, Zhou XH, Gao Y, Lv LH. Recent progress of one-dimensional nanomaterials for microwave absorption: A review. *ACS Appl Nano Mater.* 2023;6(9):7107-7122.

   doi: 10.1021/acsanm.3c00818

4. Jie H, Zhao Z, Zeng Y, *et al*. A review of intentional electromagnetic interference in power electronics: Conducted and radiated susceptibility. *IET Power Electron*. 2024;17(12):1487-1506.

   doi: 10.1049/pel2.12685

5. Lin J, Huang J, Guo Z, *et al*. Hydrophobic multilayered PEG@ PAN/MXene/PVDF@ SiO_2 composite film with excellent thermal management and electromagnetic interference shielding for electronic devices. *Small*. 2024;20(46):2402938.

   doi: 10.1002/smll.202402938

6. Albert AA, Parthasarathy V, Kumar PS. Review on recent progress in epoxy-based composite materials for electromagnetic interference (EMI) shielding applications. *Polym Compos.* 2024;45(3):1956-1984.

   doi: 10.1002/pc.27928

7. Ma Q, Dong K, Li F, Yu M, Xiong Y. Inverse design of material, structure, and process for dielectric properties of additively manufactured PLA/$BaTiO_3$ polymer composites. *Compos Commun*. 2025;55:102314.

   doi: 10.1016/j.coco.2025.102314

8. Shi S, Jiang Y, Ren H, *et al*. 3D-printed carbon-based conformal electromagnetic interference shielding module for integrated electronics. *Nanomicro Lett.* 2024;16(1):85.

   doi: 10.1007/s40820-023-01317-w

9. Xia Y, Gao W, Gao C. A review on graphene-based

electromagnetic functional materials: Electromagnetic wave shielding and absorption. *Adv Funct Mater*. 2022;32(42):2204591.

doi: 10.1002/adfm.202204591

10. Gong D, Chen T, Cui S, Zhang D, Cai J. Recent advances and future prospects for construction strategies of flexible electromagnetic protection patches. *Adv Mater Technol*. 2025;10(5):2401497.

doi: 10.1002/admt.202401497

11. Cao WQ, Zhang M, Cao MS. A perspective of tailoring dielectric genes for 2D materials toward advanced electromagnetic functions. *Adv Funct Mater*. 2024;34(52):2410928.

doi: 10.1002/adfm.202410928

12. Ning Y, Zeng X, Huang J, Shen ZY, Gao Y, Che R. Multifunctional electromagnetic responsive porous materials synthesized by freeze casting: Principles, progress, and prospects. *Adv Funct Mater.* 2025;35(6):2414838.

doi: 10.1002/adfm.202414838

13. Lan D, Hu Y, Wang M, Wang Y, Gao Z, Jia Z. Perspective of electromagnetic wave absorbing materials with continuously tunable effective absorption frequency bands. *Compos Commun.* 2024;50:101993.

doi: 10.1016/j.coco.2024.101993

14. Zhang X, Zhao Z, Xu J, *et al*. N-doped carbon nanotube arrays on reduced graphene oxide as multifunctional materials for energy devices and absorption of electromagnetic wave. *Carbon*. 2021;177:216-225.

doi: 10.1016/j.carbon.2021.02.085

15. Cheng Z, Cao Y, Wang R, *et al*. Hierarchical surface engineering of carbon fiber for enhanced composites interfacial properties and microwave absorption performance. *Carbon*. 2021;185:669-680.

doi: 10.1016/j.carbon.2021.09.053

16. Shi Y, Ding X, Pan K, Gao Z, Du J, Qiu J. A novel multi-dimensional structure of graphene-decorated composite foam for excellent stealth performance in microwave and infrared frequency bands. *J Mater Chem A*. 2022;10(14):7705-7717.

doi: 10.1039/D2TA00030J

17. Gao Q, Ye X, He E, *et al*. 3D printed fabrication of ultra-structured composites of carbonyl iron powder@ carbon@ carbon black/polylactic acid for efficient microwave absorption. *Polym Compos.* 2024;45(15):13829-13843.

doi: 10.1002/pc.28738

18. Cai Y, Yu H, Cheng L, *et al*. Structure design, surface modification, and application of CNT microwave-absorbing composites. *Adv Sustain Syst.* 2023;7(12):2300272.

doi: 10.1002/adsu.202300272

19. Zhao R, Liang B, Shi Y, *et al*. Recent progress of carbon-based magnetic fibers for electromagnetic wave absorption. *Carbon*. 2024;229:119513.

doi: 10.1016/j.carbon.2024.119513

20. Ma Y, Liu R, Sun L, Wei S, Li X. Progress on microwave absorption performance of carbon fiber reinforced composites. *ChemistrySelect*. 2024;9(21):e202305226.

doi: 10.1002/slct.202305226

21. Tang W, Dong S, Cui T, *et al*. Lightweight zirconium modified carbon-carbon composites with excellent microwave absorption and mechanical properties. *Compos A Appl Sci Manuf.* 2024;180:108102.

doi: 10.1016/j.compositesa.2024.108102

22. Lei H, Shan M, Zhang Y, Zhao P, Yu C, Huang Y. Design-manufacturing-evaluation integration of microwave absorbing metastructures based on additive manufacturing. *Compos Sci Technol.* 2023;243:110270.

doi: 10.1016/j.compscitech.2023.110270

23. Ma Q, Dong K, Li F, *et al*. Additive manufacturing of polymer composite millimeter-wave components: Recent progress, novel applications, and challenges. *Polym Compos.* 2025;46(1):14-37.

doi: 10.1002/pc.28985

24. Gao B, Yan Y, Liu Y, *et al*. A design project of multifunctional broadband electromagnetic-wave-absorbing carbon fiber fabric composite by regulating periodic structure. *J Chem Eng.* 2025;508:161031.

doi: 10.1016/j.cej.2025.161031

25. Zhang F, Li N, Shi JF, *et al*. Recent progress on carbon-based microwave absorption materials for multifunctional applications: A review. *Compos B Eng.* 2024;283:111646.

doi: 10.1016/j.compositesb.2024.111646

26. Peng J, Wang S, Liang B, *et al*. Review of micro and nano scale 3D printing of electromagnetic metamaterial absorbers: Mechanism, fabrication, and functionality. *Virtual Phys Prototyp.* 2024;19(1):e2378937.

doi: 10.1080/17452759.2024.2378937

27. Zhang J, Li D, Wang M. Multi-material fused deposition modelling of structural–functional integrated absorber with multi-scale structure possessing tunable broadband microwave absorption. *Mater Des.* 2024;246:113315.

doi: 10.1016/j.matdes.2024.113315

28. Goh GD, Sing SL, Yeong WY. A review on machine learning in 3D printing: Applications, potential, and challenges. *Artif Intell Rev.* 2021;54(1):63-94.

doi: 10.1007/s10462-020-09876-9

29. Živković M, Žujović M, Milošević J. Architectural 3d-printed

structures created using artificial intelligence: A review of techniques and applications. *Appl Sci*. 2023;13(19):10671.

doi: 10.3390/app131910671

30. Zhu Z, Ng DWH, Park HS, McAlpine MC. 3D-printed multifunctional materials enabled by artificial-intelligence-assisted fabrication technologies. *Nat Rev Mater*. 2021;6(1):27-47.

doi: 10.1038/s41578-020-00235-2

31. Wang J, Zhou L, Fan C. A machine learning-based method for co-design and optimization of microwave-absorbing/load-bearing multifunctional structures. *Smart Mater Struct*. 2024;33(4):045023.

doi: 10.1088/1361-665X/ad31cf

32. Zhang Y, Shan M, Lei H, Zhao P, Yu C, Huang Y. Evolutionary algorithm-based integrated design of material-structural microwave absorption using material extrusion. *Compos A Appl Sci Manuf*. 2024;177:107891.

doi: 10.1016/j.compositesa.2023.107891

33. Du Y, Liu Y, Wang A, Kong J. Research progress and future perspectives on electromagnetic wave absorption of fibrous materials. *iScience*. 2023;26(10):107873.

doi: 10.1016/j.isci.2023.107873

34. Sista KS, Dwarapudi S, Kumar D, Sinha GR, Moon AP. Carbonyl iron powders as absorption material for microwave interference shielding: A review. *J Alloys Compd*. 2021;853:157251.

doi: 10.1016/j.jallcom.2020.157251

35. Cheng J, Zhang H, Xiong Y, *et al*. Construction of multiple interfaces and dielectric/magnetic heterostructures in electromagnetic wave absorbers with enhanced absorption performance: A review. *J Materiomics*. 2021;7(6):1233-1263.

doi: 10.1016/j.jmat.2021.02.017

36. Qin M, Zhang L, Wu H. Dielectric loss mechanism in electromagnetic wave absorbing materials. *Adv Sci (Weinh)*. 2022;9(10):2105553.

doi: 10.1002/advs.202105553

37. Zhang S, Lan D, Zheng J, Zhao Z, Jia Z, Wu G. Insights into polarization relaxation of electromagnetic wave absorption. *Cell Rep Phys Sci*. 2024;5(9):102206.

doi: 10.1016/j.xcrp.2024.102206

38. Elhassan A, Lv X, Abdalla I, Yu J, Li Z, Ding B. Efficient synthesis of Fe_3O_4/PPy double-carbonized core-shell-like composites for broadband electromagnetic wave absorption. *Polymers*. 2024;16(8):1160.

doi: 10.3390/polym16081160

39. Portes RC, Lopes BH, Rezende MC, Amaral-Labat G, Baldan MR. Enhancing metacomposite properties and electromagnetic interference shielding: Exploring the interplay between manufacturing processability of carbon fiber elastomeric composite and permittivity/permeability effects. *Adv Compos Hybrid Mater*. 2024;7(6):208.

doi: 10.1007/s42114-024-01036-9

40. Tang W, Sun J, Wang Y, *et al*. Electromagnetic absorption properties of 3D printed fiber-oriented composites under different paths. *Constr Build Mater*. 2024;416:135140.

doi: 10.1016/j.conbuildmat.2024.135140

41. Peng H, Zhang D, Xie Z, Lu S, Liu Y, Liang F. Recent advances in structural design of carbon/magnetic composites and their electromagnetic wave absorption applications. *Small*. 2025;21:2408570.

doi: 10.1002/smll.202408570

42. Cui L, Han X, Wang F, Zhao H, Du Y. A review on recent advances in carbon-based dielectric system for microwave absorption. *J Mater Sci*. 2021;56:10782-10811.

doi: 10.1007/s10853-021-05941-y

43. Liu JT, Zheng YC, Hou X, Feng XR, Jiang K, Wang M. Structured carbon for electromagnetic shielding and microwave absorption from carbonization of waste polymer: A review. *Chem Eng J*. 2024;496:154013.

doi: 10.1016/j.cej.2024.154013

44. Yim YJ, Lee JJ, Tugirumubano A, Go SH, Kim HG, Kwac LK. Electromagnetic interference shielding behavior of magnetic carbon fibers prepared by electroless FeCoNi-plating. *Materials (Basel)*. 2021;14(14):3774.

doi: 10.3390/ma14143774

45. Quan B, Liang X, Ji G, Zhang Y, Xu G, Du Y. Cross-linking-derived synthesis of porous Co_x Ni_y/C nanocomposites for excellent electromagnetic behaviors. *ACS Appl Mater Interfaces*. 2017;9(44):38814-38823.

doi: 10.1021/acsami.7b13411

46. Wu T, Huan X, Jia X, *et al*. 3D printing nanocomposites with enhanced mechanical property and excellent electromagnetic wave absorption capability via the introduction of ZIF-derivative modified carbon fibers. *Compos B Eng*. 2022;233:109658.

doi: 10.1016/j.compositesb.2022.109658

47. Tan H, Wang Y, Wang C, *et al*. Carbon nanotubes/carbon nanofibers@ carbon fiber construction of 3D network hierarchical structures toward multiple synergistic losses for electromagnetic wave absorption. *Vacuum*. 2024;219:112722.

doi: 10.1016/j.vacuum.2023.112722

48. Abdalla I, Shen J, Yu J, Li Z, Ding B. Co_3O_4/carbon composite nanofibrous membrane enabled high-efficiency electromagnetic wave absorption. *Sci Rep*. 2018;8(1):12402.

doi: 10.1038/s41598-018-30871-2

49. Yuan S, Wang T, Feng T, Kong J. Electromagnetic wave absorption of fabricated Fe/Fe_3O_4/C hollow fibers derived from ceiba fiber templates. *Mater Sci Eng B*. 2024;299:117057.

doi: 10.1016/j.mseb.2023.117057

50. Zhang L, Jiang Y, Wang L, Zhang C, Liu S. Hierarchical porous carbon nanofibers as binder-free electrode for high-performance supercapacitor. *Electrochim Acta*. 2016;196:189-196.

doi: 10.1016/j.electacta.2016.02.050

51. Bae J, Hong JY. Fabrication of nitrogen-doped porous carbon nanofibers for heavy metal ions removal. *Carbon Lett*. 2021;31(6):1339-1347.

doi: 10.1007/s42823-021-00291-w

52. Wu H, Qu S, Lin K, *et al*. Enhanced low-frequency microwave absorbing property of SCFs@ TiO_2 composite. *Powder Technol*. 2018;333:153-159.

doi: 10.1016/j.powtec.2018.04.015

53. Lv X, Yang S, Jin J, Zhang L, Li G, Jiang J. Preparation and electromagnetic properties of carbon nanofiber/epoxy composites. *J Macromol Sci Part B*. 2010;49(2):355-365.

doi: 10.1080/00222340903355750

54. Huang S, Zhou W, Luo F, Wei P, Zhu D. Mechanical and dielectric properties of short carbon fiber reinforced Al_2O_3 composites with MgO additive. *Ceram Int*. 2014;40(2):2785-2791.

doi: 10.1016/j.ceramint.2013.10.038

55. Logesh G, Srishilan C, Sabu U, *et al*. Carbon fiber reinforced composites from industrial waste for microwave absorption and electromagnetic interference shielding applications. *Ceram Int*. 2023;49(2):1922-1931.

doi: 10.1016/j.ceramint.2022.09.157

56. Dong H, Gao S, Yu C, *et al*. Design and performance of 3D-Printed ABS@ rGO/CF/CeO_2 composites for microwave absorption and mechanical strength. *Chem Eng J*. 2024;499:156696.

doi: 10.1016/j.cej.2024.156696

57. Wang J, Cheng B, Qiu H, Qi S. Enhanced microwave absorption properties of manganese dioxide/carbon fiber hybrid with polyaniline in the X band. *J Electron Mater*. 2018;47:5564-5571.

doi: 10.1007/s11664-018-6455-7

58. Cheng B, Wang J, Zhang F, Qi S. Preparation of silver/carbon fiber/polyaniline microwave absorption composite and its application in epoxy resin. *Polym Bull*. 2018;75:381-393.

doi: 10.1007/s00289-017-2035-x

59. Xia Q, Chen L, Wang X, *et al*. The microwave absorption performance of CF coated with MnO_2 nanowires grown by simple hydrothermal method. *Ceram Int*. 2024;50(24):55931-55939.

doi: 10.1016/j.ceramint.2024.11.003

60. Jun Z, Peng T, Sen W, Jincheng X. Preparation and study on radar-absorbing materials of cupric oxide-nanowire-covered carbon fibers. *Appl Surf Sci*. 2009;255(9):4916-4920.

doi: 10.1016/j.apsusc.2008.12.036

61. Huang B, Yue J, Wei Y, Huang X, Tang X, Du Z. Enhanced microwave absorption properties of carbon nanofibers functionalized by FeCo coatings. *Appl Surf Sci*. 2019;483:98-105.

doi: 10.1016/j.apsusc.2019.03.301

62. Zhang X, Qi S, Zhao Y, Wang L, Fu J, Yu M. Synthesis and microwave absorption properties of Fe@carbon fibers. *RSC Adv*. 2020;10(54):32561-32568.

doi: 10.1039/D0RA03547E

63. Yuan L, Zhao W, Miao Y, *et al*. Constructing core-shell carbon fiber/polypyrrole/$CoFe_2O_4$ nanocomposite with optimized conductive loss and polarization loss toward efficient electromagnetic absorption. *Adv Compos Hybrid Mater*. 2024;7(2):70.

doi: 10.1007/s42114-024-00864-z

64. Yu S, Wang C, Chen Z, *et al*. Additive manufacturing of broadband electromagnetic wave absorbing materials: Polymer-derived SiC/Si3N4 composites with triply periodic minimal surface meta-structure. *Chem Eng J*. 2024;483:149185.

doi: 10.1016/j.cej.2024.149185

65. Huang Y, Wu D, Zhang K, *et al*. Topological designs of mechanical-electromagnetic integrated laminate metastructure for broadband microwave absorption based on bi-directional evolutionary optimization. *Compos Sci Technol*. 2021;213:108898.

doi: 10.1016/j.compscitech.2021.108898

66. Duan Y, Liang Q, Yang Z, *et al*. A wide-angle broadband electromagnetic absorbing metastructure using 3D printing technology. *Mater Des*. 2021;208:109900.

doi: 10.1016/j.matdes.2021.109900

67. Wang G, Li D, Liu T, Zhang C, Xie YM, Liao W. Design and manufacturing of lightweight modular broadband microwave absorbing metastructure. *Compos B Eng*. 2023;266:111007.

doi: 10.1016/j.compositesb.2023.111007

68. Liang L, Yan L, Cao M, *et al*. Microwave absorption and compression performance design of continuous carbon fiber reinforced 3D printing pyramidal array sandwich structure. *Compos Commun*. 2023;44:101773.

doi: 10.1016/j.coco.2023.101773

69. Duan Y, Liang Q, Yang Z, *et al*. Bamboo-inspired composite

metastructure for broadband microwave absorption and load bearing. *Mater Res Bull*. 2023;166:112368.

doi: 10.1016/j.materresbull.2023.112368

70. Deng K, Wu H, Song B, *et al*. 3D-printed conical structure absorber based on NFG/Fe3Si/SiCnw ternary composites for multifunctional integrated electromagnetic microwave absorption. *Compos B Eng*. 2024;274:111243.

doi: 10.1016/j.compositesb.2024.111243

71. Duan Y, Liang Q, Yang Z, Wang X, Liu P, Li D. Ultrabroadband metastructure absorber with angular stability for conformal applications. *Mater Today Phys*. 2023;39:101278.

doi: 10.1016/j.mtphys.2023.101278

72. Zhang T, Li D, Yang Z, *et al*. A multi-materials 3D-printed continuous conductive fibre-based metamaterial for broadband microwave absorption. *Virtual Phys Prototyp*. 2024;19(1):e2285417.

doi: 10.1080/17452759.2023.2285417

73. Yin X, Long C, Li J, *et al*. Ultra-wideband microwave absorber by connecting multiple absorption bands of two different-sized hyperbolic metamaterial waveguide arrays. *Sci Rep*. 2015;5(1):15367.

doi: 10.1038/srep15367

74. Lim DD, Ibarra A, Lee J, Jung J, Choi W, Gu GX. A tunable metamaterial microwave absorber inspired by chameleon's color-changing mechanism. *Sci Adv*. 2025;11(3):eads3499.

doi: 10.1126/sciadv.ads3499

75. Li D, Pan W, Wang T, Wang X, Gong R. 3D printed lightweight metastructure with microwave absorption and mechanical resistance. *Mater Des*. 2023;225:111506.

doi: 10.1016/j.matdes.2022.111506

76. Zhang S, An Q, Li D, *et al*. Multifunctional meta-absorber based on CB-PLA composite and magnetic materials for electromagnetic absorption and load-bearing capacity. *Compos Sci Technol*. 2025;264:111131.

doi: 10.1016/j.compscitech.2025.111131

77. Tan R, Zhou F, Liu Y, *et al*. 3D printed propeller-like metamaterial for wide-angle and broadband microwave absorption. *J Mater Sci Technol*. 2023;144:45-53.

doi: 10.1016/j.jmst.2022.10.012

78. Lu Y, Chi B, Liu D, *et al*. Wideband metamaterial absorbers based on conductive plastic with additive manufacturing technology. *ACS Omega*. 2018;3(9):11144-11150.

doi: 10.1021/acsomega.8b01223

79. Sun H, Zhang Y, Wu Y, *et al*. Broadband and high-efficiency microwave absorbers based on pyramid structure. *ACS Appl Mater Interfaces*. 2022;14(46):52182-52192.

doi: 10.1021/acsami.2c16166

80. Gong P, Hao L, Li Y, Li Z, Xiong W. 3D-printed carbon fiber/polyamide-based flexible honeycomb structural absorber for multifunctional broadband microwave absorption. *Carbon*. 2021;185:272-281.

doi: 10.1016/j.carbon.2021.09.014

81. Yang Z, Liang Q, Duan Y, Li Z, Li D, Cao Y. A 3D-printed lightweight broadband electromagnetic absorbing metastructure with preserved high-temperature mechanical property. *Compos Struct*. 2021;274:114330.

doi: 10.1016/j.compstruct.2021.114330

82. Jiang W, Yan L, Ma H, *et al*. Electromagnetic wave absorption and compressive behavior of a three-dimensional metamaterial absorber based on 3D printed honeycomb. *Sci Rep*. 2018;8(1):4817.

doi: 10.1038/s41598-018-23286-6

83. Dong H, Gao S, Yu C, *et al*. Enhancing microwave absorption of bio-inspired structure through 3D printed concentric infill pattern. *Compos B Eng*. 2025;289:111924.

doi: 10.1016/j.compositesb.2024.111924

84. Ren J, Yin JY. 3D-printed low-cost dielectric-resonator-based ultra-broadband microwave absorber using carbon-loaded acrylonitrile butadiene styrene polymer. *Materials (Basel)*. 2018;11(7):1249.

doi: 10.3390/ma11071249

85. An Q, Li D, Liao W, *et al*. Electromagnetic absorption mechanism of TPMS-based metastructures: Synergy between materials and structures. *Adv Funct Mater*. 2025;35(5):2414629.

doi: 10.1002/adfm.202414629

86. Li D, Zheng X, Gu H, *et al*. Gradient honeycomb metastructure with broadband microwave absorption and effective mechanical resistance. *Nano Mater Sci*. 2024;6(4):456-466.

doi: 10.1016/j.nanoms.2023.09.005

87. Liu Z, Zhang R, Wang S, Zhao W, Yu G, Wu L. Design and fabrication of an all-composite ultra-broadband absorbing structure with superior load-bearing capacity. *Compos Sci Technol*. 2023;240:110094.

doi: 10.1016/j.compscitech.2023.110094

88. Qin H, Ding S, Ashour A, Zheng Q, Han B. Revolutionizing infrastructure: The evolving landscape of electricity-based multifunctional concrete from concept to practice. *Prog Mater Sci*. 2024:101310.

doi: 10.1016/j.pmatsci.2024.101310

89. Rithika K, Sudha J. Additive manufacturing of fiber-reinforced composites-a comprehensive overview. *Polym Adv Technol*. 2024;35(12):e70002.

doi: 10.1002/pat.70002

90. Zhang Y, Zheng W, Wang Y, *et al*. A review of 3D printing continuous carbon fiber reinforced thermoplastic polymers: Materials, processes, performance enhancement, and failure analysis. *Polym Compos.* 2025;46(10):1-31.

doi: 10.1002/pc.29895

91. Ding A, Tang F, Alsberg E. 4D printing: A comprehensive review of technologies, materials, stimuli, design, and emerging applications. *Chem Rev*. 2025;125(7):3663-3771.

doi: 10.1021/acs.chemrev.4c00070

92. Gackowski BM, Sharma M, Koh XQ, *et al*. Surface engineering of carbon nanotube-carbon fiber networks for enhanced strength in additive manufacturing of nylon composites. *Compos A Appl Sci Manuf.* 2024;186:108383.

doi: 10.1016/j.compositesa.2024.108383

93. Zhao X, Bai Y, Lu T, Lu Y. 3D-printed shape memory absorber based on CE/CNTs/CIP ternary composites for tunable and wideband electromagnetic wave absorption. *Appl Mater Today.* 2024;41:102504.

doi: 10.1016/j.apmt.2024.102504

94. Khan M, Refati MFAD, Arup MMR, Islam MA, Mobarak MH. Conductive polymer-based electronics in additive manufacturing: Materials, processing, and applications. *Adv Polym Technol.* 2025;1:4234491.

doi: 10.1155/adv/4234491

95. Liang J, Yue Q, Liu X, Li N. Enhancing mechanical properties of CFRP with oriented nickel plated short carbon fibers in a magnetic field. *Polym Compos.* 2024;46:7377-7389.

doi: 10.1002/pc.29436

96. Hareesh M, Joseph P, George S. Electromagnetic interference shielding: A comprehensive review of materials, mechanisms, and applications. *Nanoscale Adv.* 2025;8:1-27.

doi: 10.1039/d5na00240k

97. Nan Z, Wei W, Lin Z, Ouyang J, Chang J, Hao Y. Flexible electromagnetic interference shields: Materials, structure and multifunctionalization. *Mater Sci Eng R Rep.* 2024;160:100823.

doi: 10.1016/j.mser.2024.100823

98. Jaganathan S, Kandasamy R, Venkatachalam R, Gunalan M, Dhairiyasamy R. Advances in optimizing mechanical performance of 3D-printed polymer composites: A microstructural and processing enhancements review. *Adv Polym Technol.* 2024;1:3168252.

doi: 10.1155/2024/3168252

99. Liu F, Wang S, Zhang W, Ding X, Ferraris E, Ivens J. Mechanical and interfacial analysis of 3D-printed two-matrix continuous carbon fibre composites for enhanced structural performance. *Compos A Appl Sci Manuf.* 2024;180:108105.

doi: 10.1016/j.compositesa.2024.108105

100. Ren J, Mu Z, Sellami R, *et al*. Multifunctions of microwave-absorbing materials and their potential cross-disciplinary applications: A mini-review. *Adv Compos Hybrid Mater.* 2025;8(2):1-25.

doi: 10.1007/s42114-025-01258-5

101. Liu G, Xiong Y, Zhou L. Additive manufacturing of continuous fiber reinforced polymer composites: Design opportunities and novel applications. *Compos Commun.* 2021;27:100907.

doi: 10.1016/j.coco.2021.100907

102. Tamburrino F, Barone S, Paoli A, Razionale A. Post-processing treatments to enhance additively manufactured polymeric parts: A review. *Virtual Phys Prototyp.* 2021;16(2):221-254.

doi: 10.1080/17452759.2021.1917039

103. Loh TW, Ladani RB, Orifici A, Kandare E. Ultra-tough and *in-situ* repairable carbon/epoxy composite with EMAA. *Compos A Appl Sci Manuf.* 2021;143:106206.

doi: 10.1016/j.compositesa.2020.106206

104. Liu Y, Liu X, Lu J, *et al*. Post-treatment technologies for high-speed additive manufacturing: Status, challenge and tendency. *J Mater Res Technol.* 2024;.

doi: 10.1016/j.jmrt.2024.03.110

105. Persad J, Rocke S. A survey of 3D printing technologies as applied to printed electronics. *IEEE Access*. 2022;10:27289-27319.

doi: 10.1109/ACCESS.2022.3157833

106. Yadav RS, Anju, Kuřitka I. Spinel ferrite and MXene-based magnetic novel nanocomposites: An innovative high-performance electromagnetic interference shielding and microwave absorber. *Crit Rev Solid State Mater Sci.* 2022;48(4):441-479.

doi: 10.1080/10408436.2022.2067122

107. Fonseca JH, Jang W, Han D, Kim N, Lee H. Strength and manufacturability enhancement of a composite automotive component via an integrated finite element/artificial neural network multi-objective optimization approach. *Compos Struct.* 2024;327:117694.

doi: 10.1016/j.compstruct.2023.117694

108. Badini S, Regondi S, Pugliese R. Enhancing mechanical and bioinspired materials through generative AI approaches. *Next Mater.* 2025;6:100275.

doi: 10.1016/j.nxmate.2024.100275

109. Badini S, Regondi S, Pugliese R. Unleashing the power of artificial intelligence in materials design. *Materials* (*Basel*). 2023;16(17):5927.

doi: 10.3390/ma16175927

110. Zhu J, Li H, Yi J, *et al*. Electromagnetic techniques in carbon

fibre and carbon fibre composites manufacturing: A review. *Compos B Eng.* 2025;296:112227.

doi: 10.1016/j.compositesb.2025.112227

111. Rosario AJ, Ma B. Stimuli-responsive polymer networks: Application, design, and computational exploration. *ACS Appl Polym Mater.* 2024;6(23):14204-14228.

doi: 10.1021/acsapm.4c00002

112. Yin S, Huang Y, Wang Y, Wang Y, Xiao H. Tough and flexible poly (dimethylsiloxane) elastomer reinforced by conductive bacterial cellulose frameworks for high-performance microwave absorber. *Cellulose*. 2021;29:259-272.

doi: 10.1007/s10570-021-04276-w

113. Zhou Z, Li W, Qian J, *et al*. Flexible liquid crystal polymer technologies from microwave to terahertz frequencies. *Molecules*. 2022;27(4):1336.

doi: 10.3390/molecules27041336

114. Rajendran S, Al-Samydai A, Palani G, *et al*. Replacement of petroleum based products with plant-based materials, green and sustainable energy-a review. *Eng Rep.* 2025;7(4):e70108.

doi: 10.1002/eng2.70108

115. Zhang J, Duan C, Huang X, *et al*. A review on research progress and prospects of agricultural waste-based activated carbon: Preparation, application, and source of raw materials. *J Mater Sci.* 2024;59(13):5271-5292.

doi: 10.1007/s10853-024-09526-3

116. Wang Y, Wang K, Zhang C. Applications of artificial intelligence/machine learning to high-performance composites. *Compos B: Eng.* 2024;283:111740.

doi: 10.1016/j.compositesb.2024.111740

117. Jiang J, Xiong Y, Zhang Z, Rosen DW. Machine learning integrated design for additive manufacturing. *J Intell Manuf.* 2022;33(4):1073-1086.

doi: 10.1007/s10845-020-01715-6

118. Ren H, Chen Z, Wang D, Rosen DW, Xiong Y. Performance and manufacturability co-driven process planning for topology-optimized structures fabricated by continuous fiber-reinforced polymer additive manufacturing. *Compos A Appl Sci Manuf*. 2025;192:108813.

doi: 10.1016/j.compositesa.2025.108813

119. Sun C, Li D, Liu T, *et al*. Design of functionally gradient metastructure with ultra-broadband and strong absorption. *Compos B Eng.* 2024;280:111484.

doi: 10.1016/j.compositesb.2024.111484

120. Babu SS, Mourad AH, Harib KH, Vijayavenkataraman S. Recent developments in the application of machine-learning towards accelerated predictive multiscale design and additive manufacturing. *Virtual Phys Prototyp.* 2023;18(1):e2141653.

doi: 10.1080/17452759.2022.2141653

121. Zhao D, Zhou Z, Ruan K, *et al*. In-process density measurement for model-based process optimization of functionally graded foam microcellular structures in material extrusion additive manufacturing. *Addit Manuf.* 2025;106:104817.

doi: 10.1016/j.addma.2025.104817

122. Zhu E, Zong Z, Li E, *et al*. Frequency transfer and inverse design for metasurface under multi-physics coupling by Euler latent dynamic and data-analytical regularizations. *Nat Commun*. 2025;16(1):2251.

doi: 10.1038/s41467-025-57516-z

123. Zhao D, Wang Z, Zhou Z, *et al*. Multiscale design of CFRPC sandwich structures with foam core: Microcellular optimization and compressive property evaluation. *Polym Compos*. 2025;46(11):1-14.

doi: 10.1002/pc.30032

ACCSCIENCE PUBLISHING

Engineering Science in Additive Manufacturing

REVIEW ARTICLE

Multi-material additive manufacturing of metals: A review of structures and mechanical characteristics

Saneej N. Samad[1], Jacklyn Griffis[2], Guha Manogharan[2], and Nadia Kouraytem[1]*

[1]Department of Mechanical and Aerospace Engineering, College of Engineering, Utah State University, Logan, Utah, United States of America

[2]Department of Mechanical Engineering, College of Engineering, Pennsylvania State University, Philadelphia, Pennsylvania, United States of America

Abstract

The ability to manufacture complex designs from multiple materials has long been a key objective for applications operating in extreme environments. Multi-material (MM) additive manufacturing (MMAM) has significantly enhanced the functionality of additive manufacturing (AM) by enabling the integration of dissimilar alloys while leveraging the inherent advantages of AM, including design flexibility, reduced material waste, and rapid production, with the ability to tailor mechanical properties through spatial material distribution and local processing conditions. This process unlocks unprecedented opportunities across industries such as aerospace, automotive, biomedical, energy, and nuclear sectors. This article provides a comprehensive review of the state-of-the-art in MMAM, focusing on the manufacturing processes, molten pool formation, alloy compatibility, and bimetallic interface characteristics—including microstructural and mechanical properties—as well as modeling and simulation approaches for performance prediction and optimization, with developments tracked from 2013 to 2024. This review article predominantly focuses on: (i) MM-laser powder bed fusion, (ii) MM-directed energy deposition, and (iii) MM-wire-arc AM by detailing the mechanisms of molten pool formation at the interface and dissimilar alloy material compatibilities. Subsequently, the article provides an in-depth analysis of the meso- and micro-structural characteristics at the interface in bimetallic structures across widely employed MMAM alloys. The mechanics of MMs under various mechanical properties are presented, including microhardness/micro-indentation, tensile, flexural, compression, and fatigue strength, which are critical for MMAM applications in extreme conditions. In addition, current modeling and simulation approaches for MMAM are discussed with respect to the challenges and opportunities to increase MMAM adoption. The article concludes with a future roadmap for advancing MMAM by overcoming feedstock and build material cross-contamination, monitoring the *in situ* process, standardizing MM testing, and further developing thermo-mechanical modeling, specifically, for MMAM.

Keywords: Multi-material additive manufacturing; Interfacial boundary layers; Process–structure–property relationships; Three-dimensional printing; Mechanical behavior; Modeling and simulation

***Corresponding author:**
Nadia Kouraytem
(nadia.kouraytem@usu.edu)

Citation: Samad SN, Griffis J, Manogharan G, Kouraytem N. Multi-material additive manufacturing of metals: A review of structures and mechanical characteristics. *Eng Sci Add Manuf.* 2025;1(2):025180010. doi: 10.36922/ESAM025180010

Received: May 1, 2025

Revised: June 8, 2025

Accepted: June 13, 2025

Published online: June 30, 2025

1. Introduction

Metal additive manufacturing (AM) is revolutionizing industries with its growing adoption across automotive,[1,2] nuclear,[3-5] aerospace,[6-9] energy,[10-12] and biomedical sectors.[13-18] Utilizing a layer-by-layer approach guided by computer-aided design models,[19] metal AM offers transformative advantages over traditional manufacturing methods, including reduced material waste, accelerated production cycles, enhanced part consolidation, and unprecedented design flexibility. While significant strides have been made in fabricating single-material components, the next frontier lies in further advancing multi-material (MM) metal AM (MMAM). Enhancing the quality, reliability, and performance of MM components is critical to unlocking their full potential and meeting the rigorous demands of real-world applications—a challenge this review seeks to address following a roadmap consisting of six topics, as presented in Figure 1.

Recent advancements in AM have enabled the processing of multiple materials within a single build, a technique referred to as MMAM. Components manufactured using MMs can produce tailored mechanical properties according to spatial part design requirements, and concurrent local material assignment and processing conditions. In addition to the tailored mechanical characteristics, the MMAM approach also enables manufacturing complex structures that are otherwise cost-prohibitive or often not feasible through other manufacturing methods.[24-30] Recent advancements in material deposition have enabled AM users to achieve precision control at the voxel length scale in the order of a few hundred microns.[31,32] By leveraging the existing advantages of AM processes, ongoing advancements in MM would introduce a new paradigm and range of opportunities for design, mechanical properties, and manufacturing capabilities.[33]

Despite the numerous advantages of MMAM, limitations in the detailed understanding of the process–structure–property (P-S-P) relationships present severe constraints in fully adopting and leveraging its capabilities.[34] Some examples of the critical challenges faced by MMAM include the complex behavior at the interfaces of the dissimilar materials, heterogeneous thermal properties (melting temperature, thermal conductivity, laser absorptivity, and coefficient of thermal expansion [CTE]), and cross-contamination between virgin and used powders. Addressing these gaps is essential for qualifying MMAM for high-performance applications in aerospace, defense, energy, biomedical, and other emerging industries.

To effectively address these challenges, it is vital to examine the most widely adopted metal AM processes

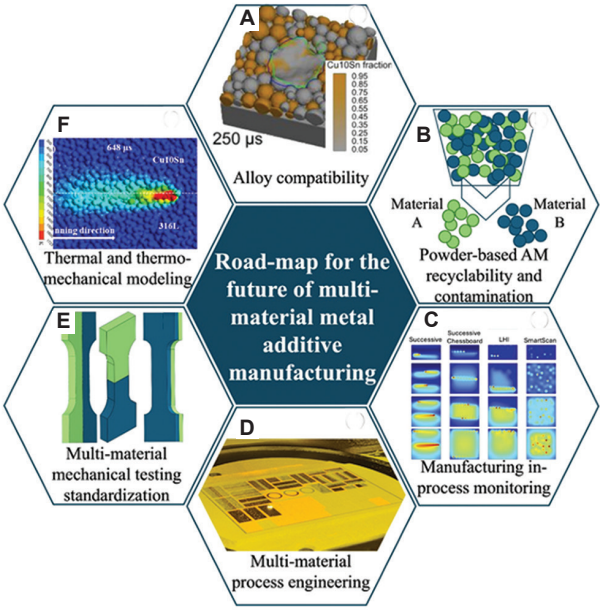

Figure 1. Road map for the future of bimetallic multi-material additive manufacturing (MMAM). Includes the discussion on (A) alloy compatibility. Reproduced with permission from Sun *et al.*[20] Copyright© Elsevier 2020. (B) Powder recyclability and contamination, (C) AM in-process monitoring techniques. Reproduced with permission from He *et al.*[21] Copyright© Elsevier 2023. (D) MMAM process engineering,[22] (E) MMAM mechanical testing standardization, and (F) modeling and simulation.[23] Reproduced with permission from Aerosint Company[22] and Gu *et al.*[23] Copyright © Elsevier 2020.

that have been proven for single metallic materials and are under rapid development for MMAM. The list includes three main processes: (i) Laser-based powder bed fusion (LPBF) and electron-beam powder bed fusion (EB-PBF), (ii) laser-directed energy deposition (LDED), and (iii) wire-arc AM (WAAM). Among these, LPBF is known for achieving higher dimensional accuracy; however, it suffers from small build volumes, low surface roughness, and low production efficiency. These drawbacks result from factors such as fine powder particles (10 – 50 µm),[35] relatively large laser spot size (50 – 80 µm),[36] small layer thickness (<100 µm),[37] and a high risk of powder cross-contamination.[38-41] In Section 2.1, the author will discuss in depth the advantages and limitations of LPBF. In contrast, LDED and WAAM offer significant advantages in terms of higher deposition rate, minimal cross-contamination between multiple materials, and suitability for large-scale component manufacturing. However, these techniques are associated with high surface roughness and low-dimensional accuracy (100 µm).[39] Given these trade-offs, recent progress has focused on leveraging all three process techniques for the fabrication of MM components. A detailed description of each process and the mechanics of melt pool formation, as well as alloy compatibility in

MMAM, is provided in Section 2. Using these processes, the transition between dissimilar materials can be either discrete or gradual.

The interfaces of MMAM structures consist of either a discrete boundary (discrete MMAM), characterized by a direct transition between two materials; a functionally graded boundary—in which the proportion of material composition varies along the interface—or a discrete boundary incorporating a third material as an interlayer, as shown in Figure 2. Functionally graded materials (FGM) enable complex and locally controlled MM component fabrication by providing smooth transitions between dissimilar materials. However, FGM comes with limitations, such as inconsistent gradient control and unpredictable feedstock deposition, which may limit the repeatability and precision of the FGM components. In contrast, discrete MMAM with direct compositional change (including adaptation of interlayer material) offers significant engineering benefits such as increased flexibility in design and production, property optimization, and the ability to realize complex functionalities.[42,43] Both FGM and discrete MMAM components can deliver localized enhancements, such as high wear resistance, high-temperature resistance, and corrosion resistance in target regions, while maintaining traditional mechanical properties at adequate level, an approach that is often restricted in single-material components.[40,44] For the reader's ease, the term MMAM will now be used interchangeably with discrete MMAM to identify a discrete compositional change between dissimilar materials using AM here on.

The adoption of MMAM has garnered increasing interest across industries such as aerospace,[22,45-49] automotive,[50,51] biomedical,[52] and nuclear energy.[53,54] In the aerospace industry, MMAM implemented functionality

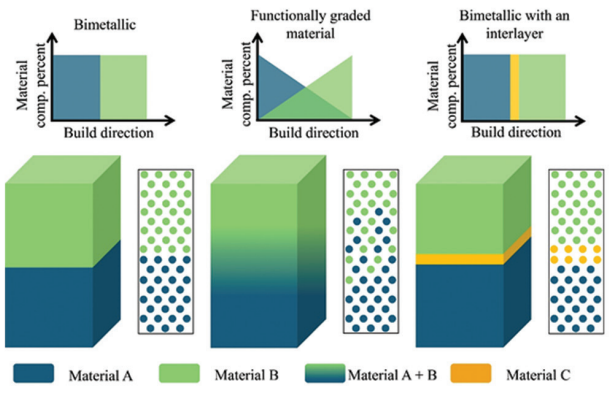

Figure 2. Schematic illustration of bimetallic, functionally graded materials, and interlayer-assisted multi-material additive manufacturing structures, highlighting the differences in materials transition and material compositional distribution characteristics across the interface
Abbreviation: Comp.: Composition.

in propulsion, heat exchangers, and other components. For instance, in 2017, the National Aeronautics and Space Administration launched the "Rapid Analysis and Manufacturing Propulsion Technology" program to reduce the cost and weight of the thrust chamber assembly. This initiative utilized bimetallic joints to directly fuse the copper (Cu) combustion chamber with the nickel (Ni) alloy nozzle, eliminating the need for additional fasteners. Cu/Ni alloy combinations are particularly suitable for propulsion applications due to the high thermal conductivity of Cu and the mechanical strength of Ni.[45-47] Another MMAM demonstration in industry integrated titanium (Ti) and aluminum (Al) to manufacture a lightweight yet corrosion-resistant spaceflight frame, capitalizing on Ti's high corrosion resistance and Al's lightweight.[48] Another example of MMAM application is the Cu/stainless steel (SS) MMAM heat exchanger fabricated by Aerosint (Belgium), where complex Cu channels were embedded in SS to produce a monolithic structure that demonstrated a relatively higher cost-effectiveness over conventional manufacturing.[22] Similarly, an SS/Ni component was manufactured through MMAM for a heat exchanger by leveraging the high-temperature performance of Ni and the higher ductility, corrosion resistance, and lower cost of SS.[49] The applications of MMAM in aerospace have extended to vital components such as propulsion systems, heat exchangers, and spacecraft body frames without compromising functional performance.

The impact of MMAM extends beyond the aerospace industry. With the growing adoption in the automotive industry, components such as electric motor rotor[51] and car chassis[50] have been fabricated using MMAM techniques with iron (Fe)/Ni and Al/SS compositions, respectively. The design flexibility enabled through LPBF allowed for the reduction of eddy currents and increased motor efficiency. Meanwhile, the Al/SS MMAM chassis helped reduce the vehicle's weight while maintaining higher strength and corrosion resistance. Similarly, to the automotive industry, the biomedical fields,[52] nuclear energy,[53,54] and anti-counterfeiting[55] have implemented MMAM. The MMAM of Ni/Ti has been explored as a viable hip implant due to its shape memory behavior and bio-compatibility.[52] In the nuclear energy industry, tungsten/Cu has been explored for use in fusion nuclear reactor components, leveraging their combined high-temperature resistance and excellent plasma radiation resistance properties.[53,54] Besides the large-scale industries, MMAM has shown promise in anti-counterfeiting, where embedded safety features, such as a quick response code, have been incorporated into metallic components made of SS/Cu alloys to allow traceability and authentication.[55]

While the array of current applications of MMAM demonstrates its versatility, a deeper understanding of the underlying microstructures, mechanical behavior, and modeling and simulation of materials used in MMAM is crucial to ensure wider adoption. The goal of this review article is to identify a potential road map for advancing the field of MMAM by providing a detailed insight into the current state of microstructure, mechanical characteristics, and modeling and simulation of MMAM structures. In contrast to previous review articles (Table A1), which have primarily focused on FGM, this article gathers and synthesizes the results reported in empirical studies that investigated the P-S-P relationships of MMAM structures, with a roadmap toward further development of MMAM. Prior literature has explored various aspects, including applications,[60-66] challenges in FGM-LDED,[60,67] challenges in thermal properties and creation of harmful compounds,[68] challenges in steel- and metal-based FGM,[69,70] progress in structures and functionality of FGM,[71] manufacturing techniques,[60,64,72-75] experimental studies on metal-metal, metal-ceramic and metal-intermetallic gradient, and numerical studies on material science and engineering,[67,76,77] and practical applications.[62,63,67,70,71,74,75,78] While these review articles provide abundant information on MMAM, a critical research gap and future direction (applicable to MMAM) concerning structures with discrete transitions remain unexplored. This article aims to address that gap in the following sections.

To systematically address these research gaps and advance the understanding of structures with discrete transitions, this review article is organized as follows. This review article is divided into five main sections, followed by a discussion and future trends. The first section includes an overview of the processing principles of the three main metal MMAM processes, along with a discussion on MM melt pool formation mechanisms and alloy compatibility observed across the discussed processes. The second section consists of a detailed review of macro- and micro-structural characteristics observed at bimetallic interfaces (e.g., microstructural growth, defects, metallurgical bonding, intermetallic phases) from reported studies. The third section focuses on the available data on the mechanical properties of MMAM (e.g., microhardness, tensile strength, flexural strength, compression, fatigue, *etc.*). The fourth section focuses on the modeling and simulation (e.g., phase transformation, melt pool formation, computer coupling of phase diagrams and thermochemistry [CALPHAD], finite element analysis [FEA]) approaches for bimetallic structures. Finally, the review article closes with a discussion on current technological roadblocks in advancing the development and adoption of MMAM, specifically: (i) Alloy compatibility, (ii) powder recyclability, (iii) AM in-process monitoring, (iv) MM process monitoring, (v) MM mechanical testing standardization, and (vi) thermal- and thermo-mechanical modeling as presented in Figure 1.

2. Overview of MMAM processes

2.1. Laser powder bed fusion (LPBF)

LPBF is a metal-AM process that utilizes a high-powered scanning laser beam to selectively melt a region of a powder bed onto a metal substrate in a layer-by-layer fashion to produce three-dimensional (3D) solid metal parts. Melting occurs on metal powder fabricated through various powder processes (e.g., gas atomization, plasma atomization, plasma rotating electrode process, hydride-dehydride, and wire atomization) inside a sealed inert gas build chamber, usually filled with argon or nitrogen, which is pumped throughout the build chamber to maintain a low oxygen content. Previous studies indicate that an oxygen content of 300 – 1,000 ppm is required to prevent oxidation during the manufacturing process.[79] In addition to maintaining a low oxygen content, inert gas is used to reduce the likelihood of defects associated with high oxygen levels, which may include irregular melt track morphology, irregular melt pool surface tension, and spattering.[80-83] The build plate, as shown in Figure 3A, is made of a material similar to the feedstock metal and can be preheated to minimize thermal gradients and reduce the buildup of thermally induced residual stresses or thermally induced part distortion.[84] LPBF imposes process-specific design constraints on part geometry and material selection but offers an elevated level of design complexity compared to traditional subtractive manufacturing methods. The metal alloys that are compatible with LPBF include Ti, Al, Fe (steels), cobalt–chromium, Ni, and Cu-based alloys (analogously, any metal that can be welded).[85] Similar to the single-material LPBF process, in MM-LPBF, the powder that is not melted is retained in the powder bed while dissimilar material is deposited over it, following a process analogous to single-material LPBF. The dissimilar material powder spreading mechanism in MM-LPBF comprised various methods, such as (i) blade-based dissimilar material spreading, (ii) ultrasonic-based dual powder dispenser, (iii) electrophotographic-based dual powder dispense, and (iv) "blade + ultrasonic" hybrid powder spreading technique, which were used.[40]

Advantages of MM-LPBF include (i) the ability to manufacture intricate 3D structures monolithically,[86] (ii) high resolution and rigorous build accuracy with dimension error lower than 100 μm,[39] (iii) better processing accuracy compared to other metal-AM due to smaller powder size (10 – 50 μm),[35] larger laser spot diameter (50 – 80 μm),[36]

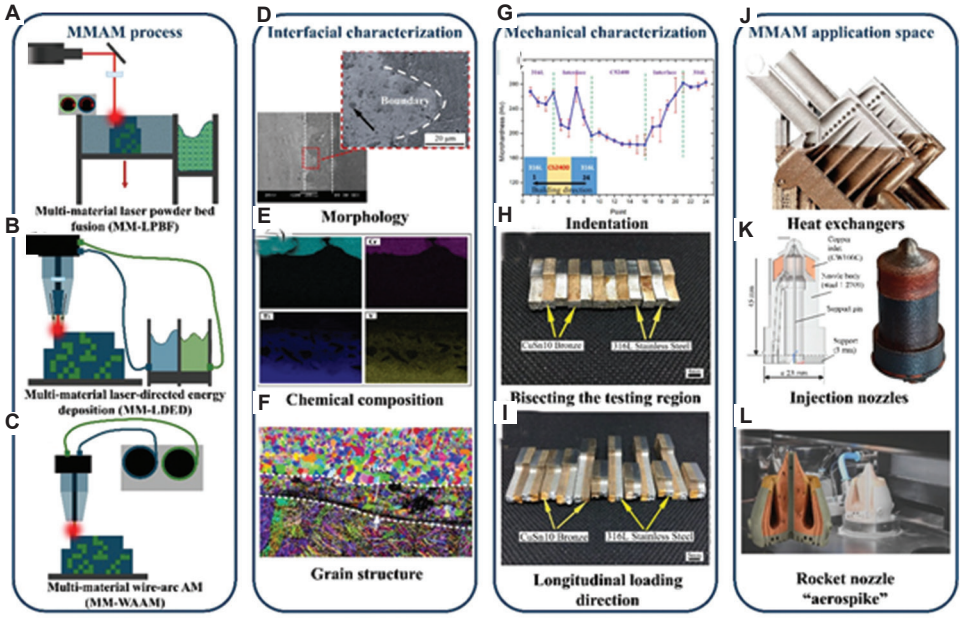

Figure 3. Summary of discrete multi-material (MM) additive manufacturing (MMAM) processes, interfacial characterization techniques, mechanical properties characterization, and industrial applications. (A-C) The three common methods of metal MMAM are MM-LPBF, MM-DED, and MM-WAAM. (D-F) Common methods of interfacial characterization, namely scanning electron microscopy,[140] energy dispersive spectroscopy,[140] and electron backscatter diffraction,[57] respectively. Scale bar: 100 μm. Reprinted with permission from Bai *et al.*[140] and Wei *et al.*[57] (G-I) Methods of mechanical characterization of MMAM structures through indentation hardness testing[140] and tensile testing with variations in material orientation.[58] Reprinted with permission from Bai *et al.*[140] and Chen *et al.*[57]. Copyright© Elsevier 2019. (J-L) Space applications of MMAM designs.[49,59,23] Reprinted with permission from Wessel and Amsterdam,[49] Schneck *et al.*,[59] and Gu *et al.*[23] Copyright© Elsevier 2021.

and smaller layer thickness (<100 μm).[37] Limitations of MM-LPBF include (i) limited build size, (ii) challenges in powder recyclability, and (iii) dependence on powder size and processing parameters.

2.2. Laser-directed energy deposition

Laser-directed energy deposition is defined as an "AM process in which focused thermal energy is used to fuse materials by melting as they are being deposited" by the ISO/ASTM 52900 standard.[87] The LDED process deposits powder feedstock directly onto the substrate by melting it in a controlled heated region using focused energy in the form of a laser, electron beam, or plasma arc.[88,89] The process of feeding molten powder or wire feedstock into a melt pool produced by the heat source beam builds material onto the substrate in a layer-wise process, followed by rapid solidification. The feedstock can be changed mid-process to produce discrete or graded heterogeneous components with tailored material properties. Inert gases are used during the AM process to prevent the molten pool from being contaminated by unmelted powder particles or porosities.[88] In multi-material LDED (MM-LDED), the fabrication process follows the same method as a single-material LDED with the inclusion of dissimilar materials through powder ejecting nozzle from different hoppers (Figure 3B). These nozzles can be mounted onto a multi-axis arm that moves around a fixed component or onto a tool head to deposit onto a component mounted in a five-axis vice.[90] Given these capabilities, MM-LDED offers unique advantages and limitations, as summarized below.

Advantages of MM-LDED include (i) inherent functionality of depositing MM and location-specific material deposition,[88,89,91] (ii) higher rate of deposition rates compared to PBF,[88,92,93] (±2.5 kg/h for LDED vs. ±0.01 kg/h for LPBF vs. ±0.25 kg/h for EB-PBF),[94] (iii) large-scale fabrication (compared to LPBF),[92,93,95] and (iv) potential use for coating, cladding,[96,97] and repairing damaged parts.[98,99] Limitations of MM-LDED include (i) limited design freedom due to lower-dimensional accuracy and higher surface roughness,[95,100] (ii) low powder efficiency and recyclability, particularly in MM, and (iii) possible shrinkage, residual stress, and deformation due to thermal process cycling. LDED is commonly paired with computer numerical control machining as a hybrid-AM solution to resolve the poor surface finish and achieve near-net shape geometry.[93]

2.3. Wire arc AM

Wire arc AM is a subset of LDED that uses a welding arc to generate a melt pool. WAAM is gaining more interest

and traction in the AM community, especially for MMAM; hence, it is presented separately here and in subsequent discussions. In WAAM, a wire of heterogeneous characteristic materials is fed into the melt pool created by the welding arc along the designed path to form a component (Figure 3C). WAAM is compatible only with wire feedstock, like the feeding rods used in most welding processes. As a result, material restrictions include only materials that are ductile enough to be pulled into the wire. Weldable materials such as SS, Ni, Ti, and Al alloys are commonly used in WAAM.[71,101] Like MM-LDED, multi-material WAAM (MM-WAAM) follows the same procedure as the dissimilar materials deposited through a wire-fed nozzle. Building upon the basic WAAM process, the major advantages and challenges associated with MM-WAAM are outlined below.

The advantages of WAAM coincide with those of LDED. While WAAM offers a higher deposition rate than PBF, it comes at the expense of increased surface roughness and reduced dimensional accuracy. To improve the surface finish and dimensional accuracy, components are often required to undergo post-processing or subtractive machining to produce near-net shape geometry. Alongside a higher deposition rate, WAAM is associated with an inexpensive machine cost, simple configuration, high efficiency, and large-scale component fabrication.[71,102-105]

2.4. Mechanisms of melt pool formation

The formation of a bi-metallic interface using MMAM processing involves thermal and fluidic interactions between the solid substrate and the unmelted feedstock of the dissimilar metal. A key challenge in MMAM processing is mitigating the defects that tend to form at the interface of the dissimilar metals, mainly caused by the mismatch in thermal properties. This mismatch may induce macro-strains near the interface and cause defects such as cracking and porosity. Understanding the mechanisms of melt pool formation and the subsequent cooling process is a necessary foundation for mitigating the formation of defects in that region.

In all metal MMAM processes, many studies characterize the interface as having grain refinement and report an increase in hardness across the transition. For processes such as MM-LPBF, a high cooling rate (10^7 K/s) compared to other laser or arc-welding processes (10^3 K/s) may cause additional grain refinement. Grain refinement may be further exaggerated for all processes while printing bi-metallic structures, which pair highly conductive materials (such as Cu alloys) with a moderate alloy (such as steel), wherein the highly conductive material may act as a heat-sink and expedite the cooling rate of the more moderate material. Generally, material pairs that have the most contrasting thermal properties are reported to have a weaker metallurgical bond at the interface. For example, a moderately conductive steel alloy, which is commonly paired with a highly conductive Cu alloy (Table 1), is usually reported as having poor bonding, where local cracking is the most common defect near the interface. Reports show that cracking occurs in these Cu alloys for two main reasons: (i) A mismatch of the thermo-physical material properties and (ii) an infiltration of Cu to the grain boundaries in steel, which provides micro-cracks during melting due to thermal mismatch. Optimizing process parameters, namely those related to the temperature distribution (e.g., laser speed, power, and scanning strategy), can help mitigate the severity of the thermal gradient across the interface and improve metallurgical bonding.

The dilution effect is another common phenomenon observed in MMAM processes and describes the gradual decrease in alloy blending as a part is built in the vertical direction. Dendritic cracking commonly occurs perpendicularly to the boundary of the fusion zone and extends gradually into the material of the higher thermal stress, which is usually the less conductive material. Dendritic cracking is influenced by the thermomechanical stresses that arise due to the temperature gradients during the solidification processes. The presence of a secondary alloy in the melt pool can exacerbate these stresses and increase the likelihood of crack formation. Cracking from dissimilar metal mixing is further discussed in Section 2.5. On a related note, element diffusion at the interface describes the causal mechanisms behind the blending of two dissimilar alloys within the melt pool. Diffusion is aided by the Marangoni convective forces, driven by the surface tension gradients of the melt pool's molten fluid. This leads to a non-homogeneous distribution of elements, commonly observed by the solidified heat-affected zones through energy dispersive spectroscopy (EDS). The difference in material density may also play a role in how the metals mix and interact under gravitational forces. All factors considered in this section play a crucial role in identifying the alloy compatibility between dissimilar materials in MMAM.

2.5. Alloy compatibility in MM mixtures

Achieving compatibility between dissimilar alloys in bimetallic structures is a critical challenge, as differing physical, chemical, and mechanical properties of each alloy can significantly influence the performance and longevity of the components. The alloys are designed precisely to tailor the elemental proportions and thermomechanical processing conditions to generate the ideal microstructural

Table 1. A comprehensive summary of the empirical literature on the metallurgical bonding in bimetallic multi-material additive manufacturing

Base material \ Deposited material	Titanium alloy	Stainless steel alloy	Nickel alloy	Aluminum alloy	Copper alloy	Ferrous alloy	Miscellaneous alloy
Stainless steel alloy	122,123	124,125	91,126-138	50	33,56,58,128, 139-146	147	148,149
Titanium alloy	150-153	154	155	—	55	—	—
Nickel alloy	52,156	91,131,132, 157-161	—	—	47,162,163	164	—
Ferrous alloy	165	166	—	—	167,168	169,170	171
Aluminum alloy	—	—	—	172-174	175	176	177
Copper alloy	—	178	—	—	179	—	—

features and mechanical properties.[39] In FGM, the element composition typically varies throughout the structure, with the ratio of elements varying with respect to the build height. A minor deviation in element content from the intended composition could disrupt the alloy's performance and fundamental properties.[106] In the discrete MMAM, the abrupt change of composition could act as a chemical potential gradient that drives alloying elements and impurities from one side to another, leading to failure mechanisms. Similar behavior could be observed in a steep property gradient of FGM, which serves as a residual stress concentration site during manufacturing. Besides the chemical composition of the alloys, properties such as thermal conductivity and melting temperature can prevent the successful joining of dissimilar alloys.

To better understand these challenges, Reichardt *et al.*[106] noted that most dissimilar joining issues can be grouped into three distinct categories: (i) Intermetallic formation and solubility limitations, (ii) thermal property mismatch, and (iii) other metallurgical effects. In Section 3, which focuses on the interfacial characteristics of the discrete MMAM structure, the aforementioned phenomena can be observed. Many of these issues have been resolved in the welding industry through effective practice of introducing filler metals, interlayer blazing, high energy density beam welding, and friction stir welding.[42,106-108] The three main categories of joining issues and strategies to overcome each will be examined in more detail. From those, the formation of brittle intermetallic phases in dissimilar alloys is the biggest challenge in the MMAM process. Most metal alloys have limitations in solid solubility and tend to form ordered intermetallic phases. This becomes more complex when considering commercial alloys with multiple elements, including impurities that could lead to detrimental phases. In cases of Ti/steel or Ti/Ni alloys (Sections 3.1, 3.2, and 3.3 for more explanation), which tend to form brittle intermetallic approaches such as introducing a third dissimilar metal alloy that acts as an interlayer can be used to resolve the problem. Apart from the intermetallic formation, the thermal property disparity between dissimilar alloys plays a significant role in metallurgical bonding.

The disparity between the thermal properties of dissimilar alloys, such as melting temperature, CTE, and thermal conductivity, is one of the issues that contribute to weaker metallurgical bonding. During the MMAM process, significant differences in melting temperature not only lead to a non-uniform heat flow and dilution but also tend to cause cracking on the low melting temperature alloy side during solidification (e.g., SS316L/W).[109] The cracking attributed to this mismatch in melting temperature can be mitigated by introducing an intermediate melting temperature alloy. Similar to the characteristics difference of dissimilar melting temperature, CTE, and thermal conductivity play a significant role in the interfacial bonding region of the bimetallic structures. Regarding CTE, thermal mismatch can result in an unequal thermal contraction, leading to a stress concentration at the interface. The disparity of thermal conductivity could cause distortion and a lack of complete fusion of the low thermal conductivity material due to insufficient heat present. In Section 3, a detailed description of the bimetallic structures that were analyzed using EDS, electron backscatter diffraction, and X-ray diffraction to understand the alloy compatibility at the abrupt change in element composition in discrete MMAM is presented.

2.6. Powder recyclability and reuse

Powder reuse presents complex challenges due to the diverse thermal properties, oxidation susceptibility, and chemical reactivity of the constituent alloys. These factors critically affect process stability, part performance, and reproducibility. In powder-based metal AM processes such as LPBF, EB-PBF, and LDED, powder degradation is influenced by its interaction with high-energy sources (e.g., laser and electron beam), molten metal, ambient

reactive chemical compounds, and contact with mechanical components present in the build chamber (i.e., recoater).[110]

Powder degradation occurs due to thermal, chemical, and mechanical effects, including but not limited to dealloying, sintering, oxidation, deformation, contamination, oxide deposition, particle fragmentation, and wear. The mechanisms are exacerbated by the intense heat input inherent in beam-based AM. LPBF and EB-PBF techniques typically operate under vacuum or inert gas conditions, mitigating oxidation and cross-contamination risks. LDED is more susceptible to such degradation as a result of relatively less controlled atmospheres.

The key contributing factor to powder degradation in powder-based metal AM is its direct interaction with the melt pool. The dynamic flow within the melt pool can lead to the ejection of molten metals, resulting in the formation of metal jets, droplets, and powder spatter. These spatters, rich in partially fused and oxidized particles, can further contaminate the powder bed, compounding degradation across build layers. This understanding of degradation mechanisms is crucial, as the degraded powder significantly impacts the mechanical behavior of printed components.

The use of degraded powder affects key mechanical properties, including chemical composition, density, porosity, tensile strength, and surface roughness. In single alloy materials, the use of recycled powder can lead to a gradual change in chemical composition, particularly in critical alloys such as IN718[111] and Ti-48Al-2Cr-2Nb,[112] which in turn influences the mechanical properties. Studies on density and porosity have shown that reused powder can lead to lower or less predictable part densities, driven by uneven particle size distributions, increased spatter presence, and incomplete melting.

Beyond the chemical composition, density, and porosity, the use of recycled powder has been shown to have a significant effect on the material's tensile properties. Properties such as ultimate tensile strength (UTS), yield strength (YS), Young's modulus, and elongation have seen the most change, though the extent varies with the alloy. Tang *et al.*[113] observed that the use of recycled Ti-6Al-4V powder alloy resulted in an increase in strength due to high oxygen content, whereas SS316[114] and AlSi10Mg[115] typically exhibit reduced strength and stiffness, mainly due to higher porosity and coarser particle sizes.

Finally, surface roughness is another critical factor that is affected by powder reuse. Recycled powders often contain larger particles that do not fully melt, leading to a rougher surface finish. This not only degrades the build quality but also increases the need for post-processing, which is both costly and time-consuming. Studies involving SS316,[114] Ti-6Al-4V,[116] and IN718[117] confirm that surface roughness worsens with powder reuse, potentially compromising fatigue resistance and overall component performance.

Given this detailed understanding of powder degradation and its consequences, it is essential to explore the current state-of-the-art recycling techniques. These range from mechanical to advanced approaches. For a more in-depth understanding, the authors recommend reviewing the articles by Lanzutti and Marin[118] and Powell *et al.*[110] A range of powder recycling and rejuvenation techniques has been explored; conventional strategies include mechanical methods (e.g., sieving and centrifugal separation), thermal treatment (e.g., vacuum degassing, re-sintering, and conventional remelting), and chemical approaches (e.g., acid and electrochemical etching). Emerging technologies such as plasma cleaning and plasma spheroidization offer promising methods as well. Plasma cleaning uses ionized gas to remove surface contaminants (e.g., moisture and trapped gases), whereas plasma spheroidization reshapes irregular powder particles to improve flowability and packing density.

While most current research focuses on single-alloy powder reuse, MM powder recyclability in MMAM remains underexplored. A detailed discussion of future research direction in MMAM powder reuse is presented in Section 6.1.

2.7. In-process monitoring

In-process monitoring has emerged as a critical enabler for ensuring process stability, defect mitigation, and quality assurance in MAM, particularly when fabricating MM components. In-process monitoring in PBF, LDED, and WAAM processes benefits from *in-situ* monitoring techniques aimed at detecting defects and ensuring part quality during fabrication. In PBF, monitoring focuses on powder spreading uniformity, laser-powder interactions, melt pool characteristics (size, shape, and temperature), scan path accuracy, and layer geometry. Optical imaging, pyrometry, infrared (IR) cameras, and data-driven methods such as computer vision and neural networks are commonly used to identify defects such as porosity or incomplete fusion.[119,120] Real-time monitoring facilitates process parameter adjustments to reduce defects and improve part consistency.

Similarly, in LDED, monitoring methods include pyrometry, IR imaging, and acoustic emission (AE) sensors to track melt pool temperature, build height, and crack formation. These sensors enable closed-loop control strategies to maintain stable thermal conditions and geometry, improving material uniformity and reducing defects.[120,121] WAAM uses comparable optical and thermal

techniques, such as near-IR cameras and optical emission spectrometry, to monitor melt pool integrity and surface finish. Emerging approaches like 3D laser scanning have also been applied to detect geometric deviations during builds.

Moreover, current state-of-the-art in-process monitoring could allow the research community to further characterize and advance MMAM, which will be further discussed in Section 6.2.

3. MM bimetallic interfacial characterization

The microstructures at the interfaces between dissimilar materials play a crucial role in dictating the mechanical properties of MMAM components. In the context of bimetallic structures, the materials involved often possess similar atomic bonds, as well as comparable physical and chemical properties, including melting temperature, CTE, thermal conductivity, and elemental composition.[39] Consequently, a fusion region is formed at the interface of dissimilar materials, facilitating the interlocking of materials and thereby enhancing their metallurgical bonding strength. Such insights underscore the importance of understanding and optimizing microstructural characteristics for the advancement of MMAM.

The interfacial microstructure of dissimilar materials exhibits varying traits, necessitating a closer examination of each material's unique characteristics. This section explores the microstructural characteristics of significant bi-metal alloys, namely Ti, SS, Ni, Al, and Cu as base materials. Each of these alloys presents distinctive interfacial characteristics influenced by factors such as composition, crystalline structure, and processing conditions. Understanding these nuances is crucial for optimizing MMAM process parameter selection and improving the mechanical properties of MMAM structures. Each subsection is focused on one base material alloy and contains a description of the relevant available literature.

3.1. Stainless steel-based bimetallic alloys

Understanding the bonding between SS and Ni has been explored numerous times (Table 1), with a few examples shown in Figure 4. This combination of alloys is relevant in extreme applications, including nuclear and aerospace, where properties such as high strength, corrosion and oxidation resistance, creep, and fatigue resistance are required.[156,180] In the work by Bodner *et al.*,[129] SS316L/IN625 bimetallic structures were fabricated using liquid-dispersed metal powder bed fusion. Due to the residual stress gradient at the interface, a zigzag-patterned crack

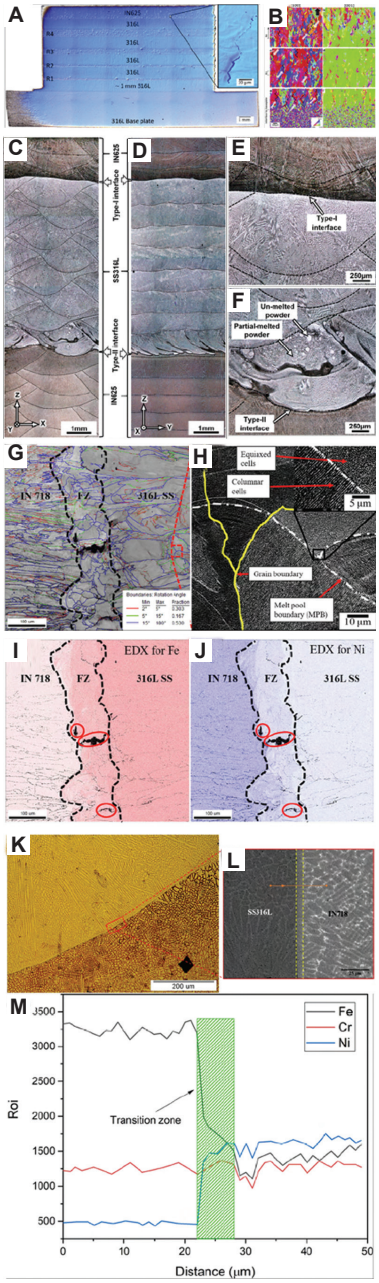

Figure 4. Interfacial meso- and microstructural characteristics of stainless steel and nickel-based bimetallic alloys fabricated through different multi-material (MM) additive manufacturing techniques. (A and B) SS316/IN625 produced by MM-laser powder bed fusion (LPBF). Scale bar: 1 mm. Reprinted with permission from Bodner *et al.*[129] Copyright © 2020, Elsevier B.V. (C-F) SS316/IN625 MM-laser-directed energy deposition (LDED). Scale bars: 1 mm and 250 μm. Reprinted with permission from Chen *et al.*[132] Copyright © 2020, Elsevier B.V. (G-J) SS316L/IN718 MM-LPBF[130] and (K-M) SS316L/IN718 MM-LDED[127]. Scale bars: 5 μm, 10 μm, 25 μm, 100 μm, 200 μm and 250 μm. Reprinted with permission from Yusuf *et al.*[130] Copyright © 2020, Elsevier B.V. and Ghanavati *et al.*[127] The images highlight significant characteristics of the interfacial morphology, phase transformation, grain structure, growth, and bonding quality influenced by the process techniques and material combinations.

propagated from the SS316L interface region and expanded into the IN625, as confirmed by scanning electron microscopy imaging. Such patterned cracks formed due to the implemented scanning strategy, which induced residual stresses and mismatches in CTEs between the sub-layers (Figure 4A and B).

Similarly, Chen *et al.*[132] fabricated multiple layers of SS316L/IN625 using MM-LDED to understand the microstructural characteristics at two types of interfaces: type I (SS316L as a substrate) and type II (IN625 as a substrate) (Figure 4C and D). This section focuses on type I interfaces, while type II will be discussed in Subsection 3.3. The type I interface exhibits a flat transition region due to less penetration compared to type II (Figure 4E and F). The shallower penetration in type I was attributed to the lower energy absorptivity and thermal conductivity of IN625 relative to SS316L. Fractography images revealed no cracks or pores at the interface due to the lower density and viscosity of SS316L compared to IN625. Beyond surface observation, the inverse pole figure map of the type I interface exhibited fine columnar grains in IN625 and equiaxed grains on SS316L. Similarly, in a hybrid-AM process where SS316L was fabricated using LPBF and IN625 using LDED, no cracks or porosity were visible on the surface,[126] which validates the earlier findings. In all cases, the interface exhibited a good transition zone with smooth, defect-free bonding due to comparable melting points and CTE values of the two alloys.

The SS316L/IN718 interface has been similarly analyzed as the SS316L/IN625-LPBF interfaces. Yusuf *et al.*[130] observed that the transition zone exhibits equiaxed grain growth with a transition zone thickness of approximately 100 μm and was characterized by columnar grains in the individual element-rich region (Figure 4G and H). Despite the presence of irregular-shaped lack-of-fusion pores (highlighted in red in Figures 4I and J), no cracks were detected. Similar observations were made by Mei *et al.*[131] and Wei *et al.*,[132] who attributed the formation of pores at the interface to energy-material mismatch and uneven powder deposition during the MM-LPBF fabrication. In contrast, Ghanavati *et al.*[127] reported a nearly defect-free interface between SS316L and IN718 (Figure 4K and L), which was attributed to the presence of a strong local temperature gradient at the interface. The microstructural solidification at the interface proceeded through a narrow planar solidification mode, driven by the high local temperature gradient.[127] An EDS analysis confirmed a smooth transition from the Fe- to Ni-rich region (Figure 4M).

Across various AM processes, the SS/Ni bimetallic structure with SS as substrate generally exhibited good metallurgical bonding. Considering the CTE of SS316L, IN625, and IN718, it is evident that IN718 has a lower CTE compared to IN625. In SS316L/IN625 structures, although the actual temperature increases from SS316L to IN625 due to the heat source, a gradual decrease in the liquid temperature within the transition zone inhibits the protrusion of SS316L into this region, resulting in a smoother interface. As reported by Bodnar *et al.*,[129] it is evident that the process parameters significantly influence the formation of zigzag cracks at the SS316L/IN625 interface. In contrast, for SS316L/IN718 bimetallic structures, porosity and cracks were clearly observed in MM-LPBF rather than MM-LDED. This behavior was attributed to the formation of brittle intermetallic phases during solidification, coupled with the lower CTE of IN718 compared to SS316L, which exacerbates thermal stress at the interface.

Besides the influence of brittle intermetallic phase formation and CTE, the authors speculate that the shielding gas flow rate differences between SS316 and IN718 could potentially have an impact on the interfacial porosity formation, attributed to the deposition of spattering and welding plume. The lack of data on shielding gas flow rate at the interface provides no evidence of the influence of gas flow rate but could be found on monolithic materials of SS316[181] and IN718.[182]

Stainless steel/Cu alloy combinations are utilized in fields such as energy[55] and automotive,[49] leveraging the mechanical strength of SS and the high thermal conductivity of Cu. Figure 5 illustrates the interfacial microstructural characteristics of dissimilar SS/Cu materials with various Cu alloys.

A bimetallic SS316L/C18400 structure fabricated through MM-LPBF exhibited sporadic cracking (Figure 5B) on the SS side of the interface, with a transition width of 750 μm (Figure 5A).[141] These cracks were attributed to the thermal mismatch between SS and Cu, whereby Cu diffuses into austenitic grain boundaries of SS316L, exerting pressure and causing cracking. Optical microscopic images revealed SS-rich regions free of porosity or defects, while a considerable number of pores were observed on the Cu-rich region due to the high reflectivity and thermal conductivity of Cu (Figure 5C and D). EDS analysis revealed a good metallurgical bonding between SS316L and C18400. With the understanding of the interfacial characteristics of SS316L/C18400, the bimetallic structure of SS316L/C25400 could also be examined. Similarly, an SS316L/C25400/SS316L MMAM structure manufactured using MM-LPBF exhibited characteristics akin to the SS316L/C18400. Bai *et al.*[140] observed the formation of a few cracks at the transition region extending to the

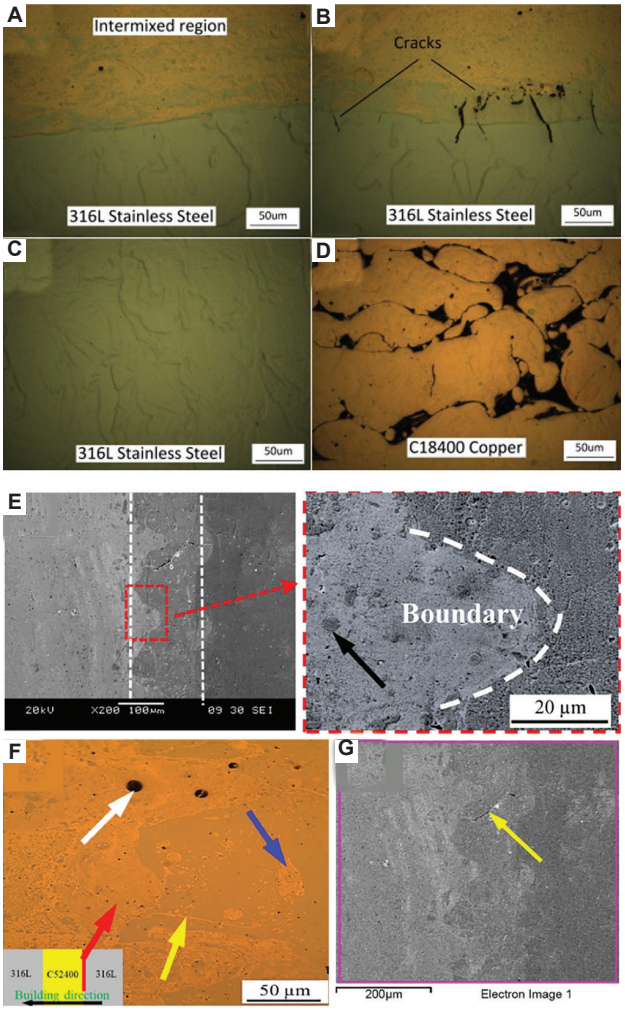

Figure 5. Interfacial meso- and microstructural characteristics of stainless steel and copper bimetallic alloys fabricated through multi-material-laser powder bed fusion. (A-D) SS316L/C18400[141] and (E-G) SS316L/C52400[140]. Scale bars: 20 µm, 50 µm, and 100 µm, magnifications: (E and G) 300×. Reprinted with permission from Liu *et al.*[141] (Copyright © 2014, Elsevier Inc.) and Bai *et al.*[140] (Copyright © 2020, Elsevier Inc.). The images reveal the interfacial characteristics associated with each copper alloy composition, highlighting variations in metallurgical bonding, porosity formation, elemental diffusion, and phase transformation.

SS316L-rich region, attributed to the high content of Cu (Figure 5E-G). Further analysis revealed that the cracks formed within the SS-rich region were visible from high-resolution optical microscopy (Figure 5F and G; indicated by the yellow arrows).

Extensive research on SS316L/CuSn10 bimetallic structures has concluded that good metallurgical bonding between SS/Cu is achievable.[58,139,142,183] The width of the transition zone between SS316L/CuSn10 and CuSn10/SS316L was about 400 µm and 160 µm, respectively, indicating a higher bonding strength on the SS316L/CuSn10 side compared to the CuSn10/SS316L side.[56] An irregular elliptical island-like heterogeneous phase appeared in both material-rich regions due to the high-energy laser beam penetrating through several layers to re-melt the solidified SS316L.[56,58,142] The rapid movement of the laser beam caused the molten pool to be unstable. However, CuSn10/SS316L exhibited fewer cracks than SS316L/CuSn10. The crack formation was attributed to liquid metal embrittlement, driven by differential elemental diffusion rates at high temperatures, consistent with the Kirkendall effect, similar to observations by Liu *et al.*[56] Similarly, in SS316L/C18400[141] and SS316L/C25400[56] bimetallic structures, cracks were observed at the transition region and extended toward the SS-rich region in both alloy combinations due to the high residual stress in SS316L owing to its low CTE. A similar behavior was observed in the SS316L/Cu/Ti-6Al-4V[123] MMAM structure using a Cu-alloy as an intermediate bonding layer (IBL).

From these studies, it is evident that in SS/Cu bimetallic structures, crack formation is primarily driven by dissimilar thermal and mechanical properties between metal alloys. Compared to SS/Ni bimetallic structures, which generally exhibited good metallurgical bonding, SS/Cu combinations were more prone to cracking, largely due to the significantly higher thermal conductivity of Cu relative to SS. In SS/Cu structures, cracks propagated in the Cu-rich region due to the deeper penetration of Cu into the SS alloy. Conversely, in Cu/SS bimetallic, a small amount of Cu penetrates the interface of SS316L, and a brittle Cu film with low strength is formed. In the subsequent cooling process, due to the difference in the thermophysical properties between Cu and SS, the degree of shrinkage between Cu and SS is not consistent due to high residual stress, resulting in thermal penetration cracking on the SS side.

In addition to the SS/Cu bimetallic structure, SS316L/Zr and SS410/Zr bimetallic structures exhibited vertical cracks during fabrication due to the differences in CTE and dissimilar thermal properties.[171] In contrast, SS316L/17-4PH structures displayed a smooth transition without intermetallic phase formation, attributed to the similarities in thermal conductivity and CTE and a narrow thermal heat gradient between the two materials.[147] Finally, SS316L/W bimetallic structures exhibited larger, irregular pores in the SS-rich region, which were closer to the transition region. These pores and cracks were formed due to inadequate process optimization, excess thermal stress gradient from high heat input from the molten pool, and mismatch of CTE values between the two materials.[148] From all the above miscellaneous studies, it was evident in SS316L/Zr, SS410/Zr, and SS316L/W that thermal properties such as thermal conductivity, CTE, and temperature gradient played a

significant role in determining the metallurgical bonding between dissimilar materials.

3.2. Titanium-based bimetallic alloys

A Ti-6Al-4V/Ti-5Al-2.5Sn bimetallic structure, manufactured via MM-LDED and tested by Wei *et al.*,[151] exhibited high-quality metallurgical bonding, attributed to optimized deposition parameters. Throughout the entire specimen, defects such as pores, cracks, and lack of fusion were notably scarce, underscoring the efficacy of the employed parameters and the presence of extremely high thermal gradients along the build direction.[151] In addition, an EDS line scanning profile of the as-built specimen revealed an interdiffusion region spanning 70 μm at the interface, with the elemental composition transitioning from Tin (Sn)-dominant to Vanadium (V)-dominant. A strong Marangoni convection allowed the V elements to move downward and the Sn elements to move upward within the molten liquid. This well-interfacial bonding between dissimilar materials increased its strength compared to Ti-5Al-2.5Sn layers. The physical and thermal properties of Ti-6Al-4V and Ti-5Al-2.5Sn were consistent, which is evidently represented in the interface bonding, indicating a smooth transition of elements from one side to another. Although the elemental composition of both alloys is different, they produced a near-homogeneous martensitic microstructure due to the high cooling rate.

In contrast, the interface in a Ti-6Al-4V/SS410 bimetallic structure observed by Onuike *et al.*[154] exhibited a narrow (15 μm) transition region with numerous cracks perpendicular to the interface due to the immiscibility of SS and Ti alloy. Both materials were discerned by a thin layer of phase mixture (Figure 6A). To overcome the immiscibility of Ti-6Al-4V and SS410, niobium (Nb)[154] and Ni-chromium alloy (NiCr)[122] were used as an IBL to optimize the metallurgical bonding. Ti-6Al-4V/Nb/SS410 fabricated using MM-LDED showed a good metallurgical bonding with no cracks or de-bonding. Due to the Marangoni convection, an upward movement of elements such as Ti, V, and Nb into the SS410 layer was observed using EDS (Figure 6B). Notably, no brittle intermetallic phases (e.g., FeTi and Fe_2Ti) were detected at the IBL, emphasizing the role of Nb as an intermediate bond and diffusion barrier layer. This highlights its effectiveness in mitigating brittle intermediate phases and reducing thermal stresses.

Conversely, in Ti-6Al-4V/NiCr/SS410, a significant number of pores were observed at the interface,

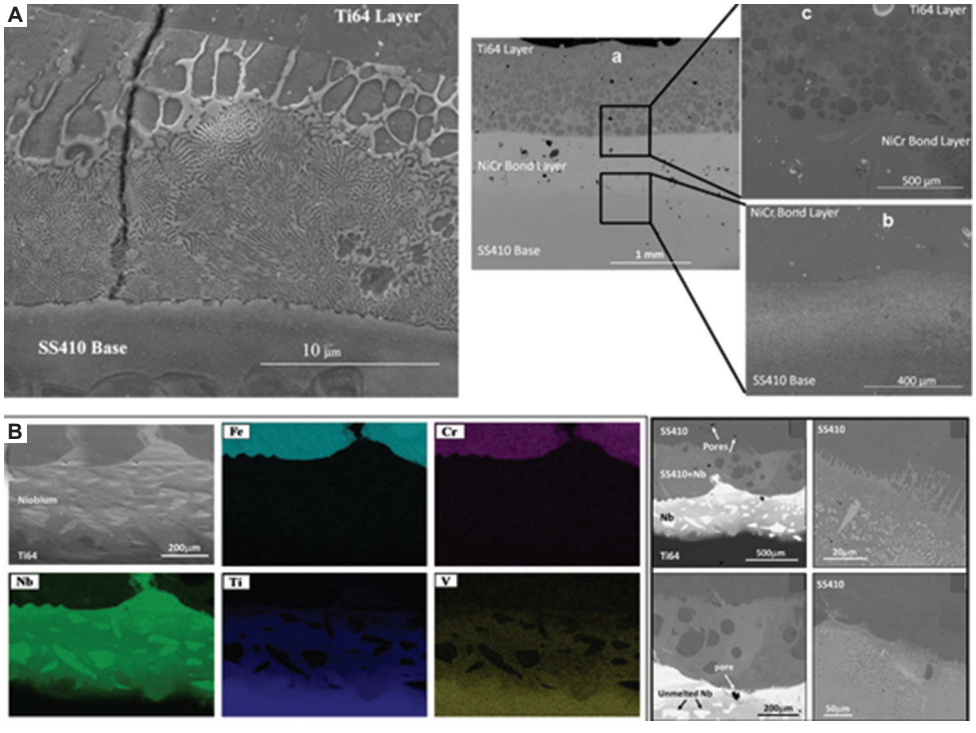

Figure 6. Interfacial characteristics of titanium (Ti)-based bimetallic structures. These structures were fabricated using (A) Ti-6Al-4V/NiCr/SS410 MM-laser-directed energy deposition (LDED)[122] and (B) Ti-6Al-4V/Nb/SS410 MM-LDED.[154] The images reveal the interfacial evolution and metallurgical bonding behavior across the Ti-base alloy combination with interlayer, with particular emphasis on elemental transition, interlayer strategies, crack formation, and phase formation. Scale bars: 10 μm, 50 μm, 200 μm, 400 μm, 500 μm, and 0.5 mm. Reprinted with permission from Sahasrabudhe *et al.*[122] (Copyright © 2014, Elsevier B.V.) and Onuike and Bandyopadhyay[156] (Copyright © 2018 Elsevier B.V.).

attributed to the inadequate energy input during NiCr layer deposition.[122] Nevertheless, Ti-6Al-4V/NiCr has amalgamated and formed a strong overall bonding, as evidenced by the presence of light and darker circles, as observed in Figure 6A. The disparity in thermal properties between Nb and NiCr contributes to the observed porosity in Ti-6Al-4V/NiCr/SS410 but not in Ti-6Al-4V/Nb/SS410. This underscores the importance of material compatibility and thermal characteristics when selecting intermediate materials. Another interesting investigation looked at the effect of transition joints on the interfacial characteristics in Ti-6Al-4V/TiC. Using dual-material transition joints, two distinct joints - (1) Butt joint and (2) interlock joints illustrated a crack-free interfacial bonding.[150] These findings shed light on the effectiveness of different joint configurations in achieving a strong and seamless bond, providing valuable insights toward the design and fabrication of dual-material transition applications. Owing to the similar physical and thermal properties of Ti-6Al-4V and TiC, the resulting bonds exhibited defect-free surfaces and microstructural characteristics resembling those observed in Ti-6Al-4V/Ti-5Al-2.5Sn joints.

3.3. Nickel-based bimetallic alloys

Bimetallic structures of IN718/SS316L[159] and IN625/SS316L,[132] fabricated using MM-LPBF and MMLDED, respectively, exhibited similar wavy characteristics at the interface. These distinctive characteristics are caused by the high degree of molten pool banding, compared to the interface between SS316L/IN625, as explained in Section 3.1 (Figure 4C, D, and F). The interface exhibited epitaxial growth, implying that irregular-shaped coarse grains are observed at the transition/composite zone. At the IN718/SS316L interface, Duval-Chaneac *et al.*[159] observed a minor crack formed due to liquation cracking (Figure 7A). Liquation cracking occurs due to the rapid solidification of alloys with high alloying content, which widens the solidification range and promotes the formation of liquation cracks. Notably, both Ni-based systems exhibited interfacial cracks resulting from solidification-induced stresses and the absence of compensating melt flow. In contrast, a Ni/Cu bimetallic structure demonstrated poor metallurgical bonding, with strong interfacial adhesion between the two alloys.[184] The high thermal conductivity of Cu allowed deeper penetration into the Ni-based substrate, promoting diffusion and metallurgical integration. Onuike *et al.*[184] examined IN718/GRCop-48 bimetallic structure fabricated using LDED and observed poor interfacial bonding, characterized by metal lump formation and the balling phenomenon. This was attributed to the extreme differences in thermal properties and poor diffusion compatibility. To address this, a compositional gradient layer was introduced, which facilitated improved bonding by gradually bridging the thermal and physical mismatches between the dissimilar alloys. This approach highlights the effectiveness of using a gradient transition layer in overcoming bonding challenges in systems with significant property disparities.

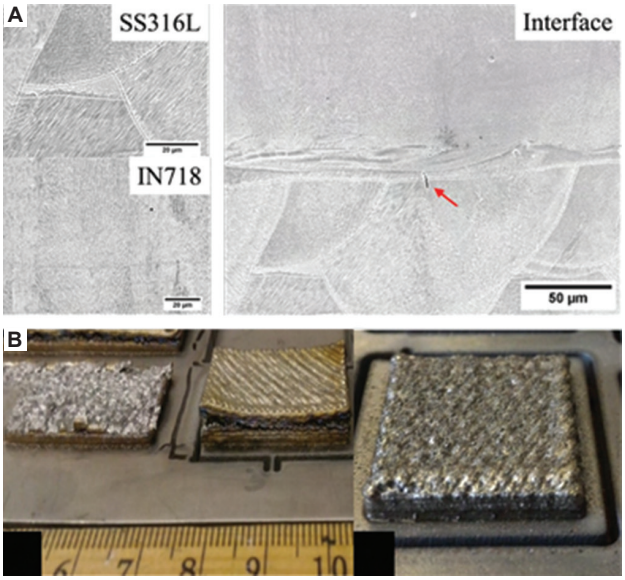

Figure 7. Interfacial characteristics of nickel (Ni)-based bimetallic alloys fabricated through multi-material laser powder bed fusion (MM-LPBF) and mixed-material laser-directed energy deposition (MM-LDED). (A) IN718/SS316L produced by MM-LPBF[159] and (B) IN718/Ti-6Al-4V produced by MM-LDED.[156] The images reveal minor crack formation, metal lump formation, and delamination at the interface across different material combinations and process techniques. Scale bars: 10 μm and 50 μm. Reprinted with permission from Onuike and Bandyopadhyay[156] (Copyright © 2018 Elsevier B.V.) and Duval-Chaneac *et al.*[159] (Copyright © 2021 Elsevier Ltd.).

Similar to previous studies, the interfacial characteristics of IN718/Ti-6Al-4V[156] and NiTi/Ti-6Al-4V[52] were observed to form lateral cracks with no visible crack formation. The lateral crack formation at the interface between IN718/Ti-6Al-4V was due to the larger dissimilarities in CTE and immiscibility, which inhibit bonding; the crack was later overcome by introducing a vanadium-carbide compositional bonding layer (Figure 7B). Vanadium-carbide serves as a bonding link for dissimilar materials and minimizes the formation of brittle intermetallic phases.[156] However, due to the close range in thermal properties between NiTi and Ti-6Al-4V and NiTi's secondary dominant composition being Ti-element, the interface exhibited good metallurgical bonding. Bartolomeu *et al.*[52] indicated that, due to the MM-LPBF fabrication strategy (removing excess powder before adding Ti-6Al-4V) along with adequate process parameters, the number of cracks was reduced, and good metallurgical bonding was achieved.

Lastly, a Ni-Al alloy dissimilar material composition was studied by Liu and Dupont.[185] They observed high solidification and sub-solidus cracking susceptibility, as well as porosity formation. The porosity formation was caused by the use of water-atomized Ni rather than gas-atomized Ni, and the cracks were formed due to the combined effect of high thermal stress and brittleness of the intermetallic. Subsolidus cracking and porosity were formed at the interface due to differences in thermal properties.

3.4. Ferrous-, aluminum-, and copper-based bimetallic alloys

In the Fe/SS (P21/SS316L)[166] bimetallic structure fabricated using MM-LDED, a good metallurgical bonding without cracks, pores, or unmelted particles was observed at the interface due to the rapid cooling and steep thermal gradient. The P21 morphology consisted of diminutive austenite and mostly of martensite. However, the interface of H13 (ferrous alloy)/Cu was observed to be discrete compared to Fe/SS, where micro-cracks and pores were observed even though Cu was able to adhere to H13 (Figure 8A and B). The cracks were formed due to the solidification cracks and higher CTE variation between H13 and Cu and propagated perpendicularly towards the H13 region.[167] However, in the 18Ni300/CuSn10 bimetallic structure, the interface appeared relatively loose, with small pores and interfacial mixing of α-Fe and α-Cu phases, as evidenced by scanning electron microscopy and EDS mapping. In contrast, in the CrMn/MS1 (ferrous/ferrous alloy) bimetallic structure, the interface exhibited a good metallurgical bonding with no cracks or pores, attributed to its similar thermal properties. At higher magnification, a curved solidification characteristic was visible due to the Marangoni convection (Figure 8C-F).[169]

In studies where Al was the base material, Wang *et al.*[172] and Sing *et al.*[175] investigated Al-12Si/Al-Cu-Mg-Si and Al-12Si/C18400, respectively. In Al-12Si/Al-Cu-Mg-Si, the interface exhibited good metallurgical bonding with no pores and few defects on the base material due to a similarity in their thermal properties. However, the Al-12Si/C18400 interface exhibited cracks compared to the Al-12Si/Al-Cu-Mg-Si due to the dissimilarities in CTE, resulting in uneven expansion and contraction during solidification.[186] However, a good metallurgical bonding was indicated with a transition region of 200 μm in both cases.

Both bimetallic structures Cu-Cr/07Cr15Ni5[178] and T2 (Cu alloy)/MS1[179] exhibited defects such as cracks and pores due to the high thermal conductivity of Cu-Cr, insufficient energy applied during manufacturing, and variations in process parameters. In the bimetallic structure of Cu/MS1, specimens were fabricated by Tan *et al.*[179] using LPBF at different scanning speeds (500 – 1,250 mm/s). At low scan speeds (500 – 950 mm/s), the interface exhibited good metallurgical bonding. However, at high scan speeds (1,100 and 1,250 mm/s), cracks due to residual stress and pores due to lack of fusion were observed (Figure 8G and H). High thermal conductive Cu enhanced the metallurgical bonding mechanism through Marangoni convection, contributing toward interfacial elemental diffusion and bonding strength.

4. Mechanical characteristics of MMAM structures

Understanding the mechanical properties of an MM composition is crucial for comprehending its characteristics. With the potential of manufacturing MM samples through AM methods, conducting mechanical testing would expand researchers' understanding of the primary, interfacial, and secondary material properties. The evaluation of the MMAM structure properties will support the qualification of components fabricated with MMs based on the target regime or environments that the materials are expected to experience.

This section explores the mechanical properties of MMAM components, organized according to the types of mechanical tests performed on MM components. These tests provide crucial insights into the performance and integrity of the interface between dissimilar materials. The mechanical evaluations include hardness (Section 4.1), tensile testing (Section 4.2), flexural strength (Section 4.3), compression test (Section 4.4), fatigue (Section 4.5), and miscellaneous testing (Section 4.6), including wear performance, thermal diffusivity, and shear bond test. Table 2 provides an overview of all mechanical testing conducted on MMAM to date, categorizing them by microhardness, tensile, flexural, and miscellaneous tests and further categorizing them according to the base material. As shown in Figure 10, microhardness and UTS are the most commonly employed techniques to evaluate the interfacial performance in MM components.

4.1. Micro-hardness/micro-indentation

Hardness testing is often conducted on MMAM specimens as a preliminary test, following the ASTM standard E384[187] for small- or large-scale specimens. Hardness testing provides data about the material's resistance to deformation, indentation, scratching, or penetration. From the empirical studies collected (Table 2), hardness testing is one of the most widely adopted testing methods

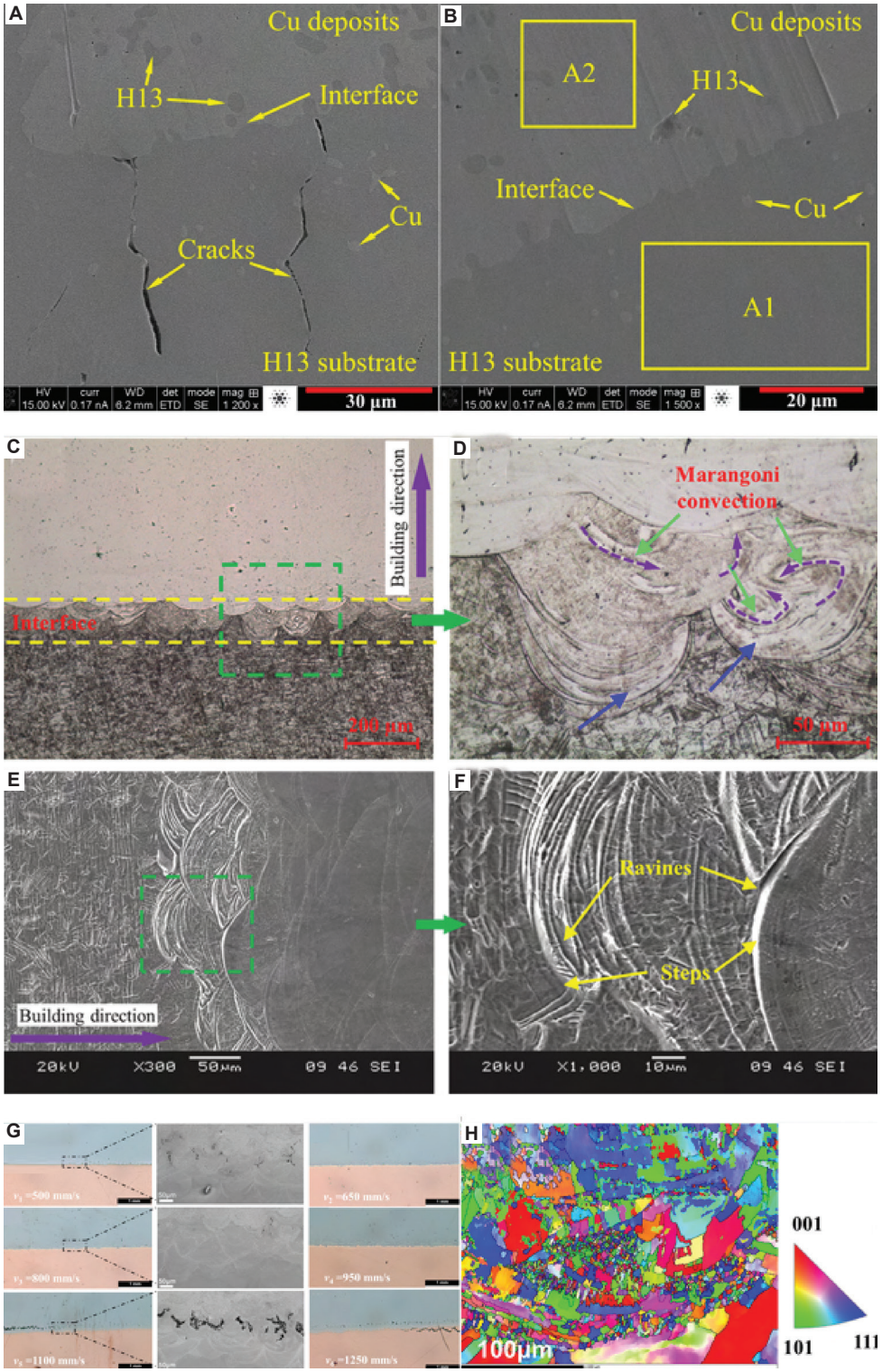

Figure 8. Interfacial characteristics of iron- and copper (Cu)-based bimetallic structures fabricated through mixed-material laser powder bed fusion (MM-LPBF) and mixed-material laser-directed energy deposition (MMLDED). (A and B) H13/pure Cu produced by MM-LDED,[167] (C-F) CrMn/MS1 produced by MM-LPBF,[169] and (G and H) T2/MS1 produced by MM-LPBF.[179] The images reveal the interfacial morphology, metallurgical bonding, elemental diffusion, and microstructural characteristics. Scale bars: 10 μm, 20 μm, 30 μm, 50 μm, 100 μm, and 200 μm, magnifications: (A) 1200×, (B) 1500×, (E) 300×, (F) 1000×. Reprinted with permission from Zhang *et al.*[167] (Copyright © 2020 Elsevier B.V.), Bai *et al.*[169] (Copyright © 2020 Elsevier B.V.), and Tan *et al.*[179] (Copyright © 2018 Elsevier Ltd.).

Table 2. Mechanical testing of each bimetallic combination

Deposited material Base material	Titanium alloy	Stainless steel alloy	Nickel alloy	Aluminum alloy	Copper alloy	Ferrous alloy	Miscellaneous alloy
Stainless steel alloy	A, B[123]		A[126,127,129,130], (A, B)[131,133,157]		A[56,128,140], (A, B, C, E, F_{com})[58], (A, C)[141], (A, B, C, E)[142], (A, B)[187]	(A, F_{com})[144,166]	(A, C)[148]
Titanium alloy	(A, F_{com})[188], (A, B)[189,151], (A) [122]	E[154]	A[155]		A[57]		
Nickel alloy	(A, F_{Shear})[52], (A)[156]	(B) [131], (A, F_{wear})[158], (A, F_{fat})[159], (A)[160]			(A)[47], (A, $F_{T herm}$)[184]		
Ferrous alloy		(F_{com})[166], (B, D, F_{Fat})[170]		A[190]	(B, E)[179], (A, C)[167]	(A, B) [169], (B, D, F_{Fat})[170]	
Aluminum alloy				(A, C)[172,173]	(A, C, E)[179], (A, E)[175]	A [167]	A[177]
Copper alloy			A, B, F_{com} [176]			A[167]	

Note: The mechanical testing conducted on each bimetallic combination is denoted alphabetically. For detailed information on the alloy composition in a specific reference within the multi-material additive manufacturing combination and specific experimental procedures, refer to Table A2.
Abbreviations: A: Hardness; B: Tensile strength (||); C: Tensile strength (=); D: Flexural strength (||); E: Flexural strength (=); F_{com}: Compression; F_{fat}: Fatigue; F_{Shear}: Bond shear; F_{wear}: Wear performance; $F_{T herm}$: Thermal diffusivity.

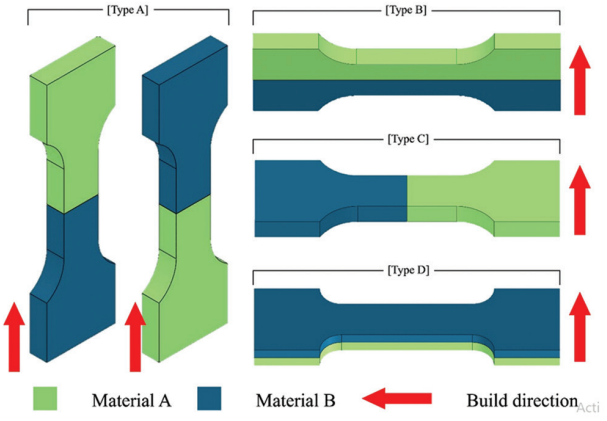

Figure 9. Build orientation of multi-material additive manufacturing samples that are used in the literature. Type A: Two distinctive materials stacked vertically. The dissimilar materials meet at the horizontal interface. Type B: Two material systems joined side by side along the vertical interface. Type C: Two materials layered on top of each other horizontally, forming a horizontal interface. Type D: Similar to Type C, with the horizontal interface at the middle of the thickness of the specimen

as it provides valuable insight into the mechanical integrity and performance of the components.

In bimetallic structures such as SS316L/Ni[126,127,129,131,157] and Ni/SS316L,[131,158-160] the interface region exhibits a smooth transition from higher to lower hardness level or vice versa, reflecting the changes from one material to another. The literature revealed a smooth gradient in hardness across the interface, with bulk-Ni alloys such as IN718 and IN625 exhibiting a hardness level of 304±16 HV and 260±13 HV, respectively. Feenstra *et al.*[157] noted that increasing the laser power resulted in a decrease in hardness, particularly at the interface region. Interestingly, the incorporation of carbon fiber IBL in IN718/SS316L MMAM structures resulted in a 1.5 to 2-fold increase in microhardness relative to the monolithic materials. The increase in hardness is attributed to the formation of chromium-rich carbides at the interface.[158] Beyond the general observation of a gradual hardness transition, both laser power and incorporation of an IBL have been shown to significantly influence the hardness level. These trends in SS/Ni structures offer a useful comparison to other bimetallic structures, such as SS/Cu, which are discussed in the following sections.

Similarly, the MMAM structures composed of SS316L/Cu[139] or Cu/SS316L[56] exhibited similar hardness transitional behavior to that of SS316L/Ni. Specifically, in SS316L/Cu, hardness levels descend from 240 ± 37 HV (SS316L) to 156 ± 4 HV, 181 HV, and 74 HV for CuSn10, C52400, and C18400, respectively (Figure 10A). A reverse trend is noted when transitioning from Cu to SS316L (Figure 10B). A smooth transition between SS and Cu alloys was revealed, attributed to the variation in Fe and Cu content in the melt pool and grain refinement at the interface. Supporting these observations, Meyer *et al.*[139] Liu *et al.*[139] observed a higher hardness level of 248.6 ± 22.5 HV in the diffusion zone when compared to the monolithic material region of SS316L and CuSn10. This increase is attributed to the presence of highly refined grains, which hinder dislocation movements and enhance microhardness, in addition to strain hardening induced by micro-strains.

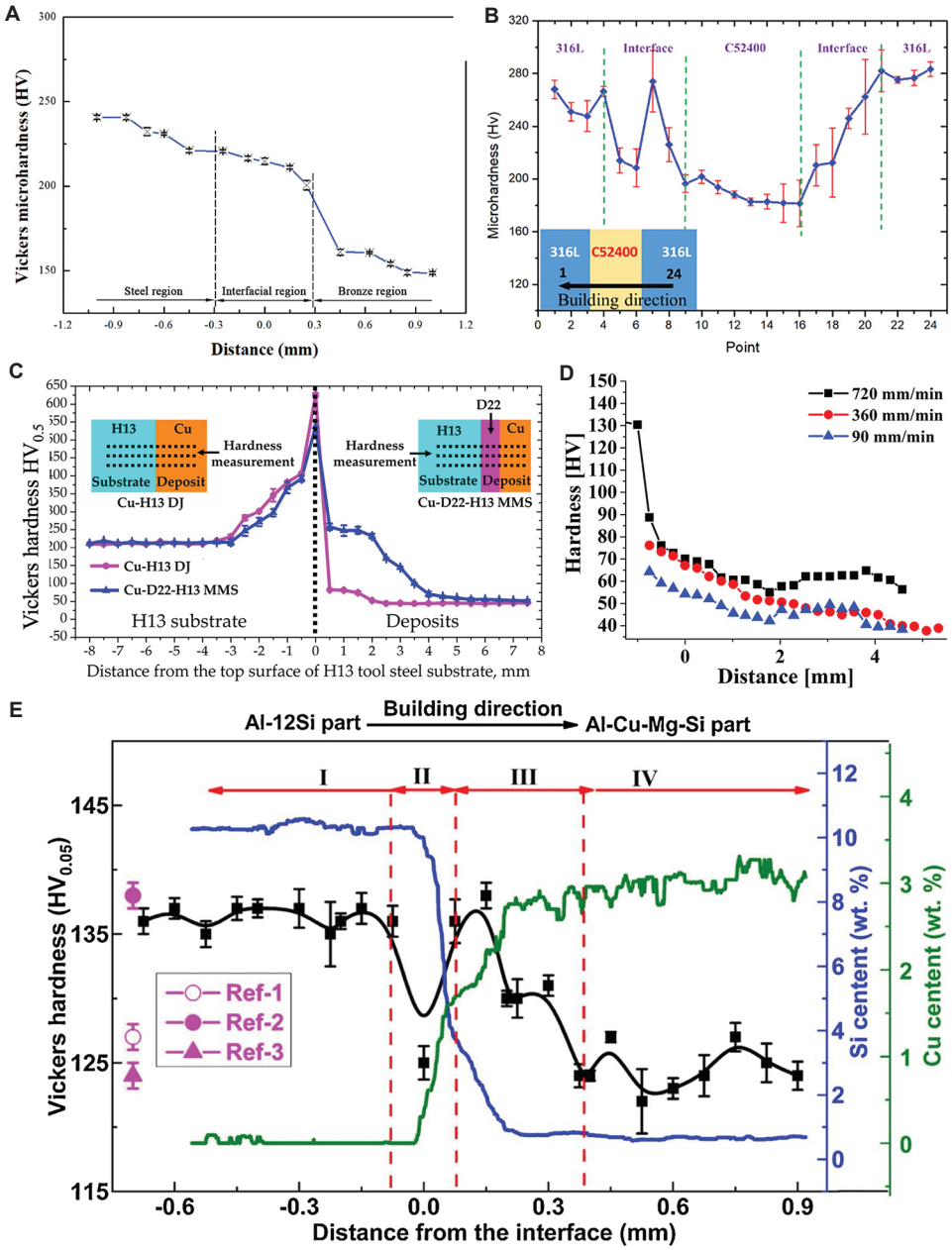

Figure 10. Representative hardness profile of various bimetallic structures fabricated through multi-material laser powder bed fusion (MM-LPBF) and multi-material laser-directed energy deposition (MM-LDED): (A) SS316L/CuSn10 (MM-LPBF);[58] (B) SS316L/C25400/SS316L (MM-LPBF);[56] (C)H13/Cu (MM-LDED);[167] (D) Al/W (MM- LDED);[177] (E) Al12Si/Al3.5Cu1.5Mg1Si (MM-LPBF).[172] These profiles illustrate the hardness gradient across interfacial regions, capturing effects due to material mismatch, processing parameters, and interlayer presence. The hardness data represent transitions across interfaces and highlight the influence of process conditions, elemental diffusion, and interlayers on local mechanical response.

The hardness level transition in the bimetallic structure of SS/Cu revealed that the grain refinement, elemental diffusion, and strain hardening played a significant role in the hardness of the components.

Extending this trend to SS-based MMAM structure, the interface region of SS316L/P21[141] and SS316L/17-4PH[147] revealed a smooth transition of hardness. This behavior was attributed to residual stresses and the finer microstructure inherent to these combinations of dissimilar materials. The bulk hardness values of P21 and 17-4PH were reported as 330 HV and 312 HV, respectively, while the interface between SS316L/17-4PH and SS316L/P21 exhibited an average hardness of 232±7 HV. Unlike SS/Fe MMAM

structures, the interfacial region of SS316L/tungsten exhibited a higher hardness of 543±3.7 HV compared to the SS316L and tungsten-rich region, which exhibited 392±1.6 HV and 411.7±3.3 HV, respectively.[148]

This increase in hardness is due to the secondary phases like Fe_2W, Fe_3W_3C, and Fe_6W_6 which disperse high levels of hardness due to the presence of brittle and intermetallic compound (IMC) phases. In bimetallic structures with SS316L as the substrate, it was revealed that the hardness mostly exhibited a smooth transition, besides cases having a poor interfacial characteristic (discussed in Section 3), which has influenced the hardness at the interface by forming intermetallic phases that have higher hardness values.

A similar trend in interfacial hardening has been observed in other combinations of MMAM structures. Wei *et al.*[151] studied the Ti-5Al-2.5Sn/Ti-6Al-4V structures and observed a smooth transition at the interface for both as-deposited and annealed specimens, noting a drop in overall hardness of the specimen due to the softening effect provided by the "$\alpha' \rightarrow \alpha$" recrystallization process. Similar to the SS316/CF/IN718 structure, the influence of the IBL in Ti-6Al-4V/SS410 was also significant—with the introduction of IBL, such as Nb and NiCr—exhibiting distinct effects on interfacial hardness. The Ti-6Al-4V/Nb/SS410 MMAM structures exhibited a smooth transition up to the interface with SS410, where the hardness value dropped due to the element diffusion and heat-affected zone.[154] However, in Ti-6Al-4V/NiCr/SS410, the hardness at the interface was observed to be smoother compared to the specimens with an Nb IBL.[122] In a Ti/Cu MM composition, it was observed that the hardness of the interface region increases with increasing Cu content, primarily due to the formation of hard IMCs and solid solution strengthening.[123] The transition through the interface in the Ti/Ti and Ti/IBL/SS bimetallic structure revealed a smooth transition in hardness. In the Ti/Ti bimetallic structure, an overall drop in hardness was observed due to annealing, while in the Ti/IBL/SS bimetallic structure, the presence of IBL influenced the interfacial region to form a smoother transition with no abnormalities.

Overall, these studies highlight that the selection of IBL and constituent materials in MMAM structures critically governs the interfacial hardness profile, with smoother transitions and tailored mechanical responses achievable through strategic material design and thermal management.

Similar to the earlier findings, in the MMAM structures of NiTi/Ti-6Al-4V[52] and IN718/Ti-6Al-4V,[154] a smooth transition with no abrupt changes at the interface was observed during transitioning. In IN718/Ti-6Al-4V, the diffusion of chromium carbide particles into the IN718 led to the formation of the Cr_3C_2 phase, which resulted in higher hardness at the interface compared to the bulk materials. Similarly, the IN718/Cu MMAM structures fabricated using MM-LPBF and MM-LDED revealed enhanced interface hardness. In MM-LPBF, this was attributed to rapid solidification effects from the localized laser remelting.[47,184] However, the MM-LDED study did not provide detailed information on the interface or the transition in hardness. The studies on Ni/Ti and Ni/Cu revealed a smooth transition similar to the earlier bimetallic structure observation. In IN718/Ti-6Al-4V, the formation of intermetallic phases resulted in superior hardness than the bulk material. These findings further affirm that in MMAM structures, smooth interfacial transitions can be achieved even between highly dissimilar materials, with interfacial hardening predominantly influenced by elemental diffusion, intermetallic formation, and process-specific thermal conditions.

In contrast, the hardness at the interface of H13/Cu did not exhibit a smooth transition. Instead, it exhibited a peak hardness at the interface attributed to the increased laser hardening, followed by a sudden drop, which was attributed to poor diffusion of elements (Figure 10C).[167] Similarly, in CrMn/MS1 bimetallic structures, a mostly smooth transition was observed, but with a sudden hardness increase at the interface, resulting from the influence of the presence of MS1.[169] Overall, in the SS316L/P21, SS316L/17-4PH, and CrMn/MS1 MMAM structures, a smooth transition from harder to weaker material was revealed, though CrMn/MS1 uniquely exhibited a localized hardness increase at the interface. In contrast, the H13/Cu bimetallic structure interface deviated significantly from this trend, showing a rapid hardness change due to laser hardening in the deposited H13 region and a subsequent drop caused by insufficient interdiffusion.

Additional insight into hardness behavior across dissimilar materials was observed in Al-based bimetallic structures. The hardness factors of Al/tungsten, AlSi10Mg/C18400, and Al12Si/Al3.5Cu1.5Mg1Si MMAM structures were analyzed extensively,[172,175] revealing unique behaviors at the interface and during transitioning. In the Al/tungsten bimetallic structure, a smooth transition from tungsten (high hardness) to Al (low hardness) was observed.[177] In addition, the hardness throughout the sample increased as the scanning speed was reduced (Figure 10D). In AlSi10Mg/C18400, a gradual hardness decrease was observed from the Al-rich to Cu-rich regions, with anomalous hardness values exhibited at the interface. Such anomalous hardness values are due to the presence of brittle intermetallic Al_2Cu, which results in hardness

ranges of 400 – 600 HV.[175] In Al12Si/Al3.5Cu1.5Mg1Si MMAM structures, the interfacial region showed a sudden drop in hardness moving away from Al12Si.[172] From the silicon-dominant region (zone II) to the Cu-dominant region (zone III) (Figure 10E), the hardness increased significantly. This was attributed to the microstructural shift from cellular to granular morphology, accompanied by the development of a <001> fiber texture. Beyond zone III, however, the hardness decreased again due to grain growth and increased silicon content.

4.2. Tensile strength

Analyzing the tensile strength of MMs is necessary to determine the tensile characteristics at the interface and the bond between the dissimilar metals based on the deposition order and design. This section delves into the tensile properties of MMAM structures, where the dissimilar material deposition configurations are classified with respect to the build direction as Types A, B, C, and D, as shown in Figure 9. For the ease of the readers, the discussion follows the same order as Section 3, beginning with SS-based to Cu-based bimetallic structures.

The tensile strength of SS/Ni bimetallic structures has been evaluated using different compositions of Ni-based alloys, such as IN625[133,157] and IN718.[131] For SS316/IN625 structures fabricated in the Type-A orientation, Feenstra *et al.*[157] and Ahsan *et al.*[133] used MM-LDED and MM-WAAM, respectively. In both cases, the UTS was found to be greater than that of wrought and as-built SS316, with the bimetallic structures exhibiting a UTS of 577 ± 16 MPa. Interestingly, elongation values ranged from 10 – 15% in MM-LDED to 40% in MM-WAAM. Both studies reported dimple-like features on the fracture surfaces, suggesting ductile failure through micro-void coalescence. For SS316L/IN718 fabricated in Type-A orientation using MM-LPBF, UTS and elongation values were 596 ± 10 MPa and 28.1%, respectively—higher UTS than AM-SS316 but lower elongation than AM-IN718. Post-fracture analysis of the fracture surface revealed similar features to SS316/IN625, with dimple-like characteristics leading to a mixed-mode fracture, where the ductile mode was prominent. In both bimetallic structures, UTS values exhibited similar trends with a variation of 19 ± 19 MPa, and elongation remained within a comparable range. The root cause of failure in both cases was the formation of micro-voids at the interface, leading to ductile fracture and lower UTS compared to monolithic Ni-based alloys. Mitigating interfacial micro-voids could potentially enhance the mechanical performance of bimetallic structures.

Extending the evaluation to SS/Cu bimetallic structures, researchers have investigated various combinations fabricated using Cu alloys such as CuSn10[58,139,183] and C18400.[141] Chen *et al.*[58] manufactured SS316L/CuSn10 specimens in both Type-A and Type-D orientations. In both cases, the tensile strength and elongation were lower than those of bulk SS316L, with UTS values of 423.3 ± 30.2 MPa and 459.1 ± 8 MPa, and elongation values of 4.6 ± 0.9% and 10.5 ± 1.7%, respectively. Type-D specimens exhibited slightly higher UTS and approximately 6% greater elongation than Type-A specimens (Figure 11A). Fractography revealed distinct fracture modes: Type-A specimens exhibited cleavage fracture (a brittle transgranular mode) at the interfacial layer, attributed to unmelted SS316 powder particles, whereas Type-D specimens demonstrated a mixed mode of transgranular and intergranular fracture, with brittle fractures concentrated at the fusion zone.

Liu *et al.*[183] reported similar trends for Type-A orientation, although they observed lower tensile strength than that reported by Chen *et al.*,[58] primarily due to the presence of pores and interfacial cracks. A comparative study between LPBF and laser-welded structures indicated that LPBF showed higher tensile stress, attributed to finer grain structures formed under higher cooling rates.[139] Compared to SS316L/CuSn10,[139] the tensile strength of SS316L/C18400 in Type-D orientation was lower (310 ± 18 MPa. However, unlike in previous SS/Cu bimetallic systems, the fracture occurred on the Cu-side (the weaker material), indicating a well-formed metallurgical bond. Between CuSn10 and C18400, the latter showed improved bonding with SS316L, likely due to the lower reactivity of Fe–Cr compared to Fe–Sn. The Fe–Sn system is prone to form brittle intermetallic phases such as $FeSn_2$. In addition, Type-D orientation marginally performed better than Type-A, which may be attributed to the larger bonding area of Type-D.

Extending beyond Cu-based bimetallic, SS316L has also been combined with dissimilar materials such as W[148] and Ti-6Al-4V,[123] yielding varied interfacial characteristics. In MM-LPBF-fabricated SS316L/W (Type-D) structures, tensile strength increased from 239.7 MPa to 257.4 MPa after heat treatment, while elongation improved significantly from 5.3% to 17%.[148] This improvement was attributed to the transformation of the brittle fracture mode to a more ductile one, driven by the formation of Fe_7W_6 near the interface—an inherently hard and brittle phase. Fractures typically initiated on the W side of the interface. For SS316L/Ti-6Al-4V (Type-A) MM-LPBF structures, in which a Cu-alloy was used as an IBL, the scanning speed was a key parameter. Tey *et al.*[123] observed that specimens built at 650 mm/s exhibited higher tensile strength and better bonding than those built at 350 mm/s.

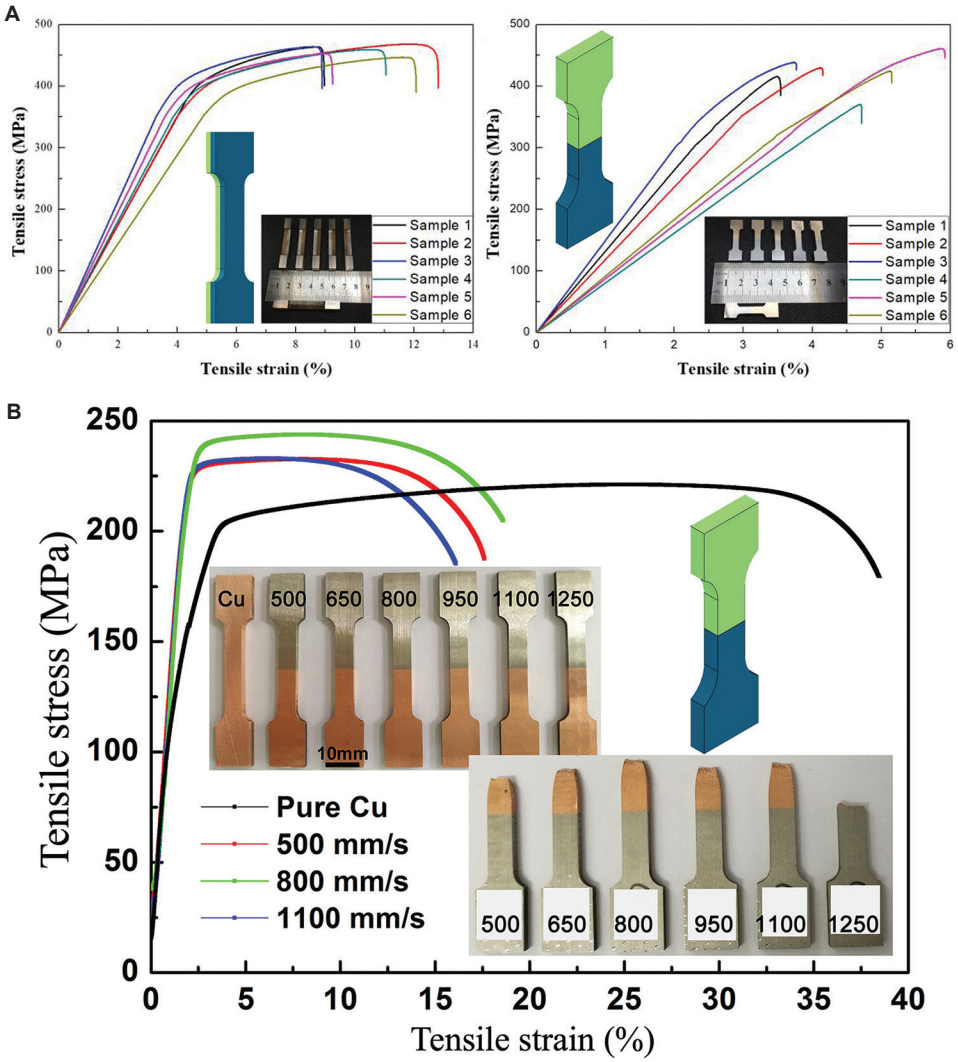

Figure 11. Quasi-static tensile stress–strain response of selected bimetallic structures fabricated throughmulti-material laser powder bed fusion: (A) SS316L/CuSn10;[58] and (B) MS1/Cu;[179] and (C) Ti-5Al-2.5Sn/Ti-6Al-4V.[151] The graphs highlight mechanical behavior across bimetallic interfaces, including differences in strength, ductility, and elongation. A schematic representation of the build orientation is also provided, consistent with that in Figure 9.

This resulted in a predominantly ductile fracture mode, in contrast to the brittle failure observed in lower-speed builds. In the above-mentioned MM-LPBF structures, the presence of defects and porosity evidently contributed to premature failure compared to the bulk materials. In both SS316L/W and SS316L/Ti-6Al-4V systems, characteristics such as heat treatment and processing parameters played a critical role in determining tensile behavior. These improvements were largely attributed to the removal of brittle IMCs and the relief of through-thickness residual stresses. Elimination of IMCs facilitated a transition from brittle to ductile fracture modes in both systems.

Although extensive research has been conducted on SS-based bimetallic structures, Ti-based bimetallics have also gained attention for their tensile strength. The tensile strength of Ti-5Al-2.5Sn/Ti-6Al-4V (Type-A) in as-deposited specimens reached a UTS of 1,034 MPa and an elongation of 4%, which is lower than that of forged Ti-alloys—primarily due to the formation of martensite microstructure.[151] Similar to the SS316/W system,[148] heat treatment increased elongation by 10%, due to the decomposition of the martensite phase, which led to a significant improvement in the strength–ductility balance. Compared to forged and AM monolithic materials, the bimetallic UTS exceeded that of forged alloys but remained lower than their AM counterparts, whereas elongation showed the opposite trend. Fractography analysis of the as-deposited bimetallic revealed that the fracture occurred on the To-5Al-2.5Sn side, due to its lower hardness compared to Ti-6Al-4V. This observation

is validated by the hardness data presented earlier in Section 3.2.

MS1/Cu (Type-A)[179] and CrMn/MS1 (Type-A)[169] bimetallic structures outperformed the weaker constituent materials when compared to the earlier examples. In the MS1/Cu system, specimens fabricated at various scanning speeds showed similar UTS and elongation, except for the one built at 1,250 mm/s. At this higher scanning speed, a fracture occurred at the interface rather than on the Cu side, which had been the fracture location in all other specimens (Figure 11B). As previously discussed in Section 3.1 (Figure 8G), the MS1/Cu interface at low scanning speeds exhibited good metallurgical bonding due to enhanced thermal conductivity and Marangoni convection. These effects, influenced by Cu and Fe dissolution, contributed to the solid-solution strengthening of the Cu at the interface. In the CrMn/MS1 bimetallic structure, specimens exhibited slightly higher tensile strength compared to wrought CrMn, but lower than AM MS1. The fracture occurred on the CrMn side, indicating good metallurgical bonding. As with earlier observations, tensile strength and elongation were influenced by process parameters, indicating that optimal scanning conditions can promote ideal metallurgical bonding. Notably, CrMn/MS1 exhibited better tensile strength than wrought CrMn due to its improved bonding. Interestingly, bimetallic structures composed of the same alloy system but with different compositions (e.g., Ti-5Al-2.5Sn/Ti-6Al-4V) demonstrated better tensile behavior than the weaker monolithic constituent. This could be attributed to good metallurgical bonding and a defect-free interface.

Similar to the other same-alloy bimetallic structures, the AlSi10Mg/C18400 (Type-D) specimen exhibited higher tensile strength than C18400, but significantly lower than AlSi10Mg.[175] Failure predominantly occurred on the Cu-rich side, reinforcing the notion that interfacial bonding between Al and Cu is stronger than the bonding within the Cu-rich region itself. Fractographic analysis revealed a mixed brittle and ductile fracture mode, with ductile features dominating. This was influenced by the presence of unmelted particles on the Cu side of the fracture surface, which acted as stress concentrators and initiated failure. Similarly, tensile testing of Al12Si/Al3.5Cu1.5Mg1Si (Type-A) revealed a higher YS of 267 ± 10 MPa compared to as-built LPBF bulk counterparts. However, the UTS was lower than that of the bulk materials due to differences in microstructure.[172] Fractographic analysis revealed a brittle fracture mode approximately 200 µm from the interface on the Al12Si side, indicating good metallurgical bonding accompanied by localized embrittlement. Finally, for the Al6060/Al5087 (Type-A) bimetallic structure fabricated using MM-WAAM in the longitudinal direction, Hauser *et al.*[173] reported that the YS of as-built monolithic Al6060 was lower, and that of as-built monolithic Al5087 was higher than that of the bimetallic counterpart. Similar trends were observed for UTS values. Upon heat treatment, all specimens—including the bimetallic—experienced improved YS and UTS as expected. The UTS of the heat-treated bimetallic structure was comparable to that of Al6060 and slightly lower than that of Al5087, confirming the beneficial influence of post-processing on mechanical performance. Consistent with earlier observations, porosity and defects negatively influenced mechanical properties in Al/Cu bimetallic structures. In contrast, Al/Al bimetallics, similar to other same-element combinations (e.g., CrMn/MS1-Fe/Fe and Ti-5Al-2.5Sn/Ti-6Al-4V–Ti/Ti), exhibited good metallurgical bonding and superior mechanical performance compared to wrought material or monolithic as-built materials.

4.3. Flexural strength

Compared to other mechanical properties, the flexural strength of MMAM structures has received relatively limited attention. Among the available literature, ferrous-based MMAM structures such as C300MS/AISI304 and C300MS/AISI1045CS, fabricated in Type-A and Type-D orientations (Figure 9), have shown promising results. Both bimetallic structures exhibited higher flexural YS and Ultimate flexural strength (UFS) compared to their monolithic counterparts.[170] Notably, while the UFS of C300MS/AISI1045CS was 9.2% lower than that of its base material AISI1045CS, the C300MS/AISI304 specimen exceeded its monolithic counterpart by 2.5% (Figure 12). This suggests that interfacial strengthening in C300MS/AISI304 is more effective, likely due to coherent grain orientation bridging across the interface, which enhances load transfer and structural integrity.

A similar interfacial effect was observed in MS1/Cu MMAM structures fabricated using LPBF in the Type-A orientation (Figure 9) under varying scanning speeds. The flexural strength varied significantly, attributed to the presence of defects and suboptimal processing conditions.[179] Among the tested parameters, a moderate scanning speed of 800 mm/s yielded the highest UFS of 557 ± 19 MPa, due to strong interfacial bonding and defect-free (Figure 12B [regarding flexural strength] and Figure 8G and H [regarding interfacial morphology]). Beyond the influence of process parameters, IBL additions can also affect the flexural properties of the MMAM structures. In SS316L/CuSn10 and CuSn10/SS316L, the flexural strength differed due to the incorporation of tin–bronze (TB). Specifically, the addition of TB flexural strength by 20% in both configurations.[58,142] Despite this reduction, both structures

exhibited good metallurgical bonding, though dendritic cracks were observed, attributed to CTE mismatch. The more significant reduction in flexural strength observed by Chen *et al.*[142] compared to Chen *et al.*[58] can be attributed to a wider transition zone, which compromises mechanical homogeneity across the interface. Finally, in AlSi10Mg/C18400 MMAM structures, the orientation of the base material significantly influenced flexural performance. When Al served as the substrate, both flexural strength and strain were higher compared to configurations where Cu was the base material.[175] This outcome is linked to the higher porosity and lower mechanical integrity of the Cu-rich region, emphasizing that most of the load-bearing capacity is retained by the Al side. In both cases, porosity formation at the interface, attributed to mismatch thermal properties, resulted in reduced flexural strength.

4.4. Compression strength

Among the available MMAM empirical studies, compression testing remains relatively underexplored, with only a limited number of investigations focusing on this mechanical property. Notably, in MMAM structures such as P21/SS316L[166] and 17-4PH/SS316L,[167] both of which employ ferrous alloys as base materials, distinct deformation behaviors were observed under compression loading. Post-failure analysis revealed that SS316L specimens exhibited axisymmetric plastic deformation, indicative of uniform plastic flow. In contrast, P21/SS316L deformed laterally due to differences in the compressive YS between the constituent materials. These experimental findings were validated by an FEA study, which accurately predicted the observed deformation patterns.[166] Further details regarding the FEA methodology and results are discussed in Section 5. The observed deformation behavior can be further explained by considering the underlying plastic deformation mechanisms. Both 17-4PH and P21 possess a body-centered cubic (BCC) structure, which impedes dislocation motion, while SS316L has a face-centered cubic (FCC) structure that facilitates dislocation slip. This mismatch in crystal structure contributes to the axisymmetric barreling plastic deformation observed (Figure 13B and C). Furthermore, residual thermal stresses arising from mismatched CTE between the materials may also contribute to strain-hardening effects.[147]

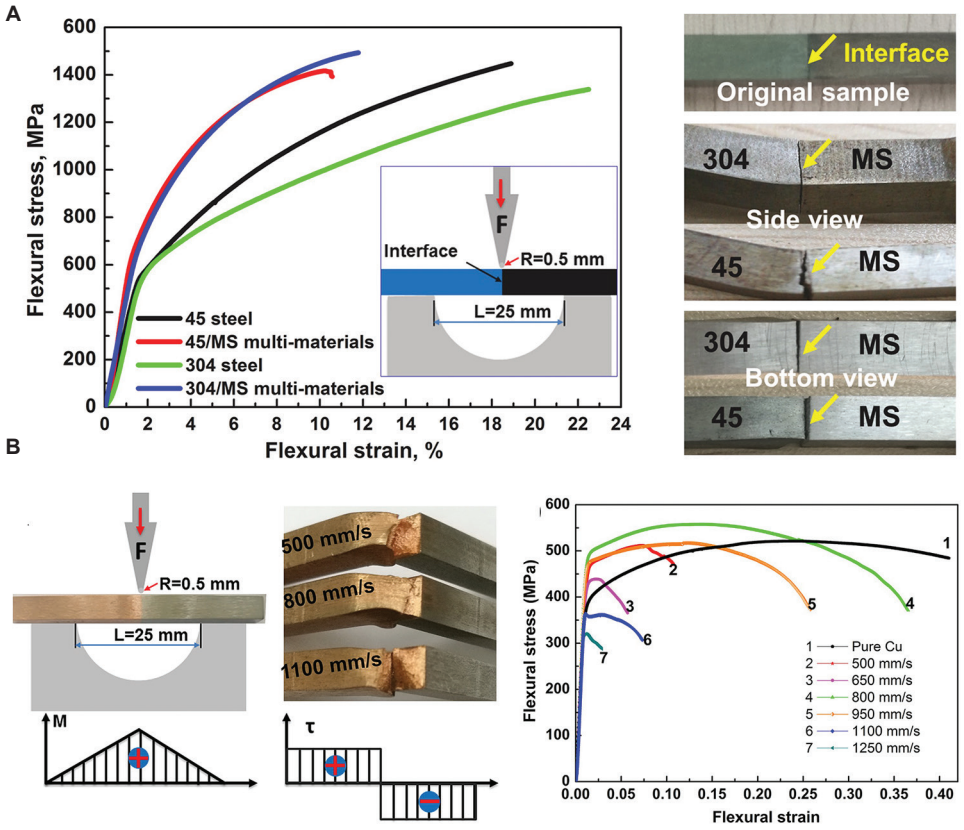

Figure 12. Flexural stress–strain response of bimetallic structures fabricated through mixed-material laser powder bed fusion. (A) C300MS/AISI304 and C300MS/AISI1045 carbon steel;[170] and (B) MS1/T2.[179] The graphs illustrate the flexural strength at the interface of the bimetallic structures and the role of metallurgical bonding under flexural loading.

In the 17-4PH/SS316L MMAM structure, the radially configured specimen exhibited a compressive YS of 654 ± 12 MPa, outperforming the double-layered, single-layered, and monolithic SS316L structures, which showed a 526 ± 4 MPa, 425 ± 7MPa, and 356 ± 17 MPa, respectively. This improvement in performance is attributed to the higher linear CTE of the outside casing (17-4PH) compared to the core (SS316L), and to the zig-zag deposition pattern, which functioned as a mechanical interlock, enhancing bond strength. Among all the tested specimens, a 1:1 premixed MM exhibited the lowest performance (Figure 13C), with a compressive YS of 303 ± 17 MPa, attributed to a reduced volume fraction of solid-solution strengthening elements, such as Ni and molybdenum by 37.5% and 40%, respectively.[147]

In a separate study, the compressive behavior of 18Ni300/CuSn10 with varying percentages of structural porosity was evaluated.[176] As expected, increasing porosity resulted in a systematic reduction in compressive YS, complicating the direct assessment of interfacial mechanical integrity due to the highly porous architecture of the specimens. Similarly, for the TiB/Ti-6Al-4V MMAM structure, the compressive response of a gyroid scaffold design was analyzed for both monolithic Ti-6Al-4V and bimetallic structures. The monolithic structure primarily exhibited a linear elastic zone, followed by an elastic–plastic transition before reaching ultimate strength. In contrast, the bimetallic lattice structure initially demonstrated a non-linear region, followed by a linear elastic response. The initial non-linear

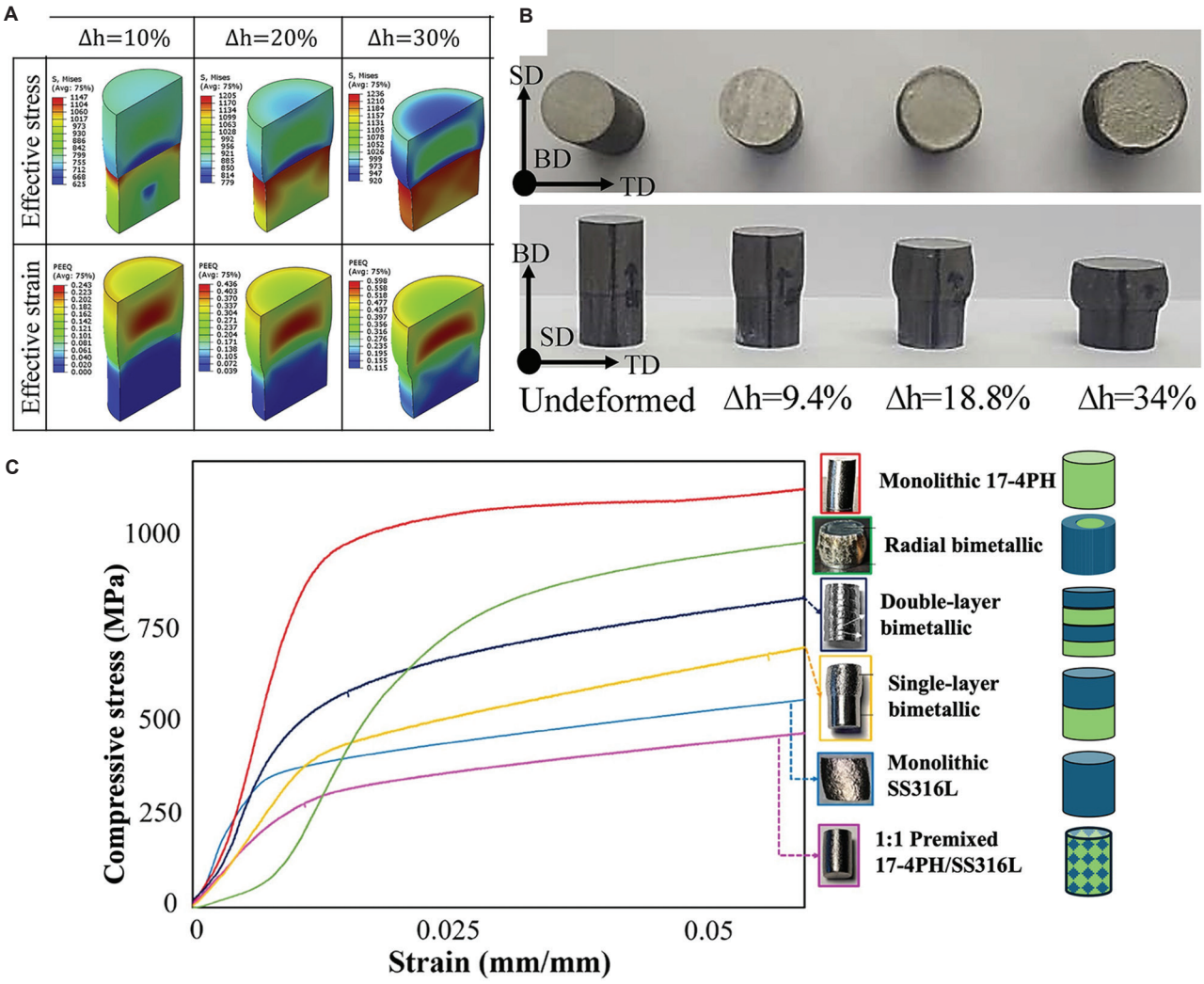

Figure 13. Compression testing of multi-material laser powder bed fusion steel-based bimetallic structures. (A and B) Corresponding numerical deformation simulations of P21/SS316L and time-stamped post-failure views (top and side);[166] and (C) Compressive stress–strain curves for various 17-4PH/SS316L configurations, including monolithic 17-4PH and SS316L, single- and double-layer bimetallic, 1:1 premixed composition, and radial bimetallic design.[147] These results present both experimental and numerical observations, highlighting the influence of architectural design and material distribution on compressive strength and deformation behavior.

behavior was attributed to surface roughness, dimensional deviation of the upper surface, and unevenness of the bottom surface.[189]

4.5. Fatigue life

Fatigue testing remains a fundamental approach for assessing the failure mechanisms of structural components under cyclic loading. Its application in bimetallic structures has gained increasing attention in recent years. Unlike other mechanical properties such as tensile strength and hardness, fatigue failure often occurs without prior visible deformation, potentially leading to catastrophic structural failures. As a result, fatigue testing is considered a critical indicator of dynamic mechanical performance, providing essential insights into the service life and reliability of MM structures, especially in high-cycle applications involving alternating stresses.

In a notable study, Tan *et al.*[170] investigated the fatigue behavior of MMAM structures with ferrous base materials, specifically C300MS/AISI304 and C300MS/AISI1045CS. Both bimetallic structures were evaluated at 30 Hz under 400 MPa stress. C300MS/AISI304 exhibited a significantly longer fatigue life of 4.505×10^6, compared to 0.36×10^6 cycles for C300MS/AISI1045CS. Failure in C300MS/AISI304 occurred on the AISI304 side, whereas in C300MS/AISI1045CS, failure initiated at the interface. Fractographic analysis revealed that the premature failure of C300MS/AISI1045CS was caused by the presence of interfacial pores, while the defect-free interface in C300MS/AISI304 contributed to its superior fatigue resistance.

The fatigue life of bimetallic IN718/SS316L was further examined through two configurations: crack arrester and crack divider.[159] Results indicated that the crack growth rate was influenced by the local crack tip stress intensity factor range (ΔK). Depending on the transition direction (soft-to-hard or hard-to-soft), crack propagation was affected by differences in material properties and grain structure. Fractographic analysis revealed that grain orientation and morphology significantly impacted crack tortuosity and propagation rate. Although dissimilar material interfaces did not show a pronounced effect under high ΔK conditions, crack behavior was markedly influenced by grain structure at lower ΔK values. Overall, Duval-Chaneac *et al.*[159] concluded that residual stress had minimal effect on crack propagation due to careful specimen preparation and the good coherence of grain structures at the interface.

4.6. Miscellaneous tests

While most studies have focused on common and widely available mechanical properties such as hardness and tensile strength, some have explored environmental effects, including thermal diffusivity and wear performance, which are critical for specific application domains. Understanding thermal diffusivity is vital for characterizing the heat transfer behavior of MMAM structures during manufacturing. Thermal diffusivity data provides information on a material's ability to conduct heat relative to its ability to store it. Figure 14 presents both experimental and theoretical thermal diffusivity data for MMAM structures with IN718 as the base material, along with data for the constituent single-alloy materials. The comparison illustrates how the thermal performance of the bimetallic system differs from its monolithic counterparts. Theoretical thermal diffusivity values of the bimetallic structures range from 14.37 to 17.09 mm^2/s between 50°C and 300°C.In contrast, experimental values were found to be lower, ranging from 10.30 ± 07 to 12.33 ± 0.07 mm^2/s within the same temperature range.[184] The thermal diffusivity of the bimetallic structure lies between those of monolithic IN718 and the Cu alloy, reflecting the expected thermal blending behavior.

In addition to thermal behavior, wear performance was also investigated. Wear testing was conducted on an IN718/SS316L MMAM structure with carbon fiber functioning as the IBL. The analysis included comparative wear data for both IN718 and IN718/CF/SS316L. Results showed that IN718/CF/SS316L reached a steady-state wear rate in under 80 seconds, significantly faster than wrought IN718, which stabilized after approximately 300 s.[158]

5. Modeling and simulation for MMAM

An extensive list of in-process and post-fabrication simulation software and codes currently exists for single-material AM across multiple length scales, providing insights into the state of research and development toward MMAM. Experimental investigations are often time-consuming and costly, making them prohibitive for some AM research. Consequently, simulations play a critical role in augmenting understanding, optimizing processes, and enabling process control. Simulations commonly used in single-material AM include thermodynamic modeling, melt pool dynamics, powder bed behavior (PBB), and computational fluid dynamics-volume of fluid (CFD-VOF) models. Thermal simulation modeling is employed to guide parameter selection, ranging from single melt pool point penetration to single or multiple melt pool tracks, and extending to full component modeling at micro-, meso-, and macro-length scales. Melt pool dynamic simulations focus on material behavior during interaction with the laser and heat-affected zone, providing information on melt pool morphology, cooling rates, and microstructural characteristics. PBB simulations model particle–particle interactions on the powder bed, powder

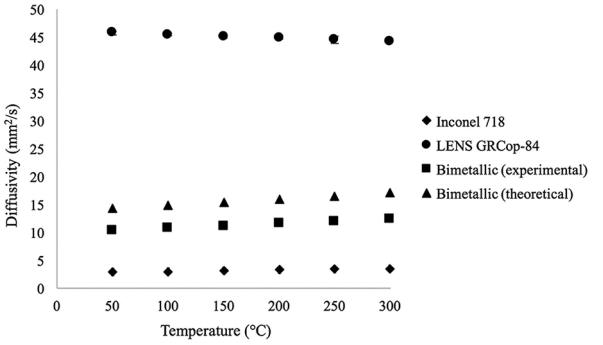

Figure 14. Thermal diffusivity of IN718/CuA bimetallic structure,[184] including measured values for monolithic IN718 and GRCop-84, alongside experimental and theoretical thermal diffusivity values for the bimetallic composition. The comparison illustrates the thermal diffusivity behavior of the bimetallic structure relative to its constituent materials across a temperature range of 50°C to 300°C.

spreading dynamics, and particle–laser interactions during melting. These simulations, often conducted using the discrete element method (DEM), help optimize powder shape or size distribution to achieve ideal powder flow characteristics, thereby improving layering and reducing mesoscale defects. The CFD-VOF model typically includes a laser heat source and a coaxial nozzle with a single powder feeder aligned with the laser path. This model captures key phenomena during LDED, such as powder and gas flow dynamics, laser–powder interactions, attenuation effects, and melt pool behavior.

5.1. Microstructural computational analysis (phase transformation, melt pool formation, and alloy mixing)

Simulating and predicting the microstructural evolution at the interface of bimetallic structures fabricated using MMAM is critical to optimizing their performance in industrial applications. Microstructural simulation and modeling serve as powerful tools to bridge the gap in understanding the links between processing conditions and final material properties. These tools enable the capture of solidification behavior, phase transformations, grain morphology, and elemental diffusion across dissimilar materials. In bimetallic structures with significant differences in thermal properties, computational analysis is essential for evaluating the nature of bonding, transition zone development, and the formation of undesired IMCs, porosity, or other defects. Various techniques—such as the Monte Carlo method, CALPHAD, Lattice Boltzmann, Cline–Anthony model (for melt pool geometry), and smoothed particle hydrodynamics (SPH)–are employed to simulate grain growth, phase diagrams, diffusion at interfaces, and microscale kinetics. Most solidification modeling software or open-source codes have been developed for single-material processes; thus, simulation platforms specifically tailored for MMAM remain underdeveloped, unvalidated, and unqualified. In this section, we review existing literature on the computational analysis of bimetallic structures and processes, with a focus on developments toward MMAM. Specifically, the remainder of this section discusses research conducted on simulating melt pool dynamics, elemental intermixing, phase diagrams, and grain growth during solidification.

Although extensive studies have been conducted on single-material melting and solidification, Sorkin *et al.*[192] presented the first published attempt at simulating MM melting using the open-source molecular dynamics software Large-scale Atomic/Modular Massively Parallel Simulator (LAMMPS), albeit with numerous simplifications. However, the model's assumptions neglected several key physical processes involved in LPBF, including surface tension forces, multiphase flow, and molten pool formation. Moreover, no experimental validation was provided to support the simulation results. Beyond melt pool dynamics, powder deposition plays a significant role in MM applications, influencing interfacial properties based on packing, design, and deposition strategies. Gu *et al.*[23] investigated various deposition patterns involving multiple materials by incorporating particle size distribution data obtained from a particle size analyzer and simulating it employing the DEM (EDEM v2019). The studied deposition patterns included evenly mixed, bimetallic separation, interlock deposition, and FGM. Further discussion on the influence of these deposition patterns on melt pool formation is provided later in this section.

The characteristics of the melt pool, including temperature gradients, thermodynamics, fluid dynamics, and laser–matter interactions, have been thoroughly studied in LPBF and LDED processes. Sun *et al.*[20] applied a DEM approach using ABAQUS FLUENT for multiphase mesoscale modeling of an MM powder bed composed of IN718/Cu10Sn (Figure 15A). This study simulated several powder configurations within a single layer (aligned parallel or perpendicular to the laser scan path, and pre-mixed by wt.%). The simulations focused on melt pool morphology and thermal behavior during single-track laser scans. To simplify the model, the two components were treated as mutually soluble, enabling microlevel mixing. When comparing tracks composed of mixed versus unmixed dissimilar powders, melt pools with a high content of IN718 exhibited higher peak temperatures due to their thermo-physical properties. In the unmixed case, the melt pool size and temperature transitioned gradually as the laser moved from one material to the other.

More recently, Gu *et al.*[23] applied a modified DEM approach to simulate multiple adjacent laser tracks of SS316L/Cu10Sn (Figure 15B and C). As noted previously, the process introduced a variety of powder deposition patterns and compared simulation outcomes with experimental data. In the study, the material was deposited horizontally and vertically to investigate melt pool morphology and temperature distribution (Figure 15C). When observing the melt pool track in both configurations, the vertical deposition of the bimetallic structure exhibited a discontinuous melt pool formation. This discontinuity is attributed to the difference in laser absorptivity between SS316L (0.35) and Cu10Sn (0.03), as well as the higher thermal conductivity of Cu10Sn compared to SS316L, which leads to highly efficient heat dissipation from the beam center to the surrounding powder. In contrast, during horizontal layer deposition, SS316L powder melted first, and the heat conducted from the molten SS316L

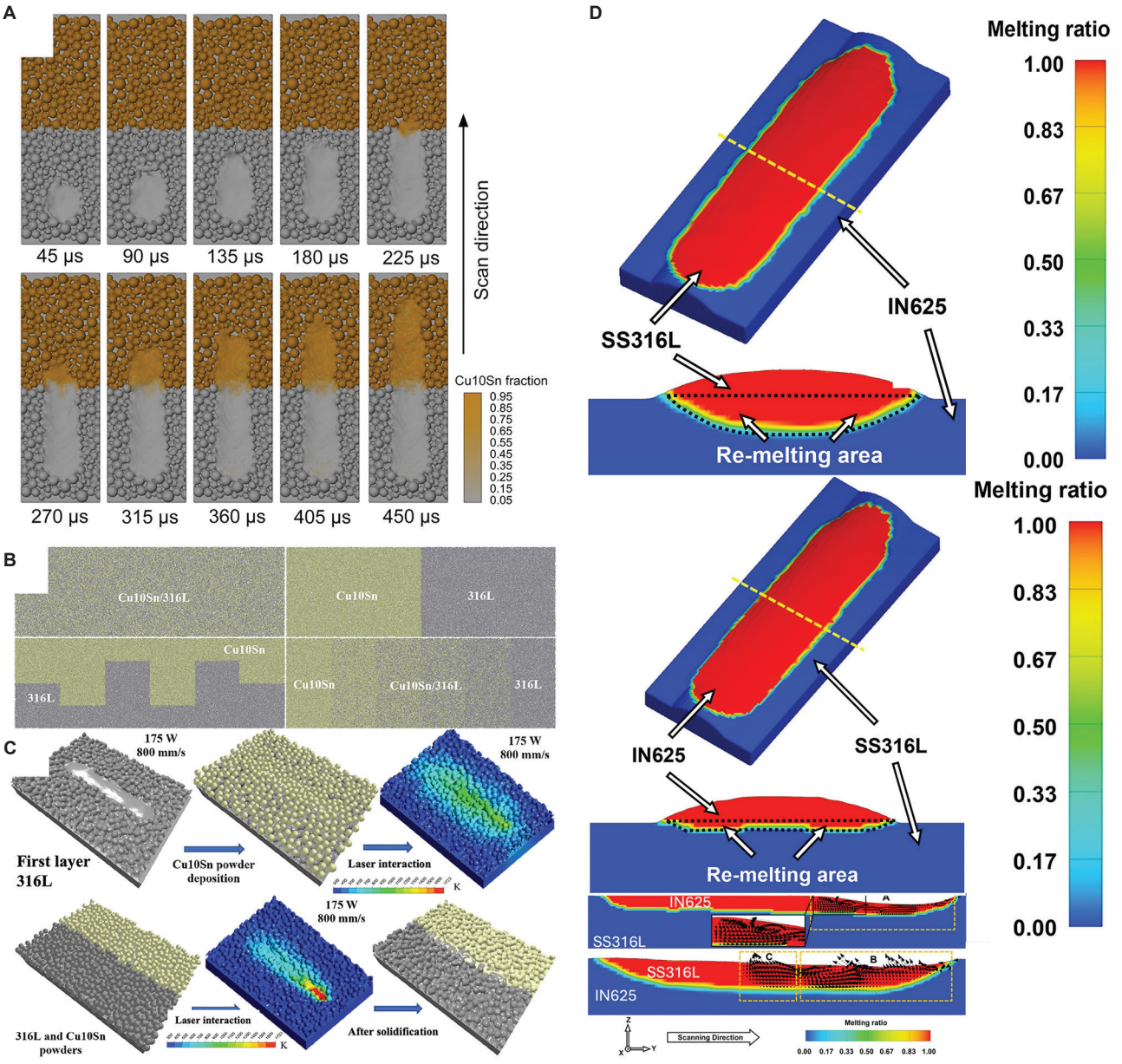

Figure 15. Single-track melting and solidification in selected bimetallic structures. (A) IN718/CuSn10 single-track melting profile;[20] (B and C) SS316L/CuSn10 solidification simulation illustrating thermal and powder solidification dynamics;[23] and (D) single-track solidification of IN625/SS316L (top: Type-A) and SS316L/IN625 (bottom: Type-B) configurations.[132] The visualizations demonstrate the influence of materials order and interfacial configuration on melt pool evolution and solidification morphology.

powder and its convection flow contributed to the melting of Cu10Sn. Scanning electron microscopy analysis further revealed that phase migration was likely driven by this convection flow, which facilitated elemental intermixing across multiple layers.

Interestingly, Zhang *et al.*[193] used the Cline–Anthony model to calculate the melt pool temperature field during the LDED process for CuCr/07Cr15Ni5. Using this model, they successfully predicted printability maps as a function of deposition layer number. A narrowing of the printability window with increasing layer number was found to enhance thermal conductivity, specific heat capacity, and effective density. The calculated results from the proposed analytical model were in good agreement with experimental data. Similarly, Li *et al.*[194] applied a CFD-based approach to model the fabrication process of FGM using MM-LDED. They developed a multiphysics, MM model to simulate thermal gradients, phase transitions, melt pool dynamics, and final part geometry, identifying non-uniformities in material gradation across the transition zone. Ghanavati *et al.*[127] identified that SS 316L is susceptible to composition changes and a lack of fusion, which can lead to porosity due to its high equilibrium vapor pressure. In contrast, IN718 is more prone to distortion, owing to the formation of larger melt pools. In a study involving MM-LPBF TiB_2/Ti-6Al-4V, Chen *et al.*[195] used a multilayer finite element model (ANSYS) to predict temperature gradients and remelting ratios. They assumed that the absorptivity of Ti-6Al-4V is equivalent to that of Ti-alloy powder, while TiB_2 behaves similarly to non-oxide ceramics with relatively high absorptivity. The results showed that the maximum temperature gradient occurred at the interface and demonstrated a direct proportionality between laser power and temperature gradient (Figure 16A), and an inverse proportionality with laser scan speed (Figure 16B). In addition to temperature gradient analysis, a CFD–DEM-based approach was applied to SS316L/W and W/SS316L interfaces to examine melt pool temperature profiles (Figure 16C). The temperature profiles were evaluated with respect to the melting temperatures of SS316L (1658 K) and W (3695 K). The observed characteristic behavior is attributed to the significantly higher thermal conductivity of W, which facilitates efficient heat dissipation. These simulations collectively demonstrate the capabilities of MM thermal-fluid dynamics models in fundamentally investigating the AM process and assessing printability.

Understanding phase stability and phase transformations under variable temperatures, pressures, and compositions is crucial for the development of advanced computational capabilities. In one example, thermodynamic calculations were employed to predict the phases present in high-strength steel/Ti-6Al-4V bimetallic structures. Using CALPHAD, Wei *et al.*[165] identified three intermetallic formations at the interface: α-Fe + Fe_2Ti, Fe_2Ti, and TiFe + β-Ti. Their analysis indicated that a compositional gradient build strategy would not be sufficient to prevent the formation of Fe_2Ti, a brittle IMC. In a similar approach, Kannan *et al.*[196] conducted a CALPHAD analysis on a compositionally graded Al-Cu-Ce-Zr/SS316L joint. They found that composition ratios of 90%, 80%, 20%, and 10% SS316L were promising for fabrication, as no primary intermetallic formations were observed. Instead, a BCC_A2 matrix formed on the Fe-rich side and an FCC_A1 matrix on the Al-rich side. Scheil simulations performed on a P21/704H bimetallic structure fabricated using MM-WAAM revealed drastic variations in volumetric CTE and freezing range due to the formation of an MC carbide phase from the liquid during solidification. This phase formation led to cracking in the intermediate region.[197] Iams *et al.*[198] performed similar testing on GRCop-42/IN718 using Scheil simulation and observed the formation of a C15 Cr_2Nb phase in the GrCop-42 composition. They also reported enrichment in Ni and Fe, which contributed to the formation of the C14 $(Cr,Ni,Fe)_2Nb$ phase and the BCC α-Cr phase. In the case of Ti-6Al-4V/Al-Cu-Mg structures, which exhibit significantly different thermal properties, the interface was found to be prone to cracking due to the formation of IMCs. Based on this understanding, Zhang *et al.*[199] used Scheil–Gulliver simulation and Malac–Distmas calculations to predict the phase diagram and diffusion path of the bimetallic structure. The binary phase diagram and diffusion path of direct Ti–Al bonding revealed high susceptibility to cracking and delamination at the interface (top two panels of Figure 16D). To mitigate interfacial cracking, a Cu interlayer was introduced. The two lower panels in Figure 16D show the predicted IMCs. Since Cu is a eutectoid-forming element with both Ti and Al, it contributes to constitutional supercooling and stabilizes the bonding interface.

Beyond thermal behavior, Chen *et al.*[132] applied a CFD-based approach to investigate melt pool morphology in MM-LDED-processed IN625/SS316L (Type-A) and SS316L/IN625 (Type-B) structures (Figure 15D). In Type-A, an anticlockwise flow at the rear of the melt pool contributed to a fully mixed zone by moving remelted SS316L toward regions of higher temperature. In contrast, the Type-B interface exhibited a clockwise flow, causing unmixed IN625 to rise into the melt pool and become trapped during solidification (Figure 4C and F for experimental validation). The simulation was used to verify and explain the experimental observations previously discussed. Using a similar CFD–DEM-based

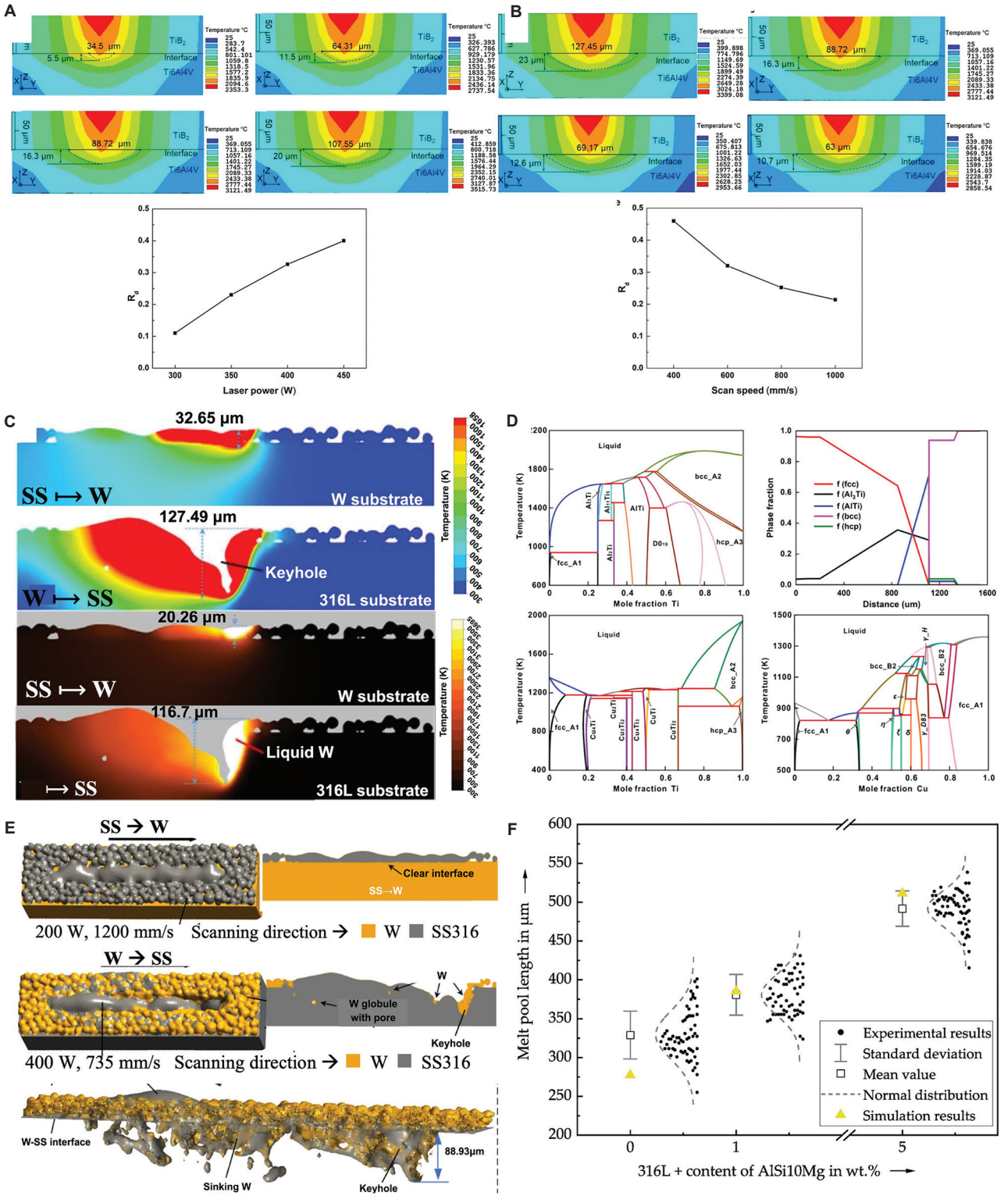

Figure 16. Temperature distribution and melt pool behavior in multi-material laser powder bed fusion (MM-LPBF). (A and B) Cross-sectional temperature profiles in Ti-6Al-4V/TiB_2 as a function of laser power and scan speed;[195] (C) Scan track morphology of SS316L/W and W/SS316L, illustrating directional dependency in bimetallic printing;[149] (D) corresponding melt pool temperature profiles ranging from 300 – 1658 K and 300 – 3695 K;[199] (E) Comparison of numerically simulated and experimentally measured melt pool lengths in SS316L/AlSi10Mg;[199] (F) CALPHAD-based phase diagram predictions for Ti-Al, Ti-Cu, and Al-Cu binary phase systems, along with diffusion path analysis for Ti-Al.[200] The images collectively illustrate the influence of process parameters, material combinations, and thermodynamic modeling on thermal behavior in MM-LPBF.

approach, Wei *et al.*[149] simulated the MMAM of SS316L/W bimetallic structures using MM-LPBF, treating the bottom layer material as a substrate (Figure 16E). At the SS316L/W interface (top of Figure 16C), good wettability with the W substrate was observed, and the cross-sectional melt pool view (right-hand side) indicated that W did not melt and no elemental mixing occurred. However, at the W/SS316L interface (bottom of Figure 16E), the SS316L appeared on top of W rather than beneath it. This was attributed to high energy density resulting in keyhole mode melting, as seen in the bottom right-hand side of Figure 16E. The application of excess heat is due to significant differences in thermal properties between SS316L and W. In a similar approach using CFD–DEM based methods, Wimmer *et al.*[200] conducted a numerical simulation of melt pool dimensions in SS/Al and compared the results to experimental data (Figure 16F), utilizing a meshless SPH method.

5.2. Mechanical behavior computational analysis

Finite element modeling (FEM) of MMAM structures is crucial for predicting the mechanical behavior of complex designs, thereby supporting the optimization of material distribution. Recent studies have applied and advanced various modeling software tools to address the structural or thermal qualification of designs using FEM. The presence of dissimilar materials with contrasting mechanical and thermal properties introduces complex residual stresses, especially near the interface. FEM enables detailed analysis of elastic and plastic deformation, residual stress accumulation, interfacial stress distribution, and potential failure mechanisms under various loading conditions. This modeling approach provides insights into the structural reliability of MM structures and is essential for identifying stress concentration zones and guiding design strategies to mitigate defects such as warping, delamination, and cracking. While most of these studies have been validated using multi-polymeric structures,[201,202] due to the relative ease of fabrication compared to metallic structures, only a few have shown the capability of modeling and verifying metallic MMAM structures. McDonnell *et al.*[125] and Zhang *et al.*[199] fabricated MMAM lattice structures using SS316L/17-PH and Ti-6Al-4V/CuA/Al-Cu-Mg, respectively. McDonell *et al.*[125] constructed a bimetallic lattice structure composed of BCC and octet truss architectures using MM-LPBF, with horizontal and vertical material separations (Figure 17A). It was observed that the deformation behavior and stress–strain response of the bimetallic lattice—featuring a combination of ductile and brittle metals—varied with lattice arrangement. The parallel bimetallic lattice structure demonstrated superior energy-absorption performance compared to the series arrangement due to its stress–strain plateau, reduced fracture, and consistent plastic deformation. FEM successfully predicted this behavior. Similarly, Zhang *et al.*[199] investigated a Ti-6AL-4V/CuA/Al-Cu-Mg MMAM gyroid lattice structure (Figure 17B) fabricated using MM-LPBF. FEM analysis of a unit cell showed that the highest levels of equivalent stress and strain occurred at the center of the inclined struts, indicating shear fracture. Due to the differences in strength and stiffness between the Al-rich and Ti-rich regions, the upper portion of the lattice deformed prior to the lower portion.

Likewise, FEA-based compression testing on a P21/SS316L bimetallic cylindrical structure fabricated using MM-LDED revealed significant stress and strain accumulation during the test (Figure 17C). Stress concentration occurred around the circumference of the P21 region as Δh percentage increased, while strain primarily accumulated on the SS316L side.[166] Throughout the test, it was observed that the softer material absorbed a larger portion of the strain, whereas the harder material bore the majority of the stress. This behavior is clearly depicted in the color intensity gradients in Figure 17A-C. It should be noted that due to limitations in software flexibility and adaptability for AM structures—including bimetallic systems—models typically assume smooth surfaces (i.e., neglecting surface roughness), the absence of defects or porosity, and ideal, crack-free interfaces. As a result, FEA results often exhibit notable discrepancies when compared with experimental data. Griffis *et al.*[203] performed site-specific MM structural FEM using local material properties in the MM-LPBF bimetallic fusion zone, modeling the interfacial region as an effective third material. Their FEA method was used to inform a localized redesign of the fusion zone geometry to interlock material regions and improve the global pull-apart strength of the interface.

Few studies have applied MM structural modeling from a computational topology optimization design perspective. Giraldo-Londona *et al.*[204] developed a multi-objective algorithm for the joint design of MM structures, considering both structural and thermal load cases. For comprehensive reviews on multiobjective topology optimization in MMAM component design, readers are referred to Zhang *et al.*[205] and Sanders *et al.*,[206] who provide detailed theoretical insights into the development of MM topology optimization algorithms.

6. Discussion and future direction

6.1. Feedstock recyclability and build material cross-contamination

Post-processing and recycling procedures for parts produced via metal AM using powder feedstock present

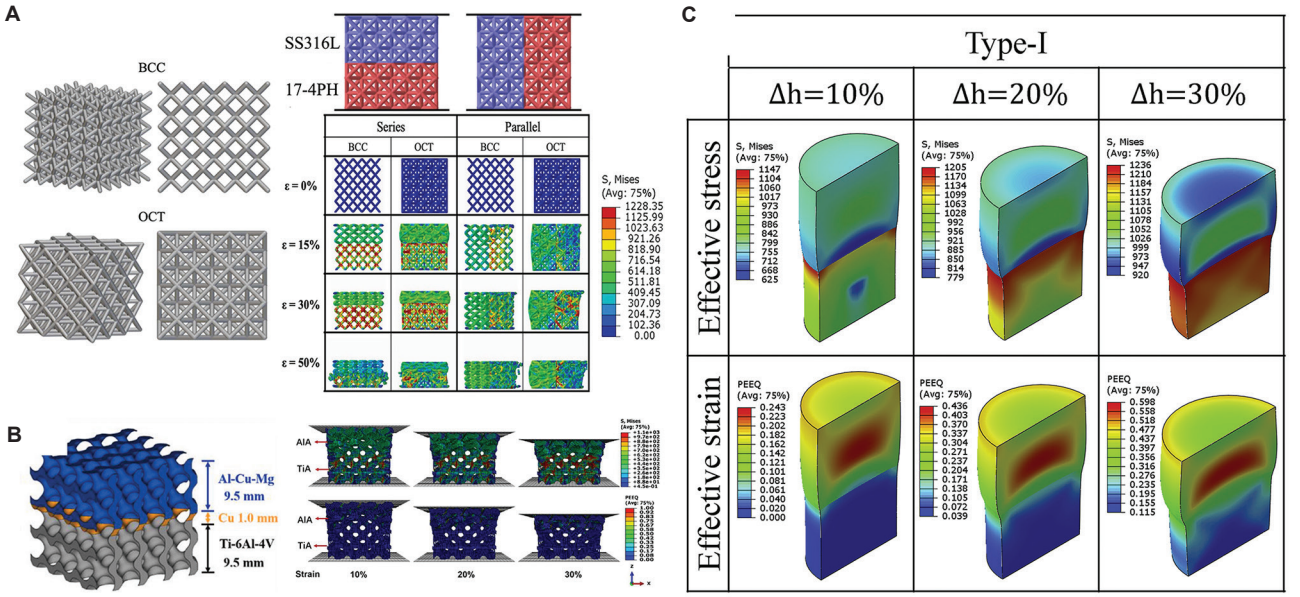

Figure 17. Compression behavior of bimetallic lattice structures fabricated through multi-material laser powder bed fusion (MM-LPBF) and multi-material laser-directed energy deposition (MM-LDED). (A) Finite element modeling-based compression simulation of body-centered cubic and octet truss 17-4PH/SS316L lattice structures fabricated through MM-LPBF;[125] (B) Simulation-based compression test on a gyroid bimetallic Ti-6Al-4V/CuA/Al-Cu-Mg lattice structure fabricated through MM-LPBF;[199] (C) Compression test on a cylindrical P21/SS316L bimetallic structure fabricated using MM-LDED.[166] The finite element analysis results highlight the influence of lattice structure and multi-material additive manufacturing process on deformation behavior under compressive loading

unique challenges compared to mono-material powder bed processing. These challenges primarily stem from the potential for cross-contamination between the materials used in fabrication. In monolithic processing, a single powder material is used across the build plate. Additional recycling steps are necessary to maintain the particle size/shape distribution and chemical composition of the powder, particularly if partial sintering or oxidation has occurred from repeated use. However, no clear standard currently exists to define recycling procedures or specify the required purity of chemical composition after post-processing. This lack of standardization complicates the transition to MM powder recycling, where up to three powder materials may be spatially mixed within a single build plate.

A few efforts have been made to separate powder materials, but none have shown significant success. Sieving can separate powders based on particle size distributions,[175,207,208] but it is ineffective for separating materials with similar particle sizes. Most powders used in LPBF typically fall within a D_{50} size distribution of 10 – 90 μm. As a result, the Gaussian distribution curves of even dissimilar powders overlap at both the upper and lower tails, making clean separation infeasible. Other proposed methods include separation based on relative density (using a particle inertia approach) or magnetic properties. However, all three methods require specific material properties to be effective and cannot be generalized to most powder combinations. To the best of the authors' knowledge, there is currently no comprehensive study on the recycling of leftover powder from MM-LPBF or MM-LDED processes, including the chemical composition analysis of separated materials. This recyclability issue is specific to MM-LPBF and MM-LDED, as there are numerous well-established methods for recycling mono-material powders to control parameters such as powder size distribution,[209-212] chemical composition,[209-211,213,214] flowability,[209-212,214] and morphology.[211-214] Generally, powder reuse introduces additional process uncertainties due to powder degradation. Many studies have reported a moderate reduction in ultimate strength after powder reuse,[211,215,216] while others have found no significant change in mechanical properties following recycling.[217,218] The material consumption and associated costs due to the lack of effective powder recycling methods remain major barriers to the industrial adoption of MMAM. In contrast, wire-fed directed energy deposition and WAAM avoid this issue by using wire-based feedstocks, thus circumventing powder waste altogether. However, the geometric resolution and as-built surface finish provided by these wire-based processes are generally insufficient for many applications unless extensive post-processing is applied.

6.2. In-process monitoring

In-situ process monitoring includes multiple techniques applicable to all MMAM processes, allowing for real-time observation and analysis of the manufacturing process. These methods are essential for assessing the build quality, particularly at the MM interface. *In-situ* monitoring data can also be used to calibrate and inform MM simulations across various length scales, depending on the monitoring technique used.

In-situ monitoring techniques can be broadly categorized into acoustic monitoring, optical imaging, and thermal imaging, and are commonly paired with machine learning algorithms for real-time defect prediction.

Acoustic monitoring utilizes sound waves detected during fabrication as predictive tools to identify internal defects. Acoustic signals generated during processing can be correlated with internal irregularities, enabling the development of AE monitoring systems capable of classifying AE wave patterns associated with specific processing conditions, such as conduction mode, lack-of-fusion pores, and keyhole pore formation.[219] Compared to other *in-situ* methods, this approach is relatively straightforward and particularly useful for detecting internal defects that are otherwise difficult to identify. Acoustic monitoring is commonly combined with complementary optical techniques (e.g., high-speed cameras, IR sensors, photodiodes) to improve detection reliability. One limitation of AE monitoring as a standalone method is the challenge of isolating AE sound waves produced by laser-material interactions from ambient noise generated by the machine or environment.[220] Machine learning algorithms are frequently used to deconvolute these signals, helping to identify and differentiate AE wave patterns associated with defective conditions.[221,222] This approach has been well studied in the context of single-material AM fabrication.[220,223-228]

Build-plate imaging is another widely used *in-situ* technique that monitors the fabrication process on a layer-by-layer basis. High-speed cameras provide real-time feedback on surface quality, layer deposition, and process anomalies such as spatter.[229,230]

Radiographic imaging, including X-ray and computed tomography, offers cross-sectional views of the process, revealing internal structures, voids, and defects.[231] In MMAM, these methods can differentiate most material pairs based on grayscale contrast related to material density. Cross-sectional imaging of the melt pool at metal interfaces provides fundamental insights into melt pool formation mechanisms, supplementing post-process techniques typically used to analyze heat-affected zones. When combined with mesoscale DEM modeling, these techniques can enhance the prediction of melt pool solidification behavior.

Thermal imaging uses IR cameras to capture emitted radiation during the AM process, allowing visualization of temperature gradients, hotspots, and cooling rates. This data is used to identify proper fusion between adjacent layers and detect anomalies with distinct thermal signatures, such as incomplete melting. Thermal maps generated through this method can also be used to calibrate and validate macro-scale process models and simulations, enhancing the understanding of thermally induced distortions and residual stresses.[232] In MMAM, metal matrices often exhibit non-uniform heating and cooling behavior due to differences in material solidification and thermal properties. Thermal imaging can thus serve as an input-control mechanism in real-time monitoring systems to maintain uniform thermal profiles—such as heating/cooling rates or thermal expansion/contraction rates—across the build plate, even in the presence of bimaterial boundaries.[233]

6.3. Standardization of MM testing

Mechanical property characterization tests conducted on monolithic materials fabricated using AM processes typically follow standard testing procedures established for conventionally manufactured specimens. While this approach is suitable for monolithic materials, it is not fully applicable to MMAM due to the unique characteristics of the MM interface between dissimilar materials. The interfacial bonding between two dissimilar materials plays a significant role in determining the failure point and overall mechanical performance of the specimen. Similar to the influence of build orientation in AM, the material deposition configuration significantly affects the mechanical performance of MMAM components. To the authors' knowledge, most experimental studies have not thoroughly investigated deposition configurations to identify optimal strategies for enhancing mechanical performance. For example, Chen *et al.*[58] manufactured SS316L/CuSn10 structures using LPBF with SS316L as the base material and conducted mechanical testing, such as microhardness, tensile, and flexural strength tests. Their tensile testing results indicated that horizontally combined specimens exhibited greater elongation than vertically combined ones, although the UTS was similar in both configurations. Similarly, Dash and Bandyopadhyay[147] fabricated vertically and radially combined SS316L/17-4PH specimens using MM-LDED and observed that radially combined specimens exhibited higher compressive strength than both vertically combined specimens and wrought SS316L. In both cases, mechanical performance

was optimized by strategically selecting the material combination configuration. The absence of standardized guidelines regarding material deposition configuration in MMAM highlights a pressing need to establish testing protocols that account for interfacial bonding strength.

To further assess interfacial strength, testing standards must be adapted to evaluate the mechanical performance of MM specimens in multiple dimensions. A notable gap exists in the literature concerning MMAM structures with complex radial interfaces in the horizontal plane while maintaining vertical consistency.

With the site-specific material deposition enabled by AM, traditional strain measurement techniques may be insufficient. In cases where dissimilar materials are deposited in non-conventional orientations (e.g., horizontally or vertically), data from extensometers, crosshead displacement, or strain gauges may not accurately capture local strain behavior within the specimen. In this context, digital image correlation (DIC) emerges as a valuable tool for strain measurement. DIC enables the acquisition of full-field local strain data across the specimen surface, allowing researchers to detect strain localization, necking, and crack initiation. Beyond these advantages, DIC also provides critical information about interface performance and enables the generation of contour maps across the entire specimen, supporting detailed visualization and quantification of strain behavior.

6.4. Thermo-mechanical modelling (part-scale)

Even though a substantial number of simulations have been conducted on MMAM, the field remains less extensive and well-developed compared to single-material AM. This research gap stems from the developmental and fundamental complexities of MMAM. MMAM introduces additional challenges in parameter selection to achieve ideal melting, mixing, and solidification conditions. In single-material AM, selecting parameters often involves optimizing laser power and scan speed for a given material; however, this approach cannot be applied to MMAM, as it would entail extensive experimental costs and time. To address this, a process simulation framework must be developed to identify reasonable process parameters, mitigate significant defects, and achieve desired cooling rates and microstructures. Such a framework would lower the experimental burden required for case-by-case validation of simulation results. The advancements in high-fidelity PBF simulations and the capability of CFD to deliver detailed, high-resolution results need to be extended to MMAM. The importance of particle-based simulations is attributed to the core understanding of the physical phenomena, such as evaporation, recoil pressure, and surface tension, factors that are currently underrepresented in numerical modeling for MMAM. These phenomena are especially critical at material interfaces, where differing thermal properties of dissimilar materials have a major influence. Beyond advancing particle-based simulation approaches, the simulation of multi-track and multi-layer builds is inevitable for linking microscale behavior to part-scale mechanical performance. Modeling of single- and multi-track and multi-layer in single-material AM has been crucial for understanding defect formation and predicting mechanical properties. This approach needs to be expanded to encompass MMAM. Recent work by Küng *et al.*[234] has begun to address this, employing a two-dimensional PBF model using the Lattice–Boltzmann-based simulation (a class of CFD simulation), as well as the DEM-SPH method.[200] To further accelerate the understanding of the multi-track and multi-layer phenomena, the community is encouraged to investigate the integration of DEM-SPH/optimal transportation meshfree—a particle-based method formulated for simulating solid and fluid flows—to address part-scale size challenges. In single-material AM, SPH has experienced extensive developments due to its algorithmic maturity and established track record, which could serve as a foundation for MMAM. Insights from multi-track and multi-layer approaches can also inform FEA simulations, helping to advance the understanding of MMAM's mechanical behavior. However, as discussed in Section 5, existing FEA simulations for MMAM often rely on assumptions that compromise accuracy when compared to experimental data. These assumptions stated throughout the studies will not provide accurate results when compared to the experimental data. Assumptions and simplifications such as a smooth, roughness-free surface, a defect-free or crack-free interface, and a well-bonded interface will yield inaccurate results in MMAM, due to their influence on mechanical behavior. One way to address these limitations is to integrate X-ray micro-computed tomography imaging data as inputs into modeling workflows, enabling more accurate mechanical behavior predictions. In 2024, Auenhammer *et al.*[235] proposed an approach to overcome the image-based numerical modeling for carbon fiber using an open-source Python script.[236] While the method has some drawbacks, it offers a promising future direction for extending image-based numerical modeling to both single- and MMAM.

6.5. Future direction

MM-AM has emerged as a transformative approach in engineering, enabling the integration of distinct metals within a single component to harness their complementary properties. However, when it comes to discrete metal transitions, such as joining high-conductivity Cu to high-strength steel or combining corrosion-resistant

Ni alloys with lightweight Al, the process introduces significant challenges. These challenges stem from the intrinsic differences in thermophysical properties that were discussed in detail in this article, such as melting points, thermal conductivity, and CTE, often leading to residual stresses, cracking, and brittle intermetallic phase formation. Addressing these issues represents a critical frontier in MMAM research and development.

A promising future direction lies in the deliberate design and fabrication of compositionally graded interlayers and engineered interface architectures that facilitate smooth transitions between dissimilar metals. Instead of abrupt material changes—which may offer advantages in certain applications but often introduce sites of mechanical weakness or metallurgical incompatibility—graded transitions and/or IBLs allow for gradual variations in composition and microstructure. These interlayers can mitigate thermal mismatch, reduce stress concentrations, and suppress the formation of brittle intermetallics, thereby enabling strong, defect-free metallurgical bonding. To advance this strategy, several enabling technologies and research methodologies must be leveraged. Computational alloy design tools informed by CALPHAD databases and density functional theory can predict phase stability and guide the development of transition compositions that optimize bonding without compromising functionality. Coupled with this, data-driven approaches such as machine learning can be employed to refine the process parameters in real time, using data from prior builds to predict optimal conditions for layer deposition and fusion quality.

Another key enabler that was discussed in this section is *in situ* monitoring during the printing process. Techniques such as optical pyrometry, thermal imaging, and AE sensing can provide real-time feedback on the thermal environment and melt pool dynamics, allowing immediate adjustment of laser power, scan speed, or feedstock composition. These monitoring strategies can provide valuable data for post-build quality assurance and digital twin development. Furthermore, multiscale modeling and simulation play a vital role in predicting the evolution of thermal gradients, phase transformations, and stress fields across the transition zone. By simulating the build process from the microstructural to the component scale, researchers can anticipate failure modes and iterate on interface designs before fabrication. The successful implementation of discrete metal transitions through MMAM unlocks a wide range of application opportunities. For example, heat exchangers can be designed with Cu-rich regions for high thermal conductivity seamlessly bonded to SS for structural support and corrosion resistance.

In aerospace and nuclear industries, components could be fabricated with spatially varying properties to withstand both mechanical loads and radiation damage. Biomedical implants could combine biocompatible surfaces with load-bearing cores, all within a single manufacturing process. In conclusion, the future of MMAM with discrete metal transitions hinges on the convergence of material science, advanced modeling, real-time sensing, and data-driven control. By developing intelligent interlayer designs and integrating process monitoring with adaptive manufacturing strategies, the field is positioned to overcome longstanding metallurgical barriers and enable a new generation of multifunctional, high-performance components.

Abbreviations

3D	Three-dimensional
AE	Acoustic emission
AM	Additive manufacturing
BCC	Body-centered cubic
CALPHAD	Calculation of phase diagram
CAD	Computer-aided design
CFD	Computational fluid dynamics
CFD-DEM	Computational fluid dynamics – discrete element method
CFD-VOF	Computational fluid dynamics – volume of fluid
CTE	Coefficient of thermal expansion
DEM	Discrete element method
DEM-SPH	Discrete element method – smoothed particle hydrodynamics
DIC	Digital image correlation
EB-PBF	Electron beam powder bed fusion
EBSD	Electron backscatter diffraction
EDS	Energy dispersive spectroscopy
F_{com}	Compression
FCC	Face-centered cubic
FEA	Finite element analysis
F_{fat}	Fatigue
F_{shear}	Shear
F_{therm}	Thermal diffusivity
F_{wear}	Wear performance
FGM	Functionally graded material
FGM-LDED	Functionally graded material laser-direct energy deposition
FSW	Friction stir welding
HV	Hardness Vickers
IBL	Intermediate bonding layer
IMC	Intermetallic compound
IR	Infrared
LDED	Laser-direct energy deposition
LPBF	Laser powder bed fusion
LAMMPS	Large-scale atomic/molecular massively parallel simulator

MM	Multi-material
MMAM	Multi-material additive manufacturing
MM-LDED	Multi-material laser direct energy deposition
MM-LPBF	Multi-material laser powder bed fusion
MM-WAAM	Multi-material wire-arc additive manufacturing
NASA	National Aeronautics and Space Administration
PBB	Powder bed behavior
P-S-P	Process-structure-property
QR	Quick response
SPH	Smoothed particle hydrodynamics
UFS	Ultimate flexural strength
UTS	Ultimate tensile strength
WAAM	Wire-arc additive manufacturing
XRD	X-ray diffraction
YS	Yield strength

Acknowledgments

None.

Funding

Saneej N. Samad and Nadia Kouraytem would like to acknowledge the support by the U.S. Nuclear Regulatory Commission under award number 31310024M0039, and startup funds from USU. Guha Manogharan would like to acknowledge the support by the NSF CMMI-EDSE award #213069, and student support from the Applied Research Laboratory (ARL) at the Pennsylvania State University for their funding contribution through the Walker Fellowship.

Conflict of interest

The authors declare they have no competing interests.

Author contributions

Conceptualization: Nadia Kouraytem, Guha Manogharan
Writing – original draft: Saneej N. Samad, Jacklyn Griffis
Writing – review & editing: All authors

Ethics approval and consent to participate

Not applicable.

Consent for publication

Not applicable.

Availability of data

As this is a review article, no primary research results, data, software, or code have been included.

References

1. Bakewell J. *Customising Production*. Berlin: Springer; 2019.
2. Csere C. How Automakers Are 3D-Printing Parts for Production Cars (and Classics). How Automakers are 3D-Printing Parts for Production Cars (and Classics); 2018. Available from: https://www.caranddriver.com/features/columns/a20684648/how-automakersare-3d-printing-parts-for-production-cars-and-classics [Last accessed on 2024 Sep 28].
3. Gandy D, Albert M. Small Modular Reactor Pressure Vessel Manufacturing and Fabrication Technology Development; 2020. Available from: https://www.energy.gov/sites/default/files/2021/03/f83/ne-amm-david-gandy-1-030221.pdf [Last accessed on 2024 Sep 28].
4. Ellis JK. 3D-Printed Nuclear Reactor Promises Faster, more Economical Path ToNuclear Energy; 2020. Available from: https://www.ornl.gov/news/3d-printed-nuclear-reactor-promisesfaster-more-economical-path-nuclear-energy [Last accessed on 2024 Sep 28].
5. Zhong Y, Rännar LE, Liu L, *et al.* Additive manufacturing of 316L stainless steel by electron beam melting for nuclear fusion applications. *J Nucl Mater*. 2017;486:234-245.
6. McMahon M. Metal AM in the Aerospace Sector: From Early Successes to The transformation of an Industry; 2023. Available from: https://www.metal-am.com/articles/metal-am-inthe-aerospace-sector-from-early-successes-to-the-transformation-of-an-industry [Last accessed on 2024 Sep 28].
7. Russell R, Wells D, Waller J, *et al.* Qualification and certification of metal additive manufactured hardware for aerospace applications. In: *Additive Manufacturing for the Aerospace Industry*. Netherlands: Elsevier; 2019. p. 33-66.
8. González-Barrio H, Calleja-Ochoa A, Lamikiz A, López De Lacalle LN. Manufacturing processes of integral blade rotors for turbomachinery, processes and new approaches. *Appl Sci*. 2020;10(9):3063.
9. Radhika C, Shanmugam R, Ramoni M, Gnanavel BK. A review on additive manufacturing for aerospace application. *Mater Res Exp.* 2024;11(2):022001.
10. Jalui S, Xuan Y, Manogharan G, O'Connor J. Development of a method for shape optimization for a gas turbine fuel injector design using metal-additive manufacturing. *J Eng Gas Turb Power*. 2025;147(1):011023.
11. He P, Sun C, Wang Y. Material distortion in laser-based additive manufacturing of fuel cell component: Three-dimensional numerical analysis. *Addit Manuf.* 2021;46:102188.
12. Hossain A, Pellicotte JT, Stewart M. A calibration approach for accelerated creep testing for electron beam melted (EBM) Ti-6Al-4V using the WCS model. In: *Industrial and Cogeneration; Manufacturing Materials and Metallurgy*. Vol. 8. Boston, Massachusetts, USA: American Society of Mechanical Engineers; 2023. p. V008T17A023.
13. Metal AM. Nexxt Spine Develops Additively Manufactured Spinal Implants using MTS Test Systems; 2019. Available from: https://www.metal-am.com/nexxt-spine-develops-

additivelymanufactured-spinal-implants-using-mts-test-systems [Last accessed on 2025 Sep 28].

14. Harrysson OLA, Marcellin-Little DJ, Horn TJ. Applications of metal additive manufacturing in veterinary orthopedic surgery. *JOM*. 2015;67(3):647-654.

15. Vilardell AM, Takezawa A, Du Plessis A, *et al.* Topology optimization and characterization of Ti6Al4V ELI cellular lattice structures by laser powder bed fusion for biomedical applications. *Mater Sci Eng A*. 2019;766:138330.

16. Tilton M, Lewis GS, Hast MW, Fox E, Manogharan G. Additively manufactured patient-specific prosthesis for tumor reconstruction: Design, process, and properties. *PLoS One*. 2021;16(7):e0253786.

17. Tilton M, Borjali A, Griffis JC, Varadarajan KM, Manogharan GP. Fatigue properties of Ti-6Al-4V TPMS scaffolds fabricated via laser powder bed fusion. *Manuf Lett.* 2023;37:32-38.

18. Shuai C, Li D, Yao X, Li X, Gao C. Additive manufacturing of promising heterostructure for biomedical applications. *Int J Extreme Manuf.* 2023;5(3):032012.

19. F42 Committee. Terminology for Additive Manufacturing - General Principles -Terminology. United States: ASTM.

doi: 10.1520/F3177-21

20. Sun Z, Chueh YH, Li L. Multiphase mesoscopic simulation of multiple and functionally gradient materials laser powder bed fusion additive manufacturing processes. *Addit Manuf*. 2020;35:101448.

21. He C, Ramani KS, Okwudire CE. An intelligent scanning strategy (SmartScan) for improved part quality in multi-laser PBF additive manufacturing. *Addit Manuf*. 2023;64:103427.

22. Aerosint Company. Aerosint. Available from: https://aerosint.com/printing-services [Last accessed on 2024 Apr 15].

23. Gu H, Wei C, Li L, *et al.* Multi-physics modelling of molten pool development and track formation in multi-track, multi-layer and multi-material selective laser melting. *Int J Heat Mass Transfer*. 2020;151:119458.

24. Toursangsaraki M. A Review of Multi-material and Composite Parts Production by Modified Additive Manufacturing Methods [Preprint]; 2018.

doi: 10.48550/arxiv.1808.01861

25. Li Y, Feng Z, Hao L, *et al.* A review on functionally graded materials and structures via additive manufacturing: From multi-scale design to versatile functional properties. *Adv Mater Technol*. 2020;5(6):1900981.

26. Mirzaali MJ, Nava AH, Gunashekar D, Nouri-Goushki M, Doubrovski EL, Zadpoor AA. Fracture behavior of bio-inspired functionally graded soft-hard composites made by multi-material 3D printing: The case of colinear cracks. *Materials* (*Basel*). 2019;12(17):2735.

27. Guessasma S, Nouri H, Roger F. Microstructural and mechanical implications of microscaled assembly in droplet-based multi-material additive manufacturing. *Polymers* (*Basel*). 2017;9(12):372.

doi: 10.3390/polym9080372

28. Vaezi M, Chianrabutra S, Mellor B, Yang S. Multiple material additive manufacturing Part 1: A review: This review paper covers a decade of research on multiple material additive manufacturing technologies which can produce complex geometry parts with different materials. *Virt Phys Prototyp.* 2013;8(1):19-50.

29. Sheydaeian E. *Systems, Materials, and Methodologies for Multi-material Hybrid Additive Manufacturing Functionally Graded Structures*. PhD thesis, University of Waterloo, Ontario, Canada; 2017.

30. Putra NE, Mirzaali MJ, Apachitei I, Zhou J, Zadpoor AA. Multi-material additive manufacturing tech- nologies for Ti-, Mg-, and Fe-based biomaterials for bone substitution. *Acta Biomater*. 2020;109:1-20.

doi: 10.1016/j.actbio.2020.03.037

31. Doubrovski EL, Tsai EY, Dikovsky D, Geraedts JMP, Herr H, Oxman N. Voxel-based fabrication through material property mapping: A design method for bitmap printing. *Comput Aided Design*. 2015;60:3-13.

32. Skylar-Scott MA, Mueller J, Visser CW, Lewis JA. Voxelated soft matter via multima- terial multinozzle 3D printing. *Nature*. 2019;575(7782):330-335.

33. Griffis JC, Shahed K, Meinert K, Yilmaz B, Lear M, Manogharan G. Multi-material laser powder bed fusion: Effects of build orientation on defects, material structure and mechanical properties. *NPJ Adv Manuf*. 2025;2(1):5.

34. Nazir A, Gokcekaya O, Billah KM, *et al.* Multi-material additive manufacturing: A systematic review of design, properties, applications, challenges, and 3D printing of materials and cellular metamaterials. *Mater Design*. 2023;226:111661.

35. Singh AW, Kapil S, Das M. A comprehensive review of the methods and mechanisms for powder feedstock handling in directed energy deposition. *Addit Manuf*. 2020;35:101388.

36. Luo X, Chang W, Zhong W, Wardle F. Hybrid machine tool design. In: *Hybrid Machining*. Netherlands: Elsevier; 2018. p. 197-214.

37. Gibson I, Rosen D, Stucker B. Directed energy deposition processes. In: *Additive Manufacturing Technologies*. New York: Springer New York; 2015. p. 245-268.

38. Tanwar RS, Jhavar S. A review on additive manufacturing of SS-Ni multi-material fabrication. In: *Materials Today: Proceedings*; 2023. p. S2214785323010866.

39. Wang D, Liu L, Deng G, *et al.* Recent progress on additive manufacturing of multi-material structures with laser powder bed fusion. *Virt Phys Prototyp.* 2022;17(2):329-365.

40. Wei C, Li L. Recent progress and scientific challenges in multi-material additive manufacturing via laser- based powder bed fusion. *Virt Phys Prototyp.* 2021;16(3):347-371.

41. Wu Z, Wilson-Heid AE, Joey Griffiths R, Elton ES. A review on experimentally observed mechanical and microstructural characteristics of interfaces in multi-material laser powder bed fusion. *Front Mech Eng*. 2023;9:1087021.

42. Sun Z, Ion JC. Laser welding of dissimilar metal combinations. *J Mater Sci*. 1995;30(17):4205-4214.

43. Mai TA, Spowage AC. Characterisation of dissimilar joints in laser welding of steel-kovar, copper-steel and copper-aluminium. *Mater Sci Eng A*. 2004;374(1-2):224-233.

44. Estrin Y, Beygelzimer Y, Kulagin R, *et al.* Architecturing materials at mesoscale: Some current trends. *Mater Res Lett*. 2021;9(10):399-421.

45. Gradl PR, Protz C, Fikes J, *et al.* Lightweight thrust chamber assemblies using multi-alloy additive manufacturing and composite overwrap. In: *AIAA Propulsion and Energy 2020 Forum*, VIRTUAL EVENT. USA: American Institute of Aeronautics and Astronautics; 2020.

46. Gradl PR, Protz CS, Ellis DL, Greene SE. Progress in Additively Manufactured Copper-Alloy GRCop-84, GRCop-42, and bimetallic combustion chambers for liquid rocket engines. In: *International Astronautical Congress*.

47. Marques A, Cunha A, Gasik M, Carvalho O, Silva FS, Bartolomeu F. Inconel 718–copper parts fabricated by 3D multi-material laser powder bed fusion: A novel technological and designing approach for rocket engine. *Int J Adv Manuf Technol*. 2022;122(3):2113-2123.

48. Bhaduri D, Penchev P, Essa K, *et al.* Evaluation of surface/interface quality, microstructure and mechanical properties of hybrid additive- subtractive aluminium parts. *CIRP Ann*. 2019;68(1):237-240.

49. Wits WW, Amsterdam E. Graded structures by multi-material mixing in laser powder bed fusion. *CIRP Ann*. 2021;70(1):159-162.

50. Nguyen DS, Park HS, Lee CM. Applying selective laser melting to join Al and Fe: An investigation of dissimilar materials. *Appl Sci*. 2019;9(15):3031.

51. Andreiev A, Hoyer KP, Dula D, *et al.* Laser beam melting of functionally graded materials with application-adapted tailoring of magnetic and mechanical performance. *Mater Sci Eng A*. 2021;822:141662.

52. Bartolomeu F, Costa MM, Alves N, Miranda G, Silva FS. Additive manufacturing of NiTi-Ti6Al4V multi- material cellular structures targeting orthopedic implants. *Optics Lasers Eng*. 2020;134:106208.

53. Tan C, Zhou K, Kuang T. Selective laser melting of tungsten-copper functionally graded material. *Mater Lett*. 2019;237:328-331.

54. Wei C, Liu L, Gu Y, *et al.* Multi-material additive- manufacturing of tungsten - copper alloy bimetallic structure with a stainless-steel interlayer and associated bonding mechanisms. *Addit Manuf*. 2022;50:102574.

55. Wei C, Sun Z, Huang Y, Li L. Embedding anti-counterfeiting features in metallic components via multiple material additive manufacturing. *Addit Manuf.* 2018;24:1-12.

56. Liu L, Wang D, Deng G, *et al.* Interfacial characteristics and formation mechanisms of copper-steel multimaterial structures fabricated via laser powder bed fusion using different building strategies. *Chin J Mech Eng Addit Manuf Front*. 2022;1(3):100045.

57. Wei C, Liu L, Cao H, *et al.* Cu10Sn to Ti6Al4V bonding mechanisms in laser-based powder bed fusion multiple material additive manufacturing with different build strategies. *Addit Manuf.* 2022;51:102588.

58. Chen J, Yang Y, Song C, Zhang M, Wu S, Wang D. Interfacial microstructure and mechanical properties of 316L/CuSn10 multi-material bimetallic structure fabricated by selective laser melting. *Mater Sci Eng A*. 2019;752:75-85.

59. Schneck M, Horn M, Schmitt M, Seidel C, Schlick G, Reinhart G. Review on additive hybrid-and multi-material-manufacturing of metals by powder bed fusion: State of technology and development potential. *Prog Addit Manuf*. 2021;6(4):881-894.

60. Ansari M, Jabari E, Toyserkani E. Opportunities and challenges in additive manufacturing of functionally graded metallic materials via powder-fed laser directed energy deposition: A review. *J Mater Process Technol*. 2021;294:117117.

61. Bhavar V, Kattire P, Thakare S, Patil S, Singh R. A review on functionally gradient materials (FGMs) and their applications. *IOP Conf Ser Mater Sci Eng*. 2017;229:012021.

62. Mahmoud D, Elbestawi M. Lattice structures and functionally graded materials applications in additive manufacturing of orthopedic implants: A review. *J Manuf Mater Process*. 2017;1(2):13.

63. Ren L, Wang Z, Ren L, Han Z, Liu Q, Song Z. Graded biological materials and additive manufacturing technologies for producing bioinspired graded materials: An overview. *Compos Part B Eng*. 2022;242:110086.

64. Saleh B, Jiang J, Fathi R, *et al.* 30 Years of functionally graded materials: An overview of manufacturing methods, Applications and Future Challenges. *Compos Part B Eng.* 2020;201:108376.

65. Xu F, Zhang X, Zhang H. A review on functionally graded structures and materials for energy absorption. *Eng Struct.* 2018;171:309-325.

66. Wei C, Zhang Z, Cheng D, Sun Z, Zhu M, Li L. An overview of laser-based multiple metallic material additive manufacturing: From macro- to micro-scales. *Int J Extreme Manuf*. 2021;3(1):012003.

67. Ostolaza M, Arrizubieta JI, Lamikiz A, Plaza S, Ortega N. Latest developments to manufacture metal matrix composites and functionally graded materials through AM: A state-of-the-art review. *Materials* (*Basel*). 2023;16(4):1746.

doi: 10.3390/ma16041746

68. Ma Z, Liu W, Li W, *et al.* Additive manufacturing of functional gradient materials: A review of research progress and challenges. *J Alloys Compd*. 2024;971:172642.

69. Ju Y, Li C, Yang X, Ba L, Wang Y, Di X. Recent progress on additive manufacturing of steel-based functionally graded materials. *Mater Today Commun*. 2024;40:109953.

70. Sanjeeviprakash K, Rajesh Kannan A, Siva Shanmugam N. Additive manufacturing of metal-based functionally graded materials: Overview, recent advancements and challenges. *J Braz Soc Mech Sci Eng*. 2023;45(5):241.

71. Srivastava M, Rathee S, Tiwari A, Dongre M. Wire arc additive manufacturing of metals: A review on processes, materials and their behaviour. *Mater Chem Phys*. 2023;294:126988.

72. Yan L, Chen Y, Liou F. Additive manufacturing of functionally graded metallic materials using laser metal deposition. *Addit Manuf*. 2020;31:100901.

73. Dev Singh D, Arjula S, Raji Reddy A. Functionally graded materials manufactured by direct energy deposition: A review. *Mater Today Proc*. 2021;47:2450-2456.

74. Tyagi SA, Manjaiah M. Laser additive manufacturing of titanium-based functionally graded materials: A review. *J Mater Eng Perform*. 2022;31(8):6131-6148.

75. Zhang R, Jiang F, Xue L, Yu J. Review of additive manufacturing techniques for large-scale metal functionally graded materials. *Crystals*. 2022;12(6):858.

76. Ghanavati R, Naffakh-Moosavy H. Additive manufacturing of functionally graded metallic materials: A review of experimental and numerical studies. *J Mater Res Technol*. 2021;13:1628-1664.

77. Karimzadeh M, Basvoju D, Vakanski A, Charit I, Xu F, Zhang X. Machine learning for additive manufacturing of functionally graded materials. *Materials*. 2024;17(15):3673.

78. Yang L, Miyanaji H, Ram DJ, Zandinejad A, Zhang S. Functionally graded ceramic based materials using additive manufacturing: Review and progress. In: Shimamura K, Kirihara S, Akedo J, Ohji T, Naito M, editors. *Ceramic Transactions Series*. 1st ed., Vol. CCLVIII. United States: Wiley; 2016. p. 43-55.

79. Delacroix T, Lomello F, Schuster F, *et al.* Influence of build characteristics and chamber oxygen concentration on powder degradation in laser powder bed fusion. *Powder Technol*. 2023;416:11823.

80. Lu SP, Fujii H, Nogi K, Sato T. Effect of oxygen content in He–O_2 shielding gas on weld shape in ultra-deep penetration TIG. *Sci Technol Weld Join*. 2007;12(8):689-695.

81. Li R, Liu J, Shi Y, Wang L, Jiang W. Balling behavior of stainless steel and nickel powder during selective laser melting process. *Int J Adv Manuf Technol*. 2012;59(9-12):1025-1035.

82. Wang D, Wu S, Fu F, *et al.* Mechanisms and characteristics of spatter generation in SLM processing and its effect on the properties. *Mater Design*. 2017;117:121-130.

83. Leung CLA, Marussi S, Towrie M, Atwood RC, Withers PJ, Lee PD. The effect of powder oxidation on defect formation in laser additive manufacturing. *Acta Mater.* 2019;166:294-305.

84. Mertens R, Dadbakhsh S, Van Humbeeck J, Kruth JP. Application of base plate preheating during selective laser melting. *Proc CIRP.* 2018;74:5-11.

85. Guan J, Wang Q. Laser powder bed fusion of dissimilar metal materials: A review. *Materials*. 2023;16(7):2757.

86. Dzogbewu TC, Du Preez WB. Additive manufacturing of Ti-based intermetallic alloys: A review and conceptualization of a next-generation machine. *Materials*. 2021;14(15):4317.

87. International Organization for Standardization. *Additive Manufacturing-General Principles-Terminology.* United Kingdom: ISO/ASTM 52900; 2018.

88. Hasanov S, Alkunte S, Rajeshirke M, *et al.* Review on additive manufacturing of multi-material parts: Progress and challenges. *J Manuf Mater Process*. 2021;6(1):4.

89. Verma A, Kapil A, Klobčar D, Sharma A. A review on multiplicity in multi-material additive manufacturing: Process, capability, scale, and structure. *Materials*. 2023;16(15):5246.

90. Thompson SM, Bian L, Shamsaei N, Yadollahi A. An overview of Direct Laser Deposition for additive manufacturing; Part I: Transport phenomena, modeling and diagnostics. *Addit Manuf*. 2015;8:36-62.

91. Ning J, Zhu L, Wang S, *et al.* Printability disparities in heterogeneous material combinations via laser directed energy deposition: A comparative study. *Int J Extreme Manuf*. 2024;6(2):025001.

92. Feenstra DR, Banerjee R, Fraser HL, Huang A, Molotnikov A, Birbilis N. Critical review of the state of the art in multi-material fabrication via directed energy deposition. *Curr Opin Solid State Mater Sci*. 2021;25(4):100924.

93. Svetlizky D, Zheng B, Vyatskikh A, *et al.* Laser-based directed energy deposition (DED-LB) of advanced materials. *Mater Sci Eng A*. 2022;840:142967.

94. Frank Medina. Fundamental of Additive Manufacturing for Production. Available from: https://www.nrc.gov/docs/ml1816/ml18164a226.pdf [Last accessed on 2025 May 02].

95. Svetlizky D, Das M, Zheng B, *et al.* Directed energy deposition (DED) additive manufacturing: Physical characteristics, defects, challenges and applications. *Mater Today*. 2021;49:271-295.

96. Xie J, Huang Z, Lu H, Zheng B, Xu X, Lei J. Additive manufacturing of tantalum-zirconium alloy coating for corrosion and wear application by laser directed energy deposition on Ti6Al4V. *Surf Coat Technol*. 2021;411:127006.

97. Rai AK, Srinivasulu B, Paul CB, *et al.* Development of thick SiC coating on thin wall tube of zircaloy-4 using laser based directed energy deposition technique. *Surf Coat Technol*. 2020;398:126088.

98. Michael Wilson J, Piya C, Shin YC, Zhao F, Ramani K. Remanufacturing of turbine blades by laser direct deposition with its energy and environmental impact analysis. *J Clean Prod*. 2014;80:170-178.

99. Saboori A, Aversa A, Marchese G, Biamino S, Lombardi M, Fino P. Application of directed energy deposition-based additive manufacturing in repair. *Appl Sci*. 2019;9(16):3316.

100. DebRoy HL, Wei JS, Zuback T, *et al.* Additive manufacturing of metallic components-Process, structure and properties. *Prog Mater Sci*. 2018;92:112-224.

101. Dhanola A, Prasad DS. A comprehensive review of wire arc additive manufacturing for metallic functionally graded materials. *Eng Res Express*. 2024;6(4):042501.

102. Bandyopadhyay A, Heer B. Additive manufacturing of multi-material structures. *Mater Sci Eng R Rep*. 2018;129:1-16.

103. Vimal KEK, Naveen Srinivas M, Rajak S. Wire arc additive manufacturing of aluminium alloys: A review. *Mater Today Proc*. 2021;41:1139-1145.

104. Ding D, Pan Z, Cuiuri D, Li H. Wire-feed additive manufacturing of metal components: Technologies, developments and future interests. *Int J Adv Manuf Technol*. 2015;81(1-4):465-481.

105. Chen Z, Yuan L, Pan Z, *et al.* A comprehensive review and future perspectives of simulation approaches in wire arc additive manufacturing (WAAM). *Int J Extreme Manuf*. 2025;7(2):022016.

106. Reichardt A, Shapiro AA, Otis R, *et al.* Advances in additive manufacturing of metal-based functionally graded materials. *Int Mater Rev*. 2021;66(1):1-29.

107. Akinlabi ET, Akinlabi SA. Friction stir welding of dissimilar metals. In: *Advances in Friction-Stir Welding and Processing*. Netherlands: Elsevier; 2014. p. 241-293.

108. Sun Z, Karppi R. The application of electron beam welding for the joining of dissimilar metals: An overview. *J Mater Process Technol*. 1996;59(3):257-267.

109. Kah P, Shrestha M, Martikainen J. Trends in joining dissimilar metals by welding. *Appl Mechan Mater*. 2013;440:269-276.

110. Powell D, Rennie AEW, Geekie L, Burns N. Understanding powder degradation in metal additive manufacturing to allow the upcycling of recycled powders. *J Clean Prod*. 2020;268:122077.

111. Renderos M, Girot F, Lamikiz A, Torregaray A, Saintier N. Ni based powder reconditioning and reuse for LMD process. *Phys Proc*. 2016;83:769-777.

112. Wang P, Nai MLS, Ng FL, *et al.* Revealing mechanisms underlying powder reusability of Ti-48Al-2Cr-2Nb intermetallic in electron beam powder bed fusion process. *Addit Manuf*. 2022;59:103155.

113. Tang Y, Zhou Y, Hoff T, Garon M, Zhao YF. Elastic modulus of 316 stainless steel lattice structure fabricated via binder jetting process. *Mater Sci Technol*. 2016;32(7):648-656.

114. McGeehan O, Oldfield S, Wilks J, Mawby J, Linaker L. *Testing and Analysis of Additive Manufactured Parts from Partially Recycled Powder*. MEng Thesi, Liverpool John Moores University, Liverpool; 2018.

115. Del Re F, Contaldi V, Astarita A, *et al.* Statistical approach for assessing the effect of powder reuse on the final quality of AlSi10Mg parts produced by laser powder bed fusion additive manufacturing. *Int J Adv Manuf Technol*. 2018;97(5-8):2231-2240.

116. Seyda V, Kaufmann N, Emmelmann C. Investigation of aging processes of Ti-6Al-4 V powder material in laser melting. *Phys Proc*. 2012;39:425-431.

117. Carroll PA, Pinkerton A, Allen J, *et al.* The effect of powder recycling in direct metal laser deposition on powder and manufactured part characteristics. In: *Proceedings of the AVT-139 Specialists Meeting on Cost Effective Manufacture via Net Shape Processing*; 2006. p. 1-8.

118. Lanzutti A, Marin E. The challenges and advances in recycling/re-using powder for metal 3D printing: A comprehensive review. *Metals*. 2024;14(8):886.

119. Mostafaei A, Zhao C, He Y, *et al.* Defects and anomalies in powder bed fusion metal additive manufacturing. *Curr Opin Solid State Mater Sci*. 2022;26(2):100974.

120. Everton SK, Hirsch M, Stravroulakis P, Leach RK, Clare AT. Review of *in-situ* process monitoring and *in-situ* metrology for metal additive manufacturing. *Mater Design*. 2016;95:431-445.

121. Grasso M, Colosimo BM. Process defects and *in situ* monitoring methods in metal powder bed fusion: A review. *Meas Sci Technol*. 2017;28(4):044005.

doi: 10.1088/1361-6501/aa5c4f

122. Sahasrabudhe H, Harrison R, Carpenter C, Bandyopadhyay A. Stainless steel to titanium bimetallic structure using LENS™. *Addit Manuf*. 2015;5:1-8.

doi: 10.1016/j.addma.2014.10.002

123. Tey CF, Tan X, Sing SL, Yeong WY. Additive manufacturing of multiple materials by selective laser melting: Ti-alloy to stainless steel via a Cu-alloy interlayer. *Addit Manufact*. 2020;31:100970.

doi: 10.1016/j.addma.2019.100970

124. Watanabe I, Sun Z, Kitano H, Goto K. Multiscale analysis of

mechanical behavior of multilayer steel structures fabricated by wire and arc additive manufacturing. *Sci Technol Adv Mater.* 2020;21(1):461-470.

doi: 10.1080/14686996.2020.1788908

125. McDonnell B, Errico V, Posa P, *et al.* Bi-metallic lattice structures manufactured via an intralayer multi-material powder bed fusion method. *Addit Manufact*. 2024;89:104301.

doi: 10.1016/j.addma.2024.104301

126. Bettencourt CJ, Kouraytem N. Microstructural characterization of the transition in SS316L and IN625 bimetallic fabricated using hybrid additive manufacturing. *JOM*. 2023;75(12):5079-5087.

doi: 10.1007/s11837-023-06119-4

127. Ghanavati R, Naffakh-Moosavy H, Moradi M, Eshraghi M. Printability and microstructure of directed energy deposited SS316l-IN718 multi-material: Numerical modeling and experimental analysis. *Sci Rep.* 2022;12(1):16600.

doi: 10.1038/s41598-022-21077-8

128. Wei C, Li L, Zhang X, Chueh YH. 3D printing of multiple metallic materials via modified selective laser melting. *CIRP Ann*. 2018;67(1):245-248.

doi: 10.1016/j.cirp.2018.04.096

129. Bodner SC, Van De Vorst LT, Zalesak J, *et al.* Inconel-steel multilayers by liquid dispersed metal powder bed fusion: Microstructure, residual stress and property gradients. *Addit Manufact*. 2020;32:101027.

doi: 10.1016/j.addma.2019.101027

130. Yusuf SM, Zhao X, Yang S, Gao N. Interfacial characterisation of multi-material 316L stainless steel/Inconel 718 fabricated by laser powder bed fusion. *Mater Lett.* 2021;284:128928.

doi: 10.1016/j.matlet.2020.128928

131. Mei X, Wang X, Peng Y, *et al.* Interfacial characterization and mechanical properties of 316L stainless steel/inconel 718 manufactured by selective laser melting. *Mater Sci Eng A*. 2019;758:185-191.

doi: 10.1016/j.msea.2019.05.011

132. Chen N, Khan HA, Wan Z, *et al.* Microstructural characteristics and crack formation in additively manufactured bimetal material of 316L stainless steel and Inconel 625. *Addit Manufact*. 2020;32:101037.

doi: 10.1016/j.addma.2020.101037

133. Ahsan MRU, Fan X, Seo GJ, *et al.* Microstructures and mechanical behavior of the bimetallic additively-manufactured structure (BAMS) of austenitic stainless steel and Inconel 625. *J Mater Sci Technol*. 2021;74:176-188.

doi: 10.1016/j.jmst.2020.10.001

134. Dharmendra C, Shakerin S, Janaki Ram GD, Mohammadi M. Wire-arc additive manufacturing of nickel aluminum bronze/stainless steel hybrid parts - interfacial characterization, prospects, and problems. *Materialia*. 2020;13:100834.

doi: 10.1016/j.mtla.2020.100834

135. Ghanavati R, Naffakh-Moosavy H, Moradi M, *et al.* Design optimization for defect-free AISI 316 L/IN718 functionally graded materials produced by laser additive manufacturing. *Mater Characterization*. 2025;220:114697.

doi: 10.1016/j.matchar.2024.114697

136. Stair J, Webler BA, Beuth JL, De Boer MP. Demonstration and analysis of conditions to obtain a high strength inconel 625 to stainless steel 304l interface by directed energy deposition. *Metall Mater Trans A*. 2024;55(7):2186-2199.

doi: 10.1007/s11661-024-07413-9

137. Li L, Shi Q, Yang S. *In-situ* bonding of horizontal bimetallic interface by laser offset during laser powder bed fusion of copper/nickel multi-material structures and underlying thermodynamic mechanisms. *J Mater Process Technol*. 2025;339:118831.

doi: 10.1016/j.jmatprotec.2025.118831

138. Chen WY, Zhang X, Li M, Xu R, Zhao C, Sun T. Laser powder bed fusion of inconel 718 on 316 stainless steel. *Addit Manuf*. 2020;36:101500.

doi: 10.1016/j.addma.2020.101500

139. Meyer I, Oel M, Ehlers T, Lachmayer R. Additive manufacturing of multi-material parts - design guidelines for manufacturing of 316L/CuCrZr in laser powder bed fusion. *Heliyon*. 2023;9(8):e18301.

doi: 10.1016/j.heliyon.2023.e18301

140. Bai Y, Zhang J, Zhao C, Li C, Wang H. Dual interfacial characterization and property in multi-material selective laser melting of 316L stainless steel and C52400 copper alloy. *Mater Characterization*. 2020;167:110489.

doi: 10.1016/j.matchar.2020.110489

141. Liu ZH, Zhang DQ, Sing SL, Chua CK, Loh LE. Interfacial characterization of SLM parts in multi-material processing: Metallurgical diffusion between 316L stainless steel and C18400 copper alloy. *Mater Characterization*. 2014;94:116-125.

142. Chen K, Wang C, Hong Q, Wen S, Zhou Y, Yan C, Shi Y. Selective laser melting 316L/CuSn10 multi-materials: Processing optimization, interfacial characterization and mechanical property. *J Mater Process Technol*. 2020;283:116701.

143. Meyer I, Messmann CO, Ehlers T, Lachmayer R. Additive manufacturing of multi- material parts - effect of heat treatment on thermal, electrical, and mechanical part properties of 316L/CuCrZr. *Mater Design*. 2025;252:113783.

doi: 10.1016/j.matdes.2025.113783

144. Bulloch A, Harris A, Groom A, Cruchley A, Tuck CJ, Simonelli

M. Fundamental investigation of the interface formation of multi-material additive manufactured 316L-CuSn10 structures. *Metall Mater Trans A*. 2025;56:2586-2603.

doi: 10.1007/s11661-025-07817-1

145. Chen J, Zhang M, Zhao D, Bi G, Bai Y, Xiao Y, Wang D. The impact of interfacial characteristics on the interfacial properties of 316 L/CuSn10 multi-material manufactured by laser powder bed fusion. *Mater Characterization*. 2024;211:113862.

doi: 10.1016/j.matchar.2024.113862

146. Sun Z, Tang C, Soh V, *et al.* Laser powder bed fusion of 316L stainless steel and K220 copper multi-material. *Virtual Phys Prototyp.* 2024;19(1):e2356078.

doi: 10.1080/17452759.2024.2356078

147. Dash A, Bandyopadhyay A. 17-4 PH and SS316L bimetallic structures via additive manufacturing. *Virtual Phys Prototyp.* 2024;19(1):e2292695.

doi: 10.1080/17452759.2023.2292695

148. Zhou Y, Duan L, Li F, Chen K, Wen S. Effect of heat treatment on the microstructure and mechanical property of W/316L multi-material fabricated by selective laser melting. *J Alloys Compd*. 2022;890:161841.

doi: 10.1016/j.jallcom.2021.161841

149. Wei C, Gu H, Gu Y, *et al.* Abnormal interfacial bonding mechanisms of multi-material additive-manufactured tungsten-stainless steel sandwich structure. *Int J Extrem Manuf.* 2022;4(2):025002.

150. Obielodan J, Stucker B. Characterization of LENS-fabricated Ti6Al4V and Ti6Al4V/TiC dual-material transition joints. *Int J Adv Manuf Technol*. 2013;66(9-12):2053-2061.

doi: 10.1007/s00170-012-4481-9

151. Wei K, Zeng X, Li F, Liu M, Deng J. Microstructure and mechanical property of Ti-5Al-2.5Sn/Ti-6Al-4V dissimilar titanium alloys integrally fabricated by selective laser melting. *JOM*. 2020;72(3):1031-1038.

doi: 10.1007/s11837-019-03988-6

152. Zhai W, Wang P, Ng FL, *et al.* Hybrid manufacturing of γ-TiAl and Ti-6Al-4V bimetal component with enhanced strength using electron beam melting. *Compos Part B Eng.* 2021;207:108587.

doi: 10.1016/j.compositesb.2020.108587

153. Wang P, Nai MLS, Lu S, Bai J, Zhang B, Wei J. Study of direct fabrication of a Ti-6Al-4V impeller on a wrought Ti-6Al-4V plate by electron beam melting. *JOM*. 2017;69(12):2738-2744.

doi: 10.1007/s11837-017-2610-5

154. Onuike B, Bandyopadhyay A. Functional bimetallic joints of Ti6Al4V to SS410. *Addit Manuf*. 2020;31:100931.

doi: 10.1016/j.addma.2019.100931

155. Scaramuccia MG, Demir AG, Caprio L, Tassa O, Previtali B. Development of processing strategies for multigraded selective laser melting of Ti6Al4V and IN718. *Powder Technol.* 2020;367:376-389.

doi: 10.1016/j.powtec.2020.04.010

156. Onuike B, Bandyopadhyay A. Additive manufacturing of Inconel 718 - Ti6Al4V bimetallic structures. *Addit Manuf.* 2018;22:844-851.

157. Feenstra DR, Molotnikov A, Birbilis N. Effect of energy density on the interface evolution of stainless steel 316L deposited upon INC 625 via directed energy deposition. *J Mater Sci.* 2020;55(27):13314-13328.

doi: 10.1007/s10853-020-04913-y

158. Gorunov AI. Investigation microstructure of carbon fibers reinforced composite on Fe and Ni-based obtained by laser metal deposition. *Surf Coat Technol.* 2019;364:279-288.

doi: 10.1016/j.surfcoat.2019.03.006

159. Duval-Chaneac MS, Gao N, Khan RHU, *et al.* Fatigue crack growth in IN718/316L multi-materials layered structures fabricated by laser powder bed fusion. *Int J Fatigue*. 2021;152:106454.

doi: 10.1016/j.ijfatigue.2021.106454

160. Hinojos A, Mireles J, Reichardt A, *et al.* Joining of inconel 718 and 316 stainless steel using electron beam melting additive manufacturing technology. *Mater Design*. 2016;94:17-27.

doi: 10.1016/j.matdes.2016.01.041

161. Li Y, Liu Z, Wei Z, *et al.* Inhibition of interfacial cracks in 304L-Inconel718 bimetal fabricated via laser powder bed fusion. *Addit Manuf*. 2024;94:104463.

doi: 10.1016/j.addma.2024.104463

162. Chang T, Fang X, Zhou Y, *et al.* Heterogeneous interfaces of aluminum bronze/Inconel 718 dissimilar alloys under different wire arc directed energy deposition sequences. *Int J Extrem Manuf*. 2025;7(1):015003.

doi: 10.1088/2631-7990/ad870f

163. Zhang L, Dong P, Zeng Y, Yao H, Chen J. Additive manufacturing of inconel 718/CuCrZr multi-metallic materials fabricated by laser powder bed fusion. *Addit Manuf*. 2024;92:104377.

doi: 10.1016/j.addma.2024.104377

164. Prestes IB, Jägle EA. Influence of the laser strategy on bi-metallic interfaces printed via multi-material laser-based powder bed fusion. *Addit Manuf Lett.* 2025;13:100274.

doi: 10.1016/j.addlet.2025.100274

165. Wei C, Zhao Z, Wang C, *et al.* Integrated laser additive manufacturing of high-strength steel and Ti6Al4V: Experimental investigations and thermodynamic calculations. *J Alloys Compd.* 2024;983:173902.

doi: 10.1016/j.jallcom.2024.173902

166. Kim DK, Woo W, Kim EY, Choi SH. Microstructure and mechanical characteristics of multi-layered materials composed of 316L stainless steel and ferritic steel produced by direct energy deposition. *J Alloys Compd*. 2019;774:896-907.

doi: 10.1016/j.jallcom.2018.09.390

167. Zhang X, Sun C, Pan T, *et al.* Additive manufacturing of copper - H13 tool steel bi-metallic structures via Ni-based multi-interlayer. *Addit Manuf*. 2020;36:101474.

doi: 10.1016/j.addma.2020.101474

168. Shi Q, Hu Y, Fan H, Yang S. Fundamental role of vertical building sequence and its thermodynamic mechanisms during multi-material additive manufacturing of 18Ni300-CuSn10 structures with IN718 interlayer. *J Manuf Processes*. 2025;144:243-260.

doi: 10.1016/j.jmapro.2025.04.048

169. Bai Y, Zhao C, Zhang Y, Wang H. Microstructure and mechanical properties of additively manufactured multi-material component with maraging steel on CrMn steel. *Mater Sci Eng A*. 2021;802:140630.

doi: 10.1016/j.msea.2020.140630

170. Tan C, Wang D, Ma W, Zhou K. Ultra-strong bond interface in additively manufactured iron-based multi-materials. *Mater Sci Eng A*. 2021;802:140642.

doi: 10.1016/j.msea.2020.140642

171. Khodabakhshi F, Farshidianfar MH, Bakhshivash S, Gerlich AP, Khajepour A. Dissimilar metals deposition by directed energy based on powder-fed laser additive manufacturing. *J Manuf Processes*. 2019;43:83-97.

doi: 10.1016/j.jmapro.2019.05.018

172. Wang P, Lao CS, Chen ZW, *et al.* Microstructure and mechanical properties of Al-12Si and Al-3.5Cu-1.5Mg-1Si bimetal fabricated by selective laser melting. *J Mater Sci Technol.* 2020;36:18-26.

doi: 10.1016/j.jmst.2019.03.047

173. Hauser T, Reisch RT, Seebauer S, *et al.* Multi-material wire arc additive manufacturing of low and high alloyed aluminium alloys with *in-situ* material analysis. *J Manuf Processes*. 2021;69:378-390.

doi: 10.1016/j.jmapro.2021.08.005

174. Ismail L, Mohamed OF, Farrah T, George P, Schiffer A. Influence of process parameters on microstructure and interfacial mechanical properties of Al6061/AlSi10Mg multi-material components fabricated via laser powder bed fusion. *Mater Sci Eng A*. 2025;928:148061.

doi: 10.1016/j.msea.2025.148061

175. Sing SL, Lam LP, Zhang DQ, Liu ZH, Chua CK. Interfacial characterization of SLM parts in multi-material processing: Intermetallic phase formation between AlSi10Mg and C18400 copper alloy. *Mater Characterization*. 2015;107:220-227.

doi: 10.1016/j.matchar.2015.07.007

176. Zhang M, Yang Y, Wang D, Song C, Chen J. Microstructure and mechanical properties of CuSn/18Ni300 bimetallic porous structures manufactured by selective laser melting. *Mater Design*. 2019;165:107583.

doi: 10.1016/j.matdes.2019.107583

177. Ramakrishnan A, Dinda GP. Microstructural control of an Al-W aluminum matrix composite during direct laser metal deposition. *J Alloys Compod*. 2020;813:152208.

178. Zhang W, Liao H, Hu Z, *et al.* Interfacial characteristics and mechanical properties of additive manufacturing martensite stainless steel on the Cu-Cr alloy substrate by directed energy deposition. *J Mater Sci Technol*. 2021;90:121-132.

doi: 10.1016/j.jmst.2021.03.008

179. Tan C, Zhou K, Ma W, Min L. Interfacial characteristic and mechanical performance of maraging steel-copper functional bimetal produced by selective laser melting based hybrid manufacture. *Mater Design*. 2018;155:77-85.

doi: 10.1016/j.matdes.2018.05.064

180. Shah K, Haq IU, Khan A, Shah SA, Khan M, Pinkerton AJ. Parametric study of development of Inconel-steel functionally graded materials by laser direct metal deposition. *Mater Design (1980-2015)*. 2014;54:531-538.

doi: 10.1016/j.matdes.2013.08.079

181. Qingpeng C, Jiachen Y, Xiangyu L, *et al.* Effect of laser powder bed fusion gas flow rate on microstructure and mechanical properties of 316 L stainless steel. *J Manuf Processes*. 2024;132:850-862.

doi: 10.1016/j.jmapro.2024.11.024

182. Jakumeit J, Huang C, Laqua R, Zielinski J, Schleifenbaum JH. Effect of evaporated gas flow on porosity and microstructure of IN718 parts produced by LPBF-processes. *IOP Conf Ser Mater Sci Eng*. 2020;861(1):012011.

doi: 10.1088/1757-899X/861/1/012011

183. Liu L, Wang D, Deng G, *et al.* Laser additive manufacturing of a 316L/CuSn10 multimaterial coaxial nozzle to alleviate spattering adhesion and burning effect in directed energy deposition. *J Manuf Processes*. 2022;82:51-63.

doi: 10.1016/j.jmapro.2022.07.038

184. Onuike B, Heer B, Bandyopadhyay A. Additive manufacturing of Inconel 718-copper alloy bimetal- lic structure using laser engineered net shaping (LENS™). *Addit Manuf*. 2018;21:133-140.

185. Liu W, Dupont JN. *In-situ* reactive processing of nickel aluminides by laser-engineered net shaping. *Metallurgical Mater Trans A*. 2003;34(11):2633-2641.

186. Bergmann JP, Petzoldt F, Schürer R, Schneider S. Solid-state welding of aluminum to copper-case studies. *Welding World*. 2013;57(4):541-550.

187. Chen J, Yang Y, Song C, Wang D, Wu S, Zhang M. Influence mechanism of process parameters on the interfacial characterization of selective laser melting 316L/CuSn10. *Mater Sci Eng A*. 2020;792:139316.

doi: 10.1016/j.msea.2020.139316

188. Zhang J, Song B, Yang L, Liu R, Zhang L, Shi Y. Microstructure evolution and mechanical properties of TiB/Ti6Al4V gradient-material lattice structure fabricated by laser powder bed fusion. *Composit Part B Eng*. 2020;202:108417.

doi: 10.1016/j.compositesb.2020.108417

189. Borisov E, Polozov I, Starikov K, Popovich A, Sufiiarov V. Structure and properties of Ti/Ti64 graded material manufactured by laser powder bed fusion. *Materials* (*Basel*). 2021;14(20):6140.

doi: 10.3390/ma14206140

190. Demir AG, Previtali B. Multi-material selective laser melting of Fe/Al-12Si components. *Manuf Lett*. 2017;11:8-11.

doi: 10.1016/j.mfglet.2017.01.002

191. E04 Committee. Test Method for Microindentation Hardness of Materials. United States: ASTM.

doi: 10.1520/E0384-22

192. Tan JL, Wong CH, Sorkin A. Multi-material modelling for selective laser melting. *Proced Eng*. 2017;216:51-57.

193. Zhang W, Zhang B, Xiao H, Yang H, Wang Y, Zhu H. A layer-dependent analytical model for printability assessment of additive manufacturing copper/steel multi-material components by directed energy deposition. *Micromachines (Basel)*. 2021;12(11):1394.

doi: 10.3390/mi12111394

194. Li W, Kishore MN, Zhang R, *et al.* Comprehensive studies of SS316L/IN718 functionally gradient material fabricated with directed energy deposition: Multi- physics and multi-materials modelling and experimental validation. *Addit Manuf.* 2023;61:103358.

195. Chen C, Gu D, Dai D, *et al.* Laser additive manufacturing of layered TiB2/Ti6Al4V multi-material parts: Understanding thermal behavior evolution. *Optics Laser Technol*. 2019;119:105666.

doi: 10.1016/j.optlastec.2019.105666

196. Kannan R, Lee Y, Pierce D, *et al.* Additive manufacturing as a processing route for steel-aluminum bimetallic structures. *Mater Design*. 2023;231:112003.

doi: 10.1016/j.matdes.2023.112003

197. Sridar S, Klecka MA, Xiong W. Interfacial characteristics of P91 steel - inconel 740H bimetallic structure fabricated using wire-arc additive manufacturing. *J Mater Processing Technol*. 2022;300:117396.

doi: 10.1016/j.jmatprotec.2021.117396

198. Iams AD, Lienert AJ, Otazu DA, Ramoni M. Effects of deposition sequence on microstructural evolution in additively manufactured Cu-Cr-Nb alloy/superalloy bimetallic structures. *Addit Manuf Lett.* 2023;6:100151.

doi: 10.1016/j.addlet.2023.100151

199. Zhang J, Wang X, Gao J, *et al.* Additive manufacturing of Ti-6Al-4V/Al-Cu-Mg multi-material structures with a Cu interlayer. *Int J Mech Sci.* 2023;256:108477.

doi: 10.1016/j.ijmecsci.2023.108477

200. Wimmer A, Yalvac B, Zoeller C, *et al.* Experimental and numerical investigations of *in situ* alloying during powder bed fusion of metals using a laser beam. *Metals*. 2021;11(11):1842.

doi: 10.3390/met11111842

201. Patel KS, Solanki SD, Shah DB, Joshi SJ, Patel KM. Finite element simulation of additive manufacturing process of carbon allotropes. *Int J Interact Design Manuf.* 2023;18:6889-6896.

doi: 10.1007/s12008-023-01221-y

202. Ali MH, Yerbolat G, Kurokawa S. Modeling and simulation of multi-materials for additive manufacturing. *Int J Interact Design Manuf.* 2020;14(3):1057-1069.

doi: 10.1007/s12008-020-00678-5

203. Griffis J, Masker A, Schreiber J, Manogharan G. Site-specific property informed interface design of multi-material laser powder bed fusion. In: *Additive Manufacturing; Advanced Materials Manufacturing; Biomanufacturing*; *Life Cycle Engineering*. Vol. 1. Knoxville, Tennessee, USA: American Society of Mechanical Engineers; 2024. p. V001T01A034.

204. Giraldo-Londoño O, Mirabella L, Dalloro L, Paulino GH. Multi-material thermomechanical topology optimization with applications to additive manufacturing: Design of main composite part and its support structure. *Computer Methods Appl Mech Eng.* 2020;363:112812.

205. Zhang XS, Paulino GH, Ramos AS. Multi-material topology optimization with multiple volume constraints: A general approach applied to ground structures with material nonlinearity. *Struct Multidiscip Optim*. 2018;57(1):161-182.

doi: 10.1007/s00158-017-1768-3

206. Sanders ED, Aguiló MA, Paulino GH. Multi-material continuum topology optimization with arbitrary volume and mass constraints. *Comput Methods Appl Mech Eng.* 2018;340:798-823.

207. Horn M, Prestel L, Schmitt M, *et al.* Multi-material additive manufacturing - recycling of binary metal powder mixtures by screening. *Procedia CIRP.* 2020;93:50-55.

doi: 10.1016/j.procir.2020.04.098

208. Chivel Y. New approach to multi-material processing in selective laser melting. *Phys Proced.* 2016;83:891-898.

doi: 10.1016/j.phpro.2016.08.093

209. Jacob G, Brown CU, Donmez MA, Watson SS, Slotwinski J. *Effects of Powder Recycling on Stainless steel Powder and Built Material Properties in Metal Powder Bed Fusion Processes*. Technical Report NIST AMS 100-6. Gaithersburg, MD: National Institute of Standards and Technology; 2017.

210. Weiss C, Haefner CL, Munk J. On the influence of AlSi10Mg powder recycling behavior in the LPBF process and consequences for mechanical properties. *JOM*. 2022;74(3):1188-1199.

doi: 10.1007/s11837-021-05080-4

211. Koushik T, Shen H, Kan WH, *et al.* Effective Ti-6Al-4V powder recycling in LPBF additive manufacturing considering powder history. *Sustainability*. 2023;15(21):15582.

doi: 10.3390/su152115582

212. Sendino S, Martinez S, Lamikiz A. Characterization of IN718 recycling powder and its effect on LPBF manufactured parts. *Procedia CIRP.* 2020;94:227-232.

doi: 10.1016/j.procir.2020.09.043

213. Ahmed F, Ali U, Sarker D, *et al.* Study of powder recycling and its effect on printed parts during laser powder-bed fusion of 17-4 PH stainless steel. *J Mater Process Technol.* 2020;278:116522.

doi: 10.1016/j.jmatprotec.2019.116522

214. He X, Kong D, Zhou Y, *et al.* Powder recycling effects on porosity development and mechanical properties of Hastelloy X alloy during laser powder bed fusion process. *Addit Manuf.* 2022;55:102840.

doi: 10.1016/j.addma.2022.102840

215. Zhang H, Li J, Li Y. Effect of powder recycling on the organization and mechanical properties of GH4169 alloy by laser metal deposition. *Coatings*. 2023;13(3):659.

doi: 10.3390/coatings13030659

216. Popov VV, Katz-Demyanetz A, Garkun A, Bamberger M. The effect of powder recycling on the mechanical properties and microstructure of electron beam melted Ti-6Al-4 V specimens. *Addit Manuf.* 2018;22:834-843.

doi: 10.1016/j.addma.2018.06.003

217. Carrion PE, Soltani-Tehrani A, Phan N, Shamsaei N. Powder recycling effects on the tensile and fatigue behavior of additively manufactured Ti-6Al-4V parts. *JOM*. 2019;71(3):963-973.

doi: 10.1007/s11837-018-3248-7

218. Nezhadfar PD, Soltani-Tehrani A, Sterling A, Tsolas N, Shamsaei N. *The Effects of Powder Recycling on the Mechanical Properties of Additively Manufactured 17-4 PH Stainless Steel*. Texas: University of Texas at Austin; 2018.

219. Drissi-Daoudi R, Masinelli G, De Formanoir C, Wasmer K, Jhabvala J, Logé RE. Acoustic emission for the prediction of processing regimes in Laser Powder Bed Fusion, and the generation of processing maps. *Addit Manuf.* 2023;67:103484.

doi: 10.1016/j.addma.2023.103484

220. Shevchik SA, Le-Quang T, Farahani FV, *et al.* Laser welding quality monitoring via graph support vector machine with data adaptive kernel. *IEEE Access*. 2019;7:93108-93122.

doi: 10.1109/access.2019.2927661

221. Wasmer K, Kenel C, Leinenbach C, Shevchik SA. *In Situ* and Real-Time Monitoring of Powder-Bed AM by Combining Acoustic Emission and Artificial Intelligence. In: Meboldt M, Klahn C, editors. *Industrializing Additive Manufacturing - Proceedings of Additive Manufacturing in Products and Applications - AMPA2017*. Cham: Springer International Publishing; 2018. p. 200-209.

222. Shevchik S, Le-Quang T, Meylan B, *et al.* Supervised deep learning for real-time quality monitoring of laser welding with X-ray radiographic guidance. *Sci Rep.* 2020;10(1):3389.

doi: 10.1038/s41598-020-60294-x

223. Koester LW, Taheri H, Bond LJ, Faierson EJ. Acoustic monitoring of additive manu- facturing for damage and process condition determination. *AIP Conf Proc*. 2019;2102:020005.

doi: 10.1063/1.5099709

224. Shevchik SA, Masinelli G, Kenel C, Leinenbach C, Wasmer K. Deep learning for in situ and real-time quality monitoring in additive manufacturing using acoustic emission. *IEEE Trans Ind Inform.* 2019;15(9):5194-5203.

doi: 10.1109/TII.2019.2910524

225. Masinelli G, Shevchik SA, Pandiyan V, Quang-Le T, Wasmer K. Artificial intelligence for monitoring and control of metal additive manufacturing. In: Meboldt M, Klahn C, editors. *Industrializing Additive Manufacturing*. Cham: Springer International Publishing; 2021. p. 205-220.

226. Eschner N, Weiser L, Häfner B, Lanza G. Classification of specimen density in Laser powder bed fusion (L-PBF) using in-process structure-borne acoustic process emissions. *Addit Manuf.* 2020;34:101324.

doi: 10.1016/j.addma.2020.101324

227. Ito K, Kusano M, Demura M, Watanabe M. Detection and location of microdefects during selective laser melting by wireless acoustic emission measurement. *Addit Manuf.* 2021;40:101915.

228. Taheri H, Koester LW, Bigelow TA, Faierson EJ, Bond LJ. *In situ* additive manufacturing process monitoring with an acoustic technique: Clustering performance evaluation using

k-means algorithm. *J Manuf Sci Eng*. 2019;141(4):041011.

doi: 10.1115/1.4042786

229. Yang L, Lo L, Ding S, Özel T. Monitoring and detection of meltpool and spatter regions in laser powder bed fusion of super alloy Inconel 625. *Prog Addit Manuf.* 2020;5(4):367-378.

doi: 10.1007/s40964-020-00140-8

230. Zhang Y, Hong GS, Ye D, Zhu K, Fuh JYH. Extraction and evaluation of melt pool, plume and spatter information for powder-bed fusion AM process monitoring. *Mater Design*. 2018;156:458-469.

doi: 10.1016/j.matdes.2018.07.002

231. Nour YA, Gupta N. *In-situ* monitoring of sub-surface and internal defects in additive manufacturing: A review. *Mater Design*. 2022;222:111063.

doi: 10.1016/j.matdes.2022.111063

232. Myers AJ, Quirarte G, Ogoke F, *et al.* High-resolution melt pool thermal imaging for metals additive manufacturing using the two-color method with a color camera. *Addit Manuf.* 2023;73:103663.

doi: 10.1016/j.addma.2023.103663

233. Griffis JC, Shahed KS, Okwudire CE, Manogharan GP. Process Modeling of Multi-Material Laser Powder Bed Fusion. In: *Solid Freeform Fabrication Symposium* 2023; 2023.

234. Küng VE, Scherr R, Markl M, Körner C. Multi-material model for the simulation of powder bed fusion additive manufacturing. *Comput Mater Sci*. 2021;194:110415.

doi: 10.1016/j.commatsci.2021.110415

235. Auenhammer RM, Oddy C, Kim J, Mikkelsen LP. X-ray scattering tensor tomography basedfinite element modelling. *NPJ Comput Mater.* 2023;10:50.

doi: 10.24433/CO.6741464.V2

236. Auenhammer RM, Oddy C, Kim J, *et al.* XX-ray scattering tensor tomography based finite element modelling of heterogeneous materials. *NPJ Comput Mater*. 2024;10(1):50.

doi: 10.1038/s41524-024-01234-5

237. Binder M, Anstaett C, Herzer F, *et al.* Potentials and Challenges of Multi-Material Processing by Laser-Based Powder Bed Fusion. In: *Solid Freeform Fabrication Symposium*; 2018.

238. Paul CP, Yadav SP, Rai AK, Narayanan JA, Bindra KS. Laser directed energy deposition based additive manufacturing of metallic multi-material: A review. *J Metall Mater Sci.* 2021;63:75-87.

doi: 10.1016/j.jmapro.2020.09.008

239. Sing SL, Huang S, Goh GD, *et al.* Emerging metallic systems for additive manufacturing: *In-situ* alloying and multi-metal processing in laser powder bed fusion. *Prog Mater Sci*. 2021;119:100795.

doi: 10.1016/j.pmatsci.2021.100795

240. Mehrpouya M, Tuma D, Vaneker T, Afrasiabi M, Bambach M, Gibson I. Multimaterial powder bed fusion techniques. *Rapid Prototyp J.* 2022;28(11):1-19.

doi: 10.1108/RPJ-01-2022-0014

241. Dzogbewu TC, De Beer D. Powder bed fusion of multimaterials. *J Manuf Mater Process.* 2023;7(1):15.

doi: 10.3390/jmmp7010015

242. Nandhakumar R, Venkatesan K. A process parameters review on selective laser melting-based additive manufacturing of single and multi-material: Microstructure, physical properties, tribological, and surface roughness. *Mater Today Commun.* 2023;35:105538.

doi: 10.1016/j.mtcomm.2023.105538

243. Chen H, He Y, Dash SS, Zou Y. Additive manufacturing of metals and alloys to achieve heterogeneous microstructures for exceptional mechanical properties. *Mater Res Lett.* 2024;12(3):149-171.

doi: 10.1080/21663831.2024.2305261

Appendix

Table A1. Summary of review articles on multi-material additive manufacturing in the past decade

Title	Primary focus	Year	References
Multiple material additive manufacturing – part 1: A review	Review of the MMAM process and principal key processes progress, technological challenges, and future trends as of 2013	2013	28
Additive manufacturing of multimaterial structures	3D-printed polymer-based, metal/metal, and metal/ceramic MMAM applications	2018	102
Potentials and challenges of multi-material processing by laser-based powder bed fusion	Provides a collection of challenges to overcome in MM-LPBF	2018	237
Multi-material additive manufacturing technologies for Ti-, Mg-, and Fe-based biomaterial for bone substitution	Provides a brief review on tissue engineering, design requirements, and metallic biomaterials fabrication technologies	2020	30
Laser direct energy deposition-based additive manufacturing of metallic multi-material: A review	Presents the current state-of-the-art and issues associated with laser-based direct energy deposition in metallic MMAM	2021	238
Critical review of the state of the art in multi-material fabrication via direct energy deposition	Provides a critical review on developing trends, design methodologies, common issues and challenges, and future trends in MM-DED	2021	92
Review on additive manufacturing of multi-material parts: Progress and challenges	Provides information on the latest progress and challenges in MMAM technologies	2021	88
Review on additive hybrid and multi-material manufacturing of metals by powder bed fusion: state of technology and develop- ment potential	Provides information on the state of technology for hybrid and MM manufacturing of metals using AM, particularly PBF processes	2021	59
Emerging metallic systems for additive manufacturing: In-situ alloying and multi-material processing in laser powder bed fusion	Covers the state-of-the-art approach within the perspective of LPBF, and namely, the in situ alloying and multi-material process strategy	2021	239
Recent progress and scientific challenges in multi-material additive manufacturing via laser-based powder bed fusion	Reviews the latest progress in MM powder deposition mechanism, molten pool behavior, process characteristics of printing metal/metal, metal/polymer, and metal/ceramic, and their potential applications	2021	40
Multi-material powder bed fusion technique	Overview of the current state of the MM-PBF techniques	2022	240
Recent progress on additive manufacturing of multi-material structures with laser powder bed fusion	Provides a comprehensive review on achievement in MM structures through LPBF, focusing on interface characteristics, strengthening methods, critical technical issues, and potential problems	2022	39
Powder bed fusion of multi-materials	Provides an overview of the current development for MM-PBF applications	2023	241
A process parameter review on selective laser melting-based additive manufacturing of single and multi-material: microstructure, physical properties, tribological, and surface roughness	Provides information on the influence of LPBF process parameters on the quality of parts fabricated from varied materials and MM structures	2023	242
Multi-material additive manufacturing: A systematic review of design, properties, applications, challenges, and 3D printing of materials and cellular metamaterials.	Presents a comprehensive summary of MMAM systems, fundamental processes, MM combinations, design, modeling, and analysis strategies, focusing on applications and opportunities for using MMAM in various industries	2023	34
A review on additive manufacturing of SS-Ni multi-material fabrication	Summarizes methods used for SS-Ni MMAM, combination strategies, fabrication quality, microstructural variation, property enhancement, challenges, and applications	2023	38
A review on multiplicity in multi-material additive manufacturing: Process, capability, scale, and structure	Covers material combinations in polymer, composites, metals/ceramics, metal alloys, and biomaterials, exploring MMAM capabilities in bi-metallic structures, and functionally or compositionally graded materials, providing insights into various scales and structural aspects	2023	89
A review on experimentally observed mechanical and microstructural characteristics of interfaces in multi-material laser powder bed fusion	Focuses on the material interface characteristics and property performance in MM-LPBF, including common challenges in MMAM	2023	41
Additive manufacturing of metal and alloys to achieve heterogeneous microstructures for exceptional mechanical properties	Reviews the four types of heterogeneous microstructures induced by AM, and discusses the advantages and potential applications of metals and alloys with heterogeneous microstructures made by AM	2024	243

Abbreviations: 3D: Three-dimensional; AM: Additive manufacturing; DED: Direct energy deposition; Fe: Iron; LPBF: Laser powder bed fusion; Mg: Magnesium; MM: Multi-material; Ni: Nickel; PBF: Powder bed fusion; SS: Stainless steel; Ti: Titanium.

Table A2. Summary of multi-material additive manufacturing mechanical testing studies available in the literature

Base material	Hardness/indentation	Bisecting tensile (||)	Longitudinal tensile (=)	Bisecting flexural (||)	Longitudinal flexural (=)	Miscellaneous tests
Stainless steel alloy	[a]SS316/IN625[129]▪ [a]SS316/IN625[132]• [a]SS316/IN625[157]• [a]SS316/IN625[126]• [a]SS316/IN625[133]♦ [a]SS316/IN718[128]▪ [a]SS316/IN718[130]▪ [a]SS316/IN718[127]• [a]SS316/CuSn10[128]▪ [a]SS316/CuSn10[58]▪ [a,d]SS316/CuSn10[142]▪ [a]SS316/CuSn10[56]▪ [a]SS316/CuSn10[187]▪ [d]SS316/C18400[141]▪ [a]SS316/C52400[140]▪ [d]SS316/W[148]▪ [a]SS316/P21[166]• [a]SS316/17-4PH [147]•	[a]SS316/IN625[133]♦ [a]SS316/IN718[130]▪ [a]SS316/CuSn10[58]▪ [a,d]SS316/CuSn10[142]▪ [a]SS316/CuSn10[187]▪	[a]SS316/CuSn10[58]▪ [a,d]SS316/CuSn10[142]▪ [d]SS316/C18400[141]▪ [d]SS316/W[148]▪		[a]SS316/CuSn10[58]▪ [a, d]SS316/CuSn10[142]▪	[a]SS316/CuSn10[58]▪ [a]SS316/P21(C) [166]• [a]SS316/17-4PH [147]•
Titanium alloy	[a]Ti-6Al-4V/IN718[155]▪ [a]TiB/Ti-6Al-4V[188]▪ [c,d]Ti/Ti-6Al-4V[189]▪ [a]Ti5Al2.5Sn/Ti-6Al-4V[151]▪ [a]Ti-6Al-4V/NiCr/SS410[122]• [a]Ti-6Al-4V/Nb/SS410[154]• [a]Ti-6Al-4V/Cu/SS316[123]•	[c,d]Ti/Ti-6Al-4V[189]▪ [a]Ti5Al2.5Sn/Ti-6Al-4V[151]▪ [a]Ti-6Al-4V/Cu/SS316[123]•			[a]Ti-6Al-4V/Nb/SS410[154]•	[a]TiB/Ti-6Al-4V[188]▪
Nickel alloy	[a]IN718/Cu[47]▪ [a]IN718/SS316[159]▪ [b]IN718/Cu[184]• [a]IN718/Ti-6Al-4V[156]• [a]IN718/CF/SS316[158]• [a]NiTi/Ti-6Al-4V[52]▪					[a]IN718/Cu (TD)[47]▪ [a]IN718/SS316(F)[159]▪ [a]IN718/CF/SS316 (WP)[158]• [a]NiTi/Ti-6Al-4V (BS)[52]▪
Ferrous alloy	[a]Fe/Al12Si[190]▪ [a]CrMn/MS1[169]▪	[a]CrMn/MS1[169]▪ [a]C300MS/AISI-304[170]▪ [a]C300MS/AISI-1045CS[170]▪ [a]MS1/Cu[179]▪		[a]C300MS/AISI-304[170]▪ [a]C300MS/AISI-1045CS[170]▪	[a]MS1/Cu[179]▪	[a]C300MS/AISI-304 (F)[170]▪ [a]C300MS/AISI-1045CS (F)[170]▪
Aluminum alloy	[d]AlSi10Mg/C18400[175]▪ [a]Al/W[177]• [a]Al-12Si/Al-3.5Cu-1.5Mg-1Si[172]▪ [a]Al5087/Al6060[173]♦		[d]AlSi10Mg/C18400[175]▪ [a]Al-12Si/Al-3.5Cu-1.5Mg-1Si[172]▪ [a]Al5087/Al6060[173]♦		[d]AlSi10Mg/C18400[175]▪	
Copper alloy	[a]CuSn10/18Ni300[176]▪ [a]CuSn10/Ti-6Al-4V[57]▪ [a]Cu/H13[167]•	[a]CuSn10/18Ni300[176]▪				[a]CuSn10/18Ni300[176]▪

Note: The build orientation of the specimens is superscripted (a–d) according to the printing type referenced in Figure 10. The superscripted symbol in each cell represents the additive manufacturing process used in the fabrication of those materials. The symbol ▪ represents multi-material laser powder bed fusion, • represents multi-material laser direct energy deposition, and ♦ represents multi-material wire-arc additive manufacturing.

Abbreviations: BS: Bond shear; C: Compression test; F: Fatigue test; TD: Thermal diffusivity; WP: Wear performance.

ACCSCIENCE PUBLISHING

Engineering Science in Additive Manufacturing

ORIGINAL RESEARCH ARTICLE

Mechanical properties and energy absorption capability improvement of Ti-6Al-4V porous materials through porous structure design optimization

Yu-Yao Chan, Yi Chao, and Che-Nan Kuo*

Department of Materials and Optoelectronic Science, National Sun Yat-sen University, Kaohsiung, Taiwan, Republic of China

Abstract

The structural materials, which exhibit high toughness and high strain energy absorption, can be used in impact-resistant applications such as bulletproof vests, automobiles, and aerospace. Numerous studies indicate that functional gradient materials, which contain non-uniform density, exhibit excellent performance in energy absorption. During the compression test, the struts of the gradient porosity materials collapsed layer by layer, and this phenomenon optimizes the energy absorption capability of the materials. Furthermore, the collapse region or direction can be predicted and controlled by the design of the gradient porosity materials. In addition to the above concepts, this research also improves its energy absorption capacity through the following two strategies: (1) Chamfering the node of the porous structure to avoid the stress concentration, and (2) optimizing the angle between the struts of the porous material to enhance the ductility of the material. To fabricate the complicated gradient porosity structure, the structural materials were printed using the selective laser melting process with Ti-6Al-4V ELI alloys. Through the experiments conducted in this study, the structural strength was enhanced by up to 28% through structure design, and the energy absorption was improved by 19% compared to the gyroid structure, which has been reported to exhibit good energy absorption capabilities.

Keywords: Energy absorption; Ti-6Al-4V; Chamfering design; Selective laser melting; Lattice structure design

***Corresponding author:**
Che-Nan Kuo
(cnkuo@mail.nsysu.edu.tw)

Citation: Chan Y, Chao Y, Kuo C. Mechanical properties and energy absorption capability improvement of Ti-6Al-4V porous materials through porous structure design optimization. *Eng Sci Add Manuf*. 2025;1(2):025170009. doi: 10.36922/ESAM025170009

Received: April 21, 2025

Revised: May 8, 2025

Accepted: May 20, 2025

Published online: June 17, 2025

1. Introduction

Ti-6Al-4V is a high-strength, low-density α+β phase titanium alloy exhibiting superior strength, corrosion resistance, and excellent biocompatibility.[1,2] Compared to other common metallic alloys (Table 1), Ti-6Al-4V results in higher specific strength,[3,4] widely utilized as a lightweight alloy. In addition to reducing weight by altering material properties, lightweight can also be achieved through structural design. Porous structures are commonly used in lightweight structural designs; it can not only maintain the strength of materials but also save materials, energy consumption, and manufacturing time effectively.[5-7] Besides, porous structures with high specific strength,

Table 1. Mechanical properties comparison of common metallic alloys

Material	Density (g/cm^3)	Compressive strength (MPa)	Specific strength (MPa·cm^3/g)	Strain (%)	Hardness (MPa)	Young's modulus (GPa)
Steel 4340	7.85	470	59.9	22	228	205
Ti6Al4V	4.43	1080	243.8	18	349	113
AlSc	2.67	474	107.5	20	115	72
CuNi	8.90	550	61.8	23	160	162

excellent energy absorption ability, and outstanding vibration-damping characteristics have demonstrated significant application in modern engineering, such as the automobile, aerospace, and defense industries.[8] For example, in the automobile industry, porous structures are utilized in the manufacture of crash energy absorption components, enhancing passenger safety and comfort;[9,10] in the aerospace sector, porous structures are applied in aircraft structural components to reduce weight and improve fuel efficiency;[11,12] in defense applications, porous structures are commonly used in energy-absorbing armor and lightweight vehicle shells, increasing their ability to absorb impact energy.[13] With design flexibility and multifunctionality, porous structures have become indispensable elements in materials engineering and structural design, continually driving the development of high-performance materials.

Porous structures can be classified into three categories: Foam (open-cell and closed-cell), honeycomb, and lattice structures. Lattice structures are composed of an array of spatial units, with each unit's shape and size being either uniform or non-uniform. Compared to foam and honeycomb structures, lattice structures exhibit better mechanical performance and have the potential to enhance compressive strength.[14-16]

Conventional manufacturing methods, such as metallic foam production, have been widely used to fabricate porous metal structures. However, these methods typically result in random, non-uniform pore architectures, making it difficult to precisely control key parameters such as strut orientation, porosity distribution, and overall geometry. Furthermore, substantial material consumption through processes such as forging, casting, and rolling are limited in producing complex shapes and are associated with high production costs and lengthy process times. To address this situation, additive manufacturing can be utilized. Additive manufacturing, also known as 3D printing, allows for the rapid production of complex geometric shapes by printing the product layer by layer.[17,18] The product's shape is based on computer-aided design (CAD) models generated by computer software. Powder bed fusion is one of the additive manufacturing technologies commonly used for metal components and can be categorized into electron beam melting (EBM) and selective laser melting (SLM). EBM employs an electron beam as the heat source, whereas SLM utilizes a laser. In this process, the metal powder on the molten powder bed is scanned according to the modeling, and the metal parts are formed by superposition layer by layer.[18] SLM features finer powder particles and a smaller melt pool, enabling the fabrication of parts with high geometric complexity and fine structural features. Moreover, the melt pool exhibits a higher cooling rate and promotes samples with higher mechanical strength.[19-21] The quality of additive manufacturing samples and the microstructure of materials will be affected by various processing parameters, such as scanning speed, laser power, hatch distances, and layer thickness.

As materials for energy absorption structures, they need to exhibit characteristics such as high strength and high ductility.[22] The mechanical properties and energy absorption effectiveness of materials can be calculated by compression testing and energy absorption formulas (specific energy absorption [SEA]). Material toughness is defined as the energy absorbed per unit volume before fracture. Toughness is related to the area under the stress–strain curve, with a larger area indicating better toughness, meaning the material must be both strong and ductile.[23] Compression testing provides the strength and strain of the material, and further calculation using Equation I determines how much energy the material can absorb before fracture.

$$\text{Specific energy absorption } (\text{J/g}) = \frac{\int_0^{\epsilon d} \sigma \, d\epsilon}{\rho} \quad \text{(I)}$$

where ρ represents the material density; σ represents the stress experienced by the material at strain ϵ; and ϵ_d represents the densification strain of the material. The unit of SEA is Joule/gram (J/g). From Equation I, it can be deduced that if the density of the material is smaller, under the same strength and ductility, the energy absorption capacity per unit weight will be higher. In other words, materials with high specific strength alloys and low-density porous structures will contribute to enhancing the capability of energy absorption during deformation.

On the other hand, data obtained from compression experiments on gradient materials show that due to the

layered pore distribution in gradient materials, the material collapses layer by layer during the collapse process instead of immediately fracturing along the direction of maximum shear force at approximately 45° from top to bottom. In addition, during the collapse process, densification stacking occurs, resulting in a higher area under the stress–strain curve for gradient materials compared to uniform density; this characteristic provides better energy absorption for gradient materials.[23-25]

In additive manufacturing, products made by SLM typically exhibit a very rough surface, often with many incompletely melted powders adhering to the surface. From a microscopic perspective, when subjected to an external force, stress concentrates at the tip of cracks. Cracks with smaller curvature radius and deeper notches experience a rapid increase in strength, causing them to withstand greater strength than other locations. Consequently, they are more likely to exceed the yield strength and plastic deformation that happened earlier. This phenomenon initiates the propagation of cracks from pre-existing flaws, resulting in material fracture, accompanied by a decrease in both strength and ductility.[26] Stress concentration can be expressed as follows (Equation II):

$$\sigma_{max} = \sigma \times (1 + 2\sqrt{\frac{d}{\rho}}) \quad \text{(II)}$$

where σ_{max} is the stress at the notch, σ is the applied stress, ρ is the curvature radius of the notch, and d is the distance from the notch tip to the surface.

Another study adopts the lattice structures with smooth surfaces based on the mathematical approach of triply periodic minimal surface (TPMS). TPMS is a class of minimal surfaces that exhibit periodicity in three-dimensional space and possess zero mean curvature at every point on the surface. Common types of TPMS structures include the gyroid, diamond, and Schwarz-Primitive surfaces, which can be mathematically defined through equations or parametric modeling.[27] With the advancement of additive manufacturing technologies, the complex geometries of TPMS structures can now be fabricated using 3D printing. TPMS structures demonstrate excellent mechanical properties and fluid permeability.[28,29] Optimizing the nodes of the struts causes changes in strength distribution, which significantly impacts the deformation behavior of the structure. This optimization can result in the structure standing more strength distribution, thereby increasing its strength.[30] The volume fraction is a crucial parameter controlling the mechanical properties of porous materials, and it can be determined by the strut diameter, optimized radius, and lattice size. When the unit size is set as a constant, increasing the strut diameter can rapidly increase the volume fraction, and the porosity of the structure will decrease to achieve the desired mechanical properties. The influence of the optimized radius on the volume fraction is presented in the stiffness and strength of the material structure, both of which are significantly enhanced.[26]

When a material is subjected to perpendicular strength, it may undergo deformation, which can be classified into two types: "bending" and "buckling." Bending occurs due to the strain behavior induced in the material by strength applied perpendicular to its principal axis, whereas buckling refers to a sudden change in the shape of the material when axial strength reaches a critical level.[31-33] This study focuses on the relationship between material strength and Young's modulus by exploring the effects of buckling and bending deformations of struts. Zhao *et al.*[34] conducted with Cubic, G7, and Rhombic dodecahedron. The results indicate that the Cubic structure mostly fractures due to compressive strength, mainly compressed by perpendicular buckling struts. On the other hand, for the G7 and Rhombic dodecahedron structures, strength is mainly compressed by bending struts under tension and compression. Through the design of strut shapes, increasing the number of buckling struts can increase the ultimate fatigue strength of the material. Conversely, an increase in bending struts prompts the material to develop fatigue cracks. The growth of fatigue cracks within the struts significantly affects the material, accelerating its fracture.

The gyroid structure is based on a TPMS. Due to its smooth surface, the gyroid structure exhibits high ductility and has been the subject of numerous studies indicating its high energy absorption capabilities.[35,36] According to the above conception, the structure with rounded corners can reduce the stress concentration at the node, and the vertical strut, which is parallel to the compression direction, can be separated by bending and buckling vector, enhancing the buckling vector could enhance the strength and ductility of the structure. Both of them can enhance the capability of energy absorption. However, the gyroid structure is already smooth enough and without any vertical struts, which means that it is difficult to improve the performance of the gyroid structure through the design optimization described above.[37] Hence, in this study, we would like to explore the performance improvement capability of tetrahedron structure[38] and compare it with the control group of gyroid structures, whose mechanical properties are reportedly better than that of tetrahedron structure. Moreover, only the relationship between structures with rounded corners and varying structural angles was explored in previous studies. Thus, this study only revealed the different angles between the struts, and research on the

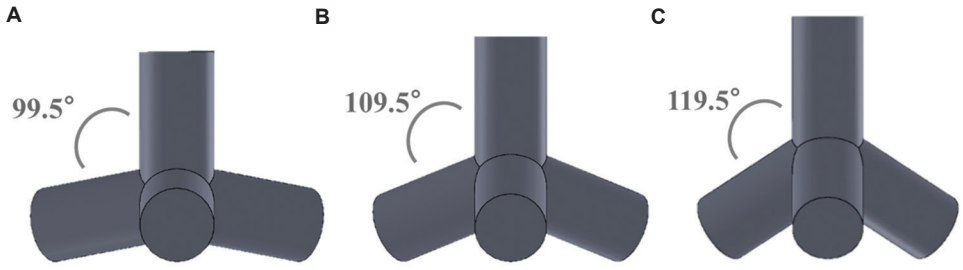

Figure 1. The CAD model of porous materials with different angles between the struts was designed by SolidWorks. The tetrahedral unit cell of different angles between the struts (A) 99.5°, (B) 109.5°, and (C) 119.5°.
Abbreviation: CAD: Computer-aided design.

rounded corner will be conducted in future studies. The current study also attempted to discuss the compression behavior and mechanical properties with different angles between the struts. The effects of rounded corners and varying strut angles in structures fabricated by SLM warrant further investigation. This study introduced and optimized the tetrahedral structure through three key strategies, including: (1) Optimization of the angles between the struts of the porous materials, (2) node chamfering of the porous materials, and (3) introduction of porosity gradient into the porous materials. During the mechanical test, the compression direction was fixed through the z-axis by the specimen. Then, how the angle between the struts and structure with rounded corners affects the capability of energy absorption was discussed. Meanwhile, the characteristics and mechanical properties of the gradient porosity materials with these two variables (rounded corners and different angles between the struts) are cautiously investigated and discussed.

2. Materials and methods

The experiment was conducted with Ti-6Al-4V powder manufactured by a domestic metal powder manufacturer (Chung Yo Materials, Taiwan), using the vacuum induction gas atomization (VIGA) method. The powder size distribution was D10 of 27 m, D50 of 38 m, and D50 of 49 m.

In this study, specimens were designed by SolidWorks with different angles of the unit cell, and the porosity of the material was varied by changing the diameters of the struts. For the tetrahedral structure in the diamond lattice, we constructed the CAD model along the z-axis, aligning the vertical struts parallel to the compressive loading direction. Then, the structure angle between the struts from its standard 109.5° was adjusted through increasing/decreasing by 10°. This modification allows us to discuss the different mechanical behavior under different angles between the struts. Initially, SolidWorks was used to draw tetrahedral unit cells with angles of 99.5°, 109.5°, and

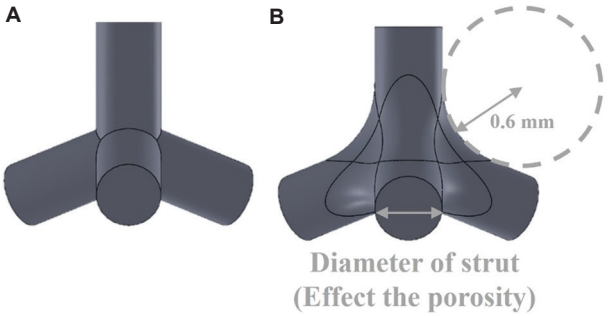

Figure 2. Demonstration of tetrahedral CAD unit cell (A) without and (B) with rounded corners
Abbreviation: CAD: Computer-aided design.

119.5° (Figure 1) and the unit cell with rounded corners or not (Figure 2). Then, the gradient structure was designed by Magics software; after designing the CAD model, the unit cells were imported into Magics and filled to create a cylinder with a diameter of 18 mm and a height of 36 mm. To prevent damage from the compression platen during compression, 1 mm thick disks were designed at the top and bottom to protect the specimens. Then, it was sliced layer by layer and exported as files that can be read by 3D printing machines.

When designing the gradient material, adjusting the thickness of the struts of each unit cell allows for adjustment of its volume fraction. Through the calculation of porosity, different gradient structures with varying porosities can be designed. In this study, specimens were divided into five gradients: 55%, 60%, 65%, 70%, and 75%. To maintain a width-to-height ratio of 1:2 and an average porosity of 65% for the middle layer and to be compared with the original single porosity of 65%, each porosity was designed to have a height ratio of 1:1:1.5:1:1 (Figure 3). Each specimen was printed in five copies to ensure the accuracy and reproducibility of the experimental data (Figure 4).

In this study, the naming of the specimens accords with the following rules. "O" signifies original design, indicating structures without rounded corners. "R" stands for

rounded, representing structures with rounded corners. The numerical values, such as 99.5/109.5/119.5 denote different structural angles. In addition, "65" indicates uniform porosity at 65%, and "G" is used for gradient porosity, 55% – 60% – 65% – 70% – 75%.

The specimens used in this experiment were all printed using the SolidMEN AM300 printer from the Industrial Technology Research Institute. To minimize powder waste and save time, a resource-based view restriction module was added to the machine, limiting the size of the build platform to 120 mm × 120 mm. This equipment utilizes SLM technology, and the scanning parameters are set according to Table 2. The chamfer was filled with argon gas

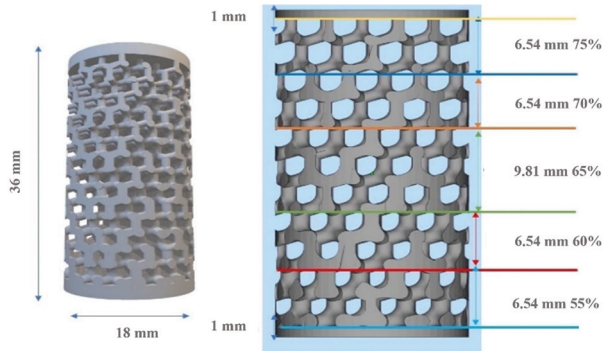

Figure 3. CAD model of cylinder specimen R_109.5_G (55% – 60% – 65% – 70% – 75%). Each porosity was designed in a height ratio of 1:1:1.5:1:1 to maintain an average porosity of 65%.
Abbreviation: CAD: Computed-aided design.

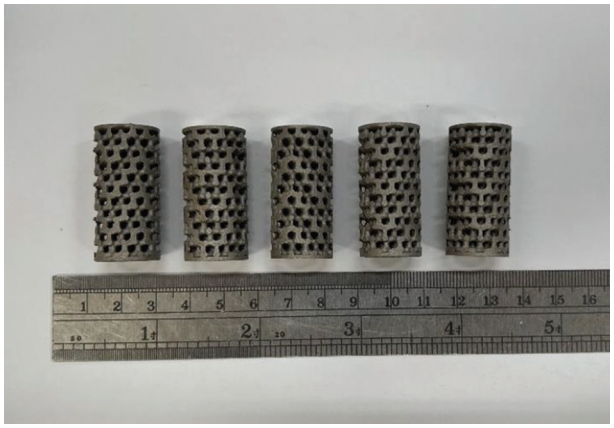

Figure 4. Five specimens in each group of samples. To ensure the accuracy and reproducibility of the test, the sample was printed by selective laser melting, with only the top and bottom surfaces subject to grinding. The image shows the representative sample O_109.5_65.

Table 2. Selective laser melting printing parameters of this study

Laser power	Scan speed	Layer thickness	Hatch distance
100 W	1087.5 mm/s	0.03 mm	0.081 mm

to provide environmental protection, preventing reactions between the samples and oxygen during fabrication.

To ensure that the porosity of the printed sample is the same as the designed CAD model, the density and the weight of the printed sample need to be calculated. Using Equation III, the porosity can be calculated:

$$\rho = (1 - \frac{V}{V_0}) \times 100\% \quad \text{(III)}$$

where ρ is the material porosity, V is the material real volume, and V_0 is the volume of a cylinder. The primary objective of compression testing is to determine the material's behavior and mechanical properties under compression by measuring fundamental variables such as strength and deformation. The compression test would be conducted with an Instron 5582 Universal testing machine (Instron, United States) at an initial strain rate of 1×10^{-4} (s^{-1}). To ensure the strain accurately from the specimen, a linear variable differential transformer was externally attached at room temperature. During compression testing, the test specimen was placed between two platens, and compression was applied using a crosshead to control displacement. Typically, the specimen would be shortening along the compression force direction while expanding outward in the perpendicular direction. Stress–strain curves were plotted using Origin software to analyze Young's modulus, yield strength, compression strength, and SEA, facilitating an assessment of the material's energy absorption capability.

To observe whether the printed specimens match the designed strut angles and to calculate the radius of curvature of the rounded corner specimens, the specimens were cut into longitudinal sections using a grinding machine operating at 2500 rpm with a feed rate of 2.5 mm/min. For further validation, image analysis software such as ImageJ was utilized to calculate the radius of curvature of the notches based on images captured using both optical and electron microscopes. Each experimental sample was sectioned, and 3 – 5 images were captured using optical microscopy for analysis with ImageJ. The optical microscope used in the experiment was Leica DM750 (Leica Microsystems, Germany), whereas the electron microscope was a tabletop model Phenom Pro XG6 (Thermo Fisher Scientific, United States).

3. Results and discussion

3.1. Measurement of specimen and microstructure analysis

After designing the specimens, the weight of the printed specimens can be measured, and the thickness of the small

Table 3. Design porosity and measurement porosity of the specimen in this study

Specimen	Design porosity (%)	Measurement porosity (%)	Deviation (%)
O_99.5_65	65.00	66.28±0.18	1.96
O_109.5_65	65.00	65.62±0.09	0.95
O_119.5_65	65.00	65.63±0.23	0.97
R_99.5_65	65.00	66.19±0.05	1.02
R_109.5_65	65.00	65.05±0.27	0.08
R_119.5_65	65.00	65.46±0.16	0.71

Note: All the porosity data were measured and calculated using Equation III.

discs can be measured by caliper. Then, the weights of the upper and lower small discs were subtracted, and the density was calculated to determine the actual porosity of the specimens. A comparison between the experimental porosity and the computer-designed porosity is shown in Table 3. According to Table 3, it can be observed that the experimental porosity is within 2% of the design porosity, indicating a close match.

Image analysis software such as ImageJ was used to observe whether the angle of the printed structure is consistent with the design. The demonstration of the measurement method is shown in Figure 5. Under the optical microscope, a large amount of unmelted powder adhered to the structure can be observed, causing roughness on the surface of the struts.

3.2. Impact of chamfer design on mechanical properties

According to the experimental results in Table 4 and Figure 6, it can be observed that structures with rounded corners have higher yield strength and compressive strength compared to structures without rounded corners.[39] Specifically, the yield strength was increased by approximately 8% and the compressive strength by about 6%. However, the improvement was only marginal compared to the effect of manipulating the angle between the struts, indicating that the influence of node with chamfer or not on mechanical properties was less significant.

Analyzing the specimens under a microscope and using ImageJ, we can measure the depth (d) and curvature radius (ρ) of the strut notches. By applying the stress concentration formula, we can calculate the maximum strength of the notch. The depth and curvature radius of the notch with and without rounded corners are depicted in Figure 7.

The results based on Equation II are summarized in Table 5. For structures without rounded corners, the strength stand by the notch (σ_{max}) under a force of F was significantly higher compared to structures with rounded

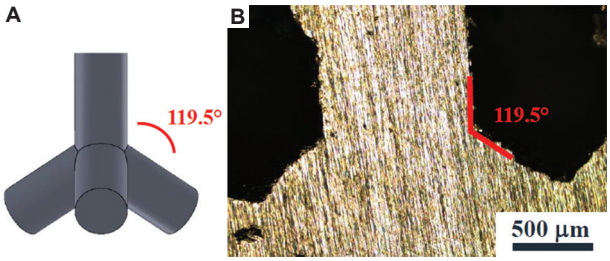

Figure 5. Demonstration of the angle between the struts in (A) CAD model and (B) analysis by ImageJ
Abbreviation: CAD: Computer-aided design.

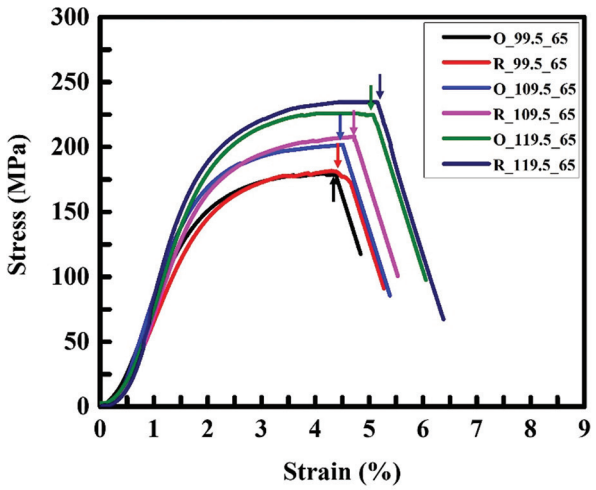

Figure 6. Compressive stress–strain curves of uniform porosity materials with different angles between the struts and with the rounded corner or not

corners, with values exceedingly twice as much. Moreover, as the stress concentration factor (k) increases, the strength has to stand for more strength by the notch. Therefore, it can be inferred that structures without rounded corners experience higher strength at the notch, leading to an earlier occurrence of the first load drop and premature crack initiation from the notch. Consequently, the crack propagation path became shorter, resulting in early fracture and a decrease in both ductility and strength.

Table 4. Mechanical properties of uniform-porosity structure fabricated by selective laser melting in this study

Specimen	Yield strength (MPa)	Compressive strength (MPa)	Strain at first load drop (%)	Strain at failure (%)	SEA (J/g)
Ti64_solid*	1213±102	1419±90	20.5	20.5	62.50
Ti64_solid	1309.67±28.11	1658.38±6.23	20.10±2.25	20.10±2.25	66.16±0.59
O_99.5_65	143.32±0.98	177.88±2.25	4.40±0.14	4.86±0.45	5.01±0.22
O_109.5_65	163.07±1.52	196.01±1.20	4.52±0.08	5.36±0.13	5.45±0.36
O_119.5_65	172.10±0.46	224.67±0.68	5.05±0.21	5.91±0.28	6.10±0.29
R_99.5_65	147.07±1.20	183.56±2.15	4.58±0.04	5.32±0.32	5.49±0.32
R_109.5_65	170.80±0.63	206.71±1.16	4.65±0.13	5.54±0.31	6.04±0.15
R_119.5_65	185.10±2.03	237.30±0.21	5.15±0.19	6.35±0.21	6.61±0.26

Note: *Mechanical properties of Ti64_solid are derived from another study,[39] for the purpose compared with the Ti64_solid printed in our laboratory.
Abbreviation: SEA: Specific energy absorption.

Table 5. Maximum strength on the node in single-porosity material

Specimen	d (mm)	ρ (mm)	k	σ (MPa)	σ_{max} (MPa)
O_99.5_65	0.71±0.01	0.16±0.01	5.21	F	5.21F
O_109.5_65	0.70±0.04	0.17±0.01	5.06	F	5.06F
O_119.5_65	0.68±0.06	0.16±0.03	5.12	F	5.12F
R_99.5_65	0.65±0.03	1.21±0.08	2.47	F	2.47F
R_109.5_65	0.66±0.05	1.25±0.04	2.45	F	2.45F
R_119.5_65	0.62±0.06	1.24±00.09	2.41	F	2.41F

However, through the compression test, we can observe the value of the difference between strain at failure and strain at first load drop, which in the rounded corner group is larger than the original group, as shown in Figure 8. This means that the structure with rounded corners could reduce the stress concentration at the node and enhance the ductility of the structure. Consequently, this causes the cracks in the rounded corner group to take longer deformation to lead the entire structure to fracture.

Besides, in reality, the specimen is a porous material, and cross-sectionally, it is not a complete circle. Upon observing the fracture of the specimen from Figure 9, it is found that the fracture surface runs along the top strut of the tetrahedral structure. Therefore, the cross-sectional area of the force applied to the specimen is corrected to 0.18 times the initial cross-sectional area, as demonstrated in Figure 10. Hence, the following analysis is based on the original force F, divided by 0.18A to obtain the corrected yield stress σ^*, representing the yield strength of a specific solid strut in the specimen. Equation IV is used to represent the maximum strength borne by a single solid structure:

$$\sigma_{max} = \sigma^* \times (1 + 2\sqrt{\frac{d}{\rho}}) \quad \text{(IV)}$$

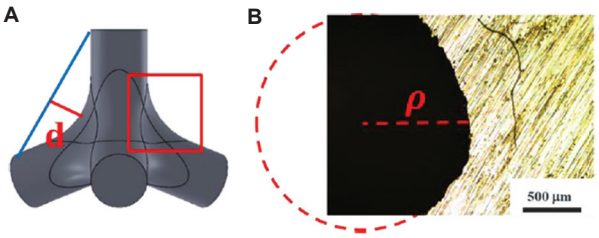

Figure 7. Demonstration of rounded corners notch depth d and curvature radius ρ in (A) CAD model and (B) magnified view of 3D printed sample of the marked area in (A). Curvature can be measured using ImageJ.

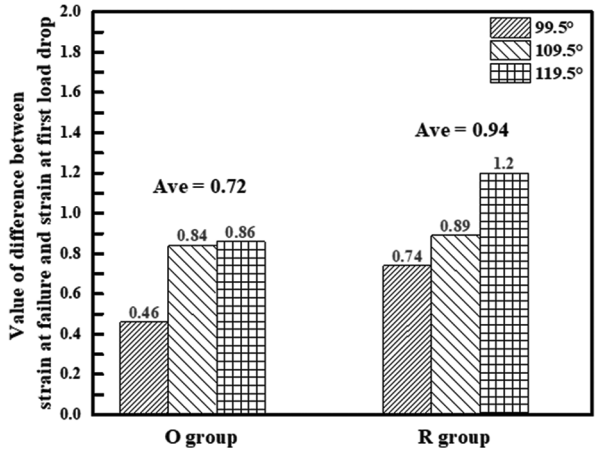

Figure 8. Value of difference between strain at failure and strain at first load drop in O group (without rounded corner) and R group (with rounded corner)

Therefore, according to the calculation results in Table 6, it can be observed that the corrected yield strength σ^* does not exceed the theoretical strength of solid Ti-6Al-4V printed by the same SLM machine, which is about 1310 MPa. However, the maximum strength σ_{max} on the notch exceeds the theoretical yield strength of 1310 MPa. This indicates that the material has reached yield at the notch, initiating plastic deformation and crack propagation,

leading to fracture at that point, resulting in a lower yield strength of the overall structure than expected.

3.3. Impact of angle between the struts on mechanical properties

Figure 6 illustrates the stress–strain curves for structures with different angles between the struts, whereas Table 4 compares the mechanical properties of structures with different support angles. According to the experimental results, structures with larger angles between the struts exhibit superior mechanical properties. Specifically, the yield strength can reach up to a maximum of 26%, and the compressive strength can reach up to 29%. In addition, they also demonstrate better energy absorption performance. Compared to the previous manipulation factor of rounded corners, structures with larger angles between the struts show greater improvements in strength.

Figure 9. Side view of specimen fracture shows the fracture on the strut node with 45°

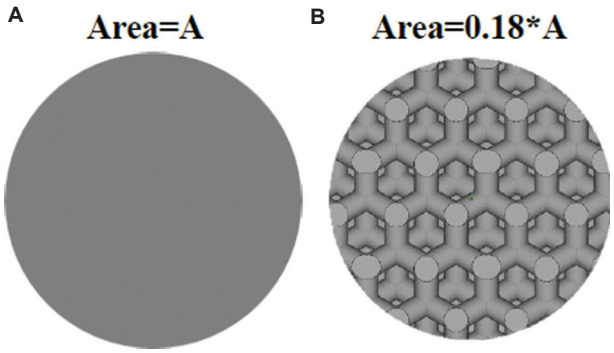

Figure 10. Test specimen cross-sectional area under compression test. (A) The area calculated by Equation II for the maximum strength of the notch; (B) the area calculated by Equation IV for the maximum strength of the notch.

When a tetrahedron is subjected to vertical compression, the strength along the strut can be divided into a buckling vector B and a bending vector D (Figure 11). Their relationship with the strut angle θ can be expressed by Equations V and VI. Furthermore, the buckling vector can be further divided into normal force N and lateral force L (Figure 12). Their relationship with the strut angle θ can be expressed by Equations VII and VIII. Combining Equations V and VI, they can be rearranged into Equations IX and X.

$$B=F \cdot \sin\theta \quad (V)$$

$$D=F \cdot \cos\theta \quad (VI)$$

$$N=B \cdot \sin\theta \quad (VII)$$

$$L=B \cdot \cos\theta \quad (VIII)$$

$$N=B \cdot \sin 2 \quad (IX)$$

$$L=B \cdot \cos\theta \cdot \sin\theta \quad (X)$$

Through the mathematical calculations presented in Table 7, it is evident that as the strut angle θ increases, lateral force L and buckling vector B increase. The increase in both the buckling vector and lateral force vectors contributes to the requirement of greater force and longer compression deformation. During compression, the material is subjected to positive compression and squeezed laterally by the structure, and the structure with a larger angle needs more deformation to achieve the angle of fracture. Consequently, when the angle between the struts becomes larger, the change in angle to achieve fracture during deformation of the tetrahedral structure also increases. This indicates that structures with larger angles require more deformation to be compressed and fracture, which also leads to the larger value of the difference between strain at failure and stain

Table 6. Maximum strength on the node of a solid strut in single porosity material

Specimen	d (mm)	ρ (mm)	k	σ (MPa)	σ^* (MPa)	σ_{max} (MPa)
O_99.5_65	0.71±0.01	0.16±0.01	5.21	143.32	796.22	4148.31
O_109.5_65	0.70±0.04	0.17±0.01	5.06	163.07	905.94	4584.06
O_119.5_65	0.68±0.06	0.16±0.03	5.12	172.10	956.11	4895.28
R_99.5_65	0.65±0.03	1.21±0.08	2.47	147.07	817.06	2018.14
R_109.5_65	0.66±0.05	1.25±0.04	2.45	170.80	948.89	2324.78
R_119.5_65	0.62±0.06	1.24±00.09	2.41	185.10	1028.33	2478.28

Table 7. Buckling vectors calculation of different angles between the struts buckling

Angle (°)	θ (°)	sinθ	cosθ	Buckling vector	Normal vector	Lateral vector
99.5	9.5	0.165	0.986	0.165F	0.027F	0.163F
109.5	19.5	0.334	0.943	0.334F	0.112F	0.315F
119.5	29.5	0.492	0.870	0.492F	0.242F	0.428F

Note: Vector can be separated by normal vector and lateral vector.

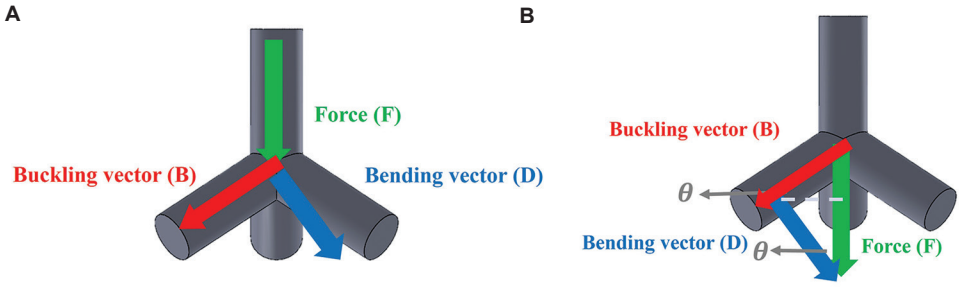

Figure 11. Demonstration of force components and angles of the tetrahedral structure. (A) The force components separated by buckling vector and bending vector; (B) the relationship between the angle between the struts and buckling vector.

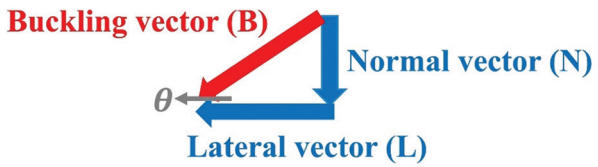

Figure 12. Buckling vector force component, which can be separated by normal vector and lateral vector

at first load drop (Figure 8). With a larger angle between the struts, the buckling vector increases, and the first load drop is delayed, resulting in a higher strain when the first strut of the entire structure fractures, accompanied by a higher strength.

3.4. Comparison between gradient material and single porosity structure

In Table 4, solid Ti-6Al-4V, without any porosity, exhibits high yield strength and ductility. However, when considering lightweight applications, gradient porous structures require less material, leading to higher SEA, as shown in Table 8. Gradient porous structures show larger strains than solid structures due to their unique collapse mechanism. The compression behavior of porous structures with uniform porosity and gradient porosity is discussed in detail below in this study.

Figure 6 and Table 8 show the stress–strain curve diagram and energy absorption of the single porosity structure, while Figure 13 and Table 8 show the stress–strain curve diagram and energy absorption of the gradient structure. Through the stress–strain curve diagram obtained from the material compression test, the area underneath can be calculated to determine the material's energy absorption. According to the experimental results, the energy absorption of the gradient material is significantly higher than that of the single porosity material. The main reason for this is that during compression, the gradient material collapses from high porosity to low porosity. As the high porosity collapses downward, it densifies the lower layers, thereby increasing strength again. This process repeats several times, leading to a layered collapse of the material, unlike the single porosity material, which fractures directly in random directions. As presented in Figure 14, two ways of different fractures between uniform porosity and gradient porosity in this experiment are shown.

Figure 15 demonstrates that as the relative density increases, the volume fraction also increases, leading to an enhancement in SEA. When compared to other studies,[40,41] the gradient structure examined in this research shows a higher energy absorption capacity at the average relative density. This indicates that optimizing the gradient structure significantly improves its energy absorption capabilities, outperforming other structural designs analyzed in previous studies.

3.5. Comparison of mechanical properties in this study

In the initial comparison between the diamond structure (O_109.5_65) and the control group (gyroid), the diamond structure showed better yield strength, whereas the gyroid exhibited superior strain and SEA (Table 9). However,

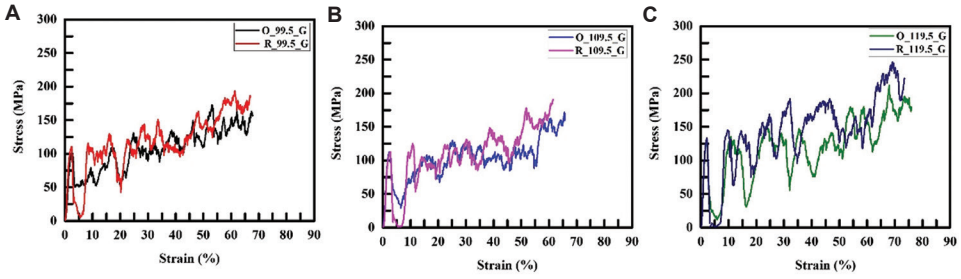

Figure 13. Compressive stress–strain curves of gradient porosity materials with angles between struts of (A) 99.5°, (B) 109.5°, and (C) 119.5°

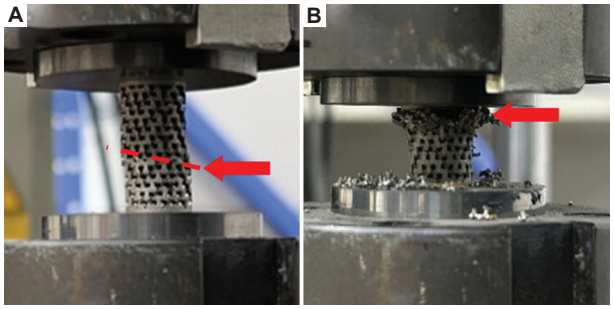

Figure 14. Compression fracture of (A) single-porosity and (B) gradient material. The deformation of the Ti-6Al-4V porous structure with single porosity occurred randomly. The gradient-porosity structure deformed from the top to the bottom layer by layer.

Table 8. Energy absorption under compression test between uniform porosity (65%) and gradient porosity (55% – 60% – 65% – 70% – 75%)

Uniform porosity	SEA (J/g)	Gradient porosity	SEA (J/g)
O_99.5_65	5.01±0.22	O_99.5_G	42.78±0.72
O_109.5_65	5.45±0.36	O_109.5_G	48.89±1.13
O_119.5_65	6.10±0.29	O_119.5_G	54.46±1.66
R_99.5_65	5.49±0.32	R_99.5_G	50.97±1.33
R_109.5_65	6.04±0.15	R_109.5_G	64.93±2.17
R_119.5_65	6.61±0.26	R_119.5_G	71.56±1.22

Abbreviation: SEA: Specific energy absorption.

after enhancing the diamond structure by adding rounded corners and increasing the angle between the struts to L_119.5_65, the yield strength increased significantly compared to the original design. When compared to the gyroid control group under gradient porosity, L_119.5_G demonstrated better energy absorption than the gyroid.

This study manipulates two main variables: The presence of rounded corners and changes in strut angles. As the radius of the rounded corners increases, the concentration of strength decreases, leading to an increase in yield strength and compressive strength. Therefore, yield strength is positively correlated with the radius of curvature of the rounded corners. As the strut angle increases, the buckling vector increases, contributing to the improvement of mechanical properties. Hence, yield strength is positively correlated with the strut angle.

The appearance of yield strength can be regarded as the starting point of plastic deformation, where the struts start to exhibit permanent deformation. The appearance of compressive strength reveals the beginning of strut fracture. In this experiment, the sizes of the strut angles were compared for both yield strength and compressive strength. As the strut angle increases, both yield strength and compressive strength increase accordingly. As the y-axis shown in Figure 16, the enhancement of yield strength and compressive strength with different angles between the struts up to 26% and 29%, respectively. The increase in strut angle contributes significantly to the improvement of mechanical properties.

However, despite the increase in stress concentration factor, the strength standing by the notch increases accordingly. Conversely, both yield strength and compressive strength decrease, but the magnitude of the difference on the y-axis is not significant, with only a 6% and 8% difference, respectively. From Figure 17, it can be observed that the majority of the differences in mechanical properties still stem from changes in the angle. Hence, the strut angle with the maximum value of 119.5° is consistently depicted at the top of the graph.

Furthermore, by multiplying the reciprocal of the two manipulated variables in this experiment, namely the strut angle and the stress concentration factor, as the x-axis and setting the y-axis as the yield strength, Figure 18 was obtained. It can be observed that they exhibit a positive correlation, with correlation coefficients (R^2) all >0.95. This indicates a minimal error, affirming the reliability of the data.

Figures 19 and 20 show that, through different scales of photography, both camera and optical microscope reveal clear differences in image results between specimens with and without rounded corners. However, specimens with rounded corners do not exhibit significant improvements in yield strength and compressive strength compared to

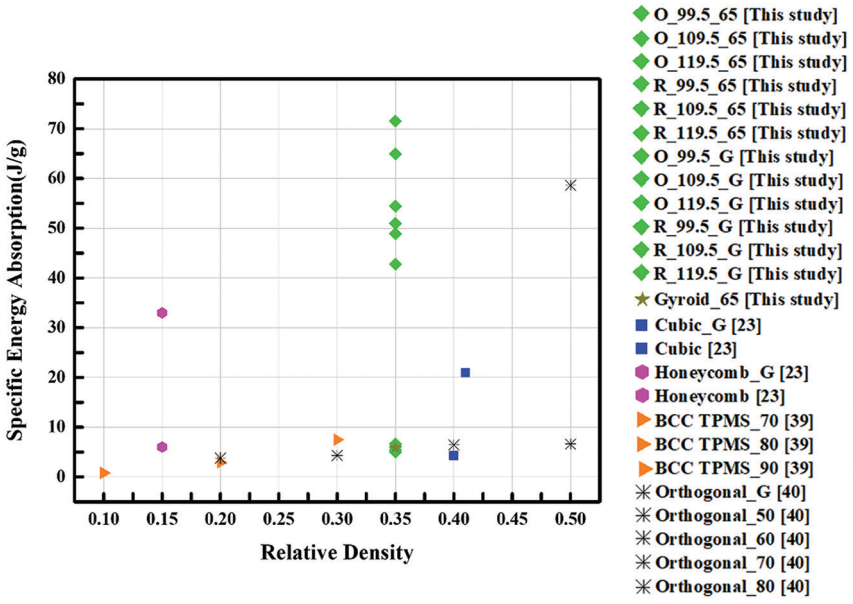

Figure 15. Comparison of the specific energy absorption with other porous structures built by selective laser melting. The black one indicates the gradient porosity; the gray one indicates the uniform porosity.

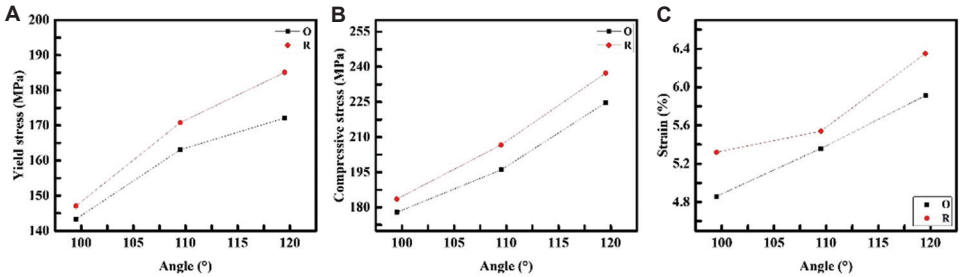

Figure 16. Compression test of (A) Yield strength, (B) Compressive strength, and (C) strain versus angle between the struts. O=the original sample, without rounded corners; R=the same with rounded corners.

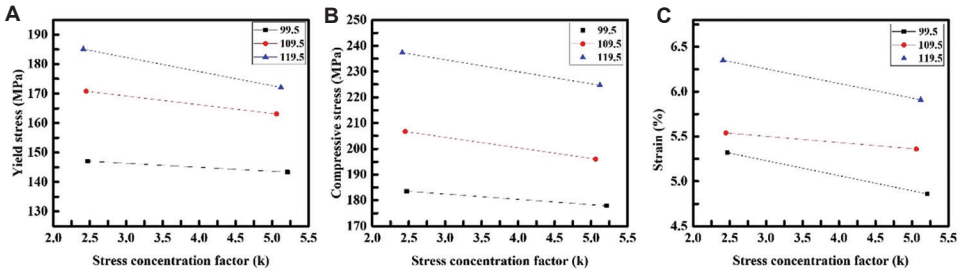

Figure 17. Compression test of (A) yield strength, (B) compressive strength, and (C) strain versus stress concentration factor

Table 9. Summary comparison under compression test in this study

Specimen	Yield strength (MPa)	Compressive strength (MPa)	Strain (%)	SEA (J/g)
Gyroid_65	155.9±3.5	210.8±0.2	6.3±0.5	5.9±0.2
O_109.5_65	163.1±1.5	196.0±1.2	5.5±0.1	5.5±0.4
R_119.5_65	185.1±2.0	237.3±0.2	6.4±0.2	6.6±0.3
R_119.5_G	135.4±3.3	249.3±3.1	74.7±1.8	71.6±1.2

Abbreviation: SEA: Specific energy absorption.

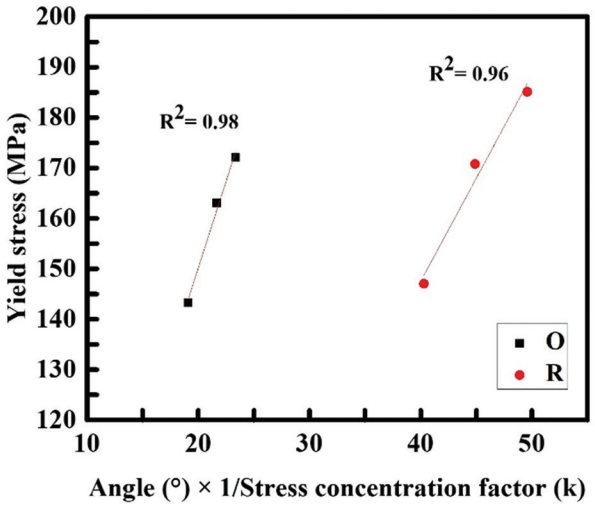

Figure 18. Yield strength versus different angles between the struts and stress concentration factor (k). The correlation coefficients (R^2) all >0.95 show the reliability of the data in this experiment. O=the original sample, without rounded corners; R=the sample with rounded corners.

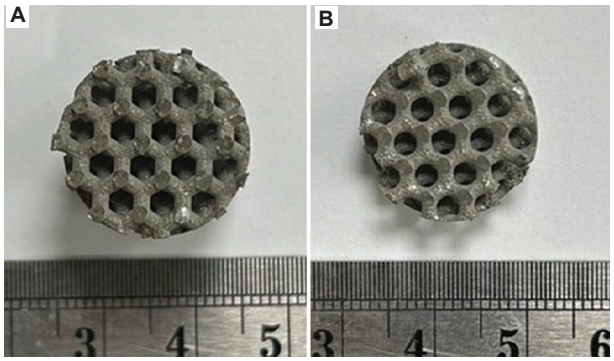

Figure 19. Top view of the specimen taken with the camera (A) without rounded corners and (B) with rounded corners

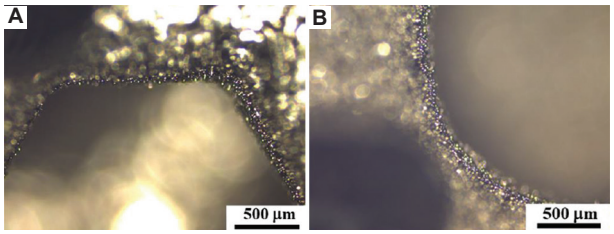

Figure 20. Optical microscope images for the top view of the specimen (A) without rounded corners and (B) with rounded corners

those without rounded corners. This is speculated to be due to the lack of post-processing of the specimens, as evidenced by the unmelted powder adhering to the struts (Figure 21). Despite the structure with rounded corners, this adherence results in substantial surface roughness, leading to stress concentration effects and eventual material failure. If the surface roughness can be reduced in the future, thereby reducing strength concentration issues, the mechanical properties of the structure are expected to improve once again.[42]

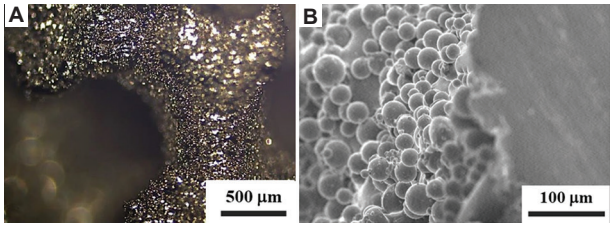

Figure 21. Unmelted powder attached on strut under (A) optical microscope and (B) scanning electron microscope

4. Conclusion

In this study, gradient porous structures and geometric optimization strategies were employed to enhance mechanical performance. Gradient porosity not only reduced sample weight but also significantly increased SEA due to layer-by-layer collapse behavior. In addition, increasing the angle between struts improved ductility and delayed structural failure, leading to enhancements in yield strength and compressive strength by approximately 26% and 29%, respectively. Node chamfering helped to reduce stress concentration and resulted in yield and compressive strength improvements of about 6 – 8%; however, its effect was limited, likely due to surface roughness caused by unmelted powder.

Furthermore, compared to the previously validated gyroid_65% structure, the optimized diamond-based design (L_119.5_65%) exhibited a 19% increase in strength, as shown in Table 9. These findings indicate that the combined implementation of gradient porosity and geometric optimization is an effective strategy for designing high-performance porous metallic structures for energy absorption applications.

Acknowledgments

The authors are grateful for the support of the Taiwan Space Agency and China Steel Corporation.

Funding

The authors gratefully acknowledge the sponsorship support from the National Science and Technology Council of Taiwan, ROC, under project no. NSTC 112-2221-E-110-019.

Conflict of interest

Che-Nan Kuo is an Editorial Board Member of this journal but was not in any way involved in the editorial and peer-review process conducted for this paper, directly

or indirectly. Separately, other authors declared that they have no known competing financial interests or personal relationships that could have influenced the work reported in this paper.

Author contributions

Conceptualization: Yu-Yao Chan, Che-Nan Kuo
Formal analysis: Yu-Yao Chan, Yi Chao
Investigation: Yu-Yao Chan, Yi Chao
Methodology: Yu-Yao Chan, Che-Nan Kuo
Writing – original draft: Yu-Yao Chan
Writing – review & editing: Che-Nan Kuo

Ethics approval and consent to participate

Not applicable.

Consent for publication

Not applicable.

Availability of data

The authors confirm that the data supporting the findings of this study are available within the article.

References

1. Simonelli M, Tse YY, Tuck C. The formation of α+ β microstructure in as-fabricated selective laser melting of Ti-6Al-4V. *J Mater Res*. 2014;29(17):2028-2035.

   doi: 10.1557/jmr.2014.166

2. Cui C, Hu B, Zhao L, Liu S. Titanium alloy production technology, market prospects and industry development. *Mater Design*. 2011;32(3):1684-1691.

   doi: 10.1016/j.matdes.2010.09.011

3. Liu S, Shin YC. Additive manufacturing of Ti6Al4V alloy: A review. *Mater Design*. 2018;164:107552.

   doi: 10.1016/j.matdes.2018.107552

4. Donachie MJ. *Titanium: A Technical Guide*. 2nd ed. Netherlands: ASM International; 2000.

   doi: 10.31399/asm.tb.ttg2.9781627082693

5. Li Y, Feng Z, Hao L, *et al*. A review on functionally graded materials and structures via additive manufacturing: From multi-scale design to versatile functional properties. *Adv Mater Technol*. 2020;5(6):1900981.

   doi: 10.1002/admt.201900981

6. Allen J. An investigation into the comparative costs of additive manufacture vs. Machine from solid for aero engine parts. *Cost Eff Manuf via Net-Shape Process*. 2006;17:1-17.

7. O'Leary R, Setchi R, Prickett P, Hankins G, Jones N. An investigation into the recycling of Ti-6Al-4V powder used within SLM to improve sustainability. *Impact J Innov Impact*. 2016;8(2):377.

8. Kas M, Yilmaz O. Radially graded porous structure design for laser powder bed fusion additive manufacturing of Ti-6Al-4V alloy. *J Mater Process Technol*. 2021;296:117186.

   doi: 10.1016/j.jmatprotec.2021.117186

9. Zhang W, Xu J. Advanced lightweight materials for automobiles: A review. *Mater Design*. 2022;221:110994.

   doi: 10.1016/j.matdes.2022.110994

10. Lv X, Xiao Z, Fang J, Li Q, Lei F, Sun G. On safety design of vehicle for protection of vulnerable road users: A review. *Thin-Walled Struct*. 2023;182:109990.

    doi: 10.1016/j.tws.2022.109990

11. Huang R, Riddle M, Graziano D, *et al*. Energy and emissions saving potential of additive manufacturing: The case of lightweight aircraft components. *J Clean Prod*. 2016;135:1559-1570.

    doi: 10.1016/j.jclepro.2015.04.109

12. Uhlmann E, Kersting R, Klein TB, Cruz MF, Borille AV. Additive manufacturing of titanium alloy for aircraft components. *Procedia Cirp*. 2015;35:55-60.

    doi: 10.1016/j.procir.2015.08.061

13. Zochowski P, Bajkowski M, Grygoruk R, *et al*. Ballistic impact resistance of bulletproof vest inserts containing printed titanium structures. *Metals*. 2021;11(2):225.

    doi: 10.3390/met11020225

14. Brennan-Craddock J, Brackett D, Wildman R, Hague R. The design of impact absorbing structures for additive manufacture. *J Phys Conf Ser*. 2012;382:012042.

    doi: 10.1088/1742-6596/382/1/012042

15. Pan C, Han Y, Lu J. Design and optimization of lattice structures: *A review. Appl Sci*. 2020;10(18):63-74.

    doi: 10.3390/app10186374

16. Park KM, Min KS, Roh YS. Design optimization of lattice structures under compression: Study of unit cell types and Cell arrangements. *Materials*. 2022;15:97.

    doi: 10.3390/ma15010097

17. Thompson SM, Bian L, Shamsaei N, Yadollahi A. An overview of direct laser deposition for additive manufacturing; part I: Transport phenomena, modeling and diagnostics. *Addit Manuf*. 2015;8:36-62.

    doi: 10.1016/j.addma.2015.07.001

18. Yap CY, Chua CK, Dong ZL, *et al*. Review of selective laser melting: Materials and applications. *Appl Phys Rev*. 2015;2(4):041101.

    doi: 10.1063/1.4935926

19. Khorasani A, Gibson I, Awan US, Ghaderi A. The effect

of SLM process parameters on density, hardness, tensile strength and surface quality of Ti-6Al-4V. *Addit Manuf*. 2019;25:176-186.

doi: 10.1016/j.addma.2018.09.002

20. Shifeng W, Shuai L, Qingsong W, Yan C, Sheng Z, Yusheng S. Effect of molten pool boundaries on the mechanical properties of selective laser melting parts. *J Mater Process Technol*. 2014;214(11):2660-2667.

doi: 10.1016/j.jmatprotec.2014.06.002

21. Ansari MJ, Nguyen DS, Park HS. Investigation of SLM process in terms of temperature distribution and melting pool size: Modeling and experimental approaches. *Materials*. 2019;12(8):1272.

doi: 10.3390/ma12081272

22. Seetoh IP, Liu X, Markandan K, Zhen L, Lai CQ. Strength and energy absorption characteristics of Ti6Al4V auxetic 3D anti-tetrachiral metamaterials. *Mech Mater*. 2021;156:103811.

doi: 10.1016/j.mechmat.2021.103811

23. Choy SY, Sun CN, Sin WJ, *et al*. Superior energy absorption of continuously graded microlattices by electron beam additive manufacturing. *Virtual Phys Prototyp*. 2021;16(1):1-15.

doi: 10.1080/17452759.2020.1868656

24. Mahamood RM, Akinlabi ET, Owolabi MG, Abdulrahman KO. Advanced manufacture of compositionally graded composite materials: An overview. In: *Hierarchical Composite Materials: Materials, Manufacturing, Engineering*. Berlin, Boston: De Gruyter; 2019. p. 41-54.

doi: 10.1515/9783110545104-003

25. Evans AG, He MY, Deshpande VS, Hutchinson JW, Jacobsen AJ, Carter WB. Concepts for enhanced energy absorption using hollow micro-lattices. *Int J Impact Eng*. 2010;37:947-959.

doi: 10.1016/j.ijimpeng.2010.03.007

26. Liu F, Zhang DZ, Zhang P, Zhao M, Jafar S. Mechanical properties of optimized diamond lattice structure for bone scaffolds fabricated via selective laser melting. *Materials*. 2018;11:374.

doi: 10.3390/ma11030374

27. Zhao M, Zhang DZ, Liu F, Li Z, Ma Z, Ren Z. Mechanical and energy absorption characteristics of additively manufactured functionally graded sheet lattice structures with minimal surfaces. *Int J Mech Sci*. 2020;167:105262.

doi: 10.1016/j.ijmecsci.2019.105262

28. Sun Q, Sun J, Guo K, Wang L. Compressive mechanical properties and energy absorption characteristics of SLM fabricated Ti6Al4V triply periodic minimal surface cellular structures. *Mech Mater*. 2022;166:104241.

doi: 10.1016/j.mechmat.2022.104241

29. Zhao X, Li Z, Zou Y, Zhao X. Compressive characteristics and energy absorption capacity of automobile energy-absorbing box with filled porous TPMS structures. *Appl Sci*. 2024;14(9):3790.

doi: 10.3390/app14093790

30. Li Z, Zhao R, Chen X, Jiao Y, Chen Z. Design approach for tuning the hybrid region of 3D-printed heterogeneous structures: Modulating mechanics and energy absorption capacity. *ACS Appl Mater Interfaces*. 2023;15(6):7686-7699.

doi: 10.1021/acsami.2c17753

31. Dong JH, Wang YJ, Jin FN, Fan HL. Crushing behaviors of buckling-induced metallic meta-lattice structures. *Def Technol*. 2022;18(8):1301-1310.

doi: 10.1016/j.dt.2021.07.014

32. Obadimu SO, Kourousis KI. Compressive behaviour of additively manufactured lattice structures: *A review. Aerospace*. 2021;8(8):207.

doi: 10.3390/aerospace8080207

33. Li Y, Wang XS, Meng XK. Buckling behavior of metal film/substrate structure under pure bending. *Appl Phys Lett*. 2008;92(13):131902.

doi: 10.1063/1.2897035

34. Zhao S, Li SJ, Hou WT, Hao YL, Yang R, Misr RDK. The influence of cell morphology on the compressive fatigue behavior of Ti-6Al-4V meshes fabricated by electron beam melting. *J Mech Behav Biomed Mater*. 2016;59:251-264.

doi: 10.1016/j.jmbbm.2016.01.034

35. Li D, Liao W, Dai N, Xie YM. Comparison of mechanical properties and energy absorption of sheet-based and strut-based gyroid cellular structures with graded densities. *Materials*. 2019;12(13):2183.

doi: 10.3390/ma12132183

36. Yang E, Leary M, Lozanovski B, *et al*. Effect of geometry on the mechanical properties of Ti-6Al-4V Gyroid structures fabricated via SLM: A numerical study. *Mater Design*. 2019;184:108165.

doi: 10.1016/j.matdes.2019.108165

37. Choy SY, Sun CN, Leong KF, Wei J. Compressive properties of Ti-6Al-4V lattice structures fabricated by selective laser melting: Design, orientation and density. *Addit Manuf*. 2017;16:213-224.

doi: 10.1016/j.addma.2017.06.012

38. Jenkins SNM. *Mechanical Properties and Structural Evaluation of Diamond Structure Ti6Al4V Lattices Made by Electron Beam Melting*. England: University of Sheffield; 2017.

39. Kurdi A, Basak AK. Micro-mechanical behaviour of selective laser melted Ti6Al4V under compression. *Mater Sci Eng A*. 2021;826:141975.

doi: 10.1016/j.msea.2021.141975

40. Zhao M, Liu F, Fu G, Zhang DZ, Zhang T, Zhou H. Improved mechanical properties and energy absorption of BCC lattice structures with triply periodic minimal surfaces fabricated by SLM. *Materials*. 2018;11(12):2411.

doi: 10.3390/ma11122411

41. Wang YP, Kuo CN. Research on energy absorption of gradient porosity structural materials. *Mater Today Proc*. 2022;70:578-582.

doi: 10.1016/j.matpr.2022.09.594

42. Kuo CN, Wang YP, Chua CK. Effect of electropolishing on mechanical property enhancement of Ti6Al4V porous materials fabricated by selective laser melting. *Virtual Phys Prototyp*. 2022;17(4):919-931.

doi: 10.1080/17452759.2022.2090383

ACCSCIENCE PUBLISHING

Engineering Science in Additive Manufacturing

ORIGINAL RESEARCH ARTICLE

Impact of machine factors on the surface quality of parts fabricated via powder bed fusion

Zhen Lu[1], Ming Jen Tan[1]*, Yi Zhang[2], Jia An[3], and Chee Kai Chua[3]

[1]Singapore Centre for 3D Printing, Nanyang Technological University, Singapore

[2]School of Integrated Circuit Science and Engineering, University of Electronic Science and Technology of China, Sichuan, China

[3]Engineering Product Development Pillar, Singapore University of Technology and Design, Singapore

Abstract

In the growing additive manufacturing industry, there is increasing demand for improved as-built surface quality of parts fabricated by the powder bed fusion (PBF) process, particularly in the aerospace, medical, and tooling industrial sectors. The surface finish of PBF parts is often suboptimal due to the inherent layer-by-layer fabrication process. Depending on the material used, the average surface roughness (Ra) of PBF components typically ranges from 5 to 50 μm. To address this issue, various strategies have been investigated, including optimizing printing process parameters, refining support designs, and upgrading laser hardware. In this study, we investigated the machine factors on the as-built surface quality of parts in the PBF process. Fully dense as-built 1.2709 tool steel parts were produced with a relative density of 99.9% using platform pre-heating. Without heat treatment, the as-built part exhibited an ultimate tensile strength of 1,135 ± 75 MPa, yield strength of 915 ± 120 MPa, and an elongation of 12 ± 3%. Vickers hardness was measured at 339 ± 35. Surface measurements were performed on parts placed across the substrate plate, with the Ra of as-built vertical walls averaging 22.6 ± 11.9 mm. Results showed that the surface quality of as-built 1.2709 tool steel parts, with a layer thickness of 30 μm, was significantly affected by their distance from the inert gas outlet and the laser center. This study demonstrates that the as-built surface quality of PBF parts can be controlled through more effective build job preparation without changing key processing parameters.

Keywords: Additive manufacturing; 3D printing; Powder bed fusion; Selective laser melting; Surface quality; Tool steel

***Corresponding author:**
Ming Jen Tan
(mmjtan@ntu.edu.sg)

Citation: Lu Z, Tan MJ, Zhang Y, An J, Chua CK. Impact of machine factors on the surface quality of parts fabricated via powder bed fusion. *Eng Sci Add Manuf*. 2025;1(2):025240014. doi: 10.36922/ESAM025240014

Received: May 13, 2055

Revised: June 14, 2025

Accepted: June 18, 2025

Published online: June 24, 2025

1. Introduction

Additive manufacturing (AM), as defined by International Standardization Organization/ASTM 52900:2021,[1] is the process of joining materials to make parts from 3D model data. Usually, materials are joined layer upon layer, as opposed to subtractive and formative methods of manufacturing. Seven families of AM are commonly recognized, while powder bed fusion (PBF) uses lasers as the energy source to fully melt and fuse the metal powder materials directly to form the near-net shape metal product, which can be fully functional.

Laser-based PBF of metals, commonly known as selective laser melting (SLM) or direct metal laser sintering, is an AM process capable of producing near-net-shape metal components for research and industrial applications. The process begins with a computer-aided design model configured with process parameters and sliced into layers using specialized software. During fabrication, metal powder is deposited onto a build plate layer-by-layer with a predefined layer thickness.[2] The laser selectively melts the powder in each layer, fusing it to form the final part.[3] PBF enables the rapid fabrication of metal components with complex geometries, offering good quality and dimensional accuracy.[4] It enhances design freedom by eliminating many of the geometric constraints imposed by conventional machining methods. In addition, PBF supports part integration, which can reduce manufacturing costs and improve overall component performance, making it well-suited for meeting industrial demands.[5] Parts are built layer-by-layer with the thickness of each layer at 20 – 100 μm. Ideal metal powder is spherical, medium-sized, with a narrow particle distribution. Oxygen level is controlled at <500 ppm. The platform can be heated up to 200°C.[6] PBF technology is compatible with many materials, highly efficient, and capable of producing complex end-products of high precision.[7,8] Companies such as General Electric, Airbus, Boeing, and Rolls-Royce are all at the forefront of using more metal AM in their production line.[9-11]

Key advantages of the PBF process include greater design freedom, enhanced functionality, reduced tooling and setup costs, lightweight structures, mass customization, and overall cost savings.[8] However, various post-processing steps, such as heat treatment, secondary machining, and polishing, are often necessary to improve the quality of parts produced by the PBF process further. Components fabricated using PBF can exhibit superior properties compared to those made by conventional methods, largely due to the refined microstructures formed during the rapid cooling and solidification cycles, with cooling rates ranging from 10^3 to 10^6°C/s. Despite its potential for producing near-net-shape components, PBF technology has yet to be widely adopted across industries. A key barrier to broader implementation is the need for additional post-processing to achieve the surface quality required for many applications.[12]

The surface roughness (Ra, the arithmetic mean deviation of the assessed profile) of metal additive manufacturing (AM) components varies between 5 and 50 μm, depending on the material used.[12] At present, additional post-processes such as computer numerical control milling and turning, grinding, and polishing are implemented to achieve <1 μm Ra.[13] In addition, the following factors are important in determining the final surface quality built by PBF: Material feedstock (type, size, and quality), surface orientation concerning the process, support interface, and key processing parameters.[14] In recent years, the effect of machine factors on Ra variation has also received attention.

A variety of process parameters influence print quality in AM, including laser power, scanning speed, hatch spacing, layer thickness, scanning strategy, spot size, and pre-heat temperature.[15] In addition, other factors, such as gas flow rate and raw material properties, can impact process stability and overall print quality. These parameters collectively affect mass and heat transfer within the melt pool, thereby influencing melt pool behavior and the resulting part quality.[16] Meanwhile, heat treatment such as annealing also has a major effect on the fracture toughness and the threshold for fatigue crack initiation.[17] Two other parameters to be considered are scanning strategy and build orientation.[18]

The main characteristics of 1.2709 tool steel are characterized by high hardness and high ductility.[19-22] Its specific mechanical properties allow usage in high-stress components due to its high wear resistance.[23-25] Lasers can also be used to diminish the Ra of 1.2709 tool steel PBF parts up to 41% and increase their hardness up to 88%.[26] The maximum operating temperatures can further reduce wear. It is commonly used for applications such as conformal cooling systems for mold devices.[27,28] Various build strategies were developed to optimize the printing process of 1.2709 tool steel.[29-33] In hybrid manufacturing applications, 1.2709 tool steel (ASTM A276/M300) is widely used and adopted.[34-36] Its performance can also be enhanced via various heat treatment methods, such as solution annealing and aging after the PBF fabrication process.[37,38] Its microstructure change during heat treatment was investigated to obtain the optimal heat treatment process.[39-42]

This study aims to produce high-quality PBF parts and investigate the machine factors affecting the surface quality of as-built parts from the PBF process, such as inert gas flow and the position of parts relative to the location of the laser spot center.

2. Data and methods

2.1. Material and manufacturing

This study used 1.2709 tool steel (ASTM A276/M300) (Nikon SLM Solutions AG, Germany). As shown in Figure 1, the powder has a spherical morphology according to the standards of the German Institute for Standardization (DIN), European Standard (EN),

and International Standardization Organization (ISO) 3252:2023, with a particle size distribution of 10 – 45 μm. Its mass density is 8.0 g/cm^3. Its chemical composition is shown in Table 1. The powder was dried before loading into the PBF machine with professional dry bags (Nikon SLM Solutions AG, Germany) to ensure that the relative humidity of the powder was <10% before starting the PBF process.

An AM machine was used for the PBF process (SLM280 Twin 700W laser, Nikon SLM Solutions, Germany). A powder layer thickness of 30 μm was maintained, with a rotating hatch angle of 67°, whereas the laser beam focus diameter was 80 – 115 μm. The substrate plate was pre-heated to 200°C before starting the fabrication process. During the fabrication process, its gas flow came from right to left, and the recoating direction came forward and backward (Figure 2). High-purity argon gas was pumped into the build chamber to maintain oxygen level below 1,000 ppm throughout the fabrication process. Argon gas flow speed was controlled at 22 m/s to ensure that heavy spattering and soot formed from the rapid melting process could be effectively removed from the powder bed. The oxygen level was closely monitored via the AM system's monitoring control system to ensure that the oxygen level was below 1,000 ppm. The metal powder was spread onto the substrate plate evenly with the calibrated recoater. The gap between the recoater blade and the substrate plate was controlled at 200 μm to ensure consistency across build jobs. Steel substrate plates were also ground smoothly, with their Ra <30 μm, to ensure that the building of the first layer on the substrate plate was smooth.

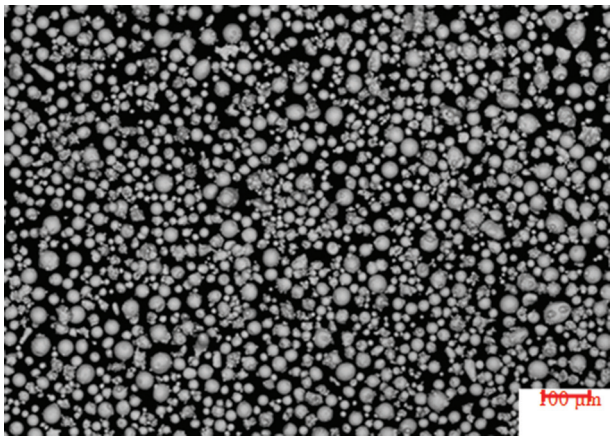

Figure 1. Powder characteristics of 1.2709 tool steel (ASTM A276/M300) metal powder. Scale bar: 100 μm; magnification: ×100.

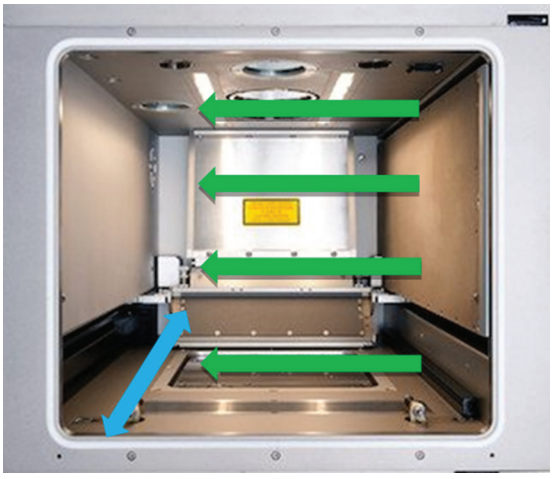

Figure 2. Gas flow and recoating direction of Nikon SLM Solutions' SLM280 twin laser additive manufacturing system.
Note: Green arrows indicate the gas flow direction, and blue arrow indicates the recoating direction.

2.2. Design of parts

In this study, the testing parts in Figure 3 were produced and measured for their surface quality. Each part consisted of a 25 × 25 × 10 mm^3 cube with a 25 mm diameter, 10 mm high cylinder on top. Twenty parts were produced per plate. The parts were removed from the substrate plate for further measurements of their surface quality. Surface quality was measured on the front, back, left, and right surfaces of every cube. Eighty measurements were performed to investigate the surface quality of as-built PBF parts against gas flow direction, recoat direction, and consistency across the full plate. The parts were stored inside sealed boxes during transportation to minimize the contamination of the part surface from the atmosphere.

2.3. Experimental and characterization methods

In this study, a 3D laser scanning microscope (VK-X200 series, KEYENCE, Japan) was used. On every surface, a 1 mm × 1 mm surface area was measured. Relative density was determined by testing specimens using light microscopy. Tensile testing was performed following the standards of DIN, EN, and ISO 6892 – 1:2020 B and conducted at room temperature. Tensile parts were processed before testing (geometry according to the standards of DIN, EN 50125:2016 – D6 × 30, and DIN 50125:2016 – C6 × 30). Hardness testing was conducted according to the standards

Table 1. Chemical composition of 1.2709 tool steel powder (mass fraction in %)

Element	Fe	Ni	Co	Mo	Ti	Al	Mn	Si	C
%	Balance	18.00 – 19.00	8.50 – 9.50	4.70 – 5.20	0.50 – 0.80	0.05 – 0.15	0.10	0.10	0.03

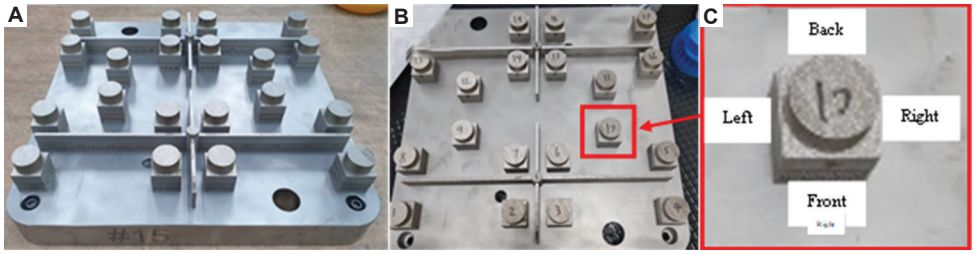

Figure 3. As-built parts are produced using the powder bed fusion system. (A) As-built parts on the substrate plate; (B) parts with labeling from the top view; (C) front, back, left, and right surfaces of parts.

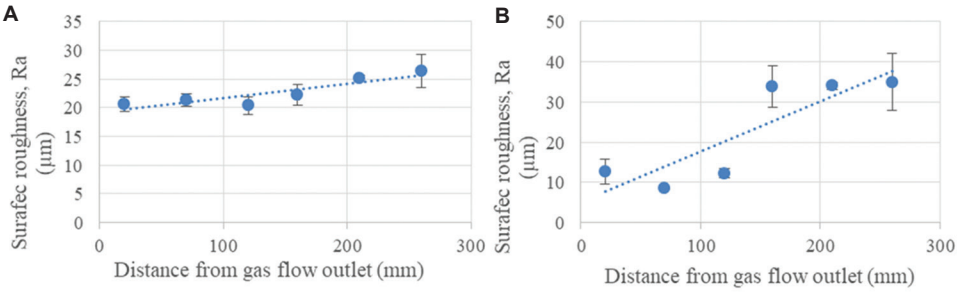

Figure 4. Surface roughness for surfaces against their distance to the gas flow outlet. (A) Overall surface. (B) left surface.

DIN, EN, and ISO 6507 – 1:2024. Measurement direction was "2" according to the Association of German Engineers (VDI) 3405 2.1.

3. Results and discussion

3.1. Mechanical properties

The results of the mechanical properties of this 1.2709 tool steel (ASTM A276/M300) metal powder produced from Nikon SLM Solutions' SLM280 twin laser AM system are shown in Table 2 after conducting respective density test, tensile test, and hardness test.

3.2. Surface quality properties

The overall average Ra of all 80 measurements in this study is 22.6 ± 11.9 μm. The average Ra of left, right, front, and back surfaces are 23.0 ± 15.3 μm, 24.5 ± 14.3 μm, 19.1 ± 6.9 μm, and 23.8 ± 9.2 μm, respectively. Detailed data of all measurements are shown in Table 3. All parts' right surfaces were the closest to the gas flow outlet, whereas their left surfaces were the furthest away from the gas flow outlet. Their front and back surfaces faced the recoater's moving direction when recoating metal powder during the PBF process.

3.3. Effect of gas flow

The effect of gas flow on surface quality was analyzed. Figure 4 and Table 4 show the change in Ra due to the change in its distance from the gas flow outlet. These results showed that the measured Ra increased gradually when the fabricated parts were placed further from the gas flow outlet. The impact of such gas flow became significant when the distance exceeded 200 mm. Ra of parts at a distance of 120 mm from the gas flow outlet was better than that at 70 mm. The potential root cause was that those parts placed at a distance of 120 mm from the gas flow outlet were closer to the center of the laser spot location. Therefore, such results also show that the distance of the part from the center of the laser position has a stronger impact on the as-built parts' Ra compared to the distance from the gas flow outlet.

Table 2. Mechanical properties of 1.2709 tool steel (ASTM A276/M300) used in this study

Properties	Values
Relative density	99.9%
Ultimate tensile strength (MPa)	1135±75
Yield strength (MPa)	915±120
Elongation (%)	12±3
Vickers hardness (HV10)	339±35

Table 3. Overall surface quality of all measurements

Surface direction	Surface roughness, Ra (μm)
Overall	22.6±11.9
Left	23.0±15.3
Right	24.5±14.3
Front	19.1±6.9
Back	23.8±9.2

The argon gas was blown from the inert gas outlet on the right of the build chamber. Spattering and soot were formed during the rapid laser melting process. Although most spattering and soot were expected to be blown away from the powder bed working area, a portion of this spattering and soot would still fall onto the powder bed, affecting the surface quality if it fell onto the edges of the fabricated parts. This issue became more significant for those parts placed on the left part of the building areas because more spattering and soot were generated from the right areas.

In addition, Figure 5 shows that the standard deviation of the Ra increases gradually when the distance to the gas flow outlet increases from 20.0 mm to 120.0, 160.0, and 260.0 mm, with the same number of measurements and parts at each location. When parts were placed further from the gas outlet, unpredictable spattering and soot would have a more significant impact on the parts' Ra. Moreover, while the argon gas flow speed was maintained inside the build chamber, its effectiveness in removing the spattering and soot decreased when the parts were further away from the gas outlet position. A sintered wall was used at the argon gas outlet to ensure a laminar flow was blown into the build chamber. Turbulence would still be formed in the chamber, especially in spaces further away from the gas flow outlet. Such turbulence would also bring some spattering and soot back to the powder bed in the left area, affecting the as-built parts' surface quality.

Table 4. Surface roughness for all surfaces against their distance to the gas flow outlet

Distance to gas flow outlet (mm)	Part number	Average surface roughness (μm)
20.0	4, 5, 16, 17	20.7±2.5
70.0	10, 11	21.4±2.1
120.0	3, 6, 15, 18	20.4±3.1
160.0	2, 7, 14, 19	22.3±3.5
210.0	9, 12	25.1±1.1
260.0	1, 8, 13, 20	26.4±5.7

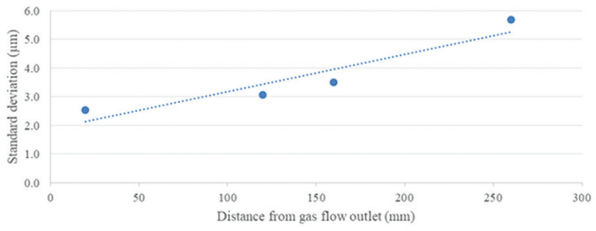

Figure 5. Standard deviation of the parts' surface roughness against their distance to the gas flow outlet

3.4. Effect of build position

The average Ra of each part is defined as the average value of its front, back, left, and right surfaces' Ra values (Equation I):

$$R_a\,(sample) = average\,(R_a[front] + R_a\,[back] + R_a\,[left] + R_a\,[right]) \quad (I)$$

In this study, a twin laser PBF system was used. The laser positions are marked as "X" in Figure 6. Detailed data of all 20 parts and their positions are shown in Figure 6. Parts placed near the center of the laser, such as parts 2, 3, 6, 7, 14, 15, 18, and 19, had a better surface quality in the range of 15 – 20 μm. Parts placed further away from the center of the laser, such as parts 1, 4, 8, and 13, had poorer surface quality in the range of 25 – 35 μm.

The effect of building positions was analyzed. Figure 7 and Table 5 show the average Ra compared to the distance of the fabricated parts from the center of the laser spot positions. Ra values of PBF fabricated parts increased gradually when the parts were placed further away from the center of the laser spot location.

When the parts were placed further away from the center of the laser spot, the laser spot became more

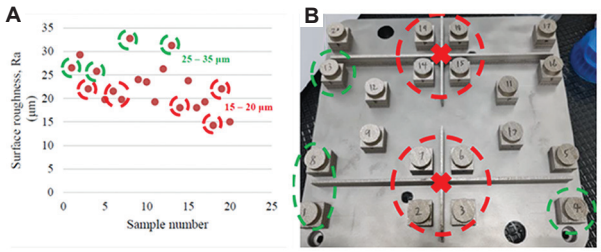

Figure 6. The position of parts in the build chamber and their overall surface quality. (A) Overall surface quality of the parts. (B) Positions of parts with labeling.
Note: The "X" marks in (B) indicate the laser position in the powder bed fusion system. Red circles indicate regions close to the center of the laser, whereas green circles indicate further regions. The parts included in rectangles in (A) correspond to the parts included in the circles of the same color in (B).

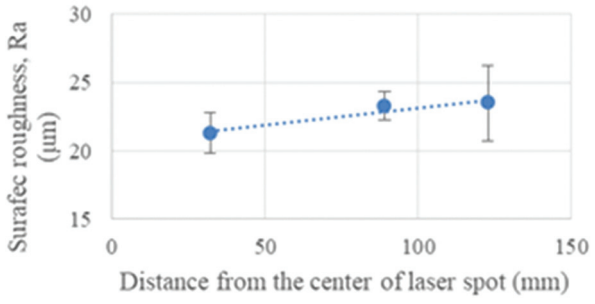

Figure 7. Surface roughness for all surfaces against their distance to the center of the laser spot

elliptical. This would result in reduced energy density, thus causing higher Ra or even forming porosity inside the part due to a lack of fusion. Figure 8 illustrates the consequence of such laser interaction due to the position of the parts. When the laser was shot directly onto the powder bed from 90° vertically, the melt pool and laser spot size were nearly a perfect round shape. However, when the part moved away from the center of the laser spot, the melt pool shape became distorted, which negatively affected the surface quality of the as-built parts.

3.5. Summary of the surface quality of parts

Figure 9 summarizes the measured surface quality of parts fabricated on different positions of the substrate plate, with the indication of the gas flow direction and recoating directions.

Table 5. Surface roughness for all surfaces against their distance to the center of the laser spot

Distance from the laser center (mm)	Part number	Average surface roughness (μm)
32.0	2, 3, 6, 7, 14, 15, 18, 19	21.3±3.0
89.0	9, 10, 11, 12	23.3±2.0
122.6	1, 4, 5, 8, 13, 16, 17, 20	23.5±5.5

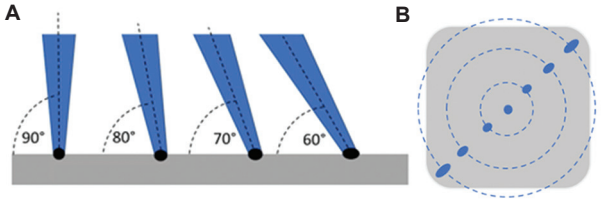

Figure 8. Illustration of laser interaction on the powder bed. (A) Laser interaction with powder bed at different incident angles. (B) Elliptical shape of the laser beam when the parts are placed at a different location on the substrate plate (courtesy Nikon SLM Solutions AG).

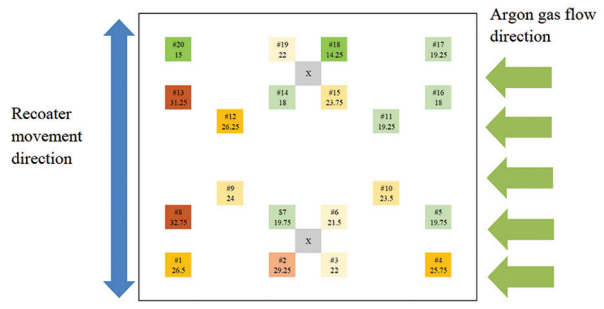

Figure 9. Surface roughness for all parts on the substrate plate.
Notes: # indicates part number. The "X" mark in gray indicates the center of the laser spot. Green boxes indicate that produced parts have a good Ra value smaller than 20 μm. Orange boxes indicate those produced parts have a relatively poor Ra value between 20 μm and 30 μm. Red boxes indicate those produced parts have a poor Ra value larger than 30 μm.

When all identical parts with the same geometry design and the same support design were fabricated inside the same build chamber, using the same argon gas settings, recoating settings, metal powder, and process parameters, their Ra varied across the full substrate plate. The key factors that account for such variations are the distance from the parts to the gas flow outlet and the center of the laser spot. For example, parts 1, 8, and 13 had the worst Ra because they were furthest away from the gas flow outlet, as well as the center of the laser spot. On the other hand, parts 5, 7, 11, 14, 16, 17, and 18 had better Ra because these parts were placed close to either the center of the laser spot or the gas flow outlets. As a general trend observed from the measurements, parts positioned on the right side of the substrate plate (which are closer to the gas flow outlet) and parts placed near the center of the laser spot have better Ra compared with those parts that are placed away from the gas flow outlet and the center of laser spot position.

4. Conclusion

In this study, 1.2709 tool steel (ASTM A276/M300) was fabricated using the PBF system. The main conclusions of the study are summarized as follows:

(i) Fully dense parts of a relative density of 99.9% were fabricated from the PBF process with platform pre-heating. Without heat treatment, its as-built ultimate tensile strength was 1,135 ± 75 MPa, yield strength was 915 ± 120 MPa, and elongation was 12 ± 3 %. It has HV10 at 339 ± 35.

(ii) Surface measurements were performed for parts placed across the substrate plate, and the average Ra for as-built vertical walls was 22.6 ± 11.9 μm.

(iii) Machine factors, such as the distance of parts to the gas flow outlet, impact the Ra of as-built parts. The Ra becomes higher when the parts are placed further away from the inert gas outlet. The distance of parts to the center of the laser spot also impacts the Ra of as-built parts. The Ra increases when the parts are placed further away from the center of the laser spot location.

This study provides guidance and reference for optimizing the PBF fabrication strategy, especially on the part placement, considering machine factors such as inert gas outlet and laser spot position.

Acknowledgments

The part fabrication work was supported by SLM Solutions Singapore Pte Ltd. The metal powder was supported by SLM Solutions Singapore Pte Ltd.

Funding

None.

Conflict of interest

The authors declare that they have no known competing financial interests or personal relationships that could have appeared to influence the work reported in this paper.

Author contributions

Conceptualization: Zhen Lu
Formal analysis: Zhen Lu
Investigation: Zhen Lu
Methodology: Zhen Lu
Writing – original draft: Zhen Lu
Writing – review & editing: All authors

Ethics approval and consent to participate

Not applicable.

Consent for publication

Not applicable.

Availability of data

The data presented in this study are available upon request from the corresponding author.

Further disclosure

Part of the findings have been presented in a conference titled "Impact of Machine Factors on the Surface Quality of Parts Fabricated by Selective Laser Melting," Materials Today: Proceedings (AMBW 2022), by Zhen Lu, Chee Kai Chua, Ming Jen Tan, Yi Zhang, and Jia An.

References

1. ISO/ASTM. *Additive Manufacturing -- General Principles -- Part 2: Overview of Process Categories and Feedstock, ISO Online Browsing Platform*; 2021. Available from: https://www.iso.org/obp/ui/#iso:std:iso-astm:52900:ed-2:v1:en [Last accessed on 2025 May 12].
2. Sing SL, Yeong WY, Wiria FE, *et al*. Direct selective laser sintering and melting of ceramics: A review. *Rapid Prototyp J*. 2017;23(3):611-623.
   doi: 10.1108/RPJ-11-2015-0178
3. Wong KV, Hernandez A. A review of additive manufacturing. *ISRN Mech Eng*. 2012;2012:208760.
   doi: 10.5402/2012/208760
4. Jiao L, Chua ZY, Moon SK, Song J, Bi G, Zheng H. Femtosecond laser produced hydrophobic hierarchical structures on additive manufacturing parts. *Nanomaterials*. 2018;8(8):601.
   doi: 10.3390/nano8080601
5. Yap CY, Chua CK, Dong ZL, *et al*. Review of selective laser melting: Materials and applications. *Appl Phys Rev*. 2015;2(4):041101.
   doi: 10.1063/1.4935926
6. Zhang B, Dembinski L, Coddet C. The study of the laser parameters and environment variables effect on mechanical properties of high compact parts elaborated by selective laser melting 316L powder. *Mater Sci Eng A*. 2013;584:21-31.
   doi: 10.1016/j.msea.2013.06.055
7. Zhang LC, Attar H. Selective laser melting of titanium alloys and titanium matrix composites for biomedical applications: A review. *Adv Eng Mater*. 2016;18(4):463-475.
   doi: 10.1002/adem.201500419
8. Tan JHK, Sing SL, Yeong WY. Microstructure modelling for metallic additive manufacturing: A review. *Virtual Phys Prototyp*. 2019;15(1):87-105.
   doi: 10.1080/17452759.2019.1677345
9. Boyer RR. An overview on the use of titanium in the aerospace industry. *Mater Sci Eng A*. 1996;213(1-2):103-114.
   doi: 10.1016/0921-5093(96)10233-1
10. Boyer RR. Applications of beta titanium alloys in airframes. *JOM*. 1993;45(7):33-46.
11. Boyer RR. Aerospace applications of beta titanium alloys. *JOM*. 1994;46(7):20-23.
12. Nagalingam AP, Yeo SH. Controlled hydrodynamic cavitation erosion with abrasive particles for internal surface modification of additive manufactured components. *Wear*. 2018;414-415:89-100.
   doi: 10.1016/j.wear.2018.08.006
13. Mumtaz K, Hopkinson N. Top surface and side roughness of Inconel 625 parts processed using selective laser melting. *Rapid Prototyp J*. 2009;15(2):96-103.
   doi: 10.1108/13552540910943397
14. Triantaphyllou A, Giusca CL, Macaulay GD, *et al*. Surface texture measurement for additive manufacturing. *Surf Topogr Metrol Prop*. 2015;3(2):024002.
   doi: 10.1088/2051-672X/3/2/024002
15. Nguyen HD, Pramanik A, Basak AK, *et al*. A critical review on additive manufacturing of Ti-6Al-4V alloy: Microstructure and mechanical properties. *J Mater Res Technol*. 2022;18:4641-4661.
   doi: 10.1016/j.jmrt.2022.04.055
16. Zhang B, Li Y, Bai Q. Defect formation mechanisms in selective laser melting: A review. *Chin J Mech Eng*. 2017;30:515-527.
   doi: 10.1007/s10033-017-0121-5
17. Belan J, Bokůvka O, Uhríčik M, Kuchariková L, Vaško A. The influence of quenching on fatigue life of Ti6Al4V alloy.

IOP Conf Ser Mater Sci Eng. 2021;1178:012006.

doi: 10.1088/1757-899X/1178/1/012006

18. Shipley H, McDonnell D, Culleton M, *et al*. Optimisation of process parameters to address fundamental challenges during selective laser melting of Ti-6Al-4V: A review. *Int J Mach Tools Manuf*. 2018;128:1-20.

doi: 10.1016/j.ijmachtools.2018.01.003

19. Żaba K, Balcerzak M, Kuczek Ł, *et al*. Application of powder-bed fusion of metals using a laser for manufacturing of M300 maraging steel tools intended for sheet metal bending. *Materials (Basel)*. 2024;17(24):6185.

doi: 10.3390/ma17246185

20. Raghuraman V, Kumar TS. The impact of different heat treatments on the surface characteristics, residual stresses, and tensile strength of maraging steel 1.2709 parts produced by LPBF. *Results Eng*. 2025;26:105509.

doi: 10.1016/j.rineng.2025.105509

21. Marchini L, Tonolini P, Montesano L, *et al*. The corrosion resistance of maraging steel 1.2709 produced by L-PBF in contact with molten Al-alloys. *Procedia Struct Integr*. 2024;53:203-211.

doi: 10.1016/j.prostr.2024.01.025

22. Sawicki J, Stachurski W, Kuryło P, *et al*. Comparative analysis of the dimensional accuracy and surface characteristics of gears manufactured using the 3D printing (DMLS) technique from 1.2709 steel. *Materials (Basel)*. 2025;18(7):1461.

doi: 10.3390/ma18071461

23. Asnafi N. Application of laser-based powder bed fusion for direct metal tooling. *Metals*. 2021;11(3):458.

doi: 10.3390/met11030458

24. Piekło J, Garbacz-Klempka A, Myszka D, Figurski K. Numerical and experimental analysis of strength loss of 1.2709 maraging steel produced by selective laser melting (SLM) under thermo-mechanical fatigue conditions. *Materials* (*Basel*). 2023;16(24):7682.

doi: 10.3390/ma16247682

25. Strakosova A, Průša F, Michalcová A, Kratochvíl P, Vojtěch D. Annealing response of additively manufactured high-strength 1.2709 maraging steel depending on elevated temperatures. *Materials (Basel)*. 2022;15(11):3753.

doi: 10.3390/ma15113753

26. Černašėjus O, Škamat J, Markovič V, *et al*. Surface laser processing of additive manufactured 1.2709 steel parts: Preliminary study. *Adv Mater Sci Eng*. 2019;2019:7029471.

doi: 10.1155/2019/7029471

27. Piekło J, Garbacz-Klempka A. Use of maraging steel 1.2709 for implementing parts of pressure mold devices with conformal cooling system. *Materials* (*Basel*). 2020;13(23):5533.

doi: 10.3390/ma13235533

28. Ravi S, Satheeshkumar V, Kumaran M. Mechanical properties and microstructure characterization of stainless steel 316L and maraging steel 1.2709 bimetallic structures fabricated by laser powder bed fusion. *J Mater Eng Perform*. 2025.

doi: 10.1007/s11665-025-11451-8

29. Jarfors AEW, Shashidhar ACGH, Yepur HK, Steggo J, Andersson NE, Stolt R. Build strategy and impact strength of SLM produced maraging steel (1.2709). *Metals*. 2021;11(1):51.

doi: 10.3390/met11010051

30. Jhabvala J, Boillat E, Antignac T, Glardon R. On the effect of scanning strategies in the selective laser melting process. *Virtual Phys Prototyp*. 2010;5(2):99-109.

doi: 10.1080/17452751003688368

31. Jägle EA, Choi PP, Van Humbeeck J, Raabe D. Precipitation and austenite reversion behavior of a maraging steel produced by selective laser melting. *J Mater Res*. 2014;29(17):2072-2079.

doi: 10.1557/jmr.2014.204

32. Hoseini SRE, Arabi H, Razavizadeh H. Improvement in mechanical properties of C300 maraging steel by application of VAR process. *Vacuum*. 2008;82(5):521-528.

doi: 10.1016/j.vacuum.2007.08.008

33. Hatos I, Hargitai H, Fekete G, Fekete I. Effect of energy density on the mechanical properties of 1.2709 maraging steel produced by laser powder bed fusion. *Materials (Basel)*. 2024;17(14):3432.

doi: 10.3390/ma17143432

34. Kumaran M, Ravi S. Influence of hybrid additive manufacturing processes on the microstructure and mechanical properties of maraging steel 1.2709 components with post-processing heat treatments. *Mater Lett*. 2024;377:137427.

doi: 10.1016/j.matlet.2024.137427

35. Vinoth V, Kumaran M, Ravi S. Investigation of heat treatment effects on hybrid manufacturing of stainless steel 316L components using directed energy deposition: Microstructural and tensile behavior analysis. *J Mater Eng Perform*. 2025.

doi: 10.1007/s11665-025-11023-w

36. Kučerová L, Zetková I, Jeníček Š, Burdová K. Production of hybrid joints by selective laser melting of maraging tool steel 1.2709 on conventionally produced parts of the same steel. *Materials* (*Basel*). 2021;14(9):2105.

doi: 10.3390/ma14092105

37. Simm TH, Sun L, Galvin DR, *et al*. The effect of a two-stage heat-treatment on the microstructural and mechanical properties of a maraging steel. *Materials* (*Basel*). 2017;10(12):1346.

doi: 10.3390/ma10121346

38. Monkova K, Zetkova I, Kučerová L, *et al*. Study of 3D printing direction and effects of heat treatment on mechanical properties of MS1 maraging steel. *Arch Appl Mech*. 2019;89:791-804.

doi: 10.1007/s00419-018-1389-3

39. Mutua J, Nakata S, Onda T, Chen ZC. Optimization of selective laser melting parameters and influence of post heat treatment on microstructure and mechanical properties of maraging steel. *Mater Des*. 2018;139:486-497.

doi: 10.1016/j.matdes.2017.11.042

40. Tan C, Zhou K, Ma W, Zhang P, Liu M, Kuang T. Microstructural evolution, nanoprecipitation behavior and mechanical properties of selective laser melted high-performance grade 300 maraging steel. *Mater Des*. 2017;134:23-34.

doi: 10.1016/j.matdes.2017.08.026

41. Mooney B, Kourousis KI, Raghavendra R. Plastic anisotropy of additively manufactured maraging steel: Influence of the build orientation and heat treatments. *Addit Manuf*. 2019;25:19-31.

doi: 10.1016/j.addma.2018.10.032

42. Bai Y, Yang Y, Wang D, Zhang M. Influence mechanism of parameters process and mechanical properties evolution mechanism of maraging steel 300 by selective laser melting. *Mater Sci Eng A*. 2017;703:116-123.

doi: 10.1016/j.msea.2017.06.033

ACCSCIENCE PUBLISHING

Engineering Science in Additive Manufacturing

ORIGINAL RESEARCH ARTICLE

Hot isostatic pressing temperature effects on the microstructure and mechanical properties of laser powder bed fusion-manufactured Hastelloy X

Bingqiu Wang[1], Rongrong Huang[1], Yiming Sun[2], Xiaohui Zhou[1], Linan Xue[2], Junjun Jiang[1], Swee Leong Sing[3], Bo Chen[1,4], Xiaoguo Song[1,4], and Caiwang Tan[1,4]*

[1]State Key Laboratory of Precision Welding and Joining of Materials and Structures, School of Materials Science and Engineering, Harbin Institute of Technology, Harbin, Heilongjiang, China

[2]Department of Welding and Materials Engineering, Beijing Power Machinery Institute, Beijing, China

[3]Department of Mechanical Engineering, College of Design and Engineering, National University of Singapore, Singapore

[4]School of Materials Science and Engineering, Shandong Institute of Shipbuilding Technology, Weihai, Shandong, China

Abstract

Hot isostatic pressing (HIP) of Hastelloy X alloy is an essential heat treatment process in manufacturing hot-end components for aerospace engines. This study investigated the microstructure evolution and mechanical properties of laser powder bed fusion-manufactured Hastelloy X superalloy at room and high temperatures under various HIP treatments. The results showed that as the HIP temperature increased, the recrystallization degree increased, with the proportion of low-angle grain boundaries decreasing from 49.7% at HIP1100 to 0% at HIP1210. The carbides along the grain boundaries evolved from particle distribution at HIP1100 to chain-like distribution at HIP1180 and coarsened at HIP1210. In the room temperature tensile test, specimens treated at HIP1100 exhibited the highest tensile strength due to restrained dislocation slip, grain refinement strengthening, and carbide dispersion strengthening. In the high-temperature tensile test, significant carbide coarsening was induced at HIP1100, while minimal changes were observed at HIP1180 and HIP1210. As the HIP temperature increased, the tensile strength and elongation both improved due to the synergistic effect of the reduced number of grain boundaries and chain-like distribution of carbides. The cracks primarily propagated along the grain boundaries, with the HIP1210 specimen showing a better capacity for crack inhibition.

Keywords: Hastelloy X superalloy; Laser powder bed fusion; High temperature tensile test; Microstructure; Carbide

***Corresponding author:**
Caiwang Tan
(tancaiwang@hitwh.edu.cn)

Citation: Wang B, Huang R, Sun Y, *et al*. Hot isostatic pressing temperature effects on the microstructure and mechanical properties of laser powder bed fusion-manufactured Hastelloy X. *Eng Sci Add Manuf.* 2025;1(2):025240015. doi: 10.36922/ESAM025240015

Received: May 14, 2025

Revised: June 20, 2025

Accepted: June 23, 2025

Published online: June 30, 2025

1. Introduction

Hastelloy X superalloy is a key structural material in the present aerospace industry due to its excellent high-temperature creep strength and exceptional corrosion

resistance.[1-3] As the core of aerospace vehicles, the turbofan engines encounter challenges such as complex structures, prolonged cycles, and high costs with casting and forging techniques.[4,5] Compared with traditional techniques, the laser powder bed fusion (LPBF) technology was employed to enable the integrated precision fabrication of complex structures.[6-8] However, the rapid layer-by-layer manufacturing process of as-built structures harmed the microstructure and mechanical properties, hindering the practical application of LPBF technology.[9,10] Therefore, heat treatment was necessary for as-built structures to enhance the comprehensive mechanical properties at room and high temperatures.[11-13]

Recently, to meet the application requirements of the above-mentioned specifications for Hastelloy X, the solution treatment was widely employed to optimize defects, homogenize the microstructure, and enhance mechanical properties. In research on room temperature mechanical properties, Keshavarzkermani *et al.*[14] analyzed the grain misorientation and grain boundary structure of as-built and solution-treated LPBF Hastelloy X samples. The result showed that the pores were eliminated, and grain recrystallization with varying degrees was induced with different solution treatment methods, accompanied by the columnar grains transforming into recrystallized equiaxed grains. Cheng *et al.*[15] investigated the strengthening mechanism between the microstructure and mechanical properties of the solution-treated Hastelloy X samples. They found that the full release of distortion energy with the complete grain recrystallization led to a significant reduction in the dislocation density and the appearance of twins. These studies succeeded in enhancing the mechanical properties at room temperature with limited grain anisotropy and twin boundary transition.

More importantly, the high-temperature mechanical properties of the Hastelloy X alloy are critical for the manufacturing of hot-end components for aerospace engines.[16-18] Montero-Sistiaga *et al.*[19] compared the high-temperature mechanical properties of as-built and solution-treated Hastelloy X specimens. They observed a substantial decline in both strength and ductility of the Hastelloy X alloy, which may be associated with carbide formation at the grain boundaries during the high-temperature tensile test. Agrawal *et al.*[20] also confirmed that the reduced ductility with the elevated temperature was attributed to the intergranular fracture caused by the carbides at the grain boundaries. Although the solution treatment of Hastelloy X alloy achieved high mechanical properties at room temperature, it failed to acquire sufficient mechanical properties in the high-temperature tensile test,[21] thereby impeding its practical application. Furthermore, it could be inferred that the low carbide content in the solution-treated Hastelloy X specimens restricted carbide formation and mechanical performance during high-temperature service. Therefore, it is imperative to devise a new heat treatment method to enhance the carbides of Hastelloy alloys.

In recent studies, hot isostatic pressing (HIP) has been considered a thermally activated process that promotes grain boundary migration and carbides with limited cooling rate.[22] A few studies reported that HIP treatment was beneficial for the enhancement of deformation capacity at high-temperature tensile tests.[23-25] It was found that the high-temperature deformation ability of HIP specimens was considered to be possibly affected by grain boundary proportion and carbide precipitation.[26-29] Marchese *et al.*[30] found that HIP-triggered recrystallization generated equiaxed grains, and the slow cooling rate led to the production of intergranular carbides and intragranular carbides in the 1160°C HIP process of Hastelloy X alloy. According to a report by Tomus *et al.*,[31] the low number of finely dispersed carbides segregating at the grain boundaries in the Hastelloy X alloy HIP-treated at 1,175°C showed minimal effect on its mechanical properties. Sanchez-Mata *et al.*[24] proposed that compared to discrete carbides along the grain boundaries under ST, HIP treatment at 1,155°C brought more continuous precipitates along grain boundaries in Hastelloy X specimens. Li *et al.*[32] proved that the chain-like and plate-like precipitates distributed at the grain boundaries under the HIP temperature of 1,100°C – 1,175°C contributed to the different mechanical properties of Hastelloy X specimens. Sun *et al.*[33] conducted HIP treatment at 1,050°C and solution treatment on LPBF-manufactured GH3536 alloy, with results showing that both tensile strength and elongation at high temperature were improved. In summary, the present HIP treatment temperature ranges from 1,050°C to 1,175°C for LPBF-manufactured Hastelloy X structures, based on casting and forging structures. However, a higher HIP temperature was required to activate the recrystallization and carbide precipitation process due to the distinctive microstructure characteristics, which are rarely reported in present studies. Therefore, by adopting elevated HIP temperature, this study primarily focused on the role of carbide control in enhancing the high-temperature mechanical properties of LPBF-manufactured Hastelloy X superalloy and the mechanism of grain recrystallization and carbides on mechanical performance following HIP treatment.

This study fabricated an LPBF as-built Hastelloy X specimen, along with those subjected to HIP treatment at 1,100°C, 1,180°C, and 1,210°C. The effects of HIP treatment on substructure, recrystallization, and carbide

characteristics were investigated, and mechanical properties at room and high temperatures were tested using failure mode analysis.

2. Experimental methods

2.1. Materials and deposition process

The Hastelloy X superalloy powder utilized in this experiment was gas atomized by Xi'an Bright Laser Technologies Co., Ltd (China). The composition of Hastelloy X superalloy powder is listed in Table 1.

The SLM280 machine produced by Solution GmbH in Germany was employed for LPBF. The laser focus diameter ranged from 80 μm to 115 μm. The experimental process was conducted under the protection of nitrogen, maintaining the proportion of oxygen below 0.2%. The pre-heat temperature of the substrate was set to 150°C to reduce the temperature gradient during the LPBF process. Before the LPBF process, the Magic24 software (version 24.0) was configured with the SLM280 to design the three-dimensional model of test samples, followed by importing the experiment parameters into SLM280 for setup. Based on the preliminary experiments, the experiment parameters for deposition were set at a laser power of 300W, scanning speed of 900 mm/s, and a layer rotation angle for scanning of 67°, as shown in Figure 1A.

The HIP treatment was conducted using the HIPEX850 HIP machine manufactured by CISRI HIPEX Technology CO., LTD. (China). The HIP machine utilized nitrogen as the pressure-transmitting medium, ensuring uniform pressure application on the component surface. According to the melting temperature of Hastelloy X alloy (1,295°C – 1,381°C), HIP treatments were performed at 1,100°C, 1,180°C, and 1,210°C, with a pressure of 160 MPa, a holding time of three hours, and a ventilation cooling rate of 4.5 K/min. The HIP specimens at 1,100°C, 1,180°C, and 1,210°C were labeled as HIP1100, HIP1180, and HIP1210, respectively.

2.2. Material characterization

The test specimens were cut from the LPBF-manufactured samples using wire electrical discharge machining, and the cross-sections were mechanically polished to achieve a smooth mirror finish. Aqua regia (hydrochloric acid: nitric acid: 3:1) was used to etch the cross-sectional surfaces of both the as-built and HIP specimens. The DSX510, manufactured by Olympus Corporation (Japan), was employed to observe the microstructural morphology and defects. The ImageJ software (version 1.53) was used to statistically analyze the rate of pores and carbides within a certain area.

The Zeiss's MERLIN Compact scanning electron microscope (SEM; Germany) was used for high-magnification microstructure observation. Energy dispersive spectroscopy integrated with the SEM was utilized for chemical composition analysis of the microstructure. After mechanical and electrolytic polishing to remove the strain layer, electron backscattered diffraction (EBSD) integrated with SEM was employed for microstructure characterization of the specimens. The TSL Orientation Imaging Microscopy analysis software (version 7.0) was used for the subsequent analysis of EBSD data.

The transmission electron microscopy (TEM) specimens were extracted from the central region of the as-built and HIP specimens. They were mechanically thinned to 60 μm using sandpaper, followed by ion milling. The ThemisZ spherical aberration-corrected TEM (Tecnai G2 F30, US) was used to analyze the substructure morphology and element distribution within the specimens.

After the sample surfaces were polished, the hardness of cross-sections of the as-built and HIP specimens

Table 1. Chemical composition of Hastelloy X

Element	Nickel	Ferum	Chromium	Molybdenum	Cobalt	Carbon	Tungsten	Silicon	Aluminum	Titanium
Content (wt.%)	Balance	18.86	21.16	9.78	2.20	0.067	0.62	0.037	0.028	<0.01

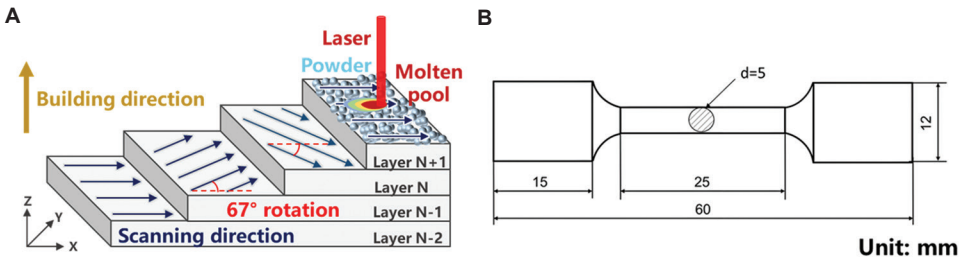

Figure 1. Schematic of building specimens. (A) A schematic diagram of the scanning strategy by laser powder bed fusion. (B) The profile of the tensile test specimen along the building direction.

was measured using Qness Q10 hardness tester (Qness, Austria), with a test load of 1 kg and a holding time of 10 s. Eight points were sampled along the central line in the building direction of each specimen. According to the GB/T 228.1-2010 standard, tensile tests at room temperature were conducted using the UTM5105X electronic universal material testing machine manufactured by SUNS (China). The tensile speed was set at 0.5 mm/min before yielding and 2.5 mm/min after yielding. The tensile test specimens were obtained by wire electrical discharge machining, and the dimensions of the tensile test specimens are shown in Figure 1B. Before the tensile test, the surfaces were polished to reduce the influence of surface roughness on the tensile properties.

Based on the average actual service temperature of hot-end components of aerospace engines manufacturing, high-temperature tensile tests at 900°C were conducted to investigate the effect of HIP temperature on high-temperature mechanical properties according to the GB/T 37783-2019 standard. The tests were performed using the SANS-CMT-52052 electronic universal testing machine (MTS Systems Corporation, China), with a tensile speed of 0.5 mm/min before yielding and 1.5 mm/min after yielding.

3. Results and discussion

3.1. Microstructures

Figure 2 presents the X-Y cross-sectional optical microscopy microstructural morphology of the as-built, HIP1100, HIP1180, and HIP1210 Hastelloy X specimens. The pores in the as-built specimen were observed at the edge of the obvious laser scanning tracks, as depicted in Figure 2A. However, the pores were effectively eliminated after the HIP treatments, and the laser scanning tracks completely disappeared at HIP1180 and HIP1210. The fine and coarse equiaxed grains were distributed at the edge and the center of the scanning tracks at HIP1100, respectively, as shown in Figure 2B. An uneven distribution of grain size was observed at HIP1180, as shown in Figure 2C. The finer equiaxed grains were engulfed by larger ones at HIP1210, resulting in a more uniform grain size distribution, as depicted in Figure 2D.

Figure 3 shows the EBSD results of the as-built, HIP1100, HIP1180, and HIP1210 specimens to investigate the microstructural evolution after various HIP treatments. The columnar grains in the as-built specimen were characterized by a small aspect ratio, with a length of 80 – 100 μm, corresponding to the set laser scanning spacing, as shown in Figure $3A_1$. In addition, the grains were observed with a maximum multiple of uniform density (MUD) value of 6.4, as depicted in Figure $3A_3$. After the HIP1100 treatment, the columnar grains of the as-built specimen transformed into equiaxed grains without a specific grain orientation, accompanied by a MUD value of 4.834, as shown in Figure $3B_1$ and B_3. At HIP1180 and HIP1210, the MUD values decreased to 2.915 and 3.487, respectively, indicating that the texture in the as-built specimen was almost eliminated, as depicted in Figure $3C_1$, C_3, D_1, and D_3. Therefore, it could be inferred that as the HIP temperature increased, a random grain orientation was achieved and the microstructure anisotropy was restrained.

Moreover, the angle distribution of the grain boundary changed, as shown in Figure $3A_2$, B_2, C_2, and D_2. Low-angle grain boundaries were observed in the as-built specimen, accounting for 51.5% (the ratio of low-angle grain boundary length to the total grain boundary length), as shown in Figure $3A_2$. This indicated the presence of a large number

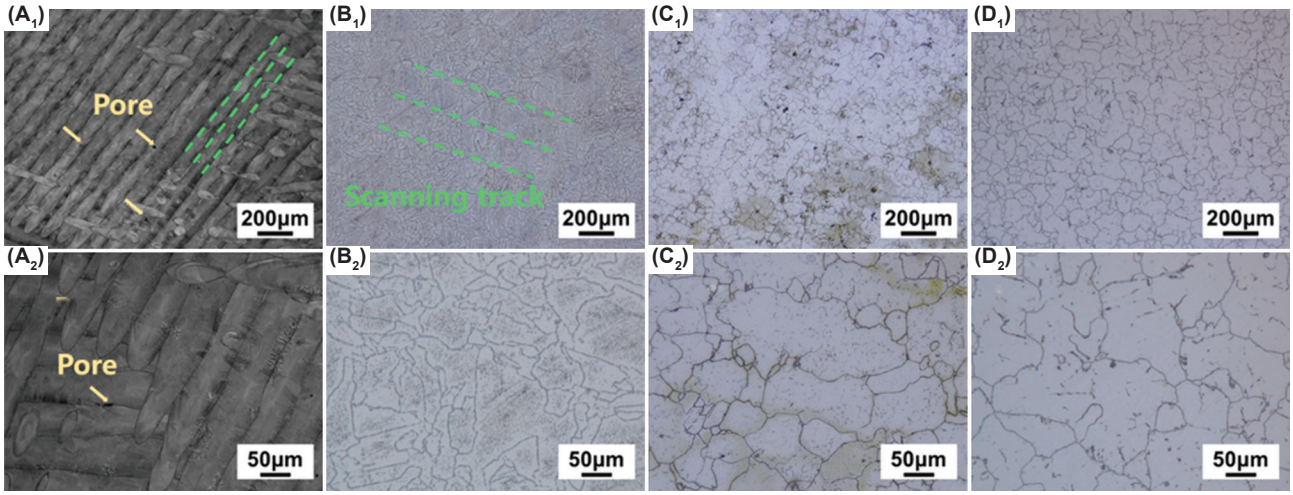

Figure 2. Optical microscopy microstructural morphology and local magnified region of (A_1 and A_2) as built, (B_1 and B_2) HIP1100, (C_1 and C_2) HIP1180, and (D_1 and D_2) HIP1210 specimens. Scale bar: 50 μm, magnification: (A_1-D_1) ×200; (A_2-D_2) ×1,000.
Abbreviation: HIP: Hot isostatic pressing.

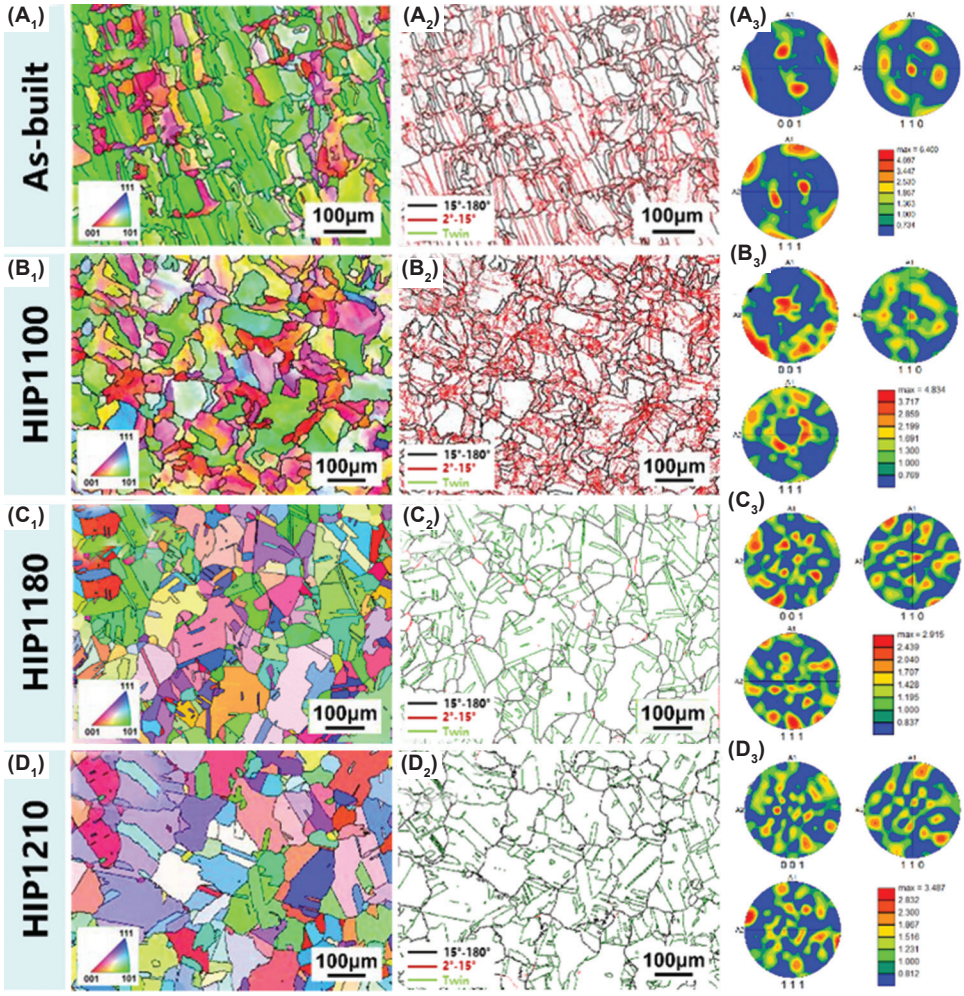

Figure 3. Electron backscattered diffraction results of the as-built, HIP1100, HIP1180, and HIP1210 specimens. (A_1, B_1, C_1, and D_1) Inverse pole figure maps, (A_2, B_2, C_2, and D_2) grain boundary maps, and (A_3, B_3, C_3, and D_3) pole figure map. Scale bar: 100 μm, magnification: ×500.
Abbreviation: HIP: Hot isostatic pressing.

of substructure boundaries, accompanied by high-density dislocations. Numerous low-angle grain boundaries were also observed at HIP1100, with the proportion decreasing to 49.7%, suggesting that the substructures remained, as shown in Figure $3B_2$. At HIP1180, the low-angle grain boundaries almost disappeared with a proportion of 4.3%, as displayed in Figure $3C_2$. In addition, a large number of annealing twins appeared and were measured at approximately 31% (the ratio of twin boundary length to the total grain boundary length), the low interface energy of which was beneficial for alleviating the stress concentration within the specimen. At HIP1210, the low-angle grain boundaries were completely replaced by the high-angle grain boundaries and twin boundaries, as displayed in Figure $3D_2$.

To intuitively characterize the grain recrystallization under different HIP treatments, the EBSD data were processed, and the kernel average misorientation map was employed to mark the recrystallized grains by setting a specific range for local strain, as shown in Figure $4A_1$, B_1, C_1, and D_1. The as-built specimen showed minimal recrystallization, while more recrystallization occurred in the HIP specimens. At HIP1100, the incomplete recrystallization of the Hastelloy X specimen was observed, with recrystallized grains accounting for 43% of the total. At HIP1180 and HIP1210, 98% and 100% of the equiaxed grains underwent recrystallization, respectively, indicating that the recrystallization process was almost completed. The diagrams of grain size distribution were statistically analyzed in Figure $4A_2$, B_2, C_2, and D_2. In the as-built specimen, the grain size was below 60 μm, with an average value of 16.4 μm. At HIP1100, a large number of microstructure characteristics in the as-built specimen were retained with an average grain size of

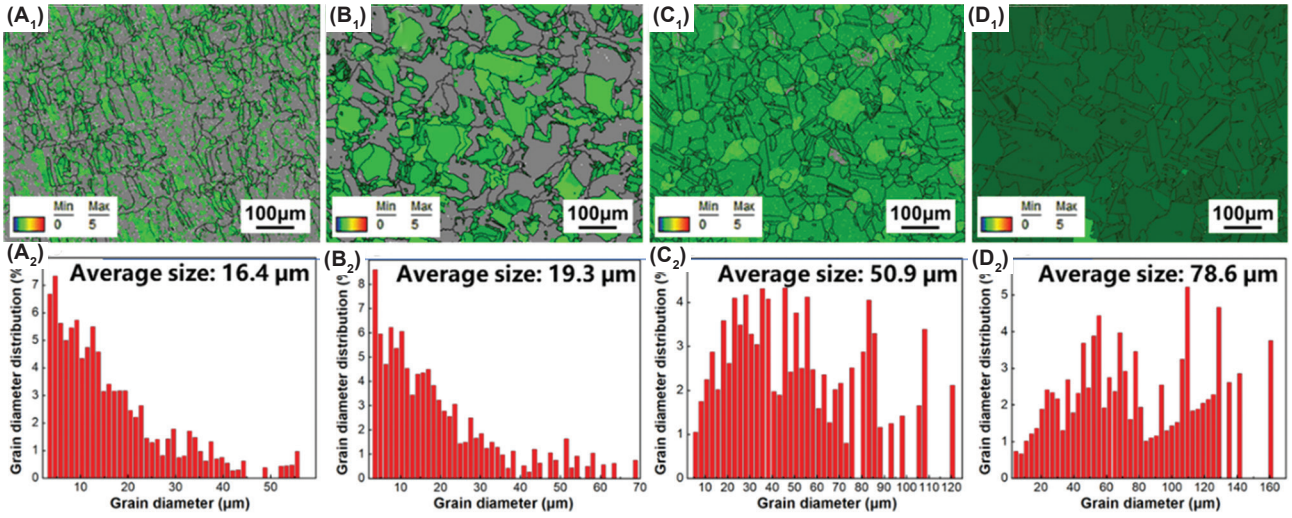

Figure 4. Kernel average misorientation map and the corresponding diagrams of grain size distribution. Results of (A_1 and A_2) as built, (B_1 and B_2) HIP1100, (C_1 and C_2) HIP1180, and (D_1 and D_2) HIP1210 specimens. Scale bar: 100 μm, magnification: ×500.
Abbreviation: HIP: Hot isostatic pressing.

19.3 μm. At HIP1180, the microstructure transitioned into the stage of complete recrystallization, leading to an increase in the average grain size to 50.9 μm. At HIP1210, the average grain diameter developed to 78.6 μm due to grain engulfment. In summary, the grain recrystallization process was prompted as the HIP temperature increased, accompanied by the microstructure transformation from the fine columnar grains to coarse equiaxed grains.

To investigate phase evolution within the grains and along the grain boundaries, the SEM morphology of carbides in HIP1100, HIP1180, and HIP1210 specimens was examined, and the corresponding diagrams of carbide size distribution are presented in Figure 5. In all HIP-treated specimens, white precipitates were observed both intragranularly and along grain boundaries. This can be attributed to the extended holding time with the carbide precipitation temperature range during the HIP soaking process, compared to the as-built specimen, which promoted more extensive carbide precipitation.[34] At HIP1100, carbides were distributed within the grains and also appeared as discrete particles along the grain boundaries, as depicted in Figure $5A_1$-A_4. In addition, it was found that the carbide size predominantly ranged from 0.05 μm to 0.2 μm with an average size of 0.279 μm. As the HIP temperature increased to 1,180°C, the carbides inside the grains partially dissolved, while carbides along the grain boundaries distributed continuously with a chain-like pattern, as shown in Figure $5B_1$-B_4. In addition, the average size of carbides increased to 0.40 μm. At HIP1210, the carbides within the grains completely disappeared, while those at the grain boundaries coarsened to envelop the entire grain, accompanied by an average size of 0.41 μm, as shown in Figure $5C_1$-C_4.

When the HIP temperature increased from 1,100°C to 1,210°C, the solubility of the solute element carbon in nickel within the Hastelloy X alloy decreased,[35] contributing to the enhanced precipitation of carbides. This resulted in an increase in the average carbide size. Moreover, during the HIP treatments, the loose structure of the grain boundaries served as a rapid diffusion pathway for solute elements,[36] leading to a higher precipitation rate of carbides along grain boundaries compared to within the grains. Consequently, carbides segregating along the grain boundaries exhibited larger sizes. At HIP1100, the distribution of dispersed carbides within the grains and particle carbides at the grain boundaries was attributed to the limited diffusion capability of the solute elements. At HIP1180, both the carbide re-dissolution within the grains and the carbide accumulation along the grain boundaries were prompted by the enhanced diffusion capability of the solute elements. As the HIP temperature increased to 1,210°C, intragranular carbides were completely re-dissolved, while extensive diffusion of solute elements led to significant coarsening of carbides along grain boundaries.

Different types and distribution patterns of carbides contribute differently to the strengthening of mechanical properties.[37,38] To further study the carbide characteristics following HIP treatments, the TEM morphology, selected area electron diffraction map, and energy dispersive spectroscopy map of carbides in the HIP1180 specimen are displayed in Figure 6. The chain-like carbides exhibited dimensions exceeding 1 μm in length and 60 nm in width, as shown in Figure 6A and B. The carbides were identified as M_6C (rich in molybdenum) and $M_{23}C_6$ (rich in chromium), as shown in Figure 6C. An interspersed distribution of

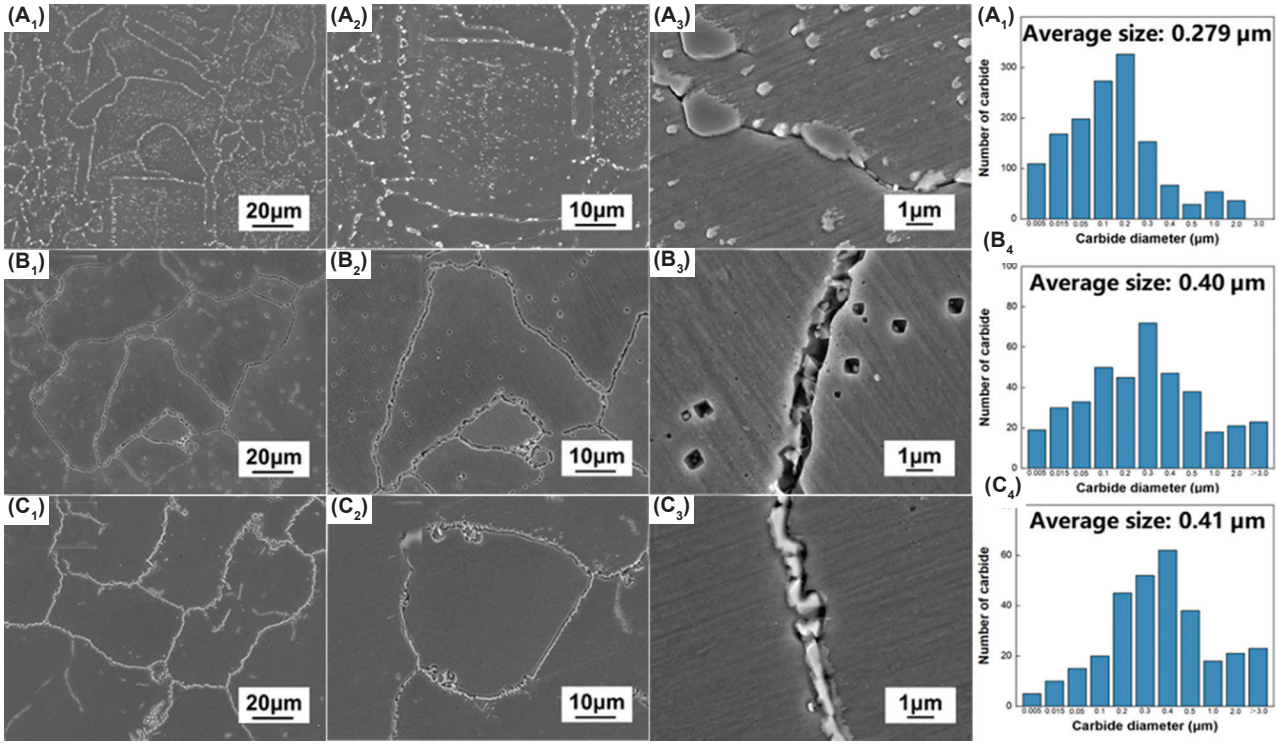

Figure 5. Carbide morphology and the corresponding diagrams of carbide size distribution. Results of (A_1-A_4) HIP1100, (B_1-B_4) HIP1180, and (C_1-C_4) HIP1210 specimens. Scale bars: (A_1-C_1) 20 μm; (A_2-C_2) 10 μm; (A_3-C_3) 1 μm, magnifications: (A_1-C_1) ×2,000; (A_2-C_2) ×5,000; (A_3-C_3) ×30,000.
Abbreviation: HIP: Hot isostatic pressing.

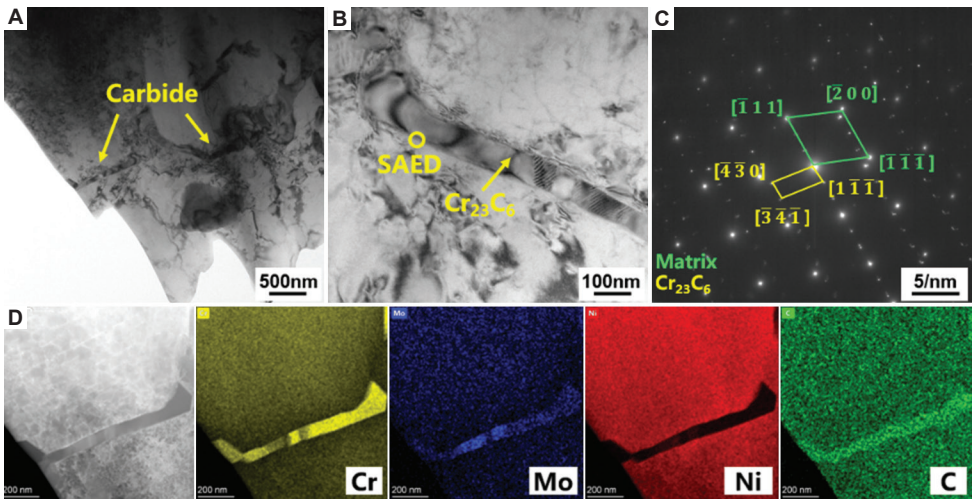

Figure 6. Transmission electron microscopic morphology of carbides in the HIP1180 specimen. (A and B) carbide morphology and local magnified region, (C) selected area electron diffraction, and (D) energy dispersive spectroscopy mapping profile of carbides. Scale bars: (A) 500 nm; (B) 100 nm; (C) 5 nm; (D) 200 nm, magnifications: (A) ×60,000; (B) ×300,000; (C) ×300,000; (D) ×150,000.
Abbreviations: C: Carbon; Cr: Chromium; Mo: Molybdenum; Ni: Nickel; HIP: Hot isostatic pressing.

the carbides consisting of M_6C and $M_{23}C_6$ was observed along the grain boundaries, as depicted in Figure 6D. This distribution pattern is attributed to the simultaneous precipitation of both carbide types in various areas, followed by preferential growth along grain boundaries.

3.2. Mechanical properties at room temperature

A comparison of the hardness of the as-built, HIP1100, HIP1180, and HIP1210 specimens is shown in Figure 7A. The as-built specimen exhibited the highest hardness with a value of 268 HV, while the HIP1100, HIP1180,

and HIP1210 specimens demonstrated hardness values of 244.24 HV, 214.42 HV, and 211.44 HV, representing a decline of 8.9%, 20.0%, and 21.1%, respectively. This could be attributed to the progressed recrystallization process with the elevated HIP temperature. The substructures gradually vanished, accompanied by a reduction in the number of low-angle grain boundaries, as depicted in Figure 3. Therefore, the hindrance for substructures to dislocation slip is reduced, leading to a decline in hardness.

Tensile tests of all specimens at room temperature were conducted, and the results are presented in Figure 7B. Compared to the as-built specimen, the tensile strength and elongation of the HIP specimens improved, while the yield strength decreased. The improvement of tensile strength of HIP specimens was achieved due to the reduction of porosity through the HIP treatment. In addition, as the HIP temperature increased, the elongation gradually improved, reaching a maximum value of 45% at HIP1210, while the yield strength and tensile strength declined. The HIP specimen, HIP1100, achieved the highest yield strength of 569 MPa and the highest tensile strength of 774 MPa, which was associated with the synergistic effect of the dislocation slip, grain size, and carbide distribution. On one hand, dislocation slip was effectively hindered at HIP1100 due to a higher proportion of low-angle grain boundaries compared to HIP1180 and HIP1210. On the other hand, the presence of fine grains and small, dispersed particle carbides contributed to grain refinement strengthening and dispersion strengthening, respectively.

Figure 8 presents the fracture surfaces of the as-built, HIP1100, HIP1180, and HIP1210 tensile specimens tested at room temperature. Cracks were observed on the fracture surfaces of the HIP1180 and HIP1210 specimens. This cracking is attributed to the precipitation and

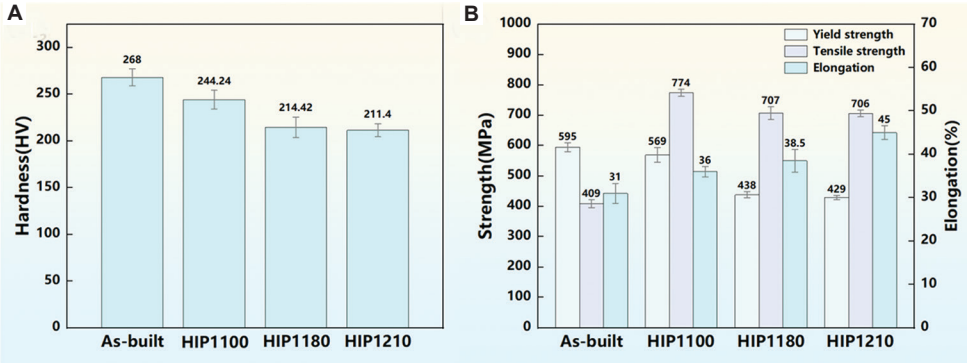

Figure 7. Mechanical properties obtained at room temperature of as-built, HIP1100, HIP1180, and HIP1210 specimens. (A) Microhardness and (B) Yield strength, tensile strength, and elongation.
Abbreviation: HIP: Hot isostatic pressing.

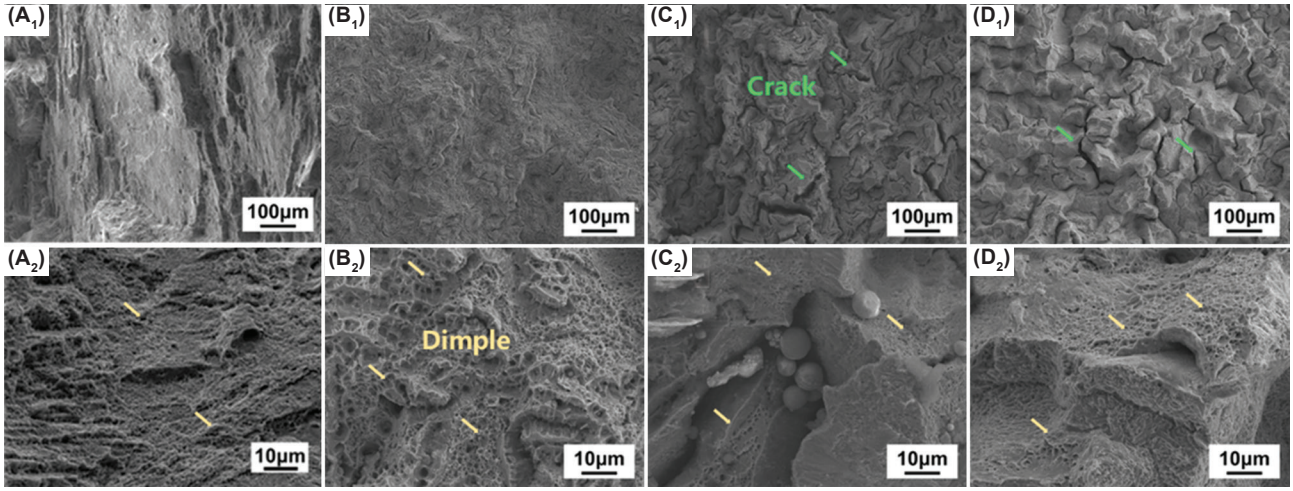

Figure 8. Fracture surfaces of Hastelloy X tensile specimens failed at room temperature. Results of (A_1 and A_2) as-built, (B_1 and B_2) HIP1100, (C_1 and C_2) HIP1180, and (D_1 and D_2) HIP 1210 specimens. Scale bars: (A_1-D_1) 100 μm; (A_2-D_2) 10 μm, magnifications: (A_1-D_1) ×500; (A_2-D_2) ×5,000.
Abbreviation: HIP: Hot isostatic pressing.

coarsening of carbides along the grain boundaries, which eventually envelop the grains and increase the brittleness of the grain boundaries, as shown in Figure 5. During subsequent plastic deformation, the secondary cracks were induced through crystal fractures.[39] Furthermore, higher magnification images revealed numerous dimples in the fracture surface of all specimens, proving that the tensile failure mode at room temperature was characteristic of ductile fracture.

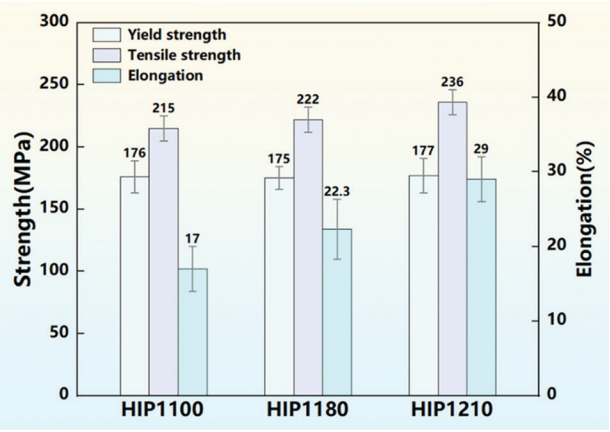

Figure 9. The yield strength, tensile strength, and elongation obtained at high temperatures for HIP1100, HIP1180, and HIP1210 specimens
Abbreviation: HIP: Hot isostatic pressing.

3.3. Mechanical properties at high temperature

To evaluate high-temperature mechanical properties, the tensile results of HIP specimens at 900°C are presented in Figure 9. As reported in recent studies,[19-21,40] HIP treatment significantly improved the high-temperature mechanical properties compared to the as-built condition. The yield strength, tensile strength, and elongation obtained in the high-temperature tensile test were lower than those at room temperature. As HIP temperature increased, the yield strength exhibited no significant changes, while the elongation gradually increased, reaching a maximum value of 29.0% at HIP1210. Interestingly, the trend for tensile strength at high temperature differed from that observed at room temperature. The tensile strength of the specimen at HIP1210 reached 236 MPa, representing an improvement of 9.8% and 6.3% compared to the HIP1100 and HIP1180 specimens, respectively.

The carbide morphology within the high-temperature deformation region and the statistical diagrams of carbide size distribution of HIP1100, HIP1180, and HIP1210 specimens are displayed in Figure 10. After the

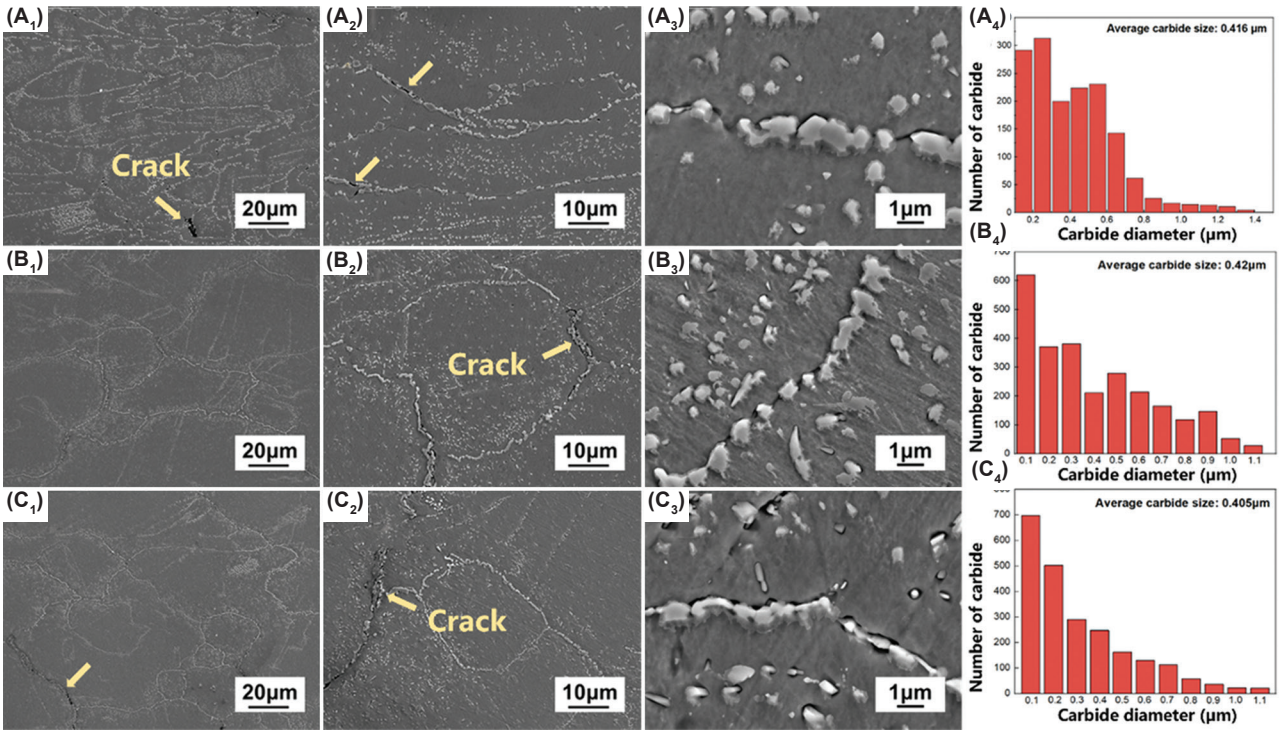

Figure 10. The carbide morphology of the deformation region failed at high tensile temperature, and the corresponding diagrams of carbide size distribution. Results of (A_1-A_4) HIP1100, (B_1-B_4) HIP1180, and (C_1-C_4) HIP1210 specimens. Scale bars: (A_1-C_1) 20 μm; (A_2-C_2) 10 μm; (A_3-C_3) 1 μm, magnifications: (A_1-C_1) ×2,000; (A_2-C_2) ×5,000; (A_3-C_3) ×30,000.
Abbreviation: HIP: Hot isostatic pressing.

high-temperature tensile test, cracks were observed in areas enriched with carbides along the grain boundaries of all specimens. The average carbide size of the HIP1100 specimen increased from 0.279 μm to 0.416 μm, as shown in Figure 10A_1-A_4. Moreover, the carbide distribution along the grain boundaries transformed from particle distribution to bulk distribution. However, the average carbide size at both HIP1180 and HIP1210 showed minimal changes compared to that of room temperature, as shown in Figure 10B_1-B_4 and C_1-C_4. Furthermore, carbides were observed within the grains in the HIP1180 and HIP1210 specimens. However, the carbides at the grain boundaries exhibited a chain-like distribution, with a higher concentration on grain boundaries compared to within the grains.

Figure 11 illustrates the microstructural morphology and the local magnified region of the deformation region failed at the 900°C tensile test of HIP specimens. Long cracks penetrating the tensile specimen were observed in the HIP1100 specimen, as shown in Figure 11A_1-A_3. In the HIP1180 specimen, the wedge cracks were confined solely to a local region, as presented in Figure 11B_1-B_3. In comparison with the HIP1100 and HIP1180 specimens, crack formation in the HIP1210 specimen was effectively suppressed, with cracks appearing smaller, as depicted in Figure 11C_1-C_3. In addition, most cracks occurred and propagated along the grain boundaries due to its brittleness.

Figure 12 illustrates the fracture surface of HIP tensile specimens at high-temperature deformation. Part of the characteristics of laser scanning morphology were retained on the fracture surface at HIP1100, accompanied by obvious cracks, as shown in Figure 12A_1 and A_2. The fracture surface of HIP1180 exhibited a pronounced massive pattern morphology, which corresponded to the brittleness of the grain boundaries, as shown in Figure 12B_1 and B_2. Compared to the HIP1100 and HIP1180 specimens, this massive feature was even more prominent in the HIP1210 specimen, demonstrating a typical characteristic of intergranular fracture, as presented in Figure 12C_1 and C_2.

Based on the above analysis, the high-temperature fracture mechanisms of the HIP specimens are presented in Figure 13. During the 900°C tensile test, carbides continued to precipitate and coarsen in the HIP specimens. Due to the enhanced diffusion capability of solute elements in the high-temperature tensile test,[37] these elements exhibited a propensity to segregate into regions of high-density dislocations and grain boundaries, promoting carbide precipitation and coarsening in those areas. Therefore, the growth rate of carbides was higher at the grain boundaries than within the grains. Due to the short duration of the high-temperature tensile test, variations in carbide morphology among the different HIP specimens were primarily governed by their morphology before deformation. In the HIP1100 specimen, the presence of numerous vacancies and the discontinuous distribution of particle carbides along the grain boundaries before deformation proved conducive to the carbides during the tensile test, as shown in Figure 13A_1 and A_2. Consequently,

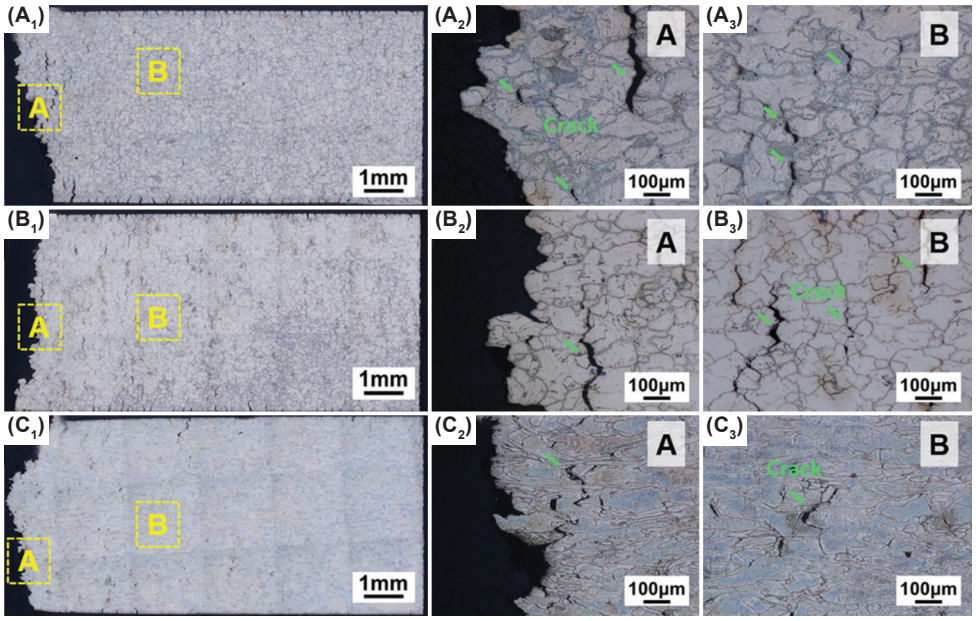

Figure 11. Microstructural morphology of the deformation region failed at high tensile temperature. Results of (A_1-A_3) HIP1100, (B_1-B_3) HIP1180, and (C_1-C_3) HIP1210 specimens. Scale bars: (A1-C1) 1 mm; (A2-C2, A3-C3) 100 μm, magnifications: (A_1-C_1) ×100; (A_2-C_2, A_3-C_3) ×500.
Abbreviation: HIP: Hot isostatic pressing.

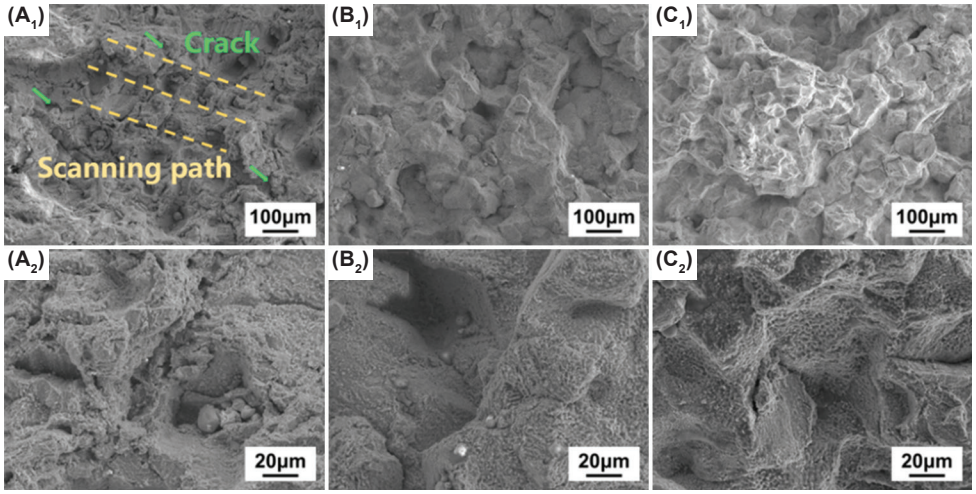

Figure 12. The fracture surface of Hastelloy X tensile specimens failed at high temperatures. Results of (A_1 and A_2) HIP1100, (B_1 and B_2) HIP1180, and (C_1 and C_2) HIP1210 specimens. Scale bars: (A_1-D_1) 100 μm; (A_2-D_2) 20 μm, magnifications: (A_1-D_1) ×500; (A_2-D_2) ×2,500.
Abbreviation: HIP: Hot isostatic pressing.

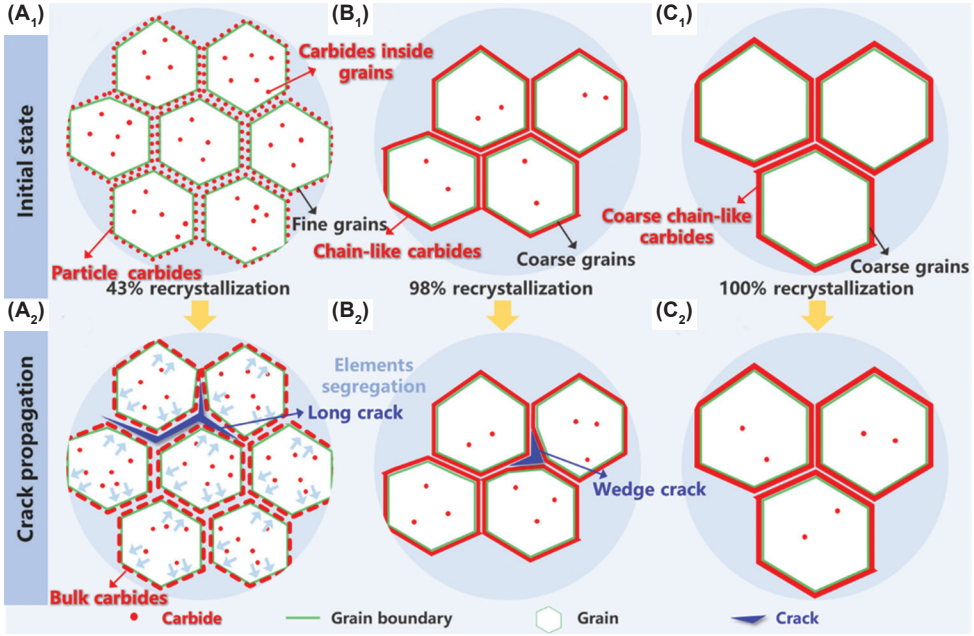

Figure 13. Schematic diagram of high-temperature fracture mechanism. (A_1 and A_2) HIP1100, (B_1 and B_2) HIP1180, and (C_1 and C_2) HIP1210 specimen.
Abbreviation: HIP: Hot isostatic pressing.

the carbides along the grain boundaries significantly coarsened with uneven carbide size after the 900°C tensile test, while the carbides within the grains remained finely dispersed. In contrast, due to the continuous carbide distribution along the grain boundaries before deformation, the carbides in the HIP1180 and HIP1210 specimens precipitated predominantly near the grain boundaries, as shown in Figure 13B_1, B_2, C_1, and C_2. Moreover, only a small number of carbides were observed to be dispersed within the grains.

In contrast to the strengthening effect during room temperature tensile testing, the weakening of grain boundaries occurred during the high temperature tensile test, contributing to differing crack propagation mechanisms in different HIP specimens. During the high-temperature tensile deformation, dislocation pile-up at grain boundaries was alleviated under the combined effect of high temperature and tensile stress,[41] contributing to the reduced strength of the grain boundaries. Therefore, grain boundary sliding and migration became more likely, with

pores preferentially forming in these weakened regions.[42] In the HIP1100 specimen, hard carbides distributed along the grain boundaries were characterized by lower ductility compared to the matrix, contributing to the desynchronized deformation between the carbides and the matrix. Moreover, the large-sized carbides among the discontinuous carbides distributed along the grain boundaries induced localized stress concentrations,[39] making these coarse carbides potential weak regions. Subsequently, cracks were prone to initiate within the bulk carbides and at grain triple junctions, propagating[20] and forming intergranular fracture surfaces and secondary cracks extending along the grain boundaries. In addition, compared to the HIP1180 and HIP1210 specimens, the small-sized grains at HIP1100 resulted in a reduction in the number of grain boundaries, which further exacerbated boundary weakening. This microstructural condition corresponded to reduced tensile strength and elongation, along with the formation of long cracks penetrating the specimens. On the contrary, when the HIP temperature increased to 1,180°C and 1,210°C, the chain-like carbides along the grain boundaries enhanced the strength of the grain boundaries, inhibiting stress concentrations. Moreover, the number of grain boundaries decreased, thereby limiting crack propagation.[22] As a result, the HIP1180 and HIP1210 specimens both achieved improved tensile strength and elongation, attributed to the synergistic effect of reduced number of grain boundaries and chain-like distribution of carbides. These specimens demonstrated fracture morphologies characterized by wedge-shaped cracks and minor cracks, respectively.

4. Conclusion

The microstructure evolution and mechanical properties of LPBF-manufactured Hastelloy X alloy following various HIP treatments at both room and high temperatures were investigated. When the HIP temperature increased from 1,100°C to 1,210°C, the recrystallization process gradually progressed and achieved completion at 1,210°C. The proportion of low-angle grain boundaries decreased from 49.7% at HIP1100 to 4.3% at HIP1180, and eventually to 0% at HIP1210. The carbides along the grain boundaries transformed from particle distribution at HIP1100 to chain-like distribution at HIP1180, and coarse chain-like distribution at HIP1210.

After the HIP treatments, the yield strength decreased, while the tensile strength and elongation increased compared to the as-built specimen. As the HIP temperature increased, the elongation of the HIP specimens gradually improved, reaching a maximum value of 45% at HIP1210. The tensile strength declined, achieving a value of 774 MPa at HIP1100 due to restrained dislocation slip, grain refinement strengthening, and carbide dispersion strengthening.

Compared to the pre-deformation condition, significant carbide coarsening occurred along the grain boundaries in the HIP1100 specimen during high-temperature tensile testing, while minimal changes were observed for the HIP1180 and HIP1210 specimens. As the HIP temperature increased, the tensile strength and elongation both improved due to the synergistic effect of reduced number of grain boundaries and the chain-like distribution of carbides, reaching a maximum tensile strength of 236 MPa and elongation of 29.0% at HIP1210.

Under room temperature tensile testing, the fracture surfaces exhibited typical ductile failure with numerous dimples. In contrast, during high-temperature tensile testing, the cracks primarily propagated along the grain boundaries, with the HIP1210 specimen exhibiting a better capacity for crack inhibition. Compared to the HIP1100 and HIP1180 specimens, the massive feature presented on the fracture surface of HIP1210 was more pronounced, demonstrating a typical characteristic of intergranular fracture.

Acknowledgments

None.

Funding

The research was supported by the National Natural Science Foundation of China (No. 52475332) and the Taishan Scholars Foundation of Shandong Province (No. tsqn202211307).

Conflict of interest

Dr. Swee Leong Sing is the Editor-in-Chief of this journal, but was not in any way involved in the editorial and peer-review process conducted for this paper, directly or indirectly. Separately, other authors declared that they have no known competing financial interests or personal relationships that could have influenced the work reported in this paper.

Author contributions

Conceptualization: Junjun Jiang
Data curation: Bingqiu Wang, Yiming Sun, Caiwang Tan
Formal analysis: Caiwang Tan
Investigation: Bingqiu Wang
Methodology: Rongrong Huang, Bo Chen, Caiwang Tan
Resources: Junjun Jiang
Supervision: Rongrong Huang, Bo Chen, Xiaoguo Song
Validation: Linan Xue
Writing – original draft: Bingqiu Wang

Writing – review & editing: Yiming Sun, Xiaohui Zhou, Swee Leong Sing

Ethics approval and consent to participate

Not applicable.

Consent for publication

Not applicable.

Availability of data

All data analyzed have been presented in the paper.

References

1. Pourbabak S, Montero-Sistiaga ML, Schryvers D, Van Humbeeck J, Vanmeensel K. Microscopic investigation of as built and hot isostatic pressed hastelloy X processed by selective laser melting. *Mater Charact*. 2019;153:366-371.

   doi: 10.1016/j.matchar.2019.05.024

2. Iveković A, Montero-Sistiaga ML, Vleugels J, Kruth JP, Vanmeensel K. Crack mitigation in laser powder bed fusion processed hastelloy X using a combined numerical-experimental approach. *J Alloys Compd*. 2021;864:158803.

   doi: 10.1016/j.jallcom.2021.158803

3. Xu L, Gao Y, Zhao L, Han Y, Jing H. Ultrasonic micro-forging post-treatment assisted laser directed energy deposition approach to manufacture high-strength hastelloy X superalloy. *J Mater Proc Technol*. 2022;299:117324.

   doi: 10.1016/j.jmatprotec.2021.117324

4. Blakey-Milner B, Gradl P, Snedden G, *et al*. Metal additive manufacturing in aerospace: A review. *Mater Design*. 2021;209:110008.

   doi: 10.1016/j.matdes.2021.110008

5. Kalender M, Kılıç SE, Ersoy S, Bozkurt Y, Salman S. Additive manufacturing and 3D printer technology in aerospace industry. *2019 9th International Conference on Recent Advances in Space Technologies (RAST)*. 2019. p. 689-694.

   doi: 10.1109/RAST.2019.8767881

6. Yu CH, Peng RL, Lee TL, Luzin V, Lundgren JE, Moverare J. Anisotropic behaviours of LPBF hastelloy X under slow strain rate tensile testing at elevated temperature. *Mater Sci Eng A*. 2022;844:143174.

   doi: 10.1016/j.msea.2022.143174

7. Markovic P, Scheel P, Wróbel R, Leinenbach C, Mazza E, Hosseini E. Cyclic mechanical response of LPBF hastelloy X over a wide temperature and strain range: Experiments and modeling. *Int J Solids Struct*. 2024;305:113047.

   doi: 10.1016/j.ijsolstr.2024.113047

8. Li X, Esmaeilizadeh R, Hosseini E. Microstructure and mechanical response of as-built and solution-annealed LPBF hastelloy X under high-temperature fatigue loading. *Add Manufact Lett*. 2024;10:100227.

   doi: 10.1016/j.addlet.2024.100227

9. Li R, Cheng L, Liu J, *et al*. Modeling and analysis of the mechanical anisotropy of hastelloy X alloy fabricated by laser powder bed fusion. *J Mater Res Technol*. 2024;33:7949-7960.

   doi: 10.1016/j.jmrt.2024.11.148

10. Kong D, Ni X, Dong C, *et al*. Anisotropic response in mechanical and corrosion properties of hastelloy X fabricated by selective laser melting. *Constr Build Mater*. 2019;221:720-729.

    doi: 10.1016/j.conbuildmat.2019.06.132

11. Li C, Liu Y, Shu T, Guan W, Wang S. Effect of solution heat treatment on microstructure, mechanical and electrochemical properties of hastelloy X fabricated by laser powder bed fusion. *J Mater Res Technol*. 2023;24:1499-1512.

    doi: 10.1016/j.jmrt.2023.03.108

12. Liu G, Li B, Zhang S, *et al*. Effect of Fe-based metallic glass on microstructure and properties of hastelloy X manufactured by laser powder bed fusion. *J Alloys Compd*. 2023;966:171561.

    doi: 10.1016/j.jallcom.2023.171561

13. Xie Y, Teng Q, Shen M, *et al*. The role of overlap region width in multi-laser powder bed fusion of hastelloy X superalloy. *Virtual Phys Prototyp*. 2023;18:e2142802.

    doi: 10.1080/17452759.2022.2142802

14. Keshavarzkermani A, Esmaeilizadeh R, Enrique PD, *et al*. Static recrystallization impact on grain structure and mechanical properties of heat-treated hastelloy X produced via laser powder-bed fusion. *Mater Charact*. 2021;173:110969.

    doi: 10.1016/j.matchar.2021.110969

15. Cheng X, Du Z, Chu S, *et al*. The effect of subsequent heating treatment on the microstructure and mechanical properties of additive manufactured hastelloy X alloy. *Mater Charact*. 2022;186:111799.

    doi: 10.1016/j.matchar.2022.111799

16. Ma Q, Dong K, Li F, *et al*. Recent progress in electromagnetic microwave absorption of additively manufactured carbon fiber-reinforced polymer structures. *ESAM*. 2025;1:025160008.

    doi: 10.36922/ESAM025160008

17. Chan YY, Chao Y, Kuo CN. Mechanical properties and energy absorption capability improvement of Ti-6Al-4V porous materials through porous structure design optimization. *ESAM*. 2025;1:025170009.

    doi: 10.36922/ESAM025170009

18. Keller C, Mokhtari M, Vieille B, Briatta H, Bernard P. Influence of a rescanning strategy with different laser powers on the microstructure and mechanical properties of hastelloy X elaborated by powder bed fusion. *Mater Sci Eng A*. 2021;803:140474.

doi: 10.1016/j.msea.2020.140474

19. Montero-Sistiaga ML, Liu Z, Bautmans L, *et al*. Effect of temperature on the microstructure and tensile properties of micro-crack free hastelloy X produced by selective laser melting. *Add Manufact*. 2021;31:100995.

doi: 10.1016/j.addma.2019.100995

20. Agrawal S, Avadhani GS, Suwas S. Deformation behaviour of additively manufactured hastelloy X at high temperatures: The role of concurrent carbide precipitation. *J Alloys Compd*. 2025;1021:179636.

doi: 10.1016/j.jallcom.2025.179636

21. Zheng L, Schmitz G, Meng Y, Chellali MR, Schlesiger R. Mechanism of intermediate temperature embrittlement of Ni and Ni-based superalloys. Crit Rev *Solid State Mater Sci*. 2012;37:181-214.

doi: 10.1080/10408436.2011.613492

22. Han Q, Mertens R, Montero-Sistiaga ML, *et al*. Laser powder bed fusion of hastelloy X: Effects of hot isostatic pressing and the hot cracking mechanism. *Mater Sci Eng A*. 2018;732:228-239.

doi: 10.1016/j.msea.2018.07.008

23. Wang H, Chen L, Dovgyy B, *et al*. Micro-cracking, microstructure and mechanical properties of hastelloy-X alloy printed by laser powder bed fusion: As-built, annealed and hot-isostatic pressed. *Add Manufact*. 2021;39:101853.

doi: 10.48550/arXiv.2011.11003

24. Sanchez-Mata O, Muñiz-Lerma JA, Wang X, *et al*. Microstructure and mechanical properties at room and elevated temperature of crack-free hastelloy X fabricated by laser powder bed fusion. *Mater Sci Eng A*. 2020;780:139177.

doi: 10.1016/j.msea.2020.139177

25. Zhou W, Tian Y, Wei D, *et al*. Effects of heat treatments on the microstructure and tensile properties of IN738 superalloy with high carbon content fabricated via laser powder bed fusion. *J Alloys Compd*. 2023;953:170110.

doi: 10.1016/j.jallcom.2023.170110

26. Yuan Z, Chang F, Chen A, *et al*. Microstructure and properties of SLM-hastelloy X alloy after different hot isostatic pressing + heat treatment. *Mater Sci Eng A*. 2022;852:143714.

doi: 10.1016/j.msea.2022.143714

27. Shaji Karapuzha A, Fraser D, Zhu Y, Wu X, Huang A. Effect of solution heat treatment and hot isostatic pressing on the microstructure and mechanical properties of hastelloy X manufactured by electron beam powder bed fusion. *J Mater Sci Technol*. 2022;98:99-117.

doi: 10.1016/j.jmst.2021.04.059

28. Mani Pandi AS, Senthil Kumar VS. A review: Fabrication techniques of the hastelloy (super alloy) composites and it impacts on the properties. *Mater Today Proc*. 2024.

doi: 10.1016/j.matpr.2024.05.115

29. Qin Y, Liu Y, Guan W, Wang K. Material corrosion characteristics of heat-treated SLM-ed hastelloy X in electrochemical machining process. *Mater Today Commun*. 2024;39:109105.

doi: 10.1016/j.mtcomm.2024.109105

30. Marchese G, Bassini E, Aversa A, *et al*. Microstructural evolution of post-processed hastelloy X alloy fabricated by laser powder bed fusion. *Materials (Basel)*. 2019;12:486.

doi: 10.3390/ma12030486

31. Tomus D, Tian Y, Rometsch PA, Heilmaier M, Wu X. Influence of post heat treatments on anisotropy of mechanical behaviour and microstructure of hastelloy-X parts produced by selective laser melting. *Mater Sci Eng A*. 2016;667:42-53.

doi: 10.1016/j.msea.2016.04.086

32. Li Y, Qi H, Hou H, Lei L. *Effects of Hot Isostatic Pressing on Microstructure and Mechanical Properties of Hastelloy X Samples Produced by Selective Laser Melting*. Netherlands: Atlantis Press; 2017. p. 31-40.

33. Sun S, Teng Q, Xie Y, *et al*. Two-step heat treatment for laser powder bed fusion of a nickel-based superalloy with simultaneously enhanced tensile strength and ductility. *Add Manufact*. 2021;46:102168.

doi: 10.1016/j.addma.2021.102168

34. Liu M, Zeng Q, Hua Y, *et al*. High-temperature tensile properties of hastelloy x produced by laser powder bed fusion with different heat treatments. *Metals*. 2022;12:1435.

doi: 10.3390/met12091435

35. Montero-Sistiaga ML, Pourbabak S, Van Humbeeck J, Schryvers D, Vanmeensel K. Microstructure and mechanical properties of hastelloy X produced by HP-SLM (high power selective laser melting). *Mater Design*. 2019;165:107598.

doi: 10.1016/j.matdes.2019.107598

36. Shu DL, Tian SG, Tian N, Xie J, Su Y. Thermodynamic analysis of carbide precipitation and effect of its configuration on creep properties of FGH95 powder nickel-based superalloy. *Mater Sci Eng A*. 2017;700:152-161.

doi: 10.1016/j.msea.2017.05.108

37. Zhang S, Wang L, Lin X, *et al*. Precipitation behavior of δ phase and its effect on stress rupture properties of selective laser-melted Inconel 718 superalloy. *Compos Part B Eng*.

2021;224:109202.

doi: 10.1016/j.compositesb.2021.109202

38. Zhang S, Lin X, Wang L, *et al*. Strengthening mechanisms in selective laser-melted inconel718 superalloy. *Mater Sci Eng A*. 2021;812:141145.

doi: 10.1016/j.msea.2021.141145

39. Liu M, Zhang K, Liu J, *et al*. High-temperature high cycle fatigue performance of laser powder bed fusion fabricated hastelloy X: Study into the microstructure and oxidation effects. *Mater Design*. 2024;243:113037.

doi: 10.1016/j.matdes.2024.113037

40. Sun Y, Huang R, Lin D, *et al*. Investigation of deformation mechanisms in hastelloy X superalloy manufactured via laser powder-bed fusion: Insights into effects of carbides and cellular structure at elevated temperatures. *J Manufact Processes*. 2023;108:165-179.

doi: 10.1016/j.jmapro.2023.10.083

41. Wu S, Dai SB, Heilmaier M, *et al*. The effect of carbides on the creep performance of hastelloy X fabricated by laser powder bed fusion. *Mater Sci Eng A*. 2023;875:145116.

doi: 10.1016/j.msea.2023.145116

42. Marchese G, Basile G, Bassini E, *et al*. Study of the microstructure and cracking mechanisms of hastelloy X produced by laser powder bed fusion. *Materials (Basel)*. 2018;11:106.

doi: 10.3390/ma11010106

ACCSCIENCE PUBLISHING

OUR JOURNALS

Materials Science in Additive Manufacturing (MSAM) aims to bridge the cutting-edge research between additive manufacturing and the entire spectrum of materials science. The journal covers all applied and fundamentals of processing, synthesis, structure, composition, properties and performance of materials designed or manipulated for additive manufacturing. The journal covers a wide scope of innovative techniques, processes, methods, and applications. Topics of particular interest include, but are not limited to:

- Theory and modelling
- Artificial intelligence
- Polymers
- Metals and alloys
- Ceramics
- Composites
- Magnetic materials
- Smart materials
- Nano-materials
- Materials for electronics
- Characterization techniques

International Journal of AI for Materials and Design is an international, peer-reviewed open-access journal that aims to bridge the cutting-edge research between AI and materials, AI and design. In recent years, the tremendous progress in AI is leading a radical shift of AI research from a mainly academic endeavor to a much broader field with increasing industrial and governmental investments. The maturation of AI technology brings about a step change in the scientific research of various domains, especially in the world of materials and design. Machine learning (ML) algorithms enable researchers to analyze extensive datasets on material properties and accurately predict their behavior in different conditions. This subsequently impact the industry to leverage on big data and advanced analytics to build scientific strategies, scale operational performance of processes and drive innovation.

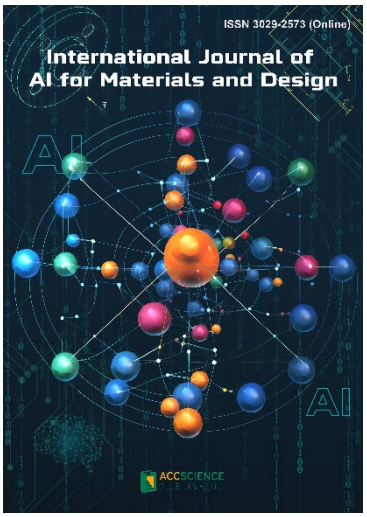

International Journal of AI for Materials and Design covers the following topics: AI or machine learning for material discovery, AI for process optimization, AI and data-driven approaches for product or systems design, application of AI in advanced manufacturing processes such as additive manufacturing, IoT, sensors, robotics, cloud-based manufacturing, intelligent manufacturing for various applications, autonomous experiments, material intelligence, energy intelligence, and AI-linked decarbonization technologies.

Start a new journal

Write to us via email if you are interested to start a new journal with AccScience Publishing. Please attach your CV, professional profile page and a brief pitch proposal in your email. We shall inform you of our decision whether we are interested to collaborate in starting a new journal.

Contact: info@accscience.com

https://accscience.com/journal/ESAM

Contact
www.accscience.com
9 Raffles Place, Republic Plaza 1 #06-00 Singapore 048619
Email: editorial@accscience.com
Phone: +65 8182 1586